

Measurement of the
Branching Fractions of
Semileptonic Kaon Decays and
Extraction of the
CKM Parameter $|V_{us}|$

DISSERTATION
ZUR ERLANGUNG DES GRADES

*„Doktor
der Naturwissenschaften“*

AM FACHBEREICH PHYSIK, MATHEMATIK UND INFORMATIK
DER
JOHANNES GUTENBERG-UNIVERSITÄT
IN MAINZ



JOHANNES GUTENBERG
UNIVERSITÄT MAINZ

Mario Christian Vormstein
GEBOREN IN WILHELMSHAVEN
MAINZ, DEN 19.10.2016

1. Berichtstatter: -

2. Berichtstatter: -

Datum der mündlichen Prüfung: 3. März 2017

ABSTRACT

Semileptonic kaon decays ($K_{l3} = K^+ \rightarrow \pi^0 l^+ \nu$ with $l = e, \mu$) provide a clean way to extract the parameter $|V_{us}|$ of the Cabibbo-Kobayashi-Maskawa (CKM) quark mixing matrix. It is one of the fundamental parameters of the Standard Model and is only accessible via experimental measurement. The NA62 collaboration collected K^+ decay data in 2007 which are analyzed in the presented work. In total $28 \cdot 10^6 K_{\mu 3}$, $37 \cdot 10^6 K_{e 3}$, and $2 \cdot 10^6 K_{2\pi}$ candidates were extracted from the data set and used to compute the ratios of branching fractions

$$\begin{aligned} \frac{\text{Br}(K_{\mu 3})}{\text{Br}(K_{2\pi})} &= 0.16066(12)_{\text{stat.}}(66)_{\text{syst.}} \\ &= 0.1607(7), \\ \frac{\text{Br}(K_{e 3})}{\text{Br}(K_{2\pi})} &= 0.24320(17)_{\text{stat.}}(41)_{\text{syst.}} \\ &= 0.2432(4), \text{ and} \\ \frac{\text{Br}(K_{\mu 3})}{\text{Br}(K_{e 3})} &= 0.66061(17)_{\text{stat.}}(245)_{\text{syst.}} \\ &= 0.6606(25) \end{aligned}$$

which represent the most precise measurements available.

The semileptonic branching fractions $\text{Br}(K_{\mu 3}) = 3.321(19)\%$ and $\text{Br}(K_{e 3}) = 5.027(22)\%$ follow from the world average of $\text{Br}(K_{2\pi})$ measurements. They are used to extract the CKM parameter $|V_{us}| = 0.2219(10)$. The new $|V_{us}|$ result leads to the unitarity relation $|V_{ud}|^2 + |V_{us}|^2 + |V_{ub}|^2 = 0.9983(6)$ which disagrees by 2.8 standard deviations with the CKM unitarity prediction.

The $e - \mu$ lepton universality is tested with the ratio of the semileptonic branching fractions $\frac{\text{Br}(K_{\mu 3})}{\text{Br}(K_{e 3})}$ and agrees with the Standard Model prediction.

ZUSAMMENFASSUNG

Semileptonische Kaonzerfälle ($K_{l3} = K^+ \rightarrow \pi^0 l^+ \nu$ with $l = e, \mu$) ermöglichen eine besonders sauberere Extraktion des Parameters $|V_{us}|$ der Cabibbo-Kobayashi-Maskawa (CKM) Quark-Mischungsmatrix. Dieser ist ein fundamentaler Parameter des Standardmodells und ist nur durch experimentelle Messungen bestimmbar. Die NA62-Kollaboration hat im Jahr 2007 K^+ -Zerfallsdaten aufgenommen, die in der präsentierten Arbeit untersucht wurden. Insgesamt wurden $28 \cdot 10^6 K_{\mu 3}$ -, $37 \cdot 10^6 K_{e 3}$ - und $2 \cdot 10^6 K_{2\pi}$ -Kandidaten selektiert. Diese werden genutzt, um die Verhältnisse

$$\begin{aligned} \frac{\text{Br}(K_{\mu 3})}{\text{Br}(K_{2\pi})} &= 0.16066(12)_{\text{stat.}}(66)_{\text{syst.}} \\ &= 0.1607(7), \\ \frac{\text{Br}(K_{e 3})}{\text{Br}(K_{2\pi})} &= 0.24320(17)_{\text{stat.}}(41)_{\text{syst.}} \\ &= 0.2432(4) \text{ und} \\ \frac{\text{Br}(K_{\mu 3})}{\text{Br}(K_{e 3})} &= 0.66061(17)_{\text{stat.}}(245)_{\text{syst.}} \\ &= 0.6606(25) \end{aligned}$$

zu bestimmen. Diese repräsentieren die derzeit genauesten verfügbaren Messungen.

Die semileptonischen Verzweungsverhältnisse $\text{Br}(K_{\mu 3}) = 3.321(19)\%$ und $\text{Br}(K_{e 3}) = 5.027(22)\%$ werden unter Nutzung des globalen Mittelwerts von $\text{Br}(K_{2\pi})$ bestimmt. Diese dienen als Grundlage für die Bestimmung des CKM-Parameters $|V_{us}| = 0.2219(10)$. Der neue $|V_{us}|$ -Wert führt zur Unitaritätsbeziehung $|V_{ud}|^2 + |V_{us}|^2 + |V_{ub}|^2 = 0.9983(6)$, die um 2.8 Standardabweichungen verschieden ist von der Standardmodell-Vorhersage für die CKM-Unitarität.

Die $e - \mu$ Leptonuniversalität wird mit dem Verhältnis $\frac{\text{Br}(K_{\mu 3})}{\text{Br}(K_{e 3})}$ überprüft und das Ergebnis stimmt mit der Standardmodell-Vorhersage überein.

CONTENTS

1	INTRODUCTION	1
1.1	Motivation	1
1.2	The Standard Model of Particle Physics	2
1.3	The CKM Quark Mixing Matrix	4
1.3.1	Status of Measurements of $ V_{ud} $, $ V_{us} $, and $ V_{ub} $	6
1.4	Semileptonic Kaon Decays	12
1.4.1	Determination of $f_+^{K^0\pi^-}$ from Theory	12
1.4.2	Isospin Breaking Correction for Charged Kaon Decays	13
1.4.3	Electroweak and Electromagnetic Corrections	14
1.4.4	Phase Space Integral $I_{K\ell}$ and Form Factors	14
2	EXPERIMENTAL SETUP	17
2.1	The Super Proton Synchrotron	17
2.2	The Coordinate system	17
2.3	The Kaon beam	18
2.4	The Fiducial volume	20
2.5	The Magnetic Spectrometer	20
2.6	The Hodoscope for Charged Particles	23
2.7	The Liquid Krypton Calorimeter	24
2.8	The Hodoscope for Neutral Particles	25
2.9	The Hadron Calorimeter	26
2.10	The Muon Veto System	27
2.11	The Photon Anti-Counters	28
2.12	The Trigger System	29
2.12.1	The Trigger for Charged Particles	31
2.12.2	The Trigger for Neutral Particles	31
2.12.3	The Trigger Supervisor	31
2.12.4	The Trigger Logic	32
2.13	The Data Acquisition	32
2.13.1	The L3 filter	32
2.14	The Data set	33
3	RECONSTRUCTION	35
3.1	Reconstruction of Magnetic Spectrometer Information	35
3.2	Reconstruction of Calorimeter Information	36
3.3	The Kaon Momentum	37
3.4	The Charged Track	37
3.4.1	The Charged Track Momentum	38
3.4.2	The Charged Vertex	38
3.5	The Neutral Pion π^0	39
3.5.1	The π^0 Momentum	40
3.5.2	The Neutral Vertex	40
3.6	Corrections	41

	3.6.1	DCH Misalignment and Magnetic Field Miscalibration	41
	3.6.2	External Magnetic Fields	42
	3.6.3	LKr Projectivity	42
	3.6.4	LKr Misalignment with Respect to the Drift Chambers	43
	3.6.5	LKr Non-Linearity Correction	44
	3.6.6	LKr Cell-by-Cell Correction	44
	3.7	Reconstruction and Analysis Software COMPACT	44
4		MONTE CARLO SIMULATION	45
	4.1	Beam Simulation	45
	4.2	Kaon Decay Generators	46
	4.2.1	The KLOE Generator	46
	4.2.2	$K^+ \rightarrow \pi^0 \mu^+ \nu$ Generator	48
	4.2.3	$K^+ \rightarrow \pi^+ \pi^0 \pi^0$ Generator	48
	4.3	Detector simulation	48
	4.4	Particle decays	49
	4.5	Corrections to the Monte-Carlo simulation	50
	4.5.1	Width of the Kaon Momentum Distribution	50
	4.5.2	Kaon Beam Halo	52
	4.5.3	Detector Corrections	52
	4.6	MC Samples and Acceptance	54
5		EVENT SELECTION AND RATIOS	57
	5.1	Decay Signatures	57
	5.2	Trigger	58
	5.3	Common Selection Criteria for e^+ , μ^+ , and π^+	58
	5.3.1	Charge and Quality	58
	5.3.2	Timing	59
	5.3.3	Geometrical Acceptance	60
	5.3.4	Track Cluster	61
	5.3.5	Charged Vertex	61
	5.4	Particle Identification of e^+ , μ^+ , and π^+	64
	5.4.1	Measurement of the Particle Identification Efficiency with E/p	64
	5.5	Selection Criteria for π^0	74
	5.6	Event Selection Criteria	84
	5.6.1	Number of reconstructed objects	84
	5.6.2	Track Momentum	84
	5.6.3	Missing Mass	87
	5.6.4	Transversal Momentum	87
	5.6.5	Combined Track and π^0 Momentum	91
	5.6.6	Kaon Mass	91
	5.6.7	Additional Energy in the LKr	99
	5.7	Reconstructed candidates	99
	5.8	Kaon flux	103
	5.9	Ratios	105

6	TRIGGER EFFICIENCY	107
6.1	Q_1 sub-trigger efficiency	108
6.2	E_{10} sub-trigger efficiency	109
6.3	TRKLM sub-trigger efficiency	109
6.4	The K_{e2} and $K_{\mu2}$ trigger efficiency	111
6.5	The L_3 -filter efficiency	112
7	SYSTEMATIC UNCERTAINTIES	113
7.1	Particle identification	113
7.2	Trigger	113
7.3	Background estimation	114
7.3.1	Background in $K_{\mu3}$	114
7.3.2	Background in K_{e3}	115
7.3.3	Background in $K_{2\pi}$	117
7.4	Corrections	119
7.4.1	Width of the kaon momentum distribution	119
7.4.2	Kaon halo	121
7.4.3	Detector corrections	121
7.5	MC properties	121
7.5.1	Form Factors in MC	121
7.5.2	Radiative processes in K_{e3}	122
7.6	Summary	124
8	RESULTS AND DISCUSSION	127
8.1	Branching fractions	127
8.2	$ V_{us} $ and CKM matrix unitarity	129
8.3	Lepton universality	131
9	CONCLUSIONS	133
A	APPENDIX	135
A.1	Correction for the width of the kaon momentum	135
A.2	$K^+ \rightarrow \mu^+ \nu_\mu$ selection	136
A.3	$K^+ \rightarrow \pi^+ \pi^0 \rightarrow \pi^+ e^+ e^- \gamma$ selection	138
A.4	Transversal momentum selection criterion	140
	BIBLIOGRAPHY	147

INTRODUCTION

1.1 MOTIVATION

The Standard Model of particle physics has been a huge success for now over 40 years. It describes a large variety of physical processes with very high precision. In many cases, this precision is higher than the current achievable experimental precision.

One requirement in the Standard Model is the unitarity of the so-called Cabibbo-Kobayashi-Maskawa matrix. In recent years, the unitarity condition on the matrix elements

$$|V_{ud}|^2 + |V_{us}|^2 + |V_{ub}|^2 = 1$$

seemed to be perfectly fulfilled. This perfection was lost since new lattice gauge theory calculations became available. These calculations connect the $|V_{us}|$ matrix element with the measurement of semileptonic kaon decays.

Since their discovery in 1947, kaons have become an integral part of studies in particle physics. The decay rates of semileptonic kaon decays currently provide the most precise way to measure the $|V_{us}|$ matrix element. The NA62 collaboration recorded a large data set of kaon decays in 2007. This data set provides an excellent opportunity to add new branching fraction measurements of the decays $K^+ \rightarrow \pi^0 e^+ \nu_e$ and $K^+ \rightarrow \pi^0 \mu^+ \nu_\mu$ to the overall picture. Additionally, the comparison of their decay rates provides a stringent test of the $e - \mu$ lepton universality.

This work presents the measurement of the branching fractions of $K^+ \rightarrow \pi^0 e^+ \nu_e$ and $K^+ \rightarrow \pi^0 \mu^+ \nu_\mu$ with NA62 data from 2007. The hadronic kaon decay $K^+ \rightarrow \pi^+ \pi^0$ is used as normalization channel. This work is organized as follows:

In the remainder of this chapter, the theoretical framework and current status of semileptonic kaon decays and the Cabibbo-Kobayashi-Maskawa matrix are discussed. The experimental setup of the detector and its data acquisition system is presented in Chapter 2. The procedures to reconstruct physical processes from the recorded raw data are explained in Chapter 3. The presented analysis depends on simulations of kaon decays employing Monte Carlo methods. These Monte Carlo simulations and mandatory corrections are described in Chapter 4. To filter out the desired decays, so-called selections are applied to the data. These selections are collections of criteria on different properties of the involved particles. The selections and their outcome

are discussed in Chapter 5. The data acquisition system was not completely efficient. The efficiency is measured from data. These trigger efficiency studies are presented in Chapter 6. Systematic effects of different sources and their impact on the measurement are discussed in Chapter 7. The results of the branching fraction measurement as well as the test of the CKM unitarity and the lepton universality are presented in Chapter 8. This work concludes with Chapter 9.

1.2 THE STANDARD MODEL OF PARTICLE PHYSICS

The Standard Model of particle physics is a theoretical framework to describe the interaction of the point-like constituents of matter with each other. These point-like particles are called Fermions and have a spin of $S = \frac{1}{2}$. Fermions are divided into three families. The first family consists of the up-quark (u), the down-quark (d), the electron (e^-), and the electron neutrino (ν_e). Both quarks build up protons and neutrons (so-called hadrons) and together with electrons they form atoms. All known stable matter is built up by these three particles.

The interactions are described by three (the electromagnetic, the weak, and the strong force) of the four known fundamental forces. Only the fourth fundamental force, gravity, has not been included up to this time. The forces are mediated by gauge bosons with spin $S = 1$. These bosons are the photons (γ) for the electromagnetic force, the gluons (g) for the strong force, and the Z^0 and W^\pm for the weak force. The three fermion families and the gauge bosons are shown in Figure 1.

Only the quarks couple to all three forces, the leptons only to the weak and, if they carry electric charge, to the electromagnetic force. The bosons themselves can also couple to other bosons. So couple gluons with other gluons and W^\pm with photons.

The Standard Model is a renormalizable quantum field theory. As a consequence, gauge bosons should be massless particles. Nonetheless, the Z^0 and W^\pm do have masses of $91 \text{ GeV}/c$ and $80 \text{ GeV}/c$, respectively. The introduction of the Higgs field [1][2][3] and the Higgs boson solves this problem. In this ansatz, gauge bosons have a mass of zero and only the coupling with the Higgs field creates the masses measured in experiment. The discovery of a Higgs-like particle in July 2012 [4][5] and the following ongoing tests of its properties have increased the likelihood that the Standard Model Higgs boson has been found [6].

Fermions of the 2nd and 3rd family, as well as other hadrons than protons or neutrons have to be created by inelastic interactions. This processes can happen naturally, e.g. by cosmic rays, or artificially in particle accelerators, e.g. the Super Proton Synchrotron (SPS) at CERN (see Chapter 2.1). After creation, these particles decay eventu-

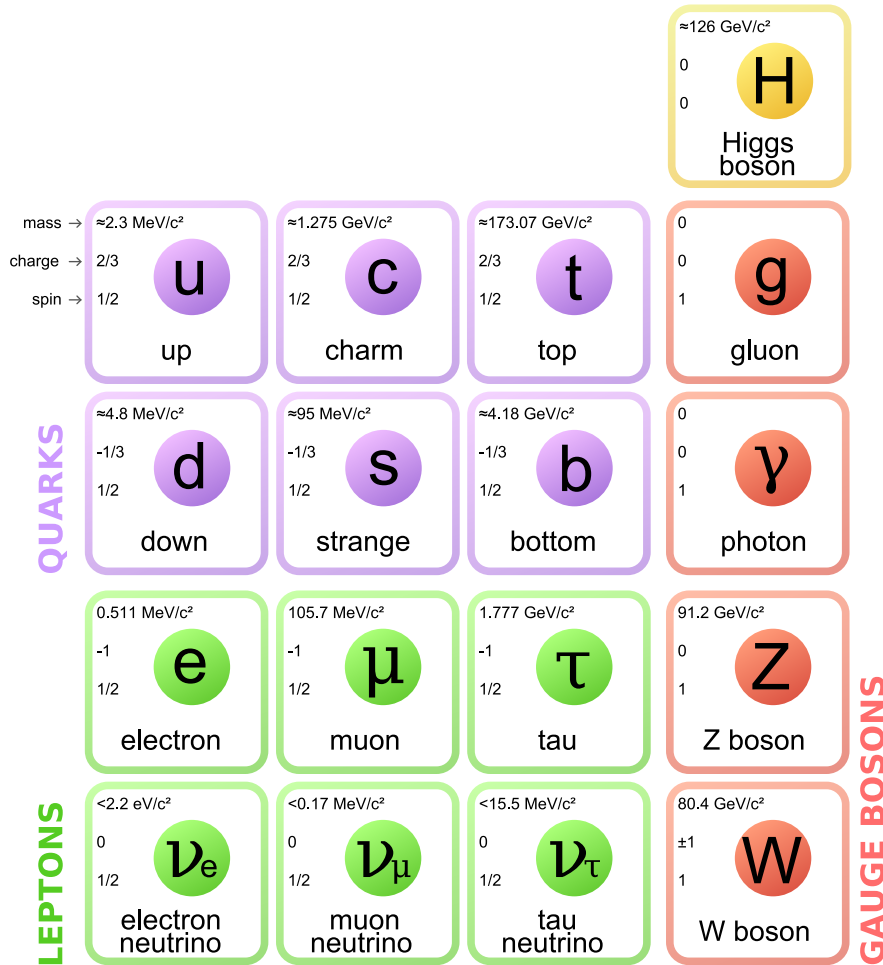


Figure 1: Elementary particles in the Standard Model [7].

ally through decay chains via strong, electromagnetic or weak force to leptons and quarks (bound as protons) of the first family.

The Standard Model is very successful in describing known interactions between particles. Precise tests of the Standard Model have been carried out in the past (e.g. the muon $g - 2$ factor [8]) or are conducted at time of this writing (e.g. the measurement of the decay $K^+ \rightarrow \pi^+ \nu \bar{\nu}$ at NA62 [9]). All former precise tests confirmed the agreement of the Standard Model with measurements. However, besides its huge success in the past, the Standard Model still leaves open questions. Some of these questions are for example why are there exactly three fermion families? Why do W^\pm and Z^0 bosons couple strongly to the Higgs field but gluons and photons not? Furthermore, dark matter, which can be observed by astronomical methods, can not be explained with Standard Model particles.

Further precision tests of the Standard Model may reveal New Physics beyond the Standard Model. An excellent probe for such tests is the Cabibbo-Kobayashi-Maskawa (CKM) quark mixing matrix.

1.3 THE CKM QUARK MIXING MATRIX

Kaons were discovered in cosmic rays in 1947. This new particle was different from other already known particles, because it decayed much slower with a lifetime of the order of magnitude of 10^{-8} s. Decays mediated by the strong or electromagnetic force have much shorter lifetimes, e.g. the $\pi^0 \rightarrow \gamma\gamma$ decay with $\tau_{\pi^0} = 8 \cdot 10^{-17}$ s. This behaviour was explained by introduction of a new quantum number, the strangeness ($S = 0, 1$). This quantum number was assumed to be conserved in the strong force and violated in the weak force. In 1963 N. Cabibbo introduced the concept of splitting the coupling of the weak force into a part without change of strangeness $\Delta S = 0$ and with change of the strangeness ($\Delta S = 1$). Cabibbo compared decay rates [10], e.g.

$$\frac{\Gamma(K^+ \rightarrow \mu^+\nu)}{\Gamma(\pi^+ \rightarrow \mu^+\nu)} = \tan^2 \Theta_c \frac{M_K \left(1 - \frac{M_\mu^2}{M_K^2}\right)^2}{M_\pi \left(1 - \frac{M_\mu^2}{M_\pi^2}\right)^2} \quad (1.1)$$

with M_i the masses of the involved particles. Cabibbo obtained $\Theta_c \approx 14^\circ$, which is today known as *Cabibbo angle*. The weight factor $\tan^2 \Theta_c \approx \frac{1}{20}$ explained the observed smaller coupling strength of the weak force in processes with $\Delta S = 1$. Cabibbo's ansatz implies, in modern language using quarks (which were not yet discovered at this time), that in a 3-dimensional flavor space the weak force does not transform an $|u\rangle$ state into a $|d\rangle$ state but into a linear combination $|d'\rangle$ of $|d\rangle$ and $|s\rangle$:

$$|d'\rangle = \cos \Theta_c |d\rangle + \sin \Theta_c |s\rangle. \quad (1.2)$$

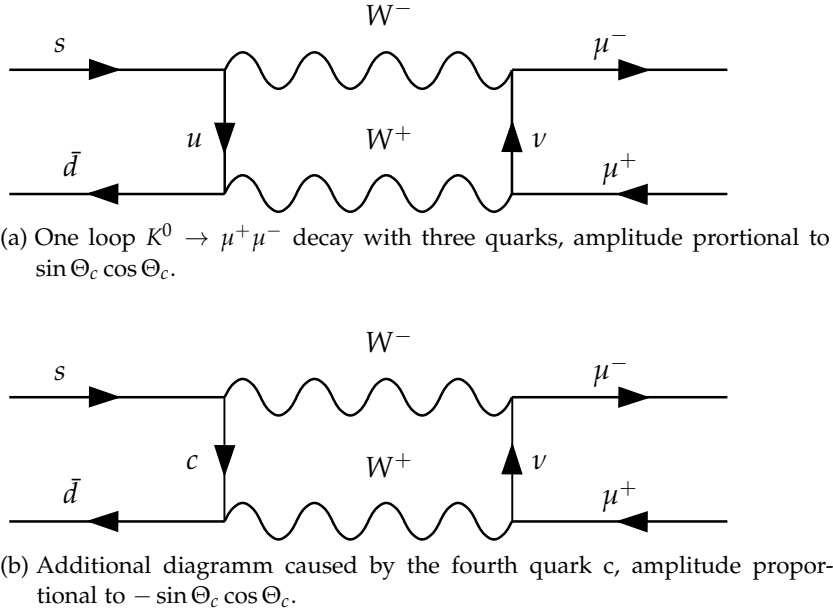
Following this ansatz, the decay $K_L^0 \rightarrow \mu^+\mu^-$ (with $K^0 = (\bar{d}s)$ or $\bar{K}^0 = (d\bar{s})$) should have a higher branching fraction than the observed ratio of $\approx 7 \cdot 10^{-9}$ [11]. Figure 2a shows the description of the decay in a box diagram with only three quarks.

In 1970 S. Glashow, J. Iliopoulos, and L. Maiani suggested a fourth quark (c) because of symmetry requirements [12]. The weak currents can then be written with a fourth quark as

$$J_\mu = \bar{U} \gamma_\mu (1 + \gamma_5) V_c D, \quad (1.3)$$

with

$$U = \begin{pmatrix} u \\ c \end{pmatrix}, V_c = \begin{pmatrix} \cos \Theta_c & \sin \Theta_c \\ -\sin \Theta_c & \cos \Theta_c \end{pmatrix}, \text{ and } D = \begin{pmatrix} d \\ s \end{pmatrix}. \quad (1.4)$$


 Figure 2: The $K^0 \rightarrow \mu^+ \mu^-$ decay.

This extension adds a further amplitude proportional to $-\sin \Theta_c \cos \Theta_c$ to the K_L^0 decay (Figure 2b). In exact flavour symmetry, both amplitudes cancel and the $K_L^0 \rightarrow \mu^+ \mu^-$ decay should be completely suppressed. Due to the different masses of up and charm quark, a small branching fraction is allowed which agrees with the measurement [13].

In 1973 M. Koabayashi and T. Maskawa proved [14] that the observed CP violation by J. Christenson, J. Cronin, V. Fitch, and R. Turlay [15] in 1964 could not be explained by a theory with only two quark doublets. CP violation can only be introduced by a complex phase. In the 2×2 matrix V_c (Equation 1.3) this is not possible. Every complex phase can be absorbed into the quark wave function by choice of the (arbitrary) wave function phase resulting in all matrix elements of V_c becoming real. Kobayashi and Maskawa suggested a third doublet, the later observed bottom and top quark. This doublet extends the V_c matrix to the 3×3 complex matrix

$$V_{\text{CKM}} = \begin{pmatrix} V_{ud} & V_{us} & V_{ub} \\ V_{cd} & V_{cs} & V_{cb} \\ V_{td} & V_{ts} & V_{tb} \end{pmatrix} \quad (1.5)$$

which is described by three real parameters and one complex phase. One possible parametrization is [16]

$$V_{\text{CKM}} = \begin{pmatrix} c_{12} c_{13} & s_{12} c_{13} & s_{13} e^{-i\delta} \\ -s_{12} c_{23} - c_{12} s_{23} s_{13} e^{i\delta} & c_{12} c_{23} - s_{12} s_{23} s_{13} e^{i\delta} & s_{23} c_{13} \\ s_{12} s_{23} - c_{12} c_{23} s_{13} e^{i\delta} & -c_{12} c_{23} - s_{12} c_{23} s_{13} e^{i\delta} & c_{23} c_{13} \end{pmatrix},$$

(1.6)

with $s_{ij} = \sin \Theta_{ij}$, $c_{ij} = \cos \Theta_{ij}$, and δ the complex phase. V_{CKM} is a unitary matrix and therefore it has to follow the relations

$$\sum_i V_{ij} V_{ik}^* = \delta_{jk} \quad (1.7)$$

and

$$\sum_j V_{ij} V_{kj}^* = \delta_{ik}. \quad (1.8)$$

Using Equation 1.8 we can write, e.g.

$$|V_{ud}|^2 + |V_{us}|^2 + |V_{ub}|^2 = 1 + \Delta_{\text{CKM}}. \quad (1.9)$$

The Standard Model can be tested with the relation Equation 1.9 by measuring the absolute values of the matrix elements. These values can be extracted from measurement of particle decays. $\Delta_{\text{CKM}} \neq 0$ indicates deviations from the expected value and would point to physics beyond the Standard Model.

1.3.1 Status of Measurements of $|V_{ud}|$, $|V_{us}|$, and $|V_{ub}|$

Measurements regarding the validity of Equation 1.9 provide the most stringent test of CKM matrix unitarity. $|V_{ud}|$ and $|V_{us}|$ have been measured very precisely from semileptonic transitions $d \rightarrow u$ and $s \rightarrow u$ [17]. This section gives an overview over the experimental methods to extract $|V_{ud}|$, $|V_{us}|$, and $|V_{ub}|$. More details on semileptonic kaon decays are given in Chapter 1.4.

1.3.1.1 Extraction of $|V_{ud}|$

The most precise determination of $|V_{ud}|$ is done by measuring super-allowed $0^+ \rightarrow 0^+$ Fermi transitions between nuclei [11, “ V_{ud} , V_{us} , The Cabibbo Angle, and CKM Unitarity”]. Measuring the transition energy Q and lifetimes $\tau_{1/2}$ the value f_t can be calculated, which is a measure for the transition strength. It is constant for all nuclei after applying nuclei-dependent corrections. The matrix element $|V_{ud}|$ can then be derived by [17]

$$|V_{ud}|^2 = \frac{2984.48(5) \text{ s}}{f_t(1 + RC)}, \quad (1.10)$$

with RC the nuclei dependent radiative corrections from quantum loops, isospin violating effects, and nuclear structure. Penning trap

experiments reach 0.1 keV uncertainties and have improved those measurements in the last decade. A set of 20 $0^+ \rightarrow 0^+$ beta decays from 222 individual measurements have been combined in [18] and yield

$$|V_{ud}| = 0.97417(21). \quad (1.11)$$

The study of neutron β decays is a different approach to determine $|V_{ud}|$. This method has the advantage of being free from nuclear structure effects of superallowed beta decays. The matrix element can be written as [19]

$$|V_{ud}|^2 = \frac{K}{\tau_n(1+3\lambda^2)G_F^2(1+\Delta_R)f^R} = \frac{(4908.7 \pm 1.9)\text{s}}{\tau_n(1+3\lambda^2)} \quad (1.12)$$

with τ_n the neutron lifetime, $\lambda = g_A/g_V$ the ratio of axial and vector coupling constants. The Fermi constant G_F , the phase space factor f^R , the model dependent radiative corrections Δ_R , and a normalization constant K are lumped together to $K/G_F^2(1+\Delta_R)f^R = 4908.7 \pm 1.9$. Detailed information on neutron lifetime measurement techniques are available in [20]. The ratio λ is obtained from measurements of the angular distribution of electrons in dependence of the neutron spin polarization P . The probability of an electron to be emitted under a given angle can be written as [17]

$$W(\Theta) = 1 + \frac{v}{c} P A_0 \cos \Theta \quad (1.13)$$

with v/c the electron velocity in fractions of the speed of light and

$$A_0 = -2 \frac{\lambda(\lambda+1)}{1+3\lambda^2}. \quad (1.14)$$

Using the average values for the neutron lifetime $\tau_n^{\text{avg}} = 880.0(0.9)\text{s}$ and the ratio $\lambda^{\text{avg}} = 1.2701(25)$ from [11, “ V_{ud} , V_{us} , The Cabibbo Angle, and CKM Unitarity”] Equation 1.12 yields

$$|V_{ud}| = 0.9774(5)_{\tau_n}(16)_{\lambda}(2)_{R}, \quad (1.15)$$

where the uncertainty is dominated by the λ measurement.

A third method to extract V_{ud} is the measurement of the branching fraction of $\pi^+ \rightarrow \pi^0 e^+ \nu$ (called π_{e3}). Similar to the extraction of V_{us} from semileptonic kaon decays (Chapter 1.4) the matrix element V_{ud} is extracted from the semileptonic pion decay. The PIBETA collaboration measured the branching fraction to $\text{Br}(\pi^+ \rightarrow \pi^0 e^+ \nu) = (1.036 \pm 0.006) \cdot 10^{-8}$ and obtained [21]

$$|V_{ud}| = 0.9728 \pm 0.0030, \quad (1.16)$$

compatible but not competitive to the results of the first two methods discussed. Table 1 lists the discussed results for $|V_{ud}|$.

METHOD	$ V_{ud} $ VALUE	REFERENCE
Fermi transitions	0.97417(21)	[18]
Neutron lifetime	0.9774(17)	[11]
π_β decay	0.9728(30)	[21]

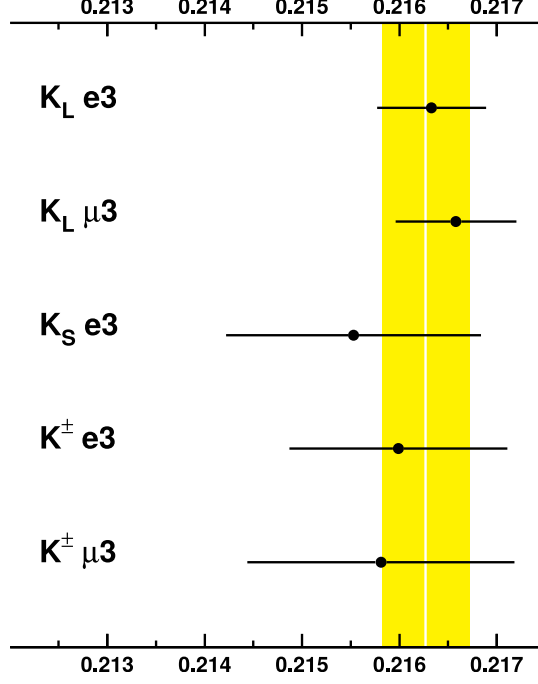
Table 1: Summary of discussed $|V_{ud}|$ measurements.

Figure 3: Comparison of $|V_{us}|f_+^{K^0\pi^-}(0)$ derived from different decay channels. The yellow band indicates the average value obtained by the FlaviaNet Working Group Kaon Decays for $|V_{us}|f_+^{K^0\pi^-}(0) = 0.2163(5)$ [22].

1.3.1.2 Extraction of $|V_{us}|$

The matrix element V_{us} has been extracted in the past from kaon decays, hyperon decays, and tau decays. In case of kaon decays, semileptonic decays ($K_{\ell 3}$) are used either from neutral or charged kaons. $|V_{us}|$ is determined through the measurement of the $K_{\ell 3}$ branching fraction. This method is used in this work and is explained in more detail in Section 1.4 on Page 12.

The FlaviaNet Working Group on Kaon Decays made an evaluation of $|V_{us}|$ from world data of five different experiments in [22]. The result of this exhaustive evaluation is

$$|V_{us}|f_+^{K^0\pi^-}(0) = 0.2163(5) \quad (1.17)$$

using $K_{\ell 3}$ decays. Figure 3 shows the contributions of the different decay channels to $|V_{us}|f_+^{K^0\pi^-}(0)$.

Applying the form factor at zero momentum transfer $f_+^{K^0\pi^-}(0) = 0.9677(27)$ [23] on the result above,

$$|V_{us}| = 0.2235(8) \quad (1.18)$$

is obtained. Details on $f_+^{K^0\pi^-}(0)$ are given in Chapter 1.4.

The matrix element $|V_{us}|$ can also be determined from the ratio of decays $K^\pm \rightarrow \ell^\pm \nu(\gamma)$ and $\pi^\pm \rightarrow \ell^\pm \nu(\gamma)$. The decay rates ratio writes

$$\frac{\Gamma_{K\ell 2}}{\Gamma_{\pi\ell 2}} = \frac{|V_{us}|^2 f_K^2 m_K (1 - m_\ell^2/m_K^2)^2}{|V_{ud}|^2 f_\pi^2 m_K (1 - m_\ell^2/m_\pi^2)^2} (1 + \delta_{EM}) \quad (1.19)$$

with f_K and f_π the kaon and pion decay constant and δ_{EM} the long-distance EM corrections. The FlaviaNet Working Group quotes [22]

$$|V_{us}/V_{ud}| \times f_K/f_\pi = 0.2758(5). \quad (1.20)$$

Using the lattice gauge calculation $f_K/f_\pi = 1.193(3)$ ($N_f = 2 + 1 + 1$) [23] and the before mentioned value $|V_{ud}| = 0.97417(21)$ [18],

$$|V_{us}| = 0.2252(7) \quad (1.21)$$

is obtained.

Semileptonic hyperon decays provide a further possible path to determine $|V_{us}|$. The decays

$$B_1 \rightarrow B_2 \ell \bar{\nu} \quad (1.22)$$

of a spin $\frac{1}{2}$ hyperon B_1 into a spin $\frac{1}{2}$ baryon B_2 , a lepton $\ell = e$ or μ and an antineutrino. $|V_{us}|$ is extracted through fits to decay rates, spin, and angular distributions. Unfortunately, measurements of $|V_{us}|$ using hyperon decays suffer from SU(3) breaking corrections. Different analyses have been performed on data sets from five hyperon decays ($\Lambda \rightarrow p e^- \bar{\nu}_e$, $\Sigma^- \rightarrow n e^- \bar{\nu}_e$, $\Xi^- \rightarrow \Lambda e^- \bar{\nu}_e$, $\Xi^- \rightarrow \Sigma^0 e^- \bar{\nu}_e$, and $\Xi^0 \rightarrow \Sigma^+ e^- \bar{\nu}_e$) obtaining different values and uncertainties. Two groups find

$$|V_{us}| = 0.2250(27)[24] \quad (1.23)$$

and

$$|V_{us}| = 0.2199(26)[25], \quad (1.24)$$

whereas Ref. [26] states that second-order symmetry breaking effects translate into a large systematic uncertainty and were not taken into account in the two analyses. This leads to a value with a rather large uncertainty:

$$|V_{us}| = 0.226(5)[26]. \quad (1.25)$$

METHOD	$ V_{us} $ VALUE	REFERENCE
$K_{\ell 3}$	0.2235(8)	[22][23]
$K_{\ell 2} / \pi_{\ell 2}$	0.2252(7)	[22][23][18]
Hyperons	0.2250(27)	[24]
	0.2199(26)	[25]
	0.226(5)	[26]
τ decays	0.2204(14)	[27]

Table 2: Summary of discussed $|V_{us}|$ measurements.

Better calculations of SU(3) symmetry breaking corrections are needed to make measurements of $|V_{us}|$ from hyperon decays competitive.

Finally, it is as well possible to determine $|V_{us}|$ from τ decays. Ref. [27] combines analyses of $\tau^- \rightarrow X_s^- \nu_\tau$ (X_s being a hadron with a s-quark component), $\tau^- \rightarrow K^- \nu_\tau$ decays, and $\Gamma(\tau^- \rightarrow K^- \nu_\tau) / \Gamma(\tau^- \rightarrow \pi^- \nu_\tau)$. The obtained results are

- $|V_{us}|_{X_s} = 0.2176(21)$,
- $|V_{us}|_{K\nu} = 0.2232(19)$, and
- $|V_{us}|_{K/\pi} = 0.2212(20)$,

respectively. The value for $|V_{us}|_{X_s}$ extracted from inclusive τ decays is significant lower than the previous presented results. It is compatible within 2.0 standard deviations to $|V_{us}|_{K\nu}$. The average computed in Ref. [27] reads

$$|V_{us}| = 0.2204(14). \quad (1.26)$$

The results for $|V_{us}|$ are summarized in Table 2. The values range between 0.226(5) and 0.2204(14). This situation clearly motivates further measurements on $|V_{us}|$ like the analysis presented in this work.

1.3.1.3 Extraction of $|V_{ub}|$

The matrix element $|V_{ub}|$ is accessible from semileptonic $B \rightarrow X_u \ell \nu$ decays with X_u a hadron with an u-quark component, ℓ a muon or electron, and ν the corresponding neutrino. Two different measurement methods are used: *inclusive* and *exclusive* measurements. The first method does not specify the X_u hadron, the latter does. Better results are reached at the moment with inclusive measurements. The Heavy Flavour Averaging Group used different measurements from B-factories to extract $|V_{ub}|$ [27]. They state for exclusive measurements (with $X_u = \pi$)

$$|V_{ub}| = 3.28(29) \cdot 10^{-3} \quad (1.27)$$

SOURCE	$ V_{us} $	$f_+^{K^0\pi^-}(0)$ OR f_K/f_π	Δ_{CKM}	σ
$K_{\ell 3}$	0.2235(8)	0.9677(27)	-0.0010(5)	-1.9
$K_{\ell 2}$	0.2252(7)	1.193(3)	-0.0003(5)	-0.5
Hyperons	0.226(5)	—	0.0001(23)	0.0
τ decays	0.2204(14)	—	-0.0024(7)	-3.2

Table 3: CKM unitarity test with different values for $|V_{us}|$.

and for inclusive measurements

$$|V_{ub}| = 4.45(16)_{\text{exp}}(22)_{\text{theo}} \cdot 10^{-3}. \quad (1.28)$$

The uncertainties on exclusive measurements results from uncertainties on the required form factors. Uncertainties on the inclusive measurements are induced by large $B \rightarrow X_c \ell \nu_\ell$ backgrounds. “Review on Semileptonic B Meson Decays and the Determination of V_{cb} and V_{ub} ” [11] gives a combination of exclusive and inclusive measurement results of

$$|V_{ub}| = 4.13(49) \cdot 10^{-3}. \quad (1.29)$$

However, this combination should be treated with caution due to the large discrepancy between both results.

1.3.1.4 CKM Matrix Unitarity

The presented values for $|V_{ud}|$, $|V_{us}|$, and $|V_{ub}|$ are used together with Equation 1.9

$$|V_{ud}|^2 + |V_{us}|^2 + |V_{ub}|^2 = 1 + \Delta_{\text{CKM}}$$

to test the CKM matrix unitarity. The focus is set on the different values of $|V_{us}|$. The values from kaon decays, hyperon decays (taking the conservative estimate from Equation 1.25), and the τ decay average are used together with $|V_{ud}| = 0.97417(21)$ [18] and $|V_{ub}| = 4.13(49) \cdot 10^{-3}$ [11]. Table 3 shows the used value for $|V_{us}|$ and its source, the corresponding lattice gauge theory value (if applicable), the difference Δ_{CKM} to unitarity, and the standard deviation σ of the difference to unitarity.

$K_{\ell 2}$ decays agree very well with unitarity. Same is true for the results based on hyperon decays, however, the uncertainty is not competitive at all. It should be noted that $|V_{us}|$ obtained from $K_{\ell 2}$ is correlated with the $|V_{ud}|$ result. A tensions is observed for results obtained from τ decays. The results from $K_{\ell 3}$ have a smaller tension with unitarity. Nonetheless, a new measurement with $K_{\ell 3}$ decays is strongly motivated.

PARAMETER	K_{e3} AND $K_{\mu3}$	REFERENCE
$G_F[\text{GeV}^{-2}]$	$1.1663787(6) \cdot 10^{-5}$	[11]
$f_+^{K^0\pi^-}(0)$	0.9677(27)	[23]
$\delta_{SU(2)}^{K^+\pi^0}$	0.029(4)	[28]
S_{EW}	1.0232(3)	[29][30][31]
$\tau_K[\text{s}]$	$1.2380(21) \cdot 10^{-8}$	[11]

Table 4: Common input parameters for K_{e3} and $K_{\mu3}$ decays in Equation 1.30.

PARAMETER	K_{e3}	$K_{\mu3}$	REFERENCE
$\delta_{EM}^{K\ell} [\%]$	0.050(125)	0.008(125)	[29]
$I_{K\ell}$	0.15922(18)	0.10559(17)	[22]

Table 5: Input parameters for K_{e3} and $K_{\mu3}$ decays in Equation 1.30.

1.4 SEMILEPTONIC KAON DECAYS

Semileptonic kaon decays ($K \rightarrow \pi\ell\nu_\ell$) give access to the matrix element $|V_{us}|$ through [22]

$$\Gamma_{K\ell3} = \frac{G_F^2 m_K^5}{192\pi^3} C_K^2 S_{EW} \left(|V_{us}| f_+^{K^0\pi^-}(0) \right)^2 I_{K\ell} \left(1 + \delta_{EM}^{K\ell} + \delta_{SU(2)}^{K\pi} \right)^2. \quad (1.30)$$

Here, G_F is the Fermi constant, m_K is the kaon mass, C_K is a Clebsch-Gordan coefficient (1 for K^0 and $\frac{1}{\sqrt{2}}$ for K^\pm), S_{EW} is the short-distance electroweak correction, $f_+^{K^0\pi^-}(0)$ is the vector form factor at zero momentum transfer for $K^0 \rightarrow \pi^-$, $I_{K\ell}$ is the phase-space integral, $\delta_{EM}^{K\ell}$ are the channel-depended long-distance EM corrections, and $\delta_{SU(2)}^{K\pi}$ the isospin breaking correction.

The measured branching fractions (Chapter 8 on Page 127) for K_{e3} and $K_{\mu3}$ from this work together with Equation 1.30 and the input parameters from Table 4 and Table 5 are used to compute $|V_{us}|$ (Section 8.2 on Page 129). The next sections gives an overview about the tabulated input parameters.

1.4.1 Determination of $f_+^{K^0\pi^-}$ from Theory

The hadronic matrix element of the weak charge between K and π at zero momentum transfer $f_+^{K^0\pi^-}(0)$ [32] requires to be extracted from theory. If the mass terms of the light quarks are treated as perturbations in the chiral limit, $f_+^{K^0\pi^-}$ can be written as an expansion

$$f_+^{K^0\pi^-} = f_0 + f_1 + f_2 + \dots \quad (1.31)$$

where f_0 , f_1 and f_2 are of the order 1, m_q , and m_q^2 . Leutwyler and Roos [32] find

$$\Delta f \equiv f_2 + \dots = 0.016(8) \text{ and } f_+^{K^0\pi^-} = 0.961(8) \quad (1.32)$$

in their original quark model estimates. Calculations in lattice QCD have gained more precision in recent years. $f_+^{K^0\pi^-}(0)$ is determined by three point functions at non-vanishing momenta on the lattice [22]. Latest averaged lattice results on $f_+^{K^0\pi^-}$ provided by the FLAG Working Group [23] based on FNAL/MILC 12I [33] and RBC/UKQCD 15A [34] give (including Up, Down, and Strange quark or $N_f = 2 + 1$)¹

$$f_+^{K^0\pi^-}(0) = 0.9677(27). \quad (1.33)$$

1.4.2 Isospin Breaking Correction for Charged Kaon Decays

The vector form factor $f_+^{K^0\pi^-}(0)$ at zero momentum transfer is defined for $K^0 \rightarrow \pi^-$. In case of $K^+ \rightarrow \pi^0$ an isospin correction is needed. This is related to different masses of the u-quark and d-quark [32]. The correction is included through the term [22]

$$\delta_{\text{SU}(2)}^{K^0\pi^-} = 0, \quad \delta_{\text{SU}(2)}^{K^+\pi^0} = \frac{f_+^{K^+\pi^0}(0)}{f_+^{K^0\pi^-}(0)} - 1. \quad (1.34)$$

In first order perturbation theory the correction can be written as

$$\delta_{\text{SU}(2)}^{K^+\pi^0} = \frac{3}{4} \frac{m_d - m_u}{m_s - \tilde{m}} \quad (1.35)$$

with the masses for the u-quark (m_u), the d-quark (m_d) and $\tilde{m} = \frac{1}{2}(m_u + m_d)$ [32]. In next-to-leading order the term can be written as [22]

$$\delta_{\text{SU}(2)}^{K^+\pi^0} = \frac{3}{4} \frac{1}{Q^2} \left[\frac{m_K^2}{m_\pi^2} + \frac{\chi_{p^4}}{2} \left(1 + \frac{m_s}{\tilde{m}} \right) \right], \quad (1.36)$$

with $Q^2 = (m_s^2 - \tilde{m}) / (m_d^2 - m_u^2)$ and χ_{p^4} an $\mathcal{O}(p^4)$ correction. Ref. [28] finds

$$\delta_{\text{SU}(2)}^{K^+\pi^0} = 0.029(4). \quad (1.37)$$

It is also possible to determine $\delta_{\text{SU}(2)}^{K^+\pi^0}$ from data, by taking the ratio of $|V_{us}|f_+^{K^0\pi^-}(0)$ extracted from charged and neutral Kaon decays (without applying the SU(2) correction). This experimental estimate has been computed by [22] to

$$\delta_{\text{SU}(2)}^{K^+\pi^0} = 0.027(4) \quad (1.38)$$

which is in good agreement with the theoretical prediction.

¹ The same paper quotes $f_+^{K^0\pi^-}(0) = 0.9704(24)(22)$ allowing additionally a Charm quark ($N_f = 2 + 1 + 1$). Due to the larger uncertainty of this result it is not used in this work.

1.4.3 Electroweak and Electromagnetic Corrections

The short distance electroweak correction is a higher order correction to the semileptonic charged-current process and can be lumped together for all semileptonic processes to an overall factor [29][30][31]

$$S_{EW} = 1.0232(3). \quad (1.39)$$

In Ref. [29], the radiative corrections to all $K_{\ell 3}$ decay modes have been studied to leading non-trivial order in the chiral effective field theory. Therefore, a fully inclusive approach for real photon emission has been used. The obtained corrections are

$$\delta_{EM}^{K^{\pm}e} = 0.050(125) \quad \text{and} \quad \delta_{EM}^{K^{\pm}\mu} = 0.008(125). \quad (1.40)$$

1.4.4 Phase Space Integral $I_{K\ell}$ and Form Factors

The Lagrangian for $K_{\ell 3}$ decays

$$L_W = \frac{G_F}{\sqrt{2}} V_{us} J_l^{+\mu} J_{h\mu} \quad (1.41)$$

is described by the weak lepton current $J_l^{+\mu}$ and the weak quark current

$$J_{h\mu} = \langle \pi^0 | \bar{s} \gamma_\mu u | K^+ \rangle = \frac{1}{\sqrt{2}} (f_+(t)(p_K + p_\pi)_\mu + f_-(t)(p_K - p_\pi)_\mu) \quad (1.42)$$

with $t = (p_K - p_\pi)^2 = (p_\ell + p_\nu)^2$ the momentum transfer on the lepton pair system. The vector form factor $f_+(t)$ represents the P-wave projection and the scalar form factor

$$f_0(t) = f_+(t) + \frac{t}{m_K^2 - m_\pi^2} f_-(t) \quad (1.43)$$

the S-wave projection of the crossed channel matrix $\langle 0 | \bar{s} \gamma^\mu u | K\pi \rangle$. Since $f_+(0) = f_0(0)$ is not accessible through measurement, it is commonly used to factor out $f_+^{K^0\pi^-}(0)$ in Equation 1.30 and to normalize the form factors as follows:

$$\bar{f}_+(t) \equiv \frac{f_+(t)}{f_+^{K^0\pi^-}}, \quad \bar{f}_0(t) \equiv \frac{f_0(t)}{f_+^{K^0\pi^-}}, \quad \bar{f}_+(0) = \bar{f}_0(0) = 1. \quad (1.44)$$

The phase space integral [22]

$$I_{K\ell} = \int_{m_\ell^2}^{t_{\max}} dt \frac{1}{m_K^8} \lambda^{3/2} \left(1 + \frac{m_\ell^2}{2t}\right) \left(1 - \frac{m_\ell^2}{2t}\right)^2 \times \left(\bar{f}_+^2(t) + \frac{3m_\ell^2 \Delta_{K\pi}^2}{(2t + m_\ell^2) \lambda} \bar{f}_0^2(t) \right) \quad (1.45)$$

with $t_{\max} = (m_K - m_\pi)^2$, $\lambda = [t - (m_K + m_\pi)^2][t - (m_K - m_\pi)^2]$, and $\Delta_{K\pi} = m_K^2 - m_\pi^2$, depends on form factors and the mass of the charged lepton ($\ell = \mu$ or e). Due to mass dependence, the term with the scalar form factor does not contribute to the integral for K_{e3} decays.

The form factors extraction is realized by fits to the $K_{\ell 3}$ Dalitz plot, which describes the phase space of a three-body decay. For such fits the form factors are parametrized. Commonly used are Taylor expansions, pole parametrization, and dispersive parametrization.

1.4.4.1 Taylor expansion

The Taylor expansion expands the form factors in the momentum transfer range $m_\ell^2 < t < (P_K - m_\pi)^2$ to

$$\bar{f}_+(t) = 1 + \lambda'_+ \frac{t}{m_{\pi^\pm}^2} + \lambda''_+ \left(\frac{t}{m_{\pi^\pm}^2} \right)^2 \quad \text{and} \quad (1.46)$$

$$\bar{f}_0(t) = 1 + \lambda'_0 \frac{t}{m_{\pi^\pm}^2}. \quad (1.47)$$

λ' and λ'' describe the slope and curvature of the form factors. The disadvantage of this power series is the absence of a physical meaning and a strong correlation between the λ parameters. This leads also to a missing sensitivity to λ'_0 , thus it is not used [22].

1.4.4.2 Pole parametrization

In the pole parametrization

$$\bar{f}_{+,0} = \frac{M_{VS}^2}{M_{VS}^2 - t} \quad (1.48)$$

the amount of free parameters is reduced to one. This parameter M_{VS} describes a $K\pi$ resonance mass. For the vector form factors the obtained value for M_V agrees well with the resonance $K^*(892)$. However, for the scalar form factor a corresponding resonance is not known [22].

1.4.4.3 Dispersive parametrization

In the dispersive parametrization, the form factors are identified as analytic functions in the complex t -plane, except for a cut along the positive real axis for $t \geq t_{\text{lim}} \equiv (m_K - m_\pi)^2$, where they develop discontinuities [22]. Ref. [35] proposes parametrizations for the form factors based on this idea. The vector form factor is written as

$$\bar{f}_+(t) = \exp \left[\frac{t}{m_\pi^2} (\Lambda_+ + H(t)) \right] \quad \text{with} \quad (1.49)$$

$$H(t) = \frac{m_\pi^2 t}{\pi} \int_{t_{\text{lim}}}^{\infty} \frac{ds}{s^2} \frac{\Phi_+(s)}{(s-t-i\epsilon)}. \quad (1.50)$$

Λ_+ is a free parameter which is determined by the fit and the phase $\Phi_+(s)$ is derived from P-wave $(K\pi)_{I=1/2}$ elastic scattering.

The scalar form factor reads

$$\bar{f}_0 = \exp \left[\frac{t}{\Delta_{K\pi}} (\ln C - G(t)) \right] \quad \text{with} \quad (1.51)$$

$$G(t) = \frac{\Delta_{K\pi}(\Delta_{K\pi} - t)}{\pi} \int_{t_{\text{lim}}}^{\infty} \frac{ds}{s} \frac{\Phi_0(s)}{(s - \Delta_{K\pi})(s - t - i\epsilon)}. \quad (1.52)$$

The phase $\Phi_0(s)$ is extracted from elastic S-wave $(K\pi)_{I=1/2}$ scattering. $\ln C$ is the free parameter to be determined.

1.4.4.4 Values for the phase space integral $I_{K\ell}$

Ref. [22] presents values for $I_{K\ell}$ derived from averages of the results of quadratic-linear $(\lambda'_+, \lambda''_+, \lambda'_0)$ and dispersive $(\Lambda_+, \ln C)$ fits using data from KTeV, KLOE, NA48 and ISTRA+. These results are for K_{e3}

$$I_{K_{e3}}^{\text{QL}} = 0.15894(21) \quad \text{and} \quad I_{K_{e3}}^{\text{Disp}} = 0.15922(18), \quad (1.53)$$

and for $K_{\mu 3}$

$$I_{K_{\mu 3}}^{\text{QL}} = 0.10564(20) \quad \text{and} \quad I_{K_{\mu 3}}^{\text{Disp}} = 0.10559(17). \quad (1.54)$$

For further calculations, the phase space integrals based on dispersive results are used.

EXPERIMENTAL SETUP

The NA62 experiment [9] is a fixed-target experiment located in the North Area of the Super Proton Synchrotron (SPS) ring at the European Organization for Nuclear Research (CERN¹). Main goal of the NA62 experiment is the measurement of the $K^+ \rightarrow \pi^+ \nu \bar{\nu}$ decay. However, in the first phase the experiment tested lepton universality by measuring the ratio $R_K = \Gamma(K_{e2})/\Gamma(K_{\mu 2}) = (2.487 \pm 0.013) \cdot 10^{-5}$ [36] in 2007. The data recorded in this phase has been used for this work. At this time the NA62 detector was still in the design phase and the NA48/2 apparatus was used.

The NA48 experiment [37] was designed to measure and quantify the presence of direct CP violation in neutral kaon decays into two pions, as expressed by the parameter $Re(\epsilon'/\epsilon)$. In the following experimental phase, called NA48/1, the focus was set on measuring rare K_S and neutral hyperon decays .

The third experimental phase, called NA48/2, was dedicated to the measurement of the slope of charge asymmetries A_g in both $K^\pm \rightarrow \pi^\pm \pi^+ \pi^-$ and $K^\pm \rightarrow \pi^\pm \pi^0 \pi^0$ processes [38].

2.1 THE SUPER PROTON SYNCHROTRON

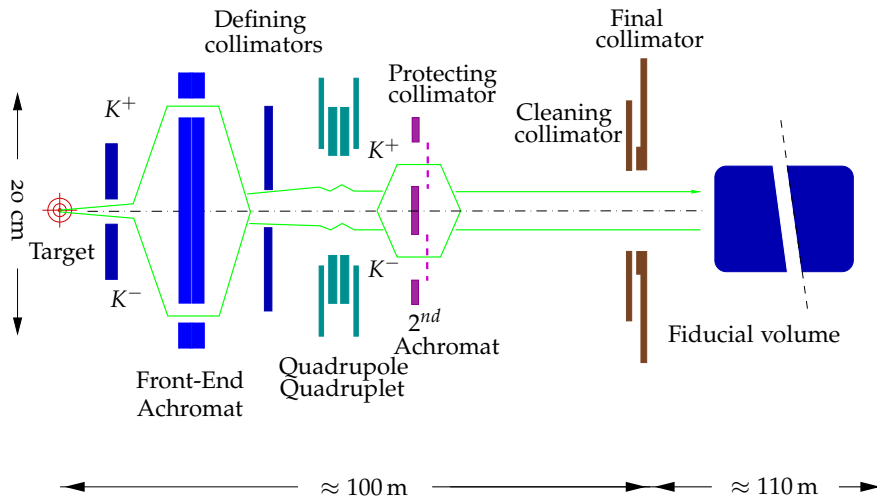
The accelerator complex at CERN (Figure 4) is a chain of accelerators starting with the Linear Accelerator (LINAC) ($E_{\max} = 50$ MeV) and ending with the Large Hadron Collider (LHC) ($E = 7$ TeV). In between these two machines are the Proton Synchrotron Booster ($E = 1.4$ GeV), the Proton Synchrotron (PS) ($E = 25$ GeV) and the SPS. Further information to these machines can be found at [40] and [41].

The SPS operates at energies up to 450 GeV. It is a ring accelerator with a circumference of nearly 7 km and was commissioned in 1976. The accelerator can handle different types of particles and nuclei. The SPS does not only feed the LHC, it also provides particles to other experiments, located in the North Area of CERN. One of these experiments is NA62.

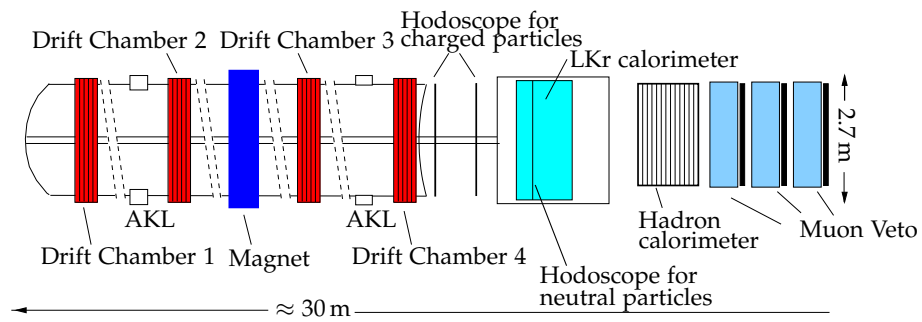
2.2 THE COORDINATE SYSTEM

The following sections give an overview of the experimental setup of the NA48/2 detector. Most of the information was extracted from

¹ Conseil Européen pour la Recherche Nucléaire (CERN) was the name of the provisional council which set up the laboratory. After dissolving the council the acronym continued to be used.



(a) Kaon beam selection and fiducial volume.



(b) The subdetectors.

Figure 5: Schematic view of the NA48/2 beam line. Note the different scales for the part until the final collimator (a), the fiducial volume (a), and the subdetectors (b). Based on [38].

merged again and passed subsequently through an acceptance defining collimator, a set of four quadrupoles for charge symmetric focusing. After the quadrupoles, the beam was again split and merged by a second achromat. Originally, at this point kaon beam spectrometers (KABES) would have measured the momentum of the beam. Unfortunately, the KABES were removed before 2007. As a consequence, the kaon momentum has been measured indirectly by reconstruction of $K^+ \rightarrow \pi^+ \pi^+ \pi^-$ decays, obtaining an average momentum for each burst. Before entering the fiducial volume, the particles passed muon sweeping magnets. The percentage of kaons (K^\pm) on the beam was about 6%. The largest part of the beam particles were pions (π^\pm).

The data set used in this analysis contains only K^+ events.

2.4 THE FIDUCIAL VOLUME

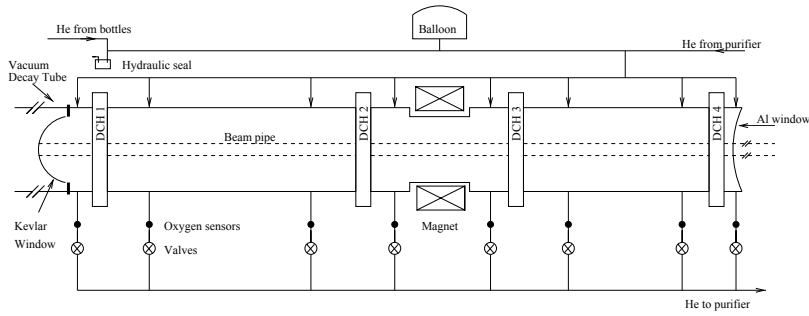
The fiducial volume was housed in a 114 m long cylindrical vacuum tank with a diameter of 1.92 m for the first 65 m, and 2.4 m for the remainder.

2.5 THE MAGNETIC SPECTROMETER

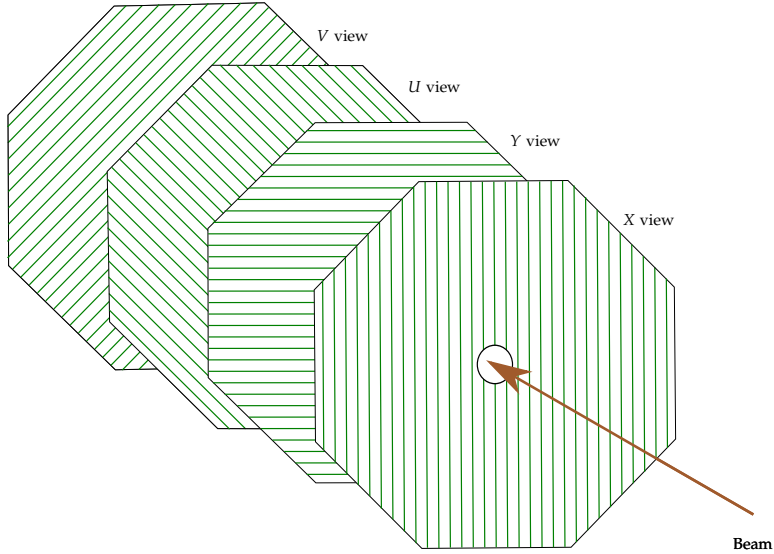
The momentum of charged particles was measured by a magnetic spectrometer which consisted of four Drift Chambers (DCHs) housed in a helium tank, and a dipole magnet (MNP33) [42]. DCH₁ and DCH₂ were positioned upstream of the magnet, DCH₃ and DCH₄ downstream.

The helium tank (Figure 6a) was made of steel and had a length of 23 m and an internal diameter of 2.8 m. The purity requirement to the helium was 95%, which was achieved by filling pure helium at the beginning of the data taking and containing it in a closed system. During the data taking a purifying system ensured a purity of 95% and better. The vacuum tanks of the fiducial volume and the helium tank were separated by a Kevlar window, made by carbon steel. The individual DCHs sections were separated by Mylar foils and the end cap of the helium tank downstream was made of aluminum. The beam was guided in vacuum through an aluminum tube with 152 mm inner diameter along the z-axis.

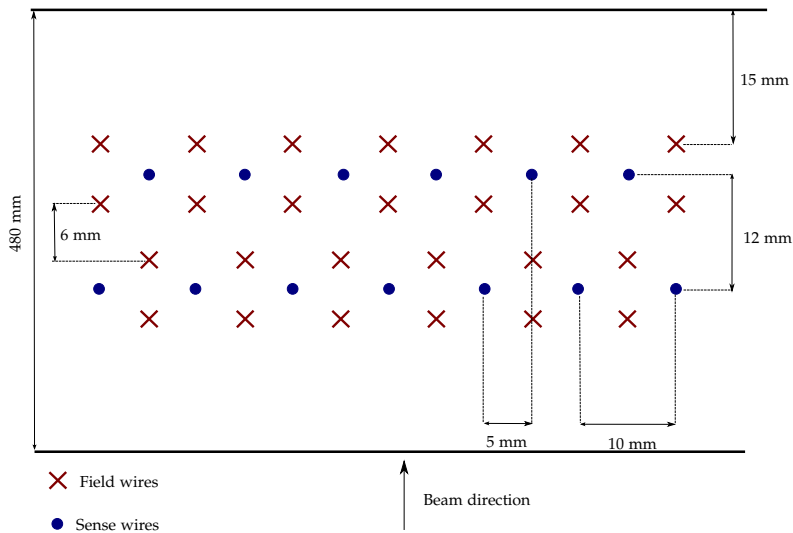
The MNP33 magnet [44], located between DCH₂ and DCH₃, had an opening between its poles of 2.40 m in vertical and 3.20 m in horizontal direction. The active fiducial diameter was determined by the helium tank to 2.37 m, providing a vertical field of 0.37 T at the center of the magnet. The magnetic field components were measured before data taking with a set of Hall probes. The measured values were compared with three-dimensional calculations. After applying corrections, the measured and computed values agreed within $3 \cdot 10^{-3}$ inside the fiducial volume [37]. During data taking the magnet current and two Hall probes were read out and the information stored for



(a) Schematic view of the helium tank. Helium in- and outlets are shown. [37].



(b) The alternating DCH views ([43], edited).



(c) The drift cell geometry ([37], edited). The drift cells are enclosed by graphite coated mylar foils (top and bottom line).

Figure 6: Overview to the helium tank and the DCHs.

later reconstruction. The integral of the magnetic field along the z -axis between DCH₂ and DCH₃ corresponded to a 257 MeV/ c transverse momentum kick for single charged particles.

The DCHs had an octagonal shape with a fiducial area of about 4.5 m² and a transverse width of 2.9 m. The chambers had a 160 mm central hole for the beam pipe. Each chamber was composed of eight planes of grounded sense wires. The planes were oriented in four directions to minimize position ambiguities for more than one measured particle. This views were named (X,X') for 0°, (Y,Y') for 90°, (U,U') for -45°, and (V,V') for 45° (Figure 6b). Each of the views included two planes staggered by 5 mm to resolve left-right ambiguities. An electric field was created between one sense wire and two potential wires on each side forming one drift cell (Figure 6c). The sense wires had a distance of 1 cm to each other. The DCHs were filled with an argon-ethane (50%-50%) gas mixture under a 1 mbar overpressure with respect to the helium tank. This prevented pollution of the gas mixture with helium.

The DCHs measured the positions of charged particles crossing the detector at a time t_1 . The particles ionized the gas along their flight path creating electron-ion pairs. These primary electrons drifted to a sense wire (diameter 20 μm made of gold-plated tungsten) along an electric field. This field was created by applying a negative voltage on two planes of field wires (diameter of 120 μm made of gold plated Ti-Cu) located on each side of the sense wire plane. The primary electrons created an electron avalanche near the sense wires which was measured by the sense wire and transformed into an electronic signal at a time t_2 . The distance z between sense wire and the location of the primary ionization can be written as

$$z = \int_{t_1}^{t_2} v_D(t) dt \quad (2.1)$$

with $v_D(t)$ the drift time of electrons in the gas. If the drift time is constant over time, Equation 2.1 simplifies to

$$z = v_D(t_2 - t_1) = v_D \Delta t. \quad (2.2)$$

The momentum was determined by measuring the curvature of the particles flight path inside the magnetic field using the positions in the DCHs.

The resolution obtained was [37]

$$\frac{\sigma_p}{p} = 0.48\% \oplus 0.009 \cdot p \text{ [GeV}/c] \%$$

where p denotes the momentum of the charged particle. The former term was due to multiple scattering in the helium tank and DCHs, and the latter due to the spatial resolution of the DCHs. The timing resolution using only DCHs was 0.7 ns.

2.6 THE HODOSCOPE FOR CHARGED PARTICLES

The Hodoscope for charged particles (CHOD)² was a two scintillator layer detector. Both layers consisted of 64 scintillator strips. The scin-

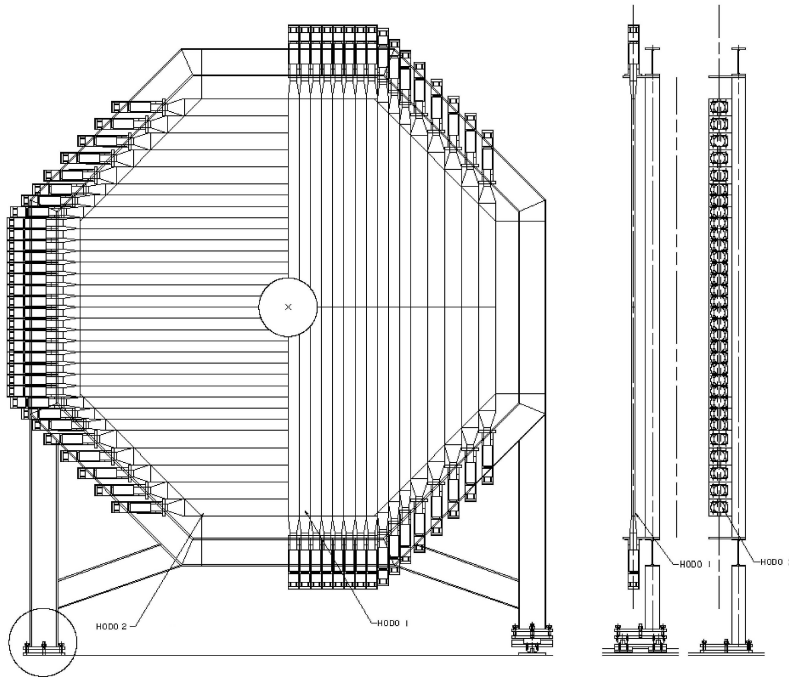


Figure 7: Front and side view of the CHOD [37].

tillator strips in the first layer (in downstream direction) were vertically oriented and the scintillator strips in the second layer horizontally (Figure 7). The distance between the layers was 74 cm. This distance made it possible to distinguish prompt signals from backscatter from the Liquid Krypton Calorimeter (Section 2.7). The CHOD was divided into four quadrants, each containing 16 scintillator strips. All scintillator strips were 2 cm thick. The width (length) varied between 6.5 cm (121 cm) close to the beam pipe and 9.9 cm (60 cm) further outside. The central hole for the beam pipe had a radius of 12.8 cm. The scintillator strips (Bicron BC408) were read out on one side by light guides connected to Photomultiplier Tubes (PMTs). Scintillators and light guides were wrapped with aluminized Mylar foil. Each plane was wrapped with a black cover for light tightness.

The CHOD information was used as t_0 signal for the trigger system (Section 2.12 on Page 29). A time resolution better than 0.2 ns was measured from data [37].

² Hodoscope: (greek) "path observer"

2.7 THE LIQUID KRYPTON CALORIMETER

The Liquid Krypton Calorimeter (LKr) [37] [45] is a quasi-homogeneous ionization chamber used as electromagnetic calorimeter³. Electrons or photons entering the active volume triggered an electromagnetic shower by electromagnetic interactions. The shower spread in the

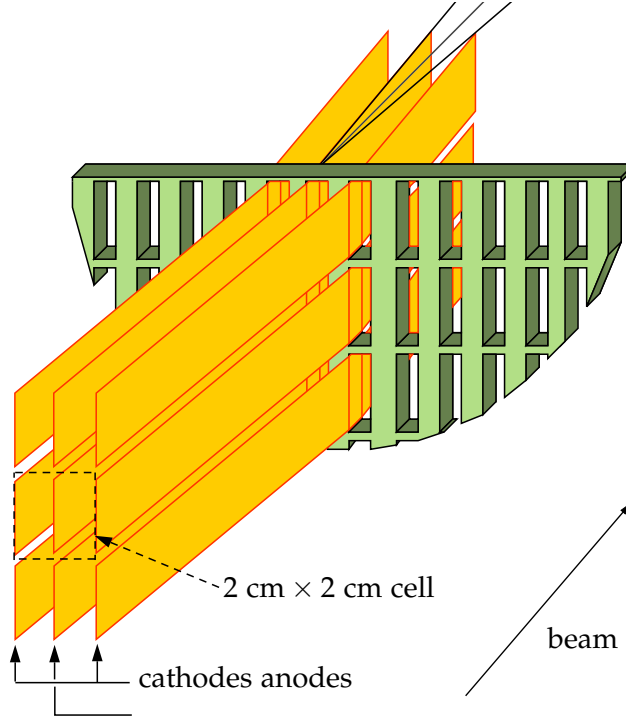


Figure 8: The LKr cell design [37].

calorimeter by repeated pair production and bremsstrahlung processes until the energy of the single particles fell below the critical energy E_C . The critical energy E_C is defined by

$$\left(\frac{dE}{dx}_{\text{Bremsstrahlung}} = \frac{dE}{dx}_{\text{Ionization}} \right) \text{ with } E = E_C. \quad (2.3)$$

Below this energy no further shower particles are produced. For krypton the critical energy is $E_{C,\text{Krypton}} = 21.51 \text{ MeV}$. Charged particles with low energy in the shower ionize krypton atoms. The released electrons drift along an electric field to an anode and are captured. The life time of these electrons in krypton is about $300 \mu\text{s}$, while the drift time to the anode is about $3 \mu\text{s}$.

The LKr was designed to detect photons from π^0 decays with excellent energy and space resolution to reduce background of the $K \rightarrow$

³ At present, the LKr is used in the new NA62 detector as a part of the Photon-Veto-System.

$\pi^0\pi^0$ decay in NA48. Liquefied krypton was used as active material which was contained in a cryostat with a volume of 9000l. The krypton was kept at a temperature of 117 K, cooled down by liquid argon, which itself was cooled down by liquid nitrogen. Krypton has a radiation length⁴ of $X_0 = 4.7$ cm and a Molière radius⁵ of $R_M = 4.7$ cm [47]. Thus full containment (larger 99 %) of electromagnetic showers within a cylindrical volume of 5.3 m^2 cross-section and 127 cm depth ($27 X_0$) could be achieved.

The active volume was segmented in 13,248 ($2 \times 1 \times 127$) cm^3 double ionization cells (Figure 8). The cells were built of 18 mm wide and 40 μm thick copper-beryllium ribbons at a distance of 1 cm from each other. The ribbons acted as electrodes to collect electrons released by krypton ionization. The amount of measured electrons is proportional to the deposited energy of the primary particle.

The limits of the active surface were the central hole for the beam pipe (diameter of 80 mm) and an octagonal outer boundary with an inscribed circle of 128 cm radius.

The energy resolution of the LKr was (E in GeV) [37]:

$$\frac{\sigma_E}{E} = \frac{0.032}{\sqrt{E}} \oplus \frac{0.09}{E} \oplus 0.0042,$$

where the first term describes statistical fluctuations, the second effects independent of the energy like noise and natural radioactivity of krypton, and the last one constant effects like calibration, material in front of the calorimeter or inhomogeneities.

The spatial resolution (in cm) was determined to [37]

$$\sigma_{X,Y} = \frac{0.42}{\sqrt{E}} \oplus 0.06,$$

and the time resolution (in ns) to [37]

$$\sigma_t = \frac{2.5}{\sqrt{E}}$$

with E in GeV.

2.8 THE HODOSCOPE FOR NEUTRAL PARTICLES

The Hodoscope for neutral particles (NHOD) was the “neutral” timing counterpart to the Hodoscope for charged particles. It provided a

⁴ The radiation length X_0 is the distance after which the energy of an electron is reduced to $1/e$ by bremsstrahlung.

⁵ The Molière radius R_M describes the transversal dimension of an electromagnetic shower. About 95 % of the energy of an electromagnetic shower is contained in a cylinder with a radius of $2 R_M$. It is connected to the radiation length X_0 and critical energy E_C through the relation $R_M = (21 \text{ MeV} \cdot X_0)/E_C$ [46, Chapter 6.1].

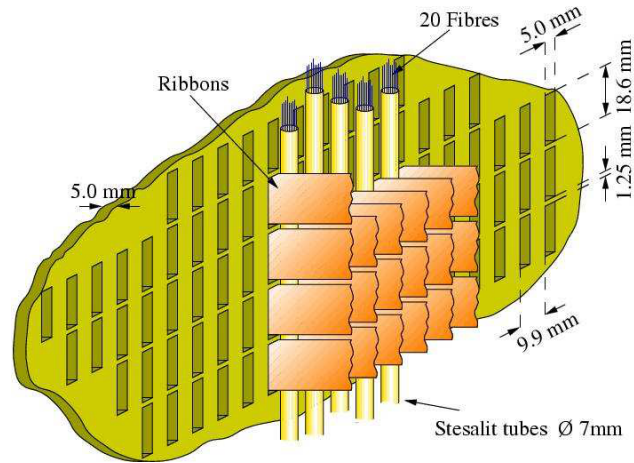


Figure 9: The NHOD fibers placed inside the LKr [37].

very precise time measurement for neutral particles which decayed to photons. As photons were not seen by the CHOD, an independent time measurement was needed.

The NHOD was a plane of scintillating fibers (1 mm diameter) inside the LKr. The fibers were placed in epoxy fiber glass tubes (inner and outer diameter of 7 and 8 mm, respectively) in bundles of 20 fibers. These tubes were installed vertically in a depth of about $9.5 X_0$, at which typical electromagnetic showers developed their maximum (Figure 9).

The fibers were read out by PMTs located inside the LKr, but outside of the active volume. Each PMT readout a bundle of fibers. A total of 32 channels were divided into 4 quadrants. The four channels closest to the beam pipe in each quadrant covered a vertical region 10 cm wide, the remaining four covered a region of 22 cm.

The time resolution was $\sigma_t = 260$ ps. The efficiency was 95 % and 99 % for photon energies above 25 GeV and 35 GeV, respectively [37].

The NHOD delivered a trigger signal ($T0N$) independent from the trigger for charged particles. In this work the $T0N$ trigger is used to measure the efficiency of the trigger chain for charged particles (Chapter 6 on Page 107).

2.9 THE HADRON CALORIMETER

The Hadron Calorimeter (HAC) was located directly after the LKr (Figure 10). It was an iron-scintillator sandwich calorimeter, split in a front and a back module. Each of the modules consisted of 24 iron and 24 scintillator layers (25 in the back module). The iron layers were each 25 mm thick and covered an area of 2.7×2.7 m². The scintillator layers were composed of 44 scintillator strips each 4.5 mm thick and varying in width and length. Each strip covered half of the detector

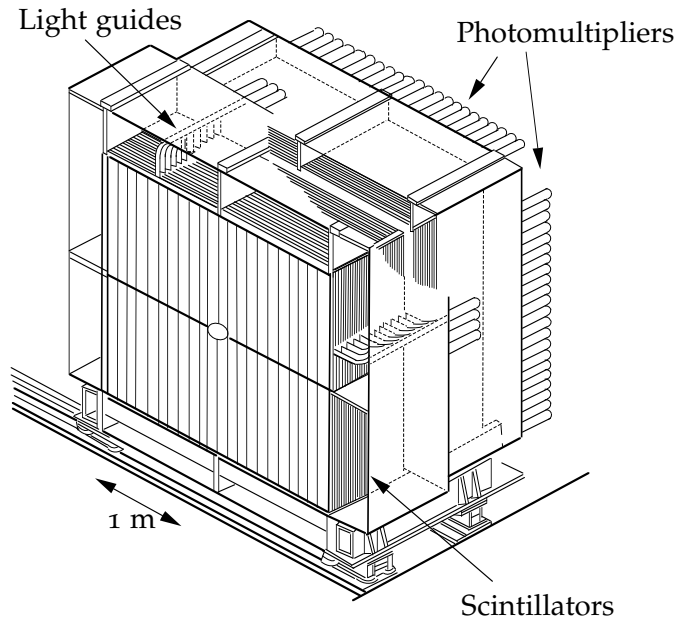


Figure 10: The HAC with its two modules [37].

length (or width). The orientation of the scintillator strips alternated between vertical and horizontal similar to the CHOD (2.6).

Particles interacting with the iron produced a shower of secondary particles. Charged secondary particles produced light proportional to the energy deposited in the scintillator strips. The scintillator light was passed through light guides to PMTs. Each PMT read out all scintillator strips of the same transversal position. The energy resolution for hadronic showers was [37]

$$\frac{\sigma(E)}{E} = \frac{69\%}{\sqrt{E}}$$

with E in GeV.

The HAC was not used in the run 2007, the information is provided for completeness here.

2.10 THE MUON VETO SYSTEM

In order to provide further π^\pm/μ^\pm separation a Muon Veto (MUV) system was used in NA48/2. The MUV was split into three stations (Figure 11). Each station consisted of one scintillator plane and a 0.8 m thick iron wall preceding the scintillator plane. The iron walls provided hadron absorption. The first two scintillator planes consisted of eleven scintillator strips and the third plane of six scintillator strips. The planes 1 and 2 were used in the trigger and data taking and plane 3 only for monitoring studies. The scintillator strips of the planes were 2.7 m long, except for the central strips of planes 1 and 2, which were divided into two parts to leave space for the beam pipe.

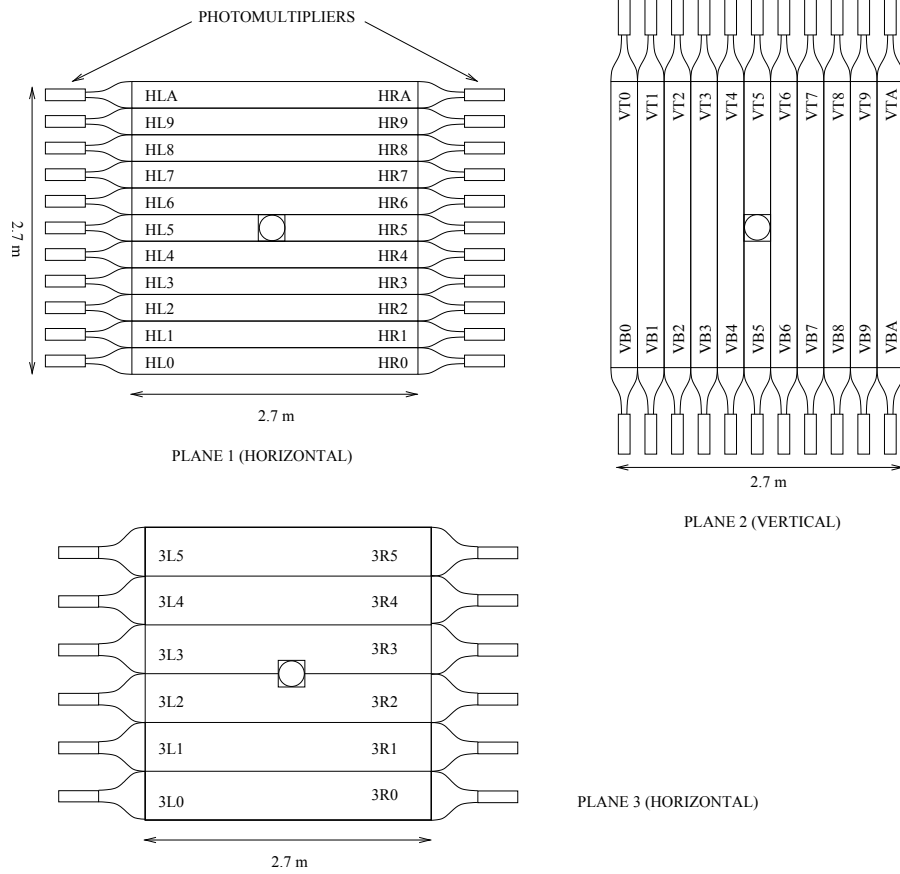


Figure 11: The MUV planes [37].

The scintillator strips for plane 1 and 2 (plane 3) were 1 cm (0.6 cm) thick and 25 cm (45 cm) wide. They were oriented horizontally (plane 1 and 3) and vertically (plane 2). All scintillator strips were connected on both sides to a PMT via a light guide.

Although the MUV was operating during the data taking in 2007, it was not used in this analysis due to non-optimal efficiencies.

2.11 THE PHOTON ANTI-COUNTERS

The Photon Anti-Counters (AKLs) were designed to veto photons outside of the LKr acceptance in a range from 10 to 50 mrad with respect to the z -axis. This was needed in NA48 to reject the decay $K_L^0 \rightarrow 3\pi^0$, hence the name “Anti- K_L ” or AKL. The AKL stations were positioned along the fiducial volumes at seven positions in so-called pockets. Each pocket was divided into two modules. The modules were composed of a 3.5 cm thick iron ring and followed by twelve (for the first four pockets) or eight (for the remaining ones) scintillator strips which were arranged to completely cover the ring (Figure 12). Photons underwent photon conversion in the iron and the result-

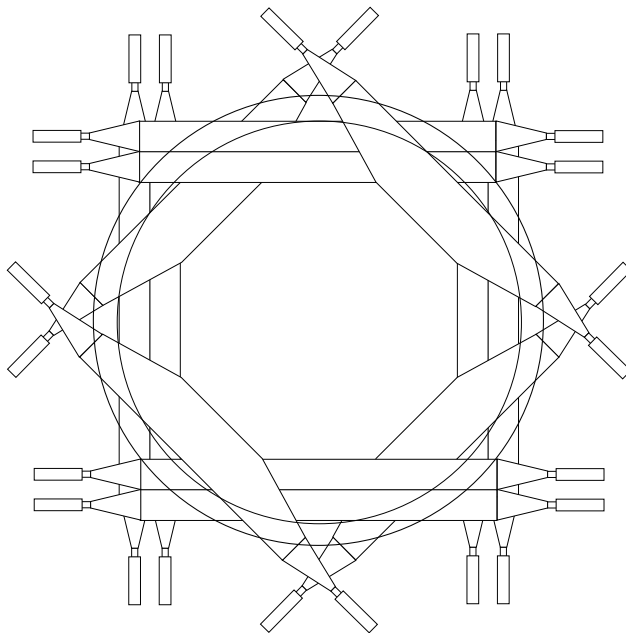


Figure 12: An AKL pocket [37].

TRIGGER	REQUIREMENT
Q_1	At least one coincidence between the two CHOD layers
E_{10}	At least 10 GeV energy deposited in the LKr
$TRKLM$	At least one hit in more than one view and less than 15 hits in any view of DCH ₁ , DCH ₂ , and DCH ₄
$T0N$	Loose coincidence between opposites halves of the NHOD

Table 6: Triggers used for this analysis.

ing positron-electron pair could be measured in the scintillator strips. The total conversion efficiency of one pocket was 95.5 %. The strips dimensions were typically $200 \times 25 \times 1 \text{ cm}^3$. The shape was either rectangular or trapezoidal. A fast signal for the trigger was provided by an OR between two segments of one pocket and summed over all AKL stations. The time resolution was $\sigma_t \approx 550 \text{ ps}$ [37].

The AKL was used in different triggers during the 2007 run. However, none of these triggers nor the AKLs were used in this analysis.

2.12 THE TRIGGER SYSTEM

The particle rate in the subdetectors was of the order of 1 MHz. This rate had to be reduced to be able to write the detector information to disk. Therefore a multi staged trigger system was in place. The

system was synchronized by a 40 MHz clock, storing every 25 ns information of each detector into a 204.8 μ s wide circular memory. Fast computation of some basic variables, e.g. total energy in the LKr or multiplicity in the DCH, made it possible to select only events of interest and to reduce the particle rate below 150 kHz. The available triggers were optimized to measure $R_K = \Gamma(K_{e2})/\Gamma(K_{\mu2})$. However, these triggers are also suitable to select K_{l3} decays. The trigger signals used for this analysis are summarized in Table 6. Figure 13 gives an overview of the trigger and data acquisition chain.

The first trigger stage, the Level 1 Trigger (L1), was divided into two independent subtrigger systems. The Trigger for Charged Particles (L1C) used information from the DCHs and CHOD. The second subtrigger system, the Trigger for Neutral Particles (L1N) used information from the LKr.

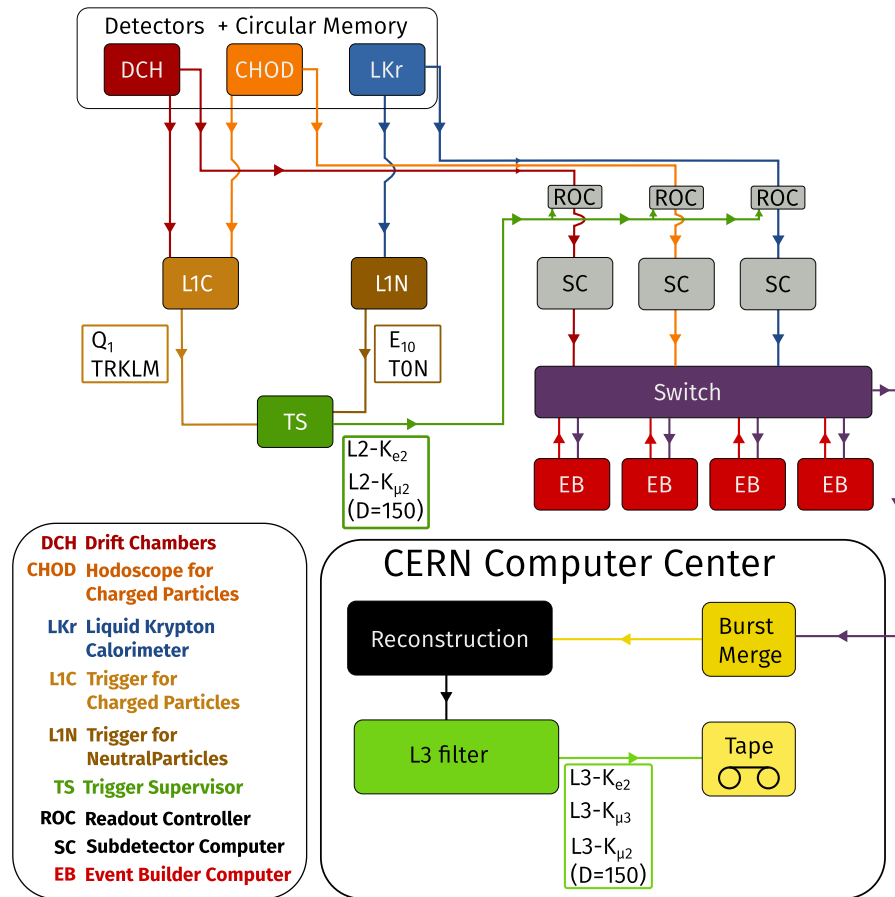


Figure 13: The trigger and data acquisition system. Only the relevant components for this analysis are included.

L2 TRIGGER	LOGIC	DOWNSCALE FACTOR
K_{e2}	$Q_1 \wedge TRKLM \wedge E_{10}$	1
$K_{\mu 2}$	$Q_1 \wedge TRKLM$	150

Table 7: Trigger logics used for this analysis.

2.12.1 *The Trigger for Charged Particles*

The CHOD provided a trigger signal called Q_x with x denoting the minimum amount of coincidences in one quadrant between both layers. The *TRKLM* trigger signal was released if in at least one view of the DCHs one or more hit was registered but not more than 15 hits in any view of DCH₁, DCH₂, and DCH₄. This suppressed events with no track as well as events with high activity, e.g. caused by photo conversion at the kevlar window of the DCH.

Timing for an event was provided by the CHOD signal Q_x for L1C or the NHOD signal *T0N* for L1N. As both signals were independent, it could happen that the same event was recorded twice (with a 25 ns time shift). This was caused by small time misalignments and had to be taken into account for the trigger efficiency measurement (Chapter 6).

2.12.2 *The Trigger for Neutral Particles*

The Neutral Trigger used only information of the LKr. It computed different quantities based on distributions of energy deposition in the LKr. For this analysis only the trigger signal E_{10} is used, which was released if the total energy deposited in the LKr was above 10 GeV.

2.12.3 *The Trigger Supervisor*

Both sub-trigger systems were controlled by a Trigger Supervisor (TS), a 40 MHz digital system which combined the charged and neutral trigger information and produced a final trigger word. The event was discarded or accepted based on the decision of the TS. If the event was accepted, the TS sent a command to the Read Out Controller (ROC) of each subdetector to provide the stored full information of the specific event from the 204.8 μ s wide circular memory. For later efficiency studies, the trigger information processed by the TS was sent to an external acquisition unit called Pattern Unit (PU).

2.12.4 The Trigger Logic

In the $R_K = \Gamma(K_{e2})/\Gamma(K_{\mu2})$ analysis two main triggers were used. The $K_{\mu2}$ main trigger required the trigger signal combination $Q_1 \wedge TRKLM$ (“ \wedge ” being the symbol for a logical AND) to preselect events with one track. The $K_{\mu2}$ main trigger was downscaled⁶ by a factor $D = 150$. The K_{e2} main trigger had the additional criterion E_{10} , which was released if more than 10 GeV energy was deposited in the LKr, leading to $Q_1 \wedge TRKLM \wedge E_{10}$. The signal signature of the decay $K_{l3} = K \rightarrow \pi^0 l^+ \nu$ in the subdetectors is one charged track in the DCH and two γ cluster from the π^0 in the LKr. This makes the K_{e2} main trigger a suitable choice for K_{l3} .

For the normalization channel $K_{2\pi} = K \rightarrow \pi^+ \pi^0$ both main triggers are in principle a suitable choice. However, in a later filter stage (Section 2.13.1) the K_{e2} main trigger was combined with further criteria which makes it a unusable trigger logic for π^+ as charged track. Instead, the $K_{\mu2}$ main trigger is used. The used trigger logics are summarized in Table 7.

2.13 THE DATA ACQUISITION

All subdetectors had a dedicated computer which controlled the read-out. When the Trigger Supervisor (TS) issued a command to the Read Out Controller (ROC) of each subdetector (Section 2.12.3), the full event information was transferred from the circular memory to the subdetector computer. The trigger decisions from the TS were sent continuously during the SPS burst to the ROC. Between two SPS bursts the subdetector computers transferred the collected information of one burst to a group of event building computers.

The event building computers merged the raw subdetector information to one event information and stored it on local disks until it was transferred to the CERN computer center.

On the CERN computer center, the event files were further merged to burst files, reconstruction algorithms (Chapter 3 on Page 35) were applied, and the raw files were converted into a more efficient data format (COMPACT) for later analysis. The reconstructed event information was sent through a last filter, called L3 filter, before finally raw and reconstructed information were stored on tape.

2.13.1 The L3 filter

At this stage in the data acquisition it is possible to combine information from different subdetectors to filter unwanted events. For example the computation of the ratio E/p between measured energy

⁶ Downscaling by a factor x : Only each x^{th} triggered event is also recorded.

L3 FILTER NAME	L2 TRIGGER	FILTER SELECTION
K_{e2}	K_{e2}	$N_{\text{Tracks}} \geq 1,$ $E/p > 0.6,$ $5 \text{ GeV}/c < p < 90 \text{ GeV}/c$
$K_{\mu3}$	K_{e2}	$N_{\text{Tracks}} \geq 1,$ $N_{\text{Cluster}} \geq 2,$ $-25 \text{ m} < z_{\text{vertex}} < 90 \text{ m},$ $0.1 \text{ GeV}/c^2 < m_{\gamma\gamma} < 0.17 \text{ GeV}/c^2$ $E/p < 0.3,$ $p < 90 \text{ GeV}/c$
$K_{\mu2}$	$K_{\mu2}$	$N_{\text{Tracks}} \geq 1,$ $p < 90 \text{ GeV}/c$

Table 8: Available L3 filters. Each filter applies to events selected by the hardware triggers K_{e2} or $K_{\mu2}$. N_{Tracks} is the number of reconstructed charged tracks and p the measured momentum in the spectrometer. N_{Cluster} is the number of reconstructed clusters and E the energy measured in the LKr. z_{vertex} is the reconstructed kaon decay vertex and $m_{\gamma\gamma}$ the invariant mass of two cluster in the LKr using z_{vertex} for computation. Chapter 3 gives further information about the reconstruction of these variables.

E in the LKr and momentum p in the DCH is possible. The available selection filters for the data taking in 2007 are listed in Table 8

For the selection of K_{e3} decays the L3 filter “ K_{e2} ” was used. A dedicated L3 filter for $K_{\mu3}$ was available and is used for selection. For the normalization channel $K_{2\pi}$ only the L3 filter “ $K_{\mu2}$ ” can be used, because no restrictions on the ratio E/p were applied. As this filter is based on the $K_{\mu2}$ main trigger, the selection is downscaled by a factor of 150.

2.14 THE DATA SET

The data set used for this analysis has been acquired in 2007 by the NA62 collaboration. The data taking took place from June 23th until October 22th 2007. However, for this analysis the full data set is not used, instead a subsample containing about 40% of the acquired data has been analyzed. This subsample has been collected during the so-called Period 5 of the data taking. It is used because it was recorded with very stable beam⁷, trigger, and detector conditions. Also, for the first half of the 2007 data taking period a lead wall was placed in front of the LKr, covering the calorimeter partially. The lead wall let only pass muons and made it possible to determine the probability to misidentify the muon for an electron. This information was very

⁷ Only a K^+ beam was used during the Period 5.

important in the $R_K = \Gamma(K_{e2})/\Gamma(K_{\mu2})$ analysis to determine the $K_{\mu2}$ background in the K_{e2} selection. In Period 5 this lead wall had been removed and allowed to use the full acceptance of the LKr detector.

RECONSTRUCTION

The detector information recorded during the data taking had to be converted into physical quantities in order to analyze them. This conversion from digital information recorded by the detector into quantities like the momentum of a particle is called *reconstruction*. For each subdetector specialized reconstruction algorithms converted the raw information into physical meaningful values. This chapter describes the reconstruction routines of the DCH (3.1) and LKr (3.2) subdetectors. Furthermore, the computation of derived information like vertices is discussed. As mentioned in Section 2.13, the first step of the reconstruction took place in the CERN computer center. Corrections to these reconstructed data are also described in this chapter.

3.1 RECONSTRUCTION OF MAGNETIC SPECTROMETER INFORMATION

The reconstruction algorithm [48] builds tracks from hits in the views of the drift chambers. The process is started by building DCH clusters¹. Clusters are a combination of a set of contiguous hits in the two staggered planes of a view in one of the DCH stations². For this step, the drift time is not taken into account. Usually, such a cluster consists of two hits and is called a doublet. If a particle is very close to one of the wires, the particle creates two signals (and hits) in the adjacent wires of the staggered plane with large drift times. Such a cluster is called triplet. If a plane is not fully efficient, a doublet can be transformed into singlets, meaning that the cluster is made up by only one hit.

Segments are built of two clusters per view (X,Y,U,V) in DCH₁ and DCH₂. A segment is a line between a cluster in DCH₁ and one in DCH₂, so it is a projection of the track in the given view. Not all possible segments are taken into account as they have to fulfill selection criteria, e.g. the extrapolated line must cross the Kevlar window at a radius smaller than 120 cm and has to be compatible with a trajectory coming from the kaon beam.

As next step a so-called *front track* is built by combining four segments from the four views, respectively. In case of only three available segments, a front track is built and matching clusters in either DCH₁ or DCH₂ are searched. Clusters are ignored if they are already assigned

¹ Note, that the term *clusters* in other parts of this work usually refers to clusters created by electromagnetic showers in the LKr.

² See Section 2.5 for more details on the plane layout.

to a four-segment front track. In case of two available segments, two clusters are searched. They must be in two different drift chambers and views. The front tracks are extrapolated³ to DCH₄. The predicted intersections with DCH₄ are compared with the measured *space points*, which consist of four clusters in the four views.

If a matching space point is found, the front track is converted to a *minitrack*. For the minitrack the drift times are taken into account, a track time and a quality variable are calculated. This quality variable is the ratio between the amount of hits in each DCH view with time close to the average time of the sample and the total amount of hits in the sample. For good tracks this quality variable is near 1, minitracks with a quality below 0.75 are rejected. At this stage there is mostly one minitrack per track. However, some tracks produce more than one minitrack. A second quality variable Q is calculated which is the ratio between the amount of hits in doublets and triplets versus the total amount of hits in the track.

The physical quantities (momentum, slopes) are computed by a fit algorithm. Subsequently a matching space point in DCH₃ is added to the track and the physical quantities are re-fitted and stored. If more than one minitrack was found, only the minitrack with the χ^2 minimum is kept.

3.2 RECONSTRUCTION OF CALORIMETER INFORMATION

The objective of the reconstruction algorithm is to build clusters from the energy depositions in the LKr-cells [49][50]. A cluster is a group of neighbouring cells in which a particle deposited its energy. In a first step the pulse signals of each cell are converted into an energy value using a known cell-dependent calibration factor. The reconstruction algorithm looks for local maxima in the energy depositions. Such a local maximum (or seed) is a cell that fulfills the conditions

- $E_{\text{seed}} > 0.25 \text{ GeV}$,
- $E_{\text{seed}} > E_i$, and
- $E_{\text{seed}} > 0.18 + 1.8 \cdot E_{\text{ave}}$.

Here, E_i ($i = 0..7$) represents the energy of the i^{th} adjacent cell of the seed and E_{ave} the average energy of the eight neighbouring cells. If an adjacent cell is a dead cell⁴, also the additional cells around the dead cell are considered. The seed and the neighbouring cells are hereinafter called cluster. For each reconstructed cluster the energy is obtained from the central cell as first estimation, the position from the barycenter (energy-weighted average coordinates) of the 3×3 cells

³ This is only possible in the y -coordinate because it is not affected by the magnetic field.

⁴ A dead cell was a cell which has been flagged during data taking as inoperative.

rectangle. If a dead cell is among those cells, the range is increased to 5×5 .

As next step all cells are checked if a cluster is closer than 11 cm. If only one cluster is inside this range, the cell energy is added to this cluster. If more than one cluster is inside this range, the energy is shared between the clusters according to the formula

$$E_i = E_{\text{cell}} \cdot \frac{W_i}{\sum_j W_j} \quad (3.1)$$

where W_i is the expected energy fraction from cluster i in the cell. This energy is computed by taking into account the first estimate of the energy, the distance between cell and cluster position and the energy profile. The energy profile is obtained from Monte-Carlo simulations. After the energies of all cells have been assigned to clusters, the cluster energies and positions are recomputed. Also known corrections, e.g. energy losses due to clusters near the beam pipe or the outer rim of the LKr are applied. The energy of dead cells is estimated using the energy profile of the clusters the cell belonged to. Finally, if a low-energy cluster is closer than 11 cm to a high-energy cluster, both clusters are merged.

3.3 THE KAON MOMENTUM

The momenta of the kaons were measured in NA48/2 by the Kaon Beam Spectrometer (KABES) consisting of six time projection chambers. However, the kaon beam spectrometer was not installed during the run in 2007. The beam momentum was measured for the R_K measurement through the decay $K^+ \rightarrow \pi^+ \pi^+ \pi^-$. This decay was fully reconstructed, thus obtaining the kaon four-vector momentum. The reconstructed values (momenta and slopes) for each event were fitted to an average value for each burst⁵ and stored in a database. If one burst had not enough events, events were cumulated over a few bursts. This database was filled for both data and Monte-Carlo simulation and is available on analysis level.

3.4 THE CHARGED TRACK

The properties of charged particles (e^+ , μ^+ , or π^+) have been measured with the magnetic spectrometer. From this information further quantities are deduced, e.g. the decay vertex of the kaon. These charged particles are referred to as charged tracks in this analysis .

⁵ See Section 2.3 for more details on the beam.

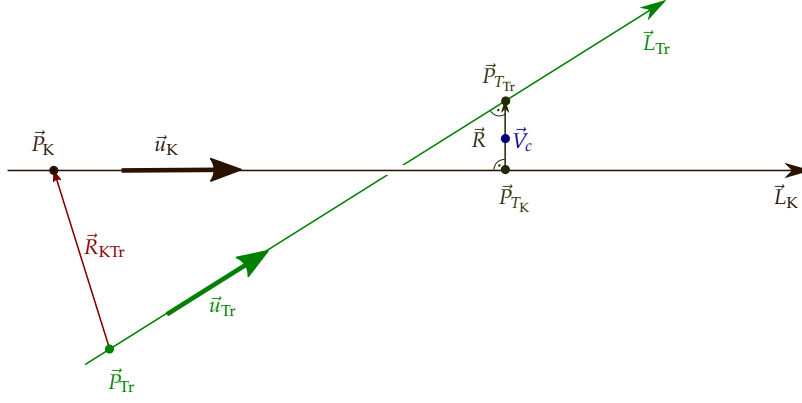


Figure 14: Reconstruction of the distance of closest approach $|\vec{R}|$ between two straight lines \vec{L}_K and \vec{L}_{Tr} . The charged vertex \vec{V}_c lays in the middle between the points \vec{P}_{T_K} and $\vec{P}_{T_{Tr}}$ on the vector \vec{R} .

3.4.1 The Charged Track Momentum

The momentum of charged tracks, in this analysis either an e^+ , μ^+ or π^+ , is reconstructed using the spectrometer information (Section 3.1 on Page 35). The measured slopes ($\frac{dx}{dz}$ and $\frac{dy}{dz}$) and absolute momentum $|\vec{p}_{tr}|$ of the track are combined to the momentum vector

$$\vec{p}_{tr} = \frac{|\vec{p}_{tr}|}{\sqrt{(dx/dz)^2 + (dy/dz)^2 + 1}} \cdot \begin{pmatrix} \frac{dx}{dz} \\ \frac{dy}{dz} \\ 1 \end{pmatrix}. \quad (3.2)$$

The four-momentum then is

$$p_{tr} = (\sqrt{m_{tr}^2 + |\vec{p}_{tr}|^2}, \vec{p}_{tr}), \quad (3.3)$$

with m_{tr} the mass for e^+ , μ^+ , or π^+ taken from [11].

3.4.2 The Charged Vertex

The charged vertex refers to the decay position of the kaon and creation point of the charged particle. This point should be the intersection between the line-of-flight of the kaon and of the charged particle. However, as the tracks are not measured perfectly, they usually do not have a common space point. In this case, the decay point is defined as the mid-point between the tracks on the line of the shortest distance. This point is calculated analytically in the following way (Figure 14):

We start the computation of the point \vec{V}_c with the parametrization of the tracks as straight lines

$$\vec{L}_K = \vec{P}_K + t \cdot \vec{u}_K \quad \text{and} \quad (3.4)$$

$$\vec{L}_{Tr} = \vec{P}_{Tr} + t \cdot \vec{u}_{Tr}. \quad (3.5)$$

with $t \in \mathbb{R}$. The vectors $\vec{u}_i = \vec{p}_i / |\vec{p}_i|$ are the normalized momentum vectors of the kaon and the charged track. The momentum vectors and the points P_i are measured with the spectrometer. The charged track information is measured for each event (Section 3.4) and the kaon information is measured on a burst-by-burst basis (Section 3.3). The vector \vec{R} connects the points \vec{P}_{T_K} and $\vec{P}_{T_{Tr}}$ which have the shortest distance of all points on \vec{L}_K and \vec{L}_{Tr} . It therefore is perpendicular on \vec{L}_K and \vec{L}_{Tr} , so

$$\vec{u}_K \cdot \vec{R} = 0 \text{ and} \quad (3.6)$$

$$\vec{u}_{Tr} \cdot \vec{R} = 0. \quad (3.7)$$

We substitute

$$\vec{R} = \vec{P}_{T_K} - \vec{P}_{T_{Tr}} = \vec{R}_{KTr} + T_K \cdot \vec{u}_K - T_{Tr} \cdot \vec{u}_{Tr}, \quad (3.8)$$

where $\vec{R}_{KTr} = \vec{P}_K - \vec{P}_{Tr}$, and write (with $\vec{u}_i \cdot \vec{u}_i = 1$)

$$T_K - (\vec{u}_K \cdot \vec{u}_{Tr}) T_{Tr} = -\vec{u}_K \cdot \vec{R}_{KTr} \text{ and} \quad (3.9)$$

$$(\vec{u}_K \cdot \vec{u}_{Tr}) T_K - T_{Tr} = -\vec{u}_{Tr} \cdot \vec{R}_{KTr}. \quad (3.10)$$

Now we solve

$$T_K = \frac{\vec{u}_K - (\vec{u}_K \cdot \vec{u}_{Tr}) \vec{u}_{Tr}}{(\vec{u}_K \cdot \vec{u}_{Tr})^2 - 1} \cdot \vec{R}_{KTr} \text{ and} \quad (3.11)$$

$$T_{Tr} = \frac{(\vec{u}_K \cdot \vec{u}_{Tr}) \vec{u}_K - \vec{u}_{Tr}}{(\vec{u}_K \cdot \vec{u}_{Tr})^2 - 1} \cdot \vec{R}_{KTr} \quad (3.12)$$

with the denominator > 0 for non-parallel lines. Finally, we compute the points \vec{P}_{T_1} and \vec{P}_{T_2}

$$\vec{P}_{T_K} = \vec{P}_K + T_K \cdot \vec{u}_K \text{ and} \quad (3.13)$$

$$\vec{P}_{T_{Tr}} = \vec{P}_{Tr} + T_{Tr} \cdot \vec{u}_{Tr}, \quad (3.14)$$

the charged vertex $\vec{V}_c = 0.5 \cdot (\vec{P}_{T_K} + \vec{P}_{T_{Tr}})$, and the distance of closest approach $|\vec{R}|$ between \vec{L}_K and \vec{L}_{Tr} . A dedicated routine⁶ performed the described calculation inside the analysis framework .

3.5 THE NEUTRAL PION π^0

The π^0 decays immediately through $\pi^0 \rightarrow \gamma\gamma$ into two photons. Both photons may hit the LKr and create electromagnetic clusters. Those clusters and the kaon decay vertex are used to reconstruct the π^0 momentum.

⁶ closap.F.

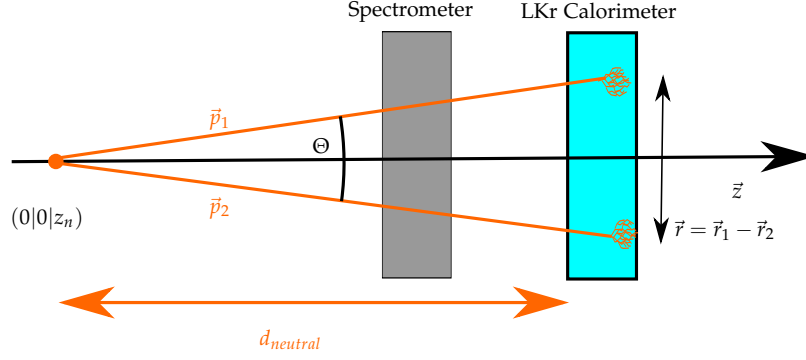


Figure 15: Reconstruction of the neutral vertex. Not to scale.

3.5.1 The π^0 Momentum

The photon momenta $p_{\gamma,i}$ ($i = 1, 2$) are derived from the deposited energy E_i in the LKr, the cluster positions⁷ \vec{r}_i and the neutral decay vertex \vec{V}_n . The unit vector pointing from the creation vertex of each photon to its corresponding cluster is built

$$\vec{r}_{\text{unit},i} = \frac{\vec{r}_i - \vec{r}_{\text{Vertex}}}{|\vec{r}_i - \vec{r}_{\text{Vertex}}|}. \quad (3.15)$$

This vector is used to build the four-vector momentum for each photon

$$p_{\gamma,i} = (E_i, \vec{r}_{\text{unit},i} \cdot E_i). \quad (3.16)$$

The π^0 momentum is the sum of both photon momenta:

$$p_{\pi^0} = \sum_{i=1}^2 p_{\gamma,i}. \quad (3.17)$$

3.5.2 The Neutral Vertex

The distance of the decay vertex of the π^0 to the LKr is reconstructed using only information from the LKr and the known π^0 mass. Figure 15 shows the relevant quantities. As a result of the short life time of the π^0 , this distance is the same for the K^+ decay vertex. The mass of the π^0 can be written with the four-vector momenta p_i of the photons as

$$m_{\pi^0}^2 = (p_1 + p_2)^2 = 2E_1E_2 - 2\vec{p}_1 \cdot \vec{p}_2 = E_1E_2(1 - \cos \Theta) \quad (3.18)$$

⁷ The x - and y -coordinates of the clusters are defined at the z -position z_{LKr} of the front plane of the LKr.

with Θ being the opening angle between both three-vector momenta. As next step the small angle approximation is applied:

$$\frac{\frac{1}{2}|\vec{r}_1 - \vec{r}_2|}{d_{\text{neutral}}} = \tan \frac{\Theta}{2} \approx \sin \frac{\Theta}{2} = \sqrt{\frac{1 - \cos \Theta}{2}} \quad (3.19)$$

which yields

$$d_{\text{neutral}} = \frac{1}{m_{\pi^0}} \sqrt{E_1 E_2} |\vec{r}_1 - \vec{r}_2|. \quad (3.20)$$

The position of the decay vertex of the π^0 , also called neutral vertex, is $\vec{V}_n = (0, 0, z_{\text{LKr}} - d_{\text{neutral}}) = (0, 0, z_n)$ with z_{LKr} the z-position of the front plane of the LKr.

3.6 CORRECTIONS

The physical quantities described in Section 3.1 and 3.2 were computed a short time after the measurement. Some corrections have been developed afterwards and have to be applied on analysis level. These will shortly be described in the following sections.

3.6.1 DCH Misalignment and Magnetic Field Miscalibration

The measured track momentum has to be corrected for a slight misalignment of the DCH stations downstream of the magnet and a miscalibration of the magnetic field in the spectrometer. Effects of misalignment and miscalibration have been studied with $K^\pm \rightarrow \pi^\pm \pi^+ \pi^-$ decays [51]. The first effect leads to a global shift in the reconstructed mass of K^+ and K^- in the same direction and the latter effect to a charge-dependent shift.

A misalignment of the downstream DCH stations is corrected by

$$p = p_0 \cdot (1 + q \cdot \alpha \cdot p_0) \quad (3.21)$$

with q the charge of the particle, p_0 the uncorrected momentum and

$$\alpha = \frac{m_{K^-} - m_{K^+}}{1.7476 \text{ GeV}/c^2}. \quad (3.22)$$

The values for m_{K^\pm} were obtained by reconstruction of $K^\pm \rightarrow \pi^\pm \pi^+ \pi^-$ decays. There was no K^- beam provided during Period 5 (Section 2.14 on Page 33). So it was not possible to calculate the α correction on a burst-by-burst basis like in Periods 1-4. Therefore one run between Period 5 and Period 6 was recorded with both kaon beams. The obtained correction $\alpha = 3.9 \cdot 10^{-5}$ was applied to the whole Period 5 data set.

A possible miscalibration ΔB of the magnetic field leads to a mis-measurement of the momentum because of $\Delta p/p = \Delta B/B$. This is corrected by

$$p = p_0 \cdot (1 + \beta) \quad (3.23)$$

with p_0 the uncorrected momentum and

$$\beta = \frac{\Delta p}{p} = \frac{m_{K^\pm,PDG} - m_{K^+}}{0.1046 \text{ GeV}/c^2}, \quad (3.24)$$

the reconstructed mass m_{K^+} from $K^+ \rightarrow \pi^+ \pi^+ \pi^-$, and the mass $m_{K^\pm,PDG}$ from the Particle Data Group (PDG) [11]. Typical values for the β -parameter were of the order of 10^{-3} .

The denominators in Equation 3.22 and 3.24 are empirical values. Equation 3.21 and 3.23 are jointly written as

$$p = p_0 \cdot (1 + q \cdot \alpha \cdot p_0) \cdot (1 + \beta). \quad (3.25)$$

The reconstructed kaon momentum $p_{K,db}$ which is read from the database (Section 3.3) has to be corrected by the β value as well:

$$p_K = p_{K,db} \cdot (1 + \beta). \quad (3.26)$$

For the Monte Carlo (MC) (Chapter 4) simulation an dedicated database for the α and β parameters exists because the simulation reproduced the misalignments and miscalibrations.

3.6.2 External Magnetic Fields

External magnetic fields in the decay volume have to be taken into account for the computation of the charged vertex. Their main source is the earth magnetic field. The NA48/NA62 collaboration carefully measured this field in the decay volume and provided a correction routine. For this routine, first the charged vertex is computed, then the routine uses the measured field map to correct the slopes of the tracks and the vertex is recomputed with the new slopes. Typical corrections to the slopes were of the order of 10^{-5} rad.

3.6.3 LKr Projectivity

The transversal positions (x, y) of clusters are defined on the front plane of the LKr. The axes of the LKr cells were tilted in such a way that they pointed to a point P (projectivity point) with a distance of 109.98 m from the front face of LKr. The transversal positions of a cluster are independent from the longitudinal shower depth if the cluster is created by a photon originating from P . However, the transversal positions need to be corrected for photons created in other positions D (Figure 16). The correction depends on the average shower depth d_{sw} which is calculated using [52]

$$d_{sw} = 16.5 + 4.3 \cdot \ln(E) \quad (3.27)$$

where E is the measured cluster energy in units of GeV and d_{sw} in cm. The position D is obtained from the charged vertex (Section 3.4.2

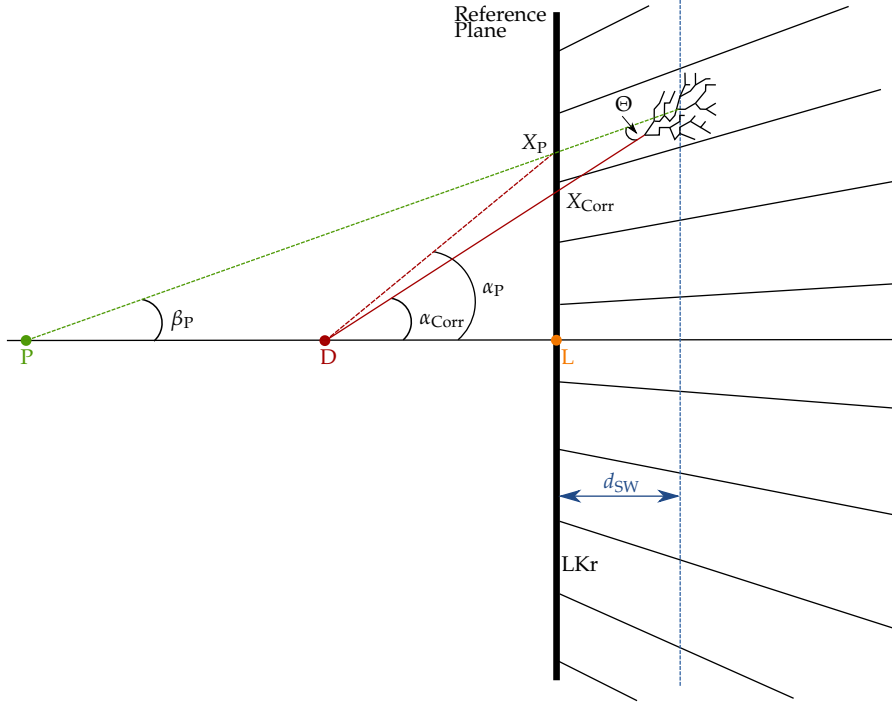


Figure 16: The geometry of the LKr required a correction to the measured position X_P of clusters created by photons originating from a point D far away from the projectivity point P . The correction can be written as $x_{Tr} \approx x_P \cdot \frac{1 + \frac{d_{sw}}{PL}}{1 + \frac{d_{sw}}{DL}} \approx X_P \cdot \left(1 + \frac{d_{sw}}{PL} - \frac{d_{sw}}{DL}\right)$ (Equation 3.30). Based on [52, P. 107]

on Page 38). The corrected transversal position x_{Corr} can be written as (using the small angle approximation):

$$x_{Corr} \approx x_P - d_{sw} \cdot \Theta, \quad (3.28)$$

where Θ is the angle between the line from the cluster to the projectivity point and the photon trajectory. This angle can be written as

$$\Theta = \alpha_{Tr} - \beta_P \approx \frac{x_{Tr}}{DL} - \frac{x_P}{PL}. \quad (3.29)$$

This leads to

$$x_{Corr} \approx x_P \cdot \frac{1 + \frac{d_{sw}}{PL}}{1 + \frac{d_{sw}}{DL}}. \quad (3.30)$$

This corresponds to a correction up to $\approx 0.5\%$.

3.6.4 LKr Misalignment with Respect to the Drift Chambers

The alignment between LKr and DCH has been tested with electrons. The position of electrons in the LKr is deduced by extrapolating the

known slopes by the spectrometer measurement from DCH₄ to the LKr. Comparison of the extrapolated position with the position measured in the LKr reveals possible shifts in the transversal plane and a rotation between both detectors. This measurement has been done by the NA62 collaboration for the $R_K = \Gamma(K_{e2})/\Gamma(K_{\mu2})$ analysis and yielded following correction [52][53]:

$$x_{\text{corr}} = x_0 + \Delta x + \Theta \cdot y_0 \quad (3.31)$$

$$y_{\text{corr}} = y_0 + \Delta y - \Theta \cdot x_0 \quad (3.32)$$

where $\Delta x = 0.136$ cm and $\Delta y = 0.3$ cm are translational shifts and $\Theta = 0.87 \cdot 10^{-3}$ rad is a rotation.

3.6.5 LKr Non-Linearity Correction

For reconstructed cluster energies below 10 GeV, a non-linearity was introduced by an energy threshold⁸ inside the LKr reconstruction. This known effect is corrected by the polynomial function

$$E_{\text{corr}} = -0.00101009 + 0.000219228 \cdot E - 1.61845 \cdot 10^{-5} \cdot E^2 + 4.17065 \cdot 10^{-7} \cdot E^3 \quad (3.33)$$

with E being the uncorrected energy in GeV.

3.6.6 LKr Cell-by-Cell Correction

In order to improve the uniformity of the LKr response, a cell-by-cell correction was introduced. This correction is provided by the collaboration and was measured for the $R_K = \Gamma(K_{e2})/\Gamma(K_{\mu2})$ analysis. A sample of K_{e3} events with selection criteria was used to measure the momentum and released energy in the LKr by the electrons. For each cell a momentum dependent correction was calculated by requiring $E/p = 1$.

3.7 RECONSTRUCTION AND ANALYSIS SOFTWARE COMPACT

As discussed in Section 2.13 on Page 32, the amount of recorded data was reduced by trigger and software filters. The remaining information was stored in a dedicated file format. To read this file format the software COMPACT⁹ is used on analysis level. It provides access to reconstructed physical quantities, e.g. momenta or positions, from data and Monte-Carlo. The database of the corrections is also accessible via COMPACT.

⁸ Also called "Zero suppression".

⁹ C OptiMized Program for Accessing Countless Terabytes

MONTE CARLO SIMULATION

The decay channels under investigation are simulated with Monte Carlo (MC) methods. This involves the simulation of the kaon beam (Section 4.1 on Page 45), the decay of a kaon into the desired decay channel (Section 4.2 on Page 46), the interactions of the kaon daughter particles with the detectors and the detector response (Section 4.3 on Page 48). The reconstruction (Chapter 3 on Page 35) eventually applied is the same for the simulation and the data. Finally, the Monte Carlo simulation is available in the same COMPACT format as the data.

In addition to the reconstructed detector information, the particle properties at generation time, e.g. the momenta or decay positions, are stored inside the COMPACT file. These so-called *true values* are helpful to test the applied selections on data. The same selections (Chapter 5 on Page 57) are applied to the data and to the Monte Carlo simulation.

The Monte Carlo simulation is used to determine the acceptance of a given selection since the number of generated events and the number of events passing the selection is known. This applies both to signal and background channels.

The Monte Carlo simulation used in this analysis has been created with the Charged Kaons Monte Carlo (CMC) package.

4.1 BEAM SIMULATION

The charged kaon beam is modeled with the Trace Unlimited Rays Through Lumped Elements (TURTLE) package [54]. This package is designed to simulate charged particle beam transport systems. TURTLE takes aberration effects into account. The beam line described in Section 2.3 on Page 18 and shown in Figure 5 (a) is implemented inside TURTLE up to and including the final collimator. The description includes the collimators and the dipole and the quadrupole magnets. The beam conditions (i.e. the dipole magnet fields, the positions of the momentum-selecting collimators, the beam position at the final collimator and the DCH₁) during data taking were recorded on a run-by-basis and later used as input for the beam simulation. The beam positions and the mean beam momentum were obtained from fully reconstructed $K^+ \rightarrow \pi^+ \pi^+ \pi^-$ decays.

4.2 KAON DECAY GENERATORS

The kaons decay inside the fiducial volume with a given probability corresponding to their lifetime. The so-called decay generator simulates the physical properties of a given decay, e.g. simple properties as momentum distributions or very sophisticated properties as radiative corrections to electrons. The decays are simulated in the rest frame of the kaon. Before the decays are handed over to the detector simulation, the momenta are boosted into the lab frame. All generated π^0 are forced to decay into $\pi^0 \rightarrow \gamma\gamma$.

4.2.1 The KLOE Generator

The decays K_{e3} and $K_{2\pi}$ are described by the KLOE generator for radiative kaon decays [55]. The generator includes the description of soft photons from internal bremsstrahlung with $E_\gamma \ll E_{\text{CM}}$ where E_γ is the energy of the photon and E_{CM} the energy of the center of mass system¹. The amplitudes $M_i \rightarrow M_{f\gamma}$ are calculated at the order of α with chiral perturbation theory. The rate of the process $i \rightarrow f$ is then described by [55]

$$\Gamma(E_\gamma) = \Gamma_0 \left(\frac{E_\gamma}{\Lambda} \right)^b (1 + O(b^2) + O(E_\gamma)), \quad (4.1)$$

with Γ_0 the decay rate for the process without radiative photons, a cut-off energy Λ (henceforth chosen as the mass M of the decaying particle), and the factor

$$b = -\frac{1}{8\pi^2} \sum_{m,n} \eta_m \eta_n e_m e_n \beta_{mn}^{-1} \ln \frac{1 + \beta_{mn}}{1 - \beta_{mn}}. \quad (4.2)$$

Here m and n run over all external particles, e_m and e_n are the particle charges, $\eta = \pm 1$ for out- and ingoing particles, and

$$\beta_{mn} = \left(1 - \frac{m_n^2 m_m^2}{(p_n \cdot p_m)^2} \right)^{1/2} \quad (4.3)$$

the relative velocity of the particles m and n in the rest frame. Differentiation of Equation 4.1 with respect to E_γ yields

$$\frac{d\Gamma(E_\gamma)}{dE_\gamma} = \frac{d\Gamma_{\text{Rad}}}{dE_\gamma} \left(\frac{E_\gamma}{M} \right)^b. \quad (4.4)$$

Here is

$$\frac{d\Gamma_{\text{Rad}}}{dE_\gamma} = \Gamma_0 \frac{b}{E_\gamma} \quad (4.5)$$

¹ E_{CM} is equivalent to the mass M of the decaying particle.

the single-photon emission probability.

The sampling of the random variables according to their probability distributions is done by a combination of the *acceptance-rejection* method and the *inverse transform* method [11, Monte Carlo Techniques]. The first is used for finite distributions whereas the latter is used for divergent distributions. Technical details on the implementation can be found in [56].

4.2.1.1 $K^+ \rightarrow \pi^0 e^+ \nu$ Generator

For semileptonic decays, chiral perturbation theory is used to order p^2 . In this case the form factors are $f_+ = 1$ and $f_- = 0$. For electrons the form factor f_- can be neglected. However, in order to keep the dependence on the variable $t = p_K - p_\pi$, the amplitude is multiplied with known expression for $f_+(t)$. This approach results for K_{e3} in small uncertainties as shown in [55]. $f_+(t)$ is parametrized by the dispersive method (Section 1.4.4.3 on Page 15) using the nominal value of $\Lambda_+ = 0.02566(41)$ [22].

The divergent function in Equation 4.5 can be split into a divergent and finite part:

$$\frac{d\Gamma_{\text{Rad}}}{dE_\gamma} = b \left(\frac{E_{\text{CM}}}{E_\gamma} \right)^{1-b} F(E_\gamma). \quad (4.6)$$

$F(E_\gamma)$ is a polynomial function of E_γ . For K_{e3} , the decay width is then [56]

$$d\Gamma_{\text{Rad}} = b(E_e) \left(\frac{M_K}{E_\gamma} \right)^{1-b(E_e)} \frac{F(E_\gamma, \cos \theta, E_e)}{E_e - p_e \cos \theta} d\Phi_4 \quad (4.7)$$

with

$$F = |A|^2 E_\gamma (E_e - \cos \theta) / b. \quad (4.8)$$

The integration variables are the photon energy E_γ , the angle θ between the photon and the electron, the electron energy E_e and momentum p_e in the kaon rest frame, and the four-body phase space factor $d\Phi_4$. The term $(E_e - p_e \cos \theta)^{-1}$ is introduced due to the dependency of $d\Gamma_{\text{Rad}}$ on θ . A represents the amplitude. The factor b (Equation 4.2) depends implicitly on E because β depends on E .

4.2.1.2 $K^+ \rightarrow \pi^+ \pi^0$ Generator

The decay width is given by [56]

$$d\Gamma_{\text{Rad}} = |A|^2 \frac{\alpha}{(2\pi)^2} \left| \frac{p_{\pi^+}}{p_{\pi^+} \cdot E_\gamma} - \frac{p_K}{p_K \cdot E_\gamma} \right|^2 \left(\frac{E_\gamma}{M_K} \right)^b d\Phi_3. \quad (4.9)$$

A is the amplitude, Φ_3 is the three-body phase space factor, p_{π^+} and p_K are the momenta of the charged pion and the kaon, respectively, and E_γ is the energy of the photon. The term $(E_\gamma M_K^{-1})^b$ cures the divergence.

4.2.2 $K^+ \rightarrow \pi^0 \mu^+ \nu$ Generator

In order to take the form factor f_- into account, $K_{\mu 3}$ decays are not generated with the KLOE generator but in three steps:

1. The momenta of the daughter particles in the rest frame of the kaon are generated using the routine *genbod* from the package collection *cernlibs* [57]. A flat phase space is assumed.
2. The event is accepted if it passes a *hit-or-miss* test of the matrix element given in Section 1.4. The form factors are parametrized by the dispersive method (Section 1.4.4.3 on Page 15) using the nominal values of $\Lambda_+ = 0.02566(41)$ and $\ln_C = 0.2004(91)$ [22].
3. Radiative corrections are introduced with the *PHOTOS* package [58]. *PHOTOS* takes the generated momenta and with a given probability it adds a photon and modifies the momenta of the other particles to respect momentum conservation. The photon itself, however, is not written to the list of true particles.

4.2.3 $K^+ \rightarrow \pi^+ \pi^0 \pi^0$ Generator

The generation of $K^+ \rightarrow \pi^+ \pi^0 \pi^0$ events follows the same recipe as the $K_{\mu 3}$ event generation without radiative corrections. The matrix element for this decay is parametrized through expansion as [11, "Dalitz plot parameters for $K \rightarrow 3\pi$ "] [59]

$$|M|^2 \propto 1 + g \left(\frac{s_3 - s_0}{m_K^2} \right) + h \left(\frac{s_3 - s_0}{m_K^2} \right)^2 \quad (4.10)$$

with

$$s_i = (p_K - p_i)^2 = (m_k - m_i)^2 - 2m_k T_i, \quad i = 1, 2, 3, \quad \text{and} \quad (4.11)$$

$$s_0 = \frac{1}{3} \sum s_i = \frac{1}{3} (m_K^2 + m_1^2 + m_2^2 + m_3^2).$$

The index $i = 3$ is used for the π^+ , p_i are the four-vector, m_i the mass, and T_i the kinetic energy of the i^{th} pion. The coefficients $g = 0.626(7)$ and $h = 0.052(8)$ are measures of the slope in the variable s_3 of the Dalitz plot and the quadratic dependence on s_3 , respectively [11].

4.3 DETECTOR SIMULATION

The daughter particles of the kaons are passed to Geant3 [60]. Geant3 is a simulation framework with the main purpose of tracking particles

through an experimental setup. It takes different effects into account to simulate the passage of particles through detector material:

- Energy loss in material through ionization,
- multiple scattering,
- bremsstrahlung effects, and
- photon conversion into electron-positron pairs, e.g. at the Kevlar window of the helium vessel of the DCH

are simulated. The energy loss simulation is important for the LKr. However, the full simulation of the response of the LKr is very time-consuming. A trade-off between statistical precision and calculation time are so-called *shower libraries* which contain different sets of fully simulated LKr responses generated with different particles and particle energies. During the MC mass production, CMC accesses the shower library for the given particle (e.g. an electron) and the given energy and selects a random LKr shower from the library. The simulation of electromagnetic showers of electrons and photons in terms of released energy and shower width is reasonably good. The agreement between data and simulation for mesons (e.g. the charged pion) on the other hand is quite bad. No showers at all are simulated for muons. This requires taking special care of selection criteria applied to the reconstructed energy of LKr cluster. The selection criteria efficiencies need to be extracted from data and then to be applied as weights to the MC. In this analysis, only the selection criterion on the ratio E/p of the cluster energy E and the track momentum p needs such treatment (Section 5.4 on Page 64).

The simulation of multiple scattering, bremsstrahlung, and photon conversion is important for the simulation of the momentum measurement with the spectrometer. Multiple scattering on the Kevlar window, in the helium, and on the DCH walls leads to mismeasurement of the track momentum. A good description is needed to yield a good simulation of the detector resolution.

Bremsstrahlung effects are needed to correctly describe electrons in the DCHs. Bremsstrahlung photons are created through interactions with the spectrometer material. The flight path of the electrons is bent by the magnet in the DCH whereas the photons travel on a straight line and may hit the LKr. To accept these events with additional photons, no criterion on the maximal allowed amount of LKr clusters is set in the selections in Chapter 5.

4.4 PARTICLE DECAYS

The kaon daughter particles may decay in the fiducial volume or inside the detectors. Only the decay of the π^0 is handled at generator

level, i.e. the photons are passed from the generator to Geant3. The remaining possible decays are $\mu^+ \rightarrow e^+ \nu_e \bar{\nu}_\mu$ ($\tau = 2.2 \cdot 10^{-6}$ s [11]) and $\pi^+ \rightarrow \mu^+ \nu_\mu$ ($2.6 \cdot 10^{-8}$ s [11]). At the given energies of ≈ 10 GeV for muons and ≈ 30 GeV for pions, only $\pi^+ \rightarrow \mu^+ \nu_\mu$ is relevant with a probability of $\approx 6\%$ to decay inside the decay volume.

4.5 CORRECTIONS TO THE MONTE-CARLO SIMULATION

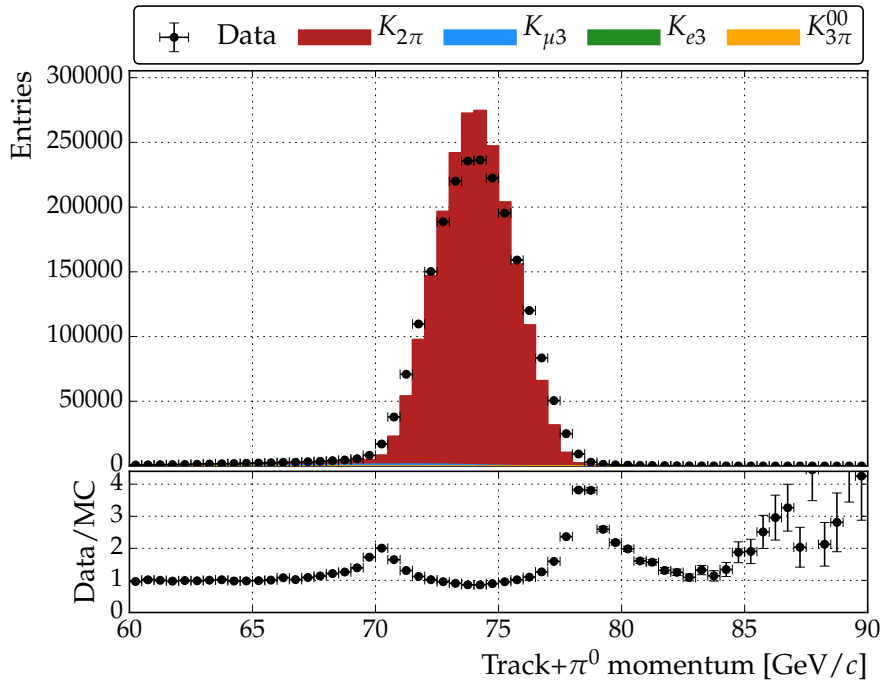
4.5.1 Width of the Kaon Momentum Distribution

During the $R_K = \Gamma(K_{e2})/\Gamma(K_{\mu2})$ analysis it turned out that the central value of the kaon momentum is simulated correctly but the width of the momentum distribution is not. Figure 17 (a) shows the kaon momentum reconstructed with $K_{2\pi}$ events in data and Monte Carlo simulation. The ratio Data/MC shows a deviation in the widths of both distributions. A correction [61] has been developed for the $R_K = \Gamma(K_{e2})/\Gamma(K_{\mu2})$ analysis which is used here, too. This correction is applied as a weight

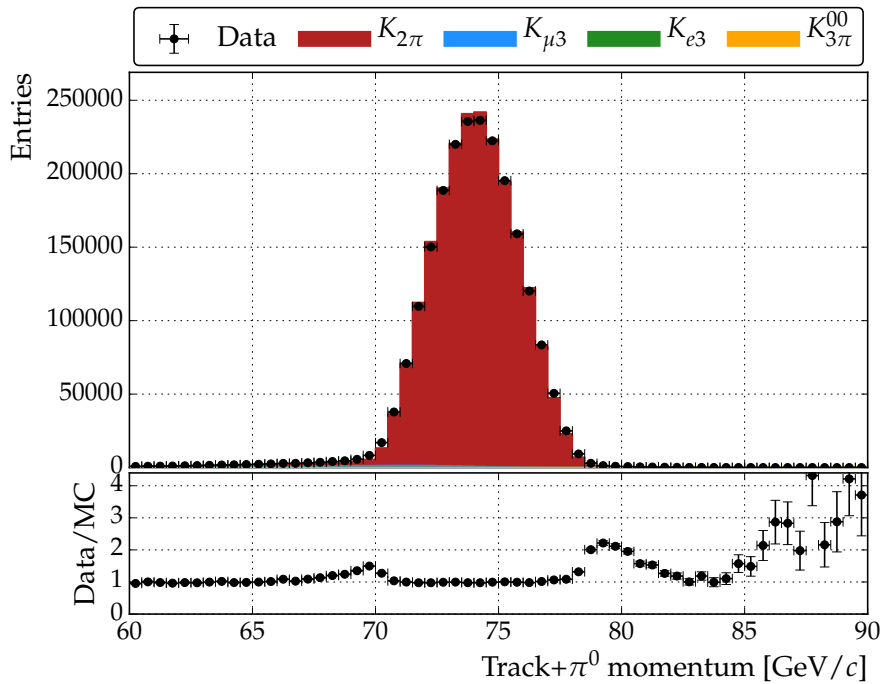
$$w_{\text{width}} = 1 + b_1 b_2 (p - 74 \text{ GeV}/c)^2 \quad (4.12)$$

to the MC events with p the *true* kaon momentum from the Monte Carlo simulation. The parameter $b_1 = 0.07$ is constant and b_2 is time (run) and *true* kaon momentum dependent². The parameters were determined by a fit to the data/MC distributions of the reconstructed kaon momentum from a $K^+ \rightarrow \pi^+ \pi^+ \pi^-$ sample. Figure 17 (b) shows the kaon momentum after applying the correction.

² The full source code for this correction is available in Appendix A.1.



(a) The uncorrected kaon momentum.



(b) The corrected kaon momentum.

Figure 17: The kaon momentum distribution reconstructed using $K_{2\pi}$ events.

4.5.2 Kaon Beam Halo

A deviation in the data/MC description of the transversal momentum of $K_{2\pi}$ was discovered in this analysis. The deviation is shown in Figure 18 (a). The effect is corrected by adding MC events with a wider beam width [62]. The kaon momentum vectors and decay positions of the additional MC events are shifted (Figure 19). A random position on a ring with radius r (or one of multiple rings with different radii) is chosen around the vector of the kaon (blue dashed) at the position $z = 45$ m. The position $z = 45$ m is arbitrarily chosen. The slope of the kaon momentum vector is modified so that the vector passes the position on the ring (red dashed). The decay vertex positions in x and y are modified accordingly. The impact on the decay vertex positions is presented in Figure 20. For this analysis, the procedure was slightly modified. Instead of fixed ring radii, the ring radii follow a Gauss distribution with mean radius r_0 and a width of σ_r .

Additional 3% of the MC events were generated where

- $\frac{2}{3}$ of these events have $r_0 = 1.38$ cm and $\sigma_r = 0.5 \times r_0$ and
- $\frac{1}{3}$ of these events have $r_0 = 1.00$ cm and $\sigma_r = 0.3 \times r_0$.

These are the best fitting values found. The impact of the correction is shown in Figure 18 (b). The description of data improves significantly. The effects of this correction on different variables were investigated. Such variables were the missing mass m_{miss}^2 (Section 5.6.3, Page 87), the transversal momentum of track and π^0 (Section 5.6.4, Page 87), and the kaon mass difference ΔM (Section 5.6.6, Page 91). Selection criteria on these variables were chosen to be far away from values on which the kaon halo correction has the largest effect. An example is given in Section 5.6.3 (Page 87).

4.5.3 Detector Corrections

The corrections described in Section 3.6 (Page 41) are applied to the Monte Carlo simulation as follows:

- The DCH misalignment and magnetic field miscalibration corrections are applied with different values of α and β for MC than data.
- The correction for external magnetic fields and the LKr projective correction are applied as on data.
- The correction for the LKr misalignment with respect to the DCH uses different parameters. The MC values are $\Delta x = 0.013$ cm, $\Delta y = 0$ cm, and $\Theta = 0$ rad.
- The LKr non-linearity correction and the LKr cell-by-cell correction are not applied on MC.

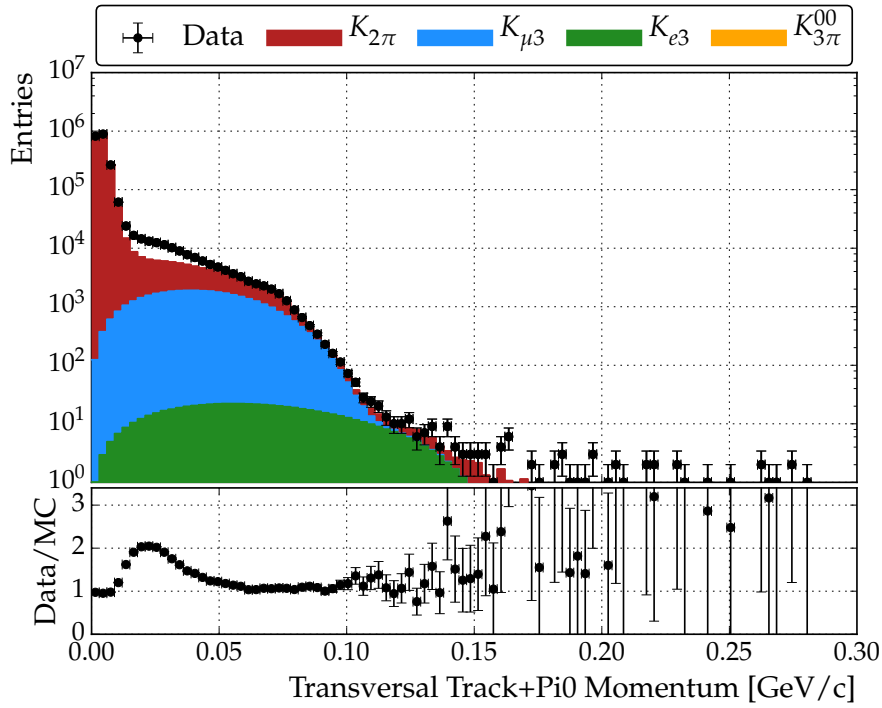
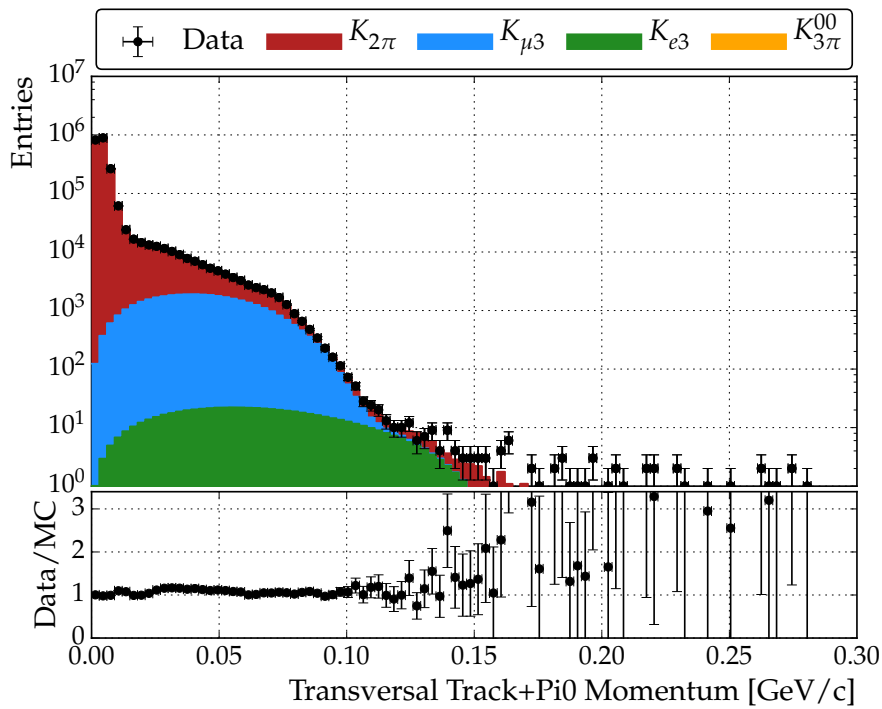
(a) $K_{2\pi}$ selection. No kaon beam halo correction.(b) $K_{2\pi}$ selection. Applied kaon beam halo correction.

Figure 18: Distribution of the track+ π^0 momentum. A notable improvement of the data/MC description is achieved by the kaon halo correction.

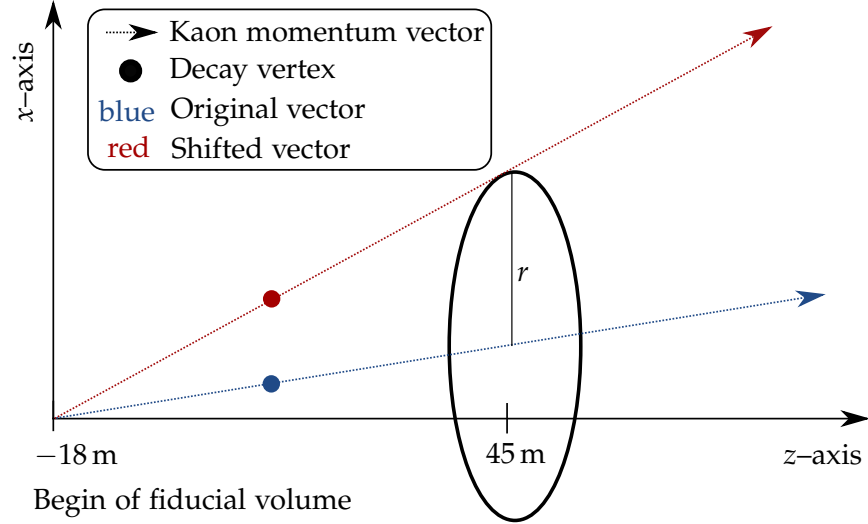


Figure 19: Sketch of the kaon halo correction.

4.6 MC SAMPLES AND ACCEPTANCE

The MC sample consists of

- $N_{\text{Total}}^{K_{\mu 3}} = 323\,943\,723$ $K_{\mu 3}$ events,
- $N_{\text{Total}}^{K_{e 3}} = 323\,843\,681$ $K_{e 3}$ events,
- $N_{\text{Total}}^{K_{2\pi}} = 215\,661\,760$ $K_{2\pi}$ events, and
- $N_{\text{Total}}^{K_{3\pi}^{00}} = 161\,707\,863$ $K_{3\pi}^{00}$ events.

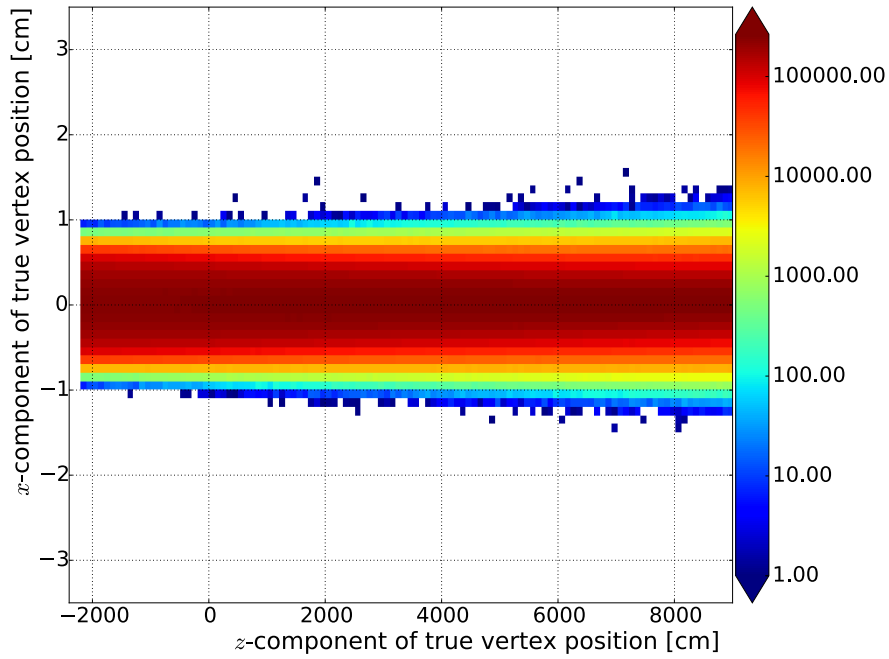
The acceptance A_{MC} is computed by dividing the number of events passing the signal selection $N_{\text{Selection}}^{\text{MC}}$ divided by the total number of weighted events $N_{\text{Total,Weighted}}^{\text{MC}}$:

$$A_{\text{MC}} = \frac{N_{\text{Selection}}^{\text{MC}}}{N_{\text{Total,Weighted}}^{\text{MC}}}. \quad (4.13)$$

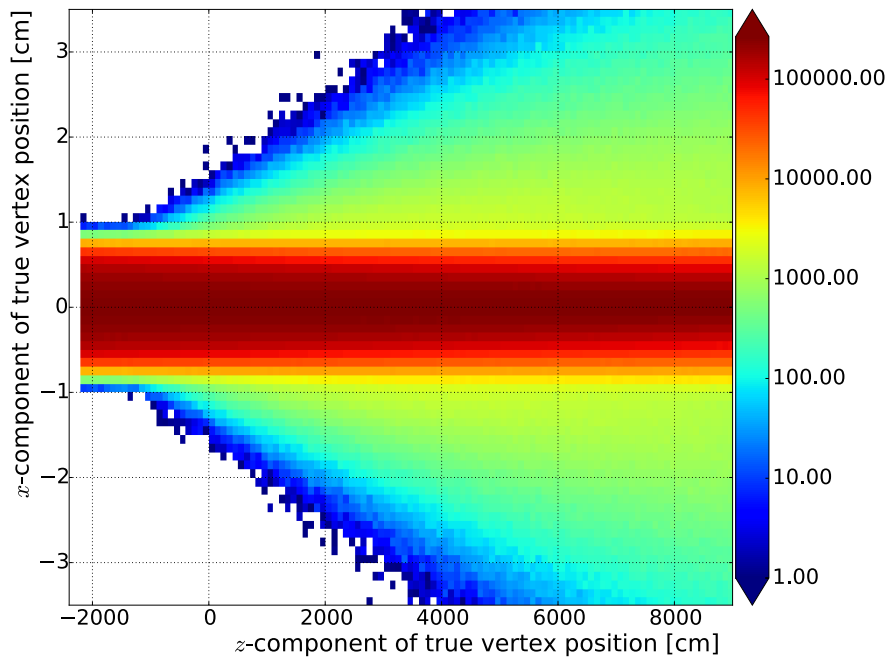
$N_{\text{Total,Weighted}}^{\text{MC}}$ is obtained by weighting each event with the correction for the width of the kaon momentum distribution w_{width} :

$$N_{\text{Total,Weighted}}^{\text{MC}} = \sum_{i=0}^{\text{Total}} w_{\text{width},i}. \quad (4.14)$$

The selected events are also weighted as a consequence. The acceptances for $K_{\mu 3}$, $K_{e 3}$, and $K_{2\pi}$ are presented in Table 9. The uncertainties of the acceptances are small (of the order of 10^{-6}) so that effects of the weighting on the uncertainties are neglected.



(a) No kaon beam halo correction.



(b) Applied kaon beam halo correction.

Figure 20: The x - and z -components of the true vertex positions in $K_{2\pi}$ MC. The correction adds MC events with a wider beam distribution.

	$K_{\mu 3}$	$K_{e 3}$	$K_{2\pi}$
$N_{\text{Total}}^{\text{MC}}$	317 568 341	317 470 661	211 417 791
$N_{\text{Total,Weighted}}^{\text{MC}}$	366 216 627	366 098 520	243 805 959
$N_{\text{Selection}}^{\text{MC}}$	31 771 696	28 823 489	40 223 759
$A_{\text{MC}} [\%]$	8.68	7.87	16.50

Table 9: Overview of the signal MC samples and acceptances. $N_{\text{Total}}^{\text{MC}}$ is the total generated amount of events for each decay channel. $N_{\text{Total,Weighted}}^{\text{MC}}$ is corrected for the beam width. $N_{\text{Selection}}^{\text{MC}}$ is the amount of events which passed the selection for the respective selection. A_{MC} is the acceptance for the respective decay channel.

EVENT SELECTION AND RATIOS

Selection criteria are applied to data and MC events to select a particular kaon decay, the so-called signal decay. These selection criteria should select the signal decay with high acceptance and reject all other decays, the so-called background decays. If decays have similar decay signatures and/or decay particle properties, a trade-off between signal acceptance and background rejection is required. The selection criteria of the signal decays $K^+ \rightarrow \pi^0 e^+ \nu_e$ (K_{e3}) and $K^+ \rightarrow \pi^0 \mu^+ \nu_\mu$ ($K_{\mu3}$), as well as of the normalization decay $K^+ \rightarrow \pi^+ \pi^0$ ($K_{2\pi}$) are described in this chapter.

The distribution of each variable on which a selection criterion is applied is shown in this chapter. The respective selection criterion is *not* applied but indicated by one or more grey lines. Data are represented as black points and MC as colored areas. The MC distributions are stacked and are normalized to the kaon flux (Section 5.8 on Page 103). Not all MC distributions indicated in the respective plot legend may be visible in linear y -axis representation.

5.1 DECAY SIGNATURES

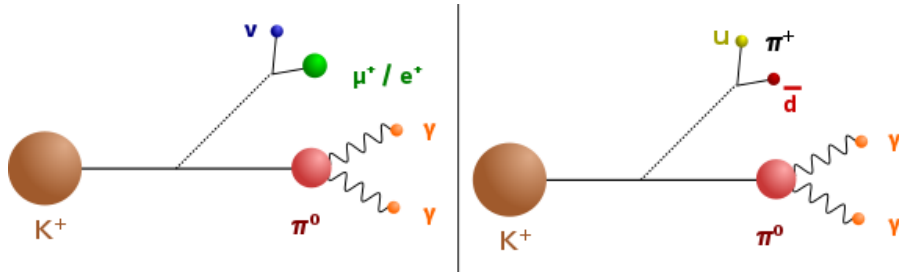


Figure 21: Visualization of the semileptonic kaon decays K_{e3} and $K_{\mu3}$ (left) and the hadronic kaon decay $K_{2\pi}$ (right).

The decays K_{e3} , $K_{\mu3}$, and $K_{2\pi}$ show very similar signatures in the detector. All three decays have a charged particle and a π^0 in the final state. (Figure 21). This fact is exploited to reduce systematic effects on the ratios $\frac{\text{Br}(K_{\mu3})}{\text{Br}(K_{2\pi})}$, $\frac{\text{Br}(K_{e3})}{\text{Br}(K_{2\pi})}$, and $\frac{\text{Br}(K_{\mu3})}{\text{Br}(K_{e3})}$ by using as similar as possible selection criteria for all three decays. The selections differ in criteria which distinguish the decays from each other. Electrons are distinctive in the LKr because they release all energy inside the active volume which allows to distinguish them from muons and charged pions. The ratio E/p of the energy E of the particle measured in the LKr

and the momentum p measured in the DCH takes advantage of this property. Electrons have E/p values around one, muons around zero and pions have a broad distribution. Muons and charged pions can pass the LKr without creating any cluster at all or create a cluster but release only a fraction of their energy (Section 5.4 on Page 64).

The decay $K_{2\pi}$ is distinct from K_{e3} and $K_{\mu3}$ due to being a two-body decay. The sum of the momenta of the π^+ and the π^0 give the kaon momentum. The neutrinos of the K_{e3} and $K_{\mu3}$ decays leave the detector unseen so that the neutrinos carry momentum away. The two-body signature is used to select $K_{2\pi}$ as signal decay and also to reject it as background for selections with K_{e3} and $K_{\mu3}$ as signal decays.

The decay $K^+ \rightarrow \pi^+ \pi^0 \pi^0$ ($K_{3\pi}^{00}$) is a background to all three signal decays. The additional π^0 is used to suppress this background.

5.2 TRIGGER

The trigger system is described in Section 2.12 on Page 29. The K_{e2} -trigger is used for the selection of K_{e3} and $K_{\mu3}$. Based on the K_{e2} -trigger, the L3 filter L3- K_{e2} is required in the K_{e3} selection. The L3 filter L3- $K_{\mu3}$ is required in the $K_{\mu3}$ selection. The L3 filter L3- $K_{\mu2}$ (based on the $K_{\mu2}$ -trigger) is required in the $K_{2\pi}$ selection. The efficiencies of the chains trigger + L3 filter are discussed in Chapter 6. Those efficiencies are applied as weight to the data during the reconstruction.

5.3 COMMON SELECTION CRITERIA FOR e^+ , μ^+ , AND π^+

Common selection criteria are used for the charged particles (also referred to as “charged tracks” or short “tracks”) and the π^0 . These criteria are not specific to a decay. Such criteria are discussed in Section 5.6 on Page 84. In this section, the common criteria on tracks are discussed. The π^0 selection criteria are discussed in Section 5.5 on Page 74. Table 10 summarizes the applied selection criteria on tracks.

5.3.1 Charge and Quality

The charge of the track is required to be $q_{\text{Track}} = 1$. The quality from the DCH reconstruction is required to be $Q_{\text{Track}} > 0.7$ which is the ratio between the number of hits in doublets and triplets versus the total number of hits in the track (Section 3.1 on Page 35).

SELECTION CRITERION	VALUE
Charge	$q_{\text{Track}} = 1$
Quality	$Q_{\text{Track}} > 0.7$
Time	$-18 \text{ ns} < t_{\text{CHOD}} - t_{\text{trigger}} < 22 \text{ ns}$
DCH Acceptance	$12 \text{ cm} < r_{\text{DCH}_1} < 115 \text{ cm}$ $13 \text{ cm} < r_{\text{DCH}_4} < 115 \text{ cm}$
LKr acceptance	$r_{\text{Track} \rightarrow \text{LKr}} > 15 \text{ cm}$ Inside outer boundaries (dedicated routine) Distance $d_{\text{Track} \rightarrow \text{LKr}} > 8 \text{ cm}$ to defective read-out electronics Exclude: $10 \text{ cm} < x_{\text{Track} \rightarrow \text{LKr}} < 20 \text{ cm}$ Exclude: $25 \text{ cm} < y_{\text{Track} \rightarrow \text{LKr}} < 35 \text{ cm}$
Distance from track ...	
... in LKr to dead cell	$ \vec{x}_{\text{Track} \rightarrow \text{LKr}} - \vec{x}_{\text{Dead Cell}} > 3 \text{ cm}$
Cluster status (if cluster)	< 4
Charged Vertex	$-12 \text{ m} < z_{\text{Charged Vertex}} < 60 \text{ m}$
Distance of closest ...	
... approach to kaon beam	$ \vec{R} < 3.5 \text{ cm}$

Table 10: Summary of common selection criteria for e^+ , μ^+ , and π^+ .

5.3.2 Timing

Selection criteria on timing information are important to make sure that all particles are part of the same triggered event. The time of the charged particle candidate measured by the CHOD must be in a 40 ns range with respect to the trigger time:

- $-18 \text{ ns} < t_{\text{CHOD}} - t_{\text{trigger}} < 22 \text{ ns}$.

The difference is not exactly centered around zero so that the time window is shifted by 2 ns. In some cases the variable t_{CHOD} was not filled during taking, in this case the event is rejected. In the MC simulation, timing information is inadequately simulated. Therefore this criterion is not applied on MC. The time distributions are presented in Figure 22. The criterion is 99.5% efficient for $K_{\mu 3}$ and $K_{e 3}$. For $K_{2\pi}$, it is lower at 98.2% due to a small increase of events around -40 ns . They are far away from the signal region and caused most probably by event overlapping inside the trigger.

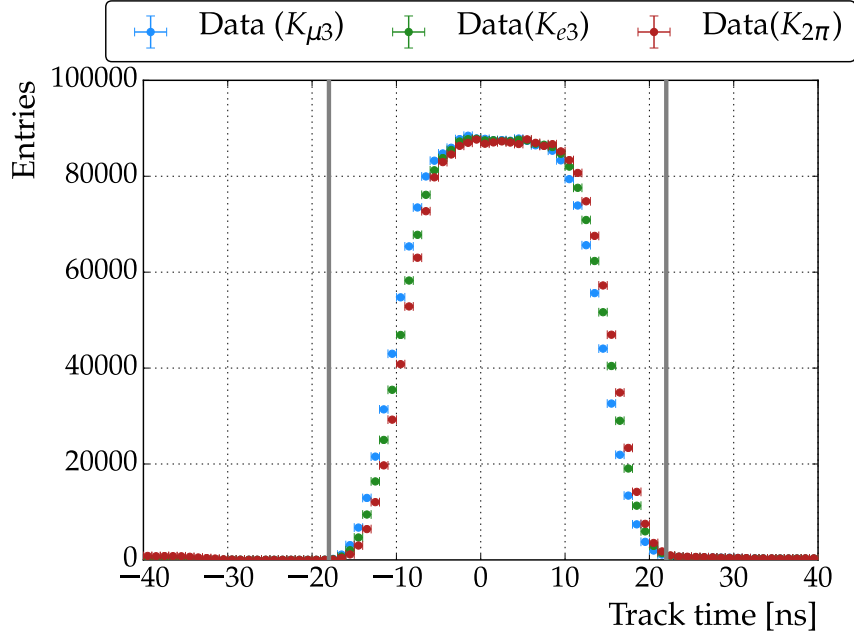


Figure 22: Distributions of the track timing $t_{\text{CHOD}} - t_{\text{trigger}}$. The $K_{\mu 3}$ and the $K_{e 3}$ distributions are normalized with respect to the $K_{2\pi}$ distribution.

5.3.3 Geometrical Acceptance

To ensure that the charged particles pass through the active volume of the detectors, criteria to the geometrical acceptance are applied. These criteria remove events in which a track passes near the beam pipe or the outer edges of the detectors where the efficiency may drop because not all hits are contained inside the detector. A second reason to avoid the edges is an imperfect detector resolution description in the Monte Carlo simulation. For the DCHs, two circular selection criteria are applied:

- $12 \text{ cm} < r_{\text{DCH}_1} < 115 \text{ cm}$ and
- $13 \text{ cm} < r_{\text{DCH}_4} < 115 \text{ cm}$.

Figure 23 and Figure 24 show the respective distributions. For $K_{\mu 3}$ and $K_{e 3}$ a small slope is visible at lower r_{DCH_1} values. Larger deviations are observed at the edge of the beam pipe. A similar picture is seen for r_{DCH_4} . However, an additional small slope for larger values of r_{DCH_4} is observed for $K_{e 3}$.

The position of the track at the front face of the LKr is obtained by extrapolation of the track slope to the LKr. This position must fulfill the requirements

- $r_{\text{Track} \rightarrow \text{LKr}} > 15 \text{ cm}$ and

- $|\vec{x}_{\text{Track} \rightarrow \text{LKr}} - \vec{x}_{\text{Dead Cell}}| > 3 \text{ cm}$.

The second requirement ensures that the track has a sufficient distance to not read-out LKr cells (also called “dead cells”). The extrapolated position is additionally used as input to a dedicated acceptance routine¹ for the LKr which takes care of the outer limits of the LKr and accounts for defective read-out electronics, the so-called Calorimeter Pipeline Digitizers (CPDs), on a run-by-run basis. The CPDs read out an array of 8×8 LKr cells. Some of these devices stopped (temporarily or permanently) working during data taking and were blacklisted². The routine checks that the position is inside the outer boundaries of the LKr and at least 8 cm away from the defective CPDs. In Figure 34 on Page 78 the dead cells are visible as white spots distributed over the area. In the bottom-right corner are the permanently missing CPDs.

Figure 34 as well shows an excluded square region between 10 cm and 20 cm for $x_{\text{Track} \rightarrow \text{LKr}}$ and between 25 cm and 35 cm for $y_{\text{Track} \rightarrow \text{LKr}}$. This region is excluded due to a localized data/MC disagreement possibly caused by additional read-out malfunctions.

5.3.4 Track Cluster

If a cluster is associated with the track, it is required that the

- cluster status < 4 .

This avoids clusters containing cells with ADC saturation or read out problems due to gain switching or timing problems [63]. Such clusters lose energy information and are rejected.

5.3.5 Charged Vertex

The kaon must decay inside the fiducial volume to be taken into consideration. This position is restricted by criteria on the charged vertex (Section 3.4.2 on Page 38). The range of accepted z-component of the decay positions is

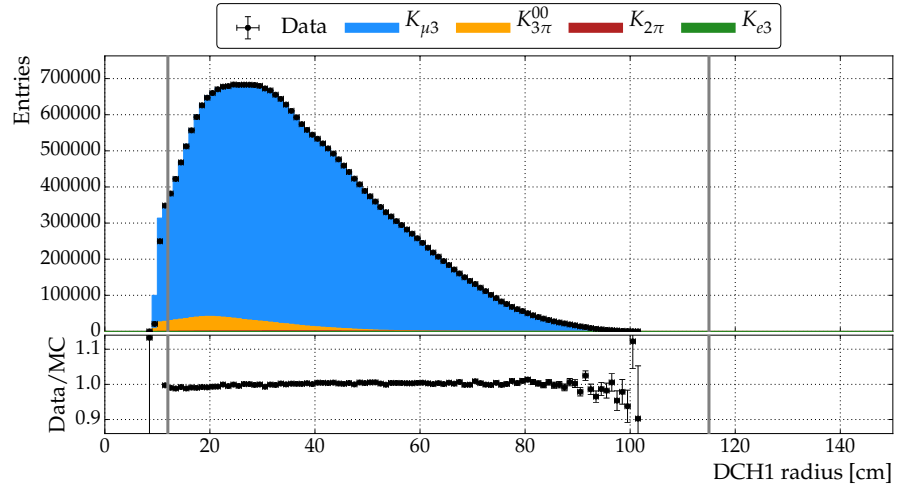
- $-12 \text{ m} < z_{\text{Charged Vertex}} < 60 \text{ m}$.

The charged vertex range starts about 8 m behind the last collimator and ends 30 m before the DCH₁. The charged vertex distributions are shown with their selection criteria in Figure 25. The Data/MC agreement for the charged vertex is very good inside the signal region. The agreement deteriorates at the edges of the distributions.

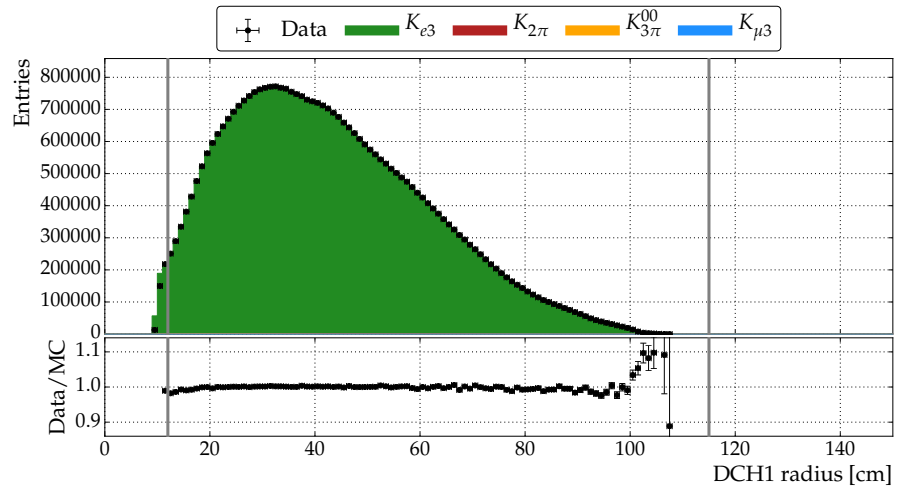
A second criterion to the charged vertex is the distance of closest approach $|\vec{R}|$ (Section 3.4.2 on Page 38). This distance is required to be

¹ lkracep_2007.c

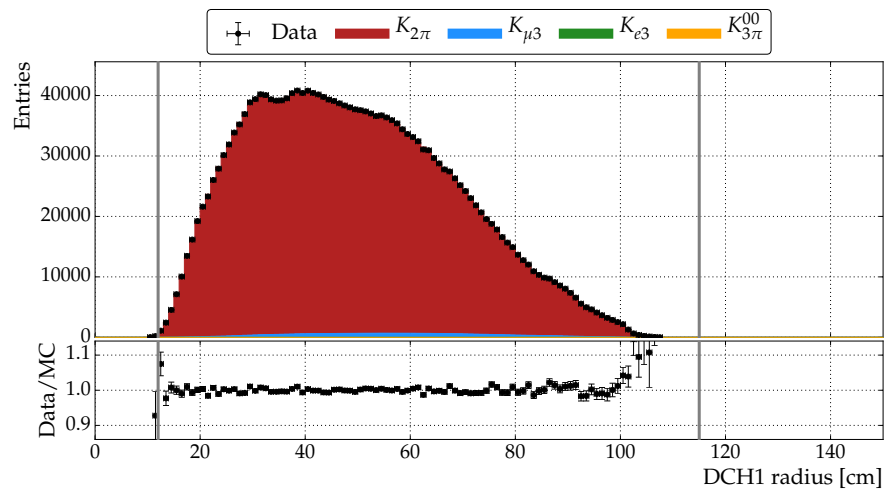
² The defective Calorimeter Pipeline Digitizers and the dead cells were two distinct issues in the LKr read-out.



(a) $K_{\mu 3}$ selection.



(b) K_{e3} selection.



(c) $K_{2\pi}$ selection.

Figure 23: Distributions of the DCH1 radius.

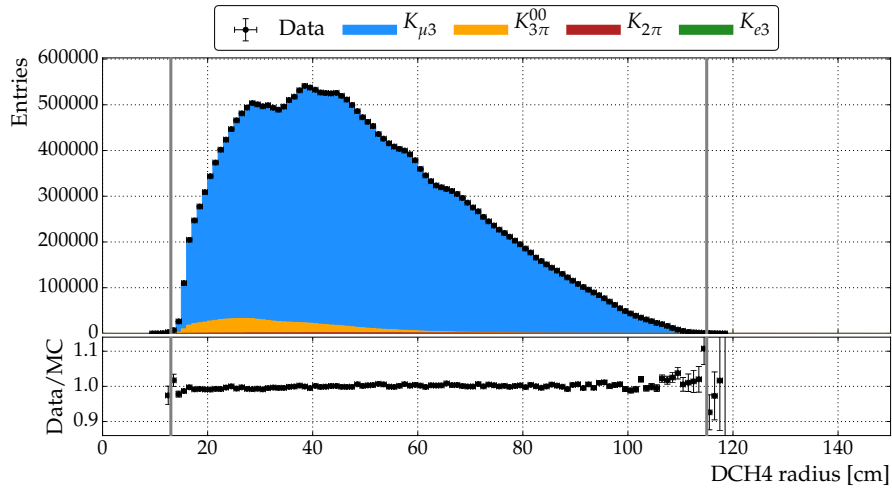
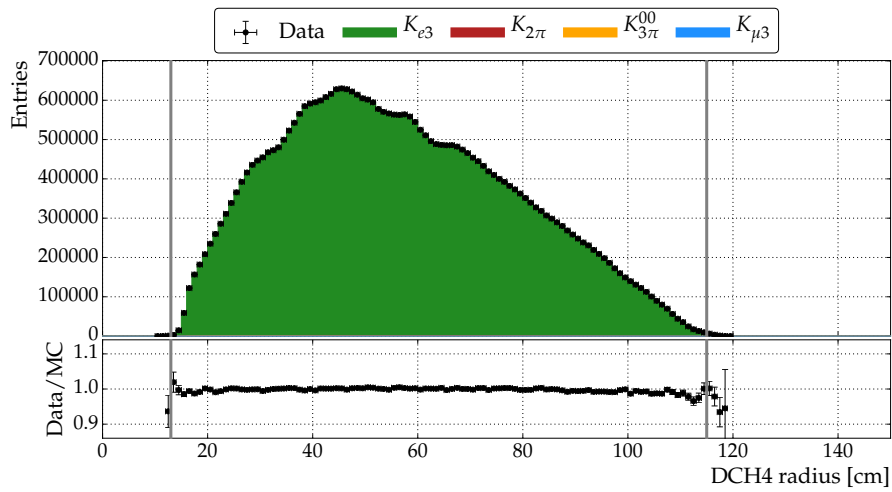
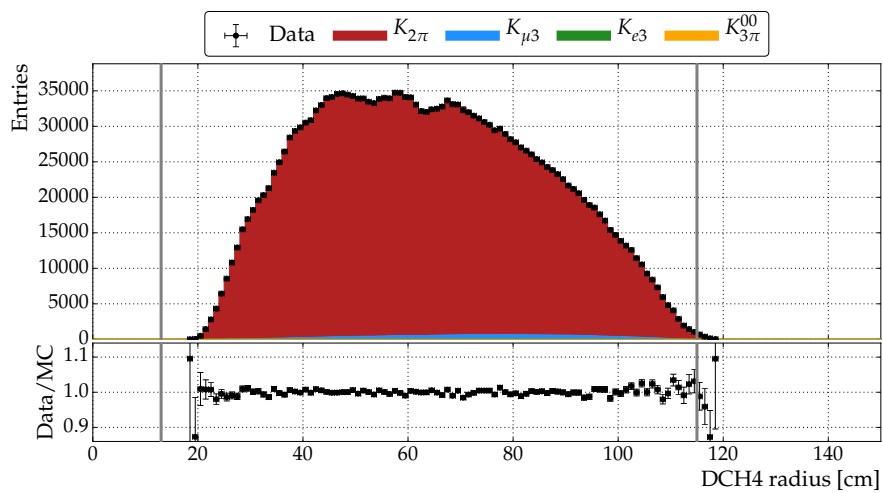
(a) $K_{\mu 3}$ selection.(b) K_{e3} selection.(c) $K_{2\pi}$ selection.

Figure 24: Distributions of the DCH4 radius.

- $|\vec{R}| < 3.5 \text{ cm}$.

which is the same selection criterion as in the $R_K = \Gamma(K_{e2})/\Gamma(K_{\mu2})$ analysis. The distributions of $|\vec{R}|$ are presented in Figure 26. The bulks of the distributions are well described by MC, however, the tails are either underestimated (Figure 26 a) or overestimated (Figure 26 b). However, the first three bins of all three selections contain more than 99% of the data.

5.4 PARTICLE IDENTIFICATION OF e^+ , μ^+ , AND π^+

A powerful tool to distinguish e^+ from π^+ and μ^+ is the ratio E/p where E is the reconstructed cluster energy which is associated with the track. The momentum p of the track is measured by the DCH. The charged particles e^+ , μ^+ , and π^+ populate different regions E/p (Figure 27).

The selection requirements are as follows:

$$K_{e3}: 0.9 < E/p < 1.5,$$

$$K_{\mu3}: E/p < 0.1, \text{ and}$$

$$K_{2\pi}: E/p < 0.9.$$

The requirements without lower limit include also events where the track has no associated track.

Electrons and Positrons are stopped inside the LKr and release all of their energy through electromagnetic interactions. The released energy is fully contained inside the LKr, thus the ratio between the energy and momentum is one.

Muons on the other hand are minimum ionizing particles which release mostly only a tiny fraction of their energy inside the LKr. This leads to values of E/p around zero.

Pions interact through hadronic interactions which lead to a broad distribution of the released energy. In most cases, the released energy is not fully contained in the LKr as muons and neutrinos may be produced. Also part of the energy is bound in nuclear forces, thus not visible to the LKr. Pions may also pass the LKr as minimum ionizing particles. The last property makes the ratio E/p less effective in the μ^+/π^+ discrimination than for example for e^+/π^+ . The threshold to identify μ^+ is set to $E/p < 0.1$. This criterion accepts most of the muons and removes about $\frac{2}{3}$ of the pions. However, further selection criteria are required to remove π^+ background.

5.4.1 Measurement of the Particle Identification Efficiency with E/p

The efficiency of the E/p criterion is measured from data as a function of the track momentum for each selection. These efficiencies are

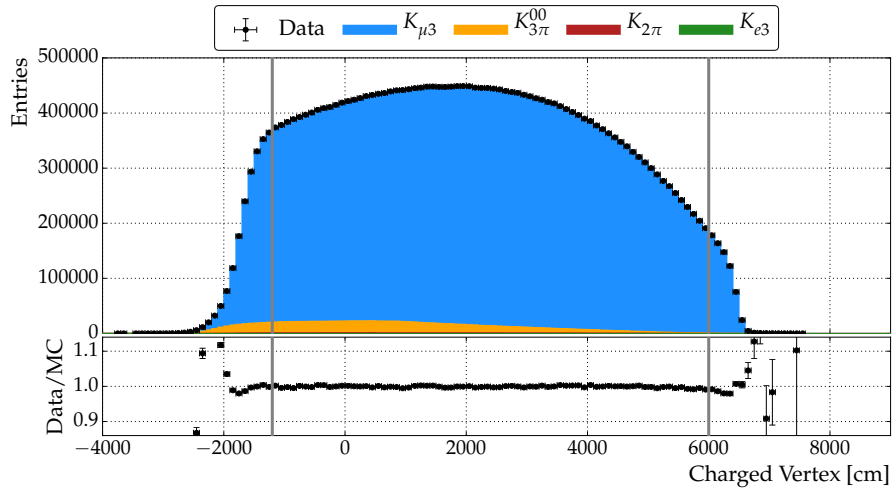
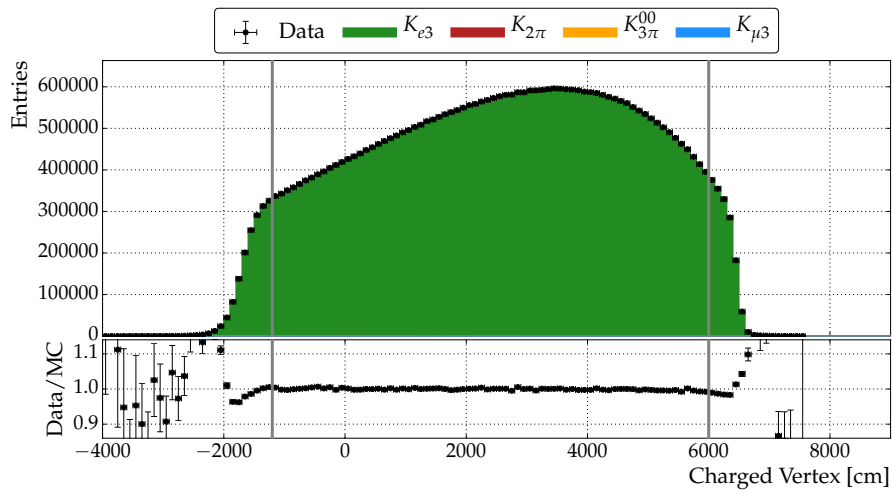
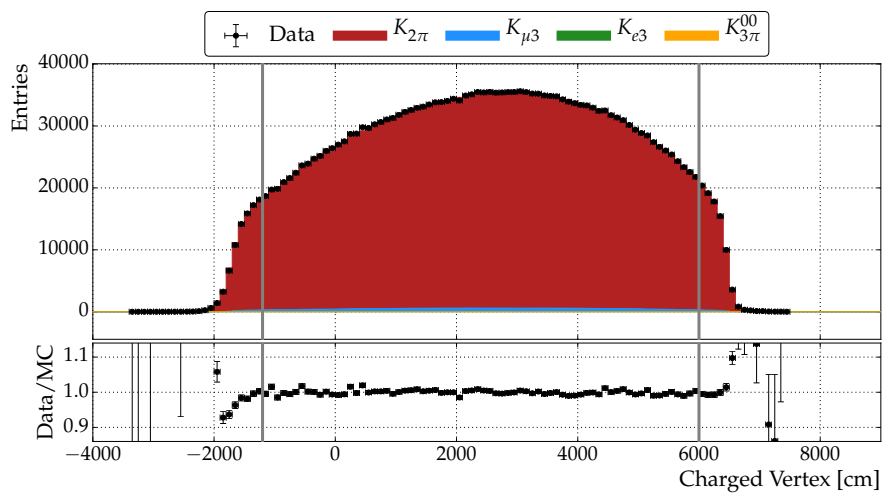
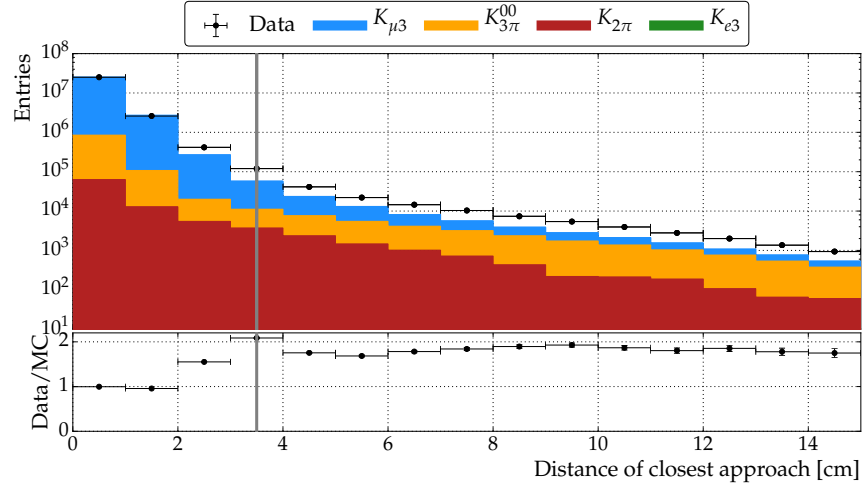
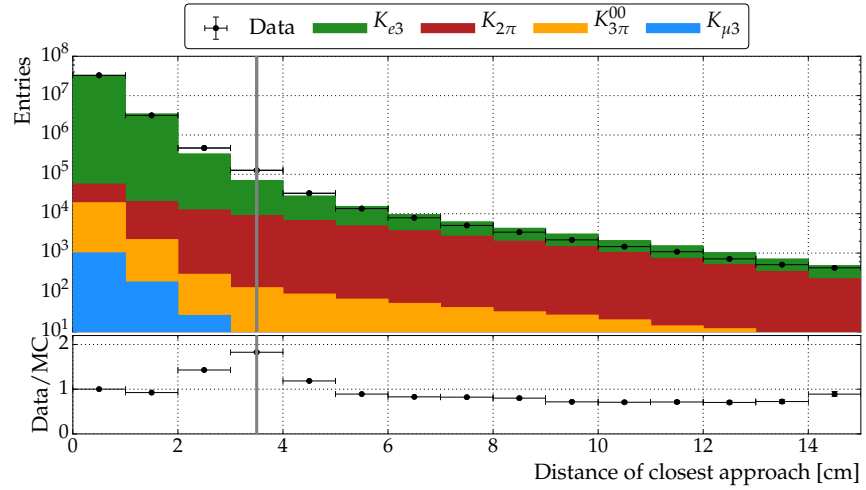
(a) $K_{\mu 3}$ selection.(b) $K_{e 3}$ selection.(c) $K_{2\pi}$ selection.

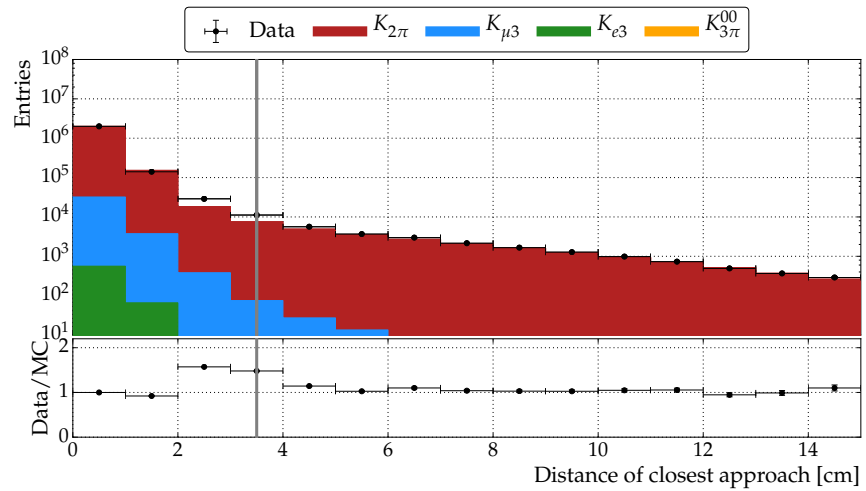
Figure 25: Distributions of the charged vertex.



(a) $K_{\mu 3}$ selection.



(b) $K_{e 3}$ selection.



(c) $K_{2\pi}$ selection.

Figure 26: Distribution of the distance of closest approach $|\vec{R}|$.

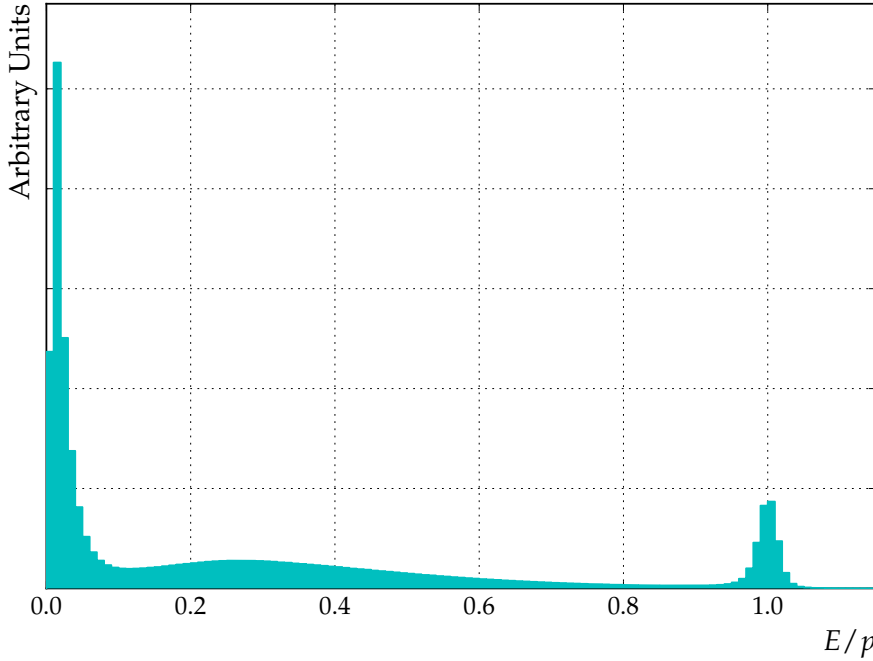


Figure 27: Distribution of E/p obtained from data by requiring the $K_{\mu 2}$ trigger, only one track, and at least two clusters in the LKr. The peak at $E/p = 0$ indicates mostly muons and to some part pions, the region between $E/p = 0.1$ and $E/p = 0.9$ is populated with pions and the peak at $E/p = 1$ represents electrons.

used as weights on MC events. This procedure is needed due to an imperfect simulation of LKr cluster for μ^+ and π^+ . Pure samples of μ^+ , e^+ , and π^+ are obtained from dedicated selections of $K^+ \rightarrow \mu^+ \nu_\mu$ ($K_{\mu 2}$) and $K^+ \rightarrow \pi^+ \pi^0$, $\pi^0 \rightarrow e^+ e^- \gamma$ ($K_{2\pi D}$).

Additionally, the misidentification probability of a pion to be identified as a electron ($E/p > 0.9$) and the probability to be misidentified as muon ($E/p < 0.1$) is determined. The misidentification probabilities $P(\mu^+ \rightarrow e^+)$ and $P(e^+ \rightarrow \mu^+)$ are found to be negligible. These values are applied as track momentum dependent weights on the MC instead of applying directly the E/p selection criterion. This avoids problems emerging from the limited amount of showers in the LKr shower libraries and imperfectly described μ^+ clusters. The measurements of efficiencies mentioned above are described in the following sections.

5.4.1.1 μ^+ -Identification Efficiency Measurement

The μ^+ identification efficiency is measured with the decay $K^+ \rightarrow \mu^+ \nu_\mu$ ($K_{\mu 2}$). The advantage of the $K_{\mu 2}$ decay is the large branching fraction of 63.55(11)% [11] and the clear signature of one track without further particles, which reduces possible background. The selection is described in Section A.2 on Page 136.

With this selection, 17,411,538 $K_{\mu 2}$ candidates are reconstructed. The main background are muons from the beam halo which do not distort the μ^+ -ID efficiency measurement. These muons account for $< 1\%$ of the selected events. The beam halo is measured from a special run without kaon decays³. Figure 28 shows the momentum distribution of the μ^+ and Figure 29a shows the E/p distribution of the μ^+ . The probability of identifying a μ^+ as a μ^+ is plotted against the μ^+ momentum in Figure 29b. The distribution is fitted with a 9th degree polynomial which is used to weight the MC as a function of the muon momentum.

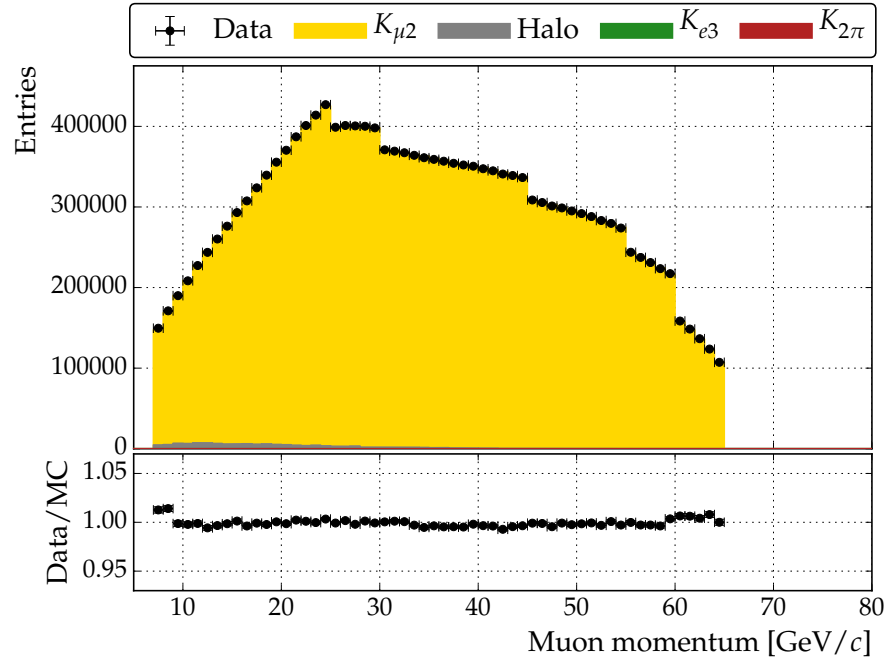


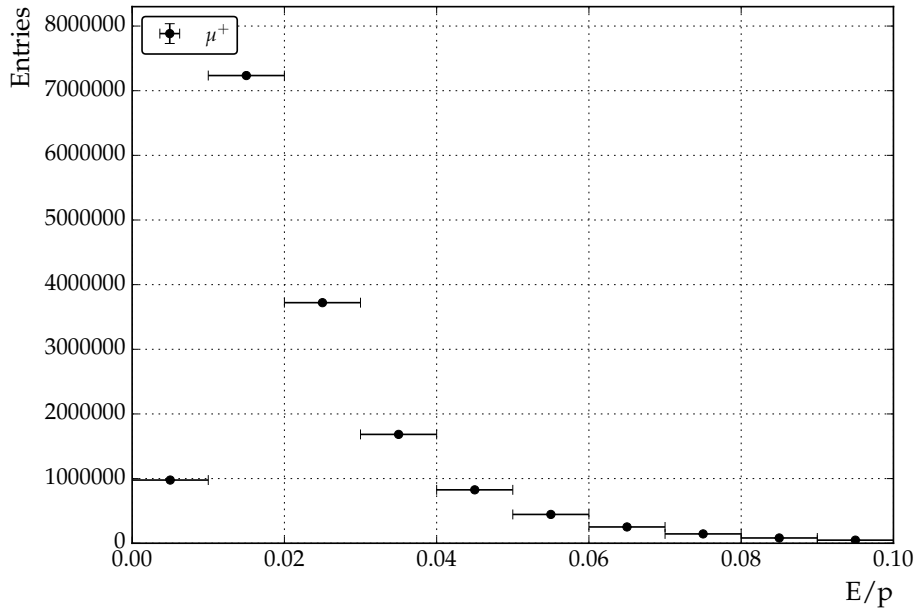
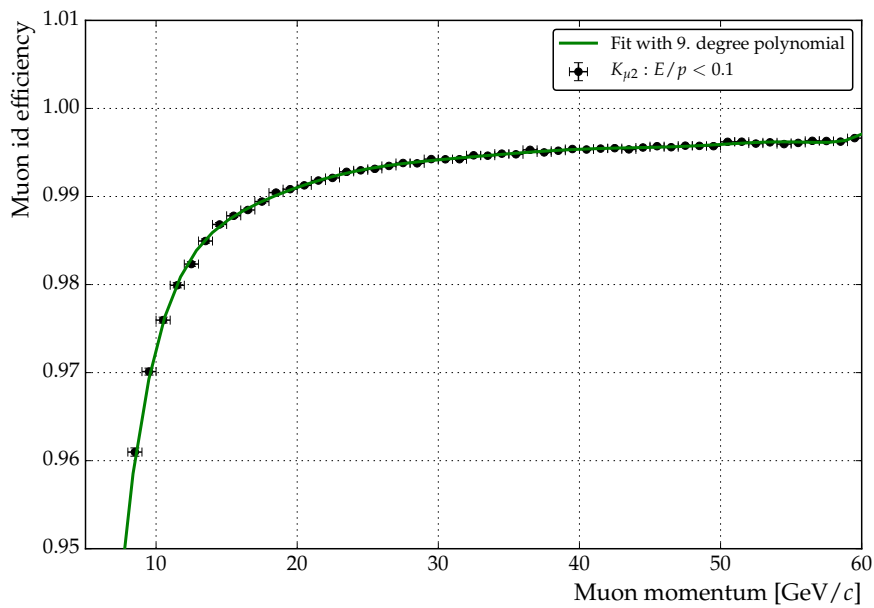
Figure 28: Distribution of the μ^+ momentum with the $K_{\mu 2}$ selection. The discontinuities in the distribution are a result of the momentum dependent $K_{\mu 2}$ selection criteria.

5.4.1.2 e^+ -Identification Efficiency Measurement

The e^+ identification efficiency is measured from a pure e^+ sample obtained from $K^+ \rightarrow \pi^+ \pi^0 \rightarrow \pi^+ e^+ e^- \gamma$ ($K_{2\pi D}$). This decay offers the possibility to obtain both a pure sample of e^+ and π^+ . It has the advantage of a clear signal in the detector with few background decays able to mimic it.

The required E/p criterion of the L3 filter is fulfilled by the e^+ . This leaves the π^+ and e^- free of E/p influence and they can be used to determine the identification efficiencies.

³ The beam is blocked by concrete blocks. This allows only the muons from the beam halo to enter the fiducial volume.

(a) The ratio E/p for μ^+ with an associated LKr cluster from $K_{\mu 2}$ decays.(b) Probability to identify a μ^+ with the criterion $E/p < 0.1$ plotted against the momentum of the μ^+ .Figure 29: μ^+ E/p distribution (a) and identification efficiency (b) using the $K_{\mu 2}$ selection. In (b) is a 9th degree polynomial fitted to the dataset.

The selection is described in Section A.3 on Page 138 and yields 255,560 $K_{2\pi D}$ candidate events. The electron momentum distribution is shown in Figure 30, the electron E/p distribution in Figure 31a, and the electron momentum dependent identification efficiency in Figure 31b. The efficiency is fitted with a 2nd degree polynomial which is used to weight the MC as a function of the electron momentum. The upper limit on the electron momentum criterion for the K_{e3} selection is defined by this measurement as the particle identification is only reliable up to 40 GeV/ c .

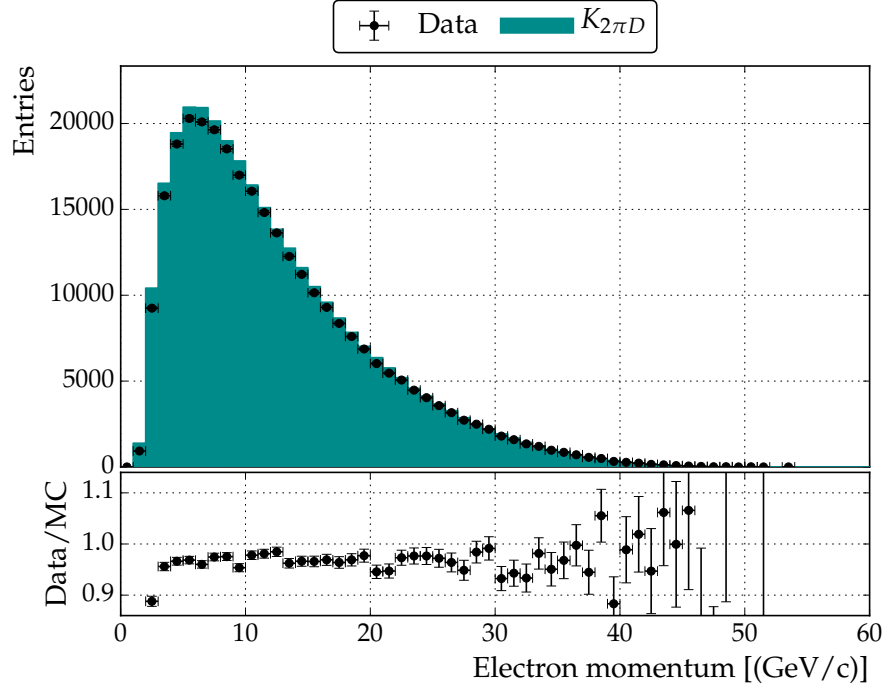
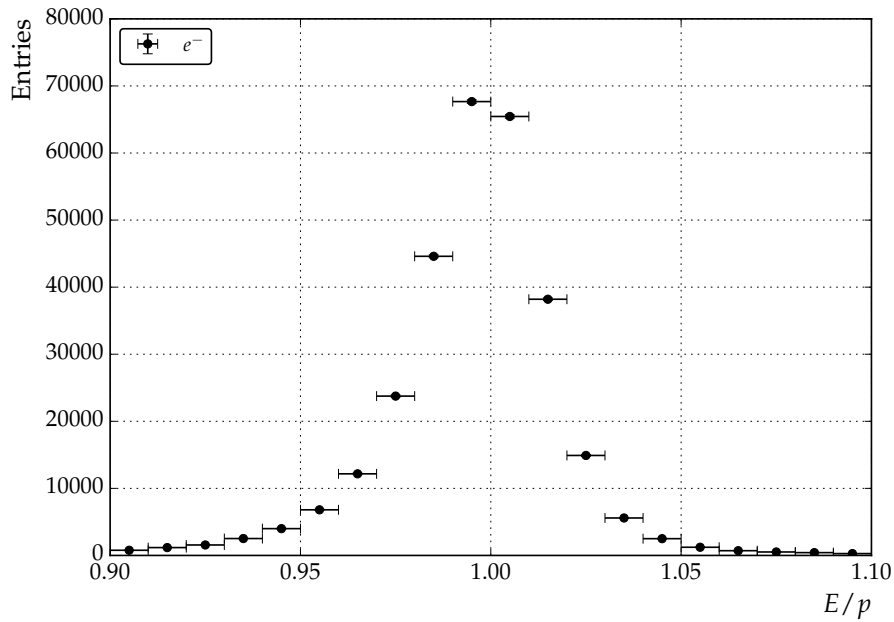


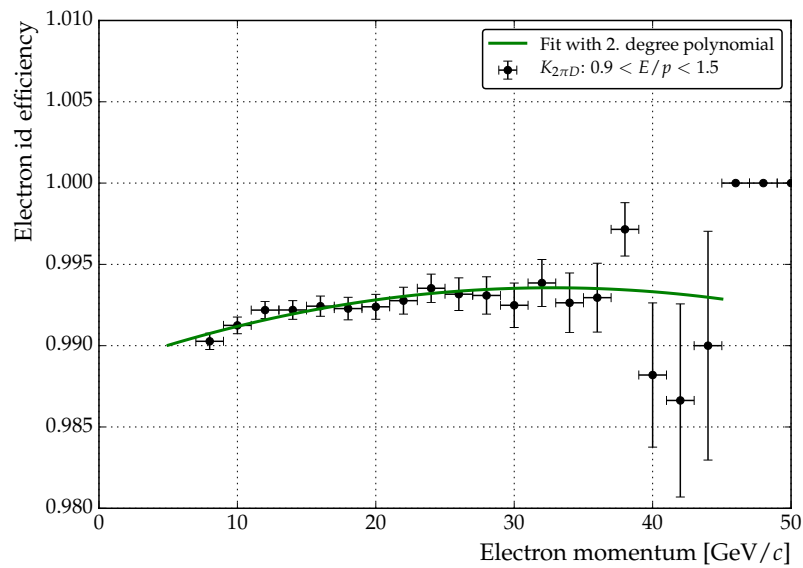
Figure 30: Distribution of the electron momentum from $K_{2\pi D}$ decays.

5.4.1.3 π^+ -Misidentification Probability Measurement

The probability of misidentifying a π^+ as a μ^+ or e^+ is measured with π^+ obtained from the $K_{2\pi D}$ selection discussed (Section A.3 on Page 138). The π^+ momentum and E/p distributions are shown in Figure 32. The misidentification probabilities $P(\pi^+ \rightarrow e^+)$ ($E/p > 0.9$) and $P(\pi^+ \rightarrow \mu^+)$ ($E/p < 0.1$) as a function of the π^+ momentum are plotted in Figure 33. Both distributions are fitted with polynomials which are then used as weights on the MC. Figure 33b shows that the discrimination of muons and pions is quite difficult with the ratio E/p . The probability of misidentifying a pion as a muon over the momentum range up to 50 GeV/ c is not lower than 30% and increases for lower momenta up to 50%. Due to this fact, further selection criteria on decay level are required to discriminate μ^+ and π^+ .

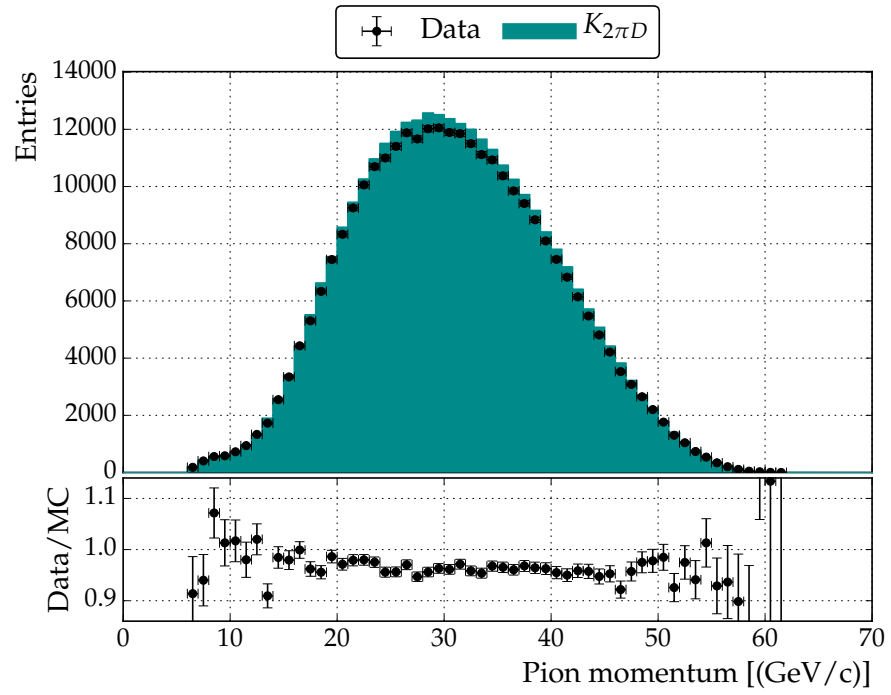
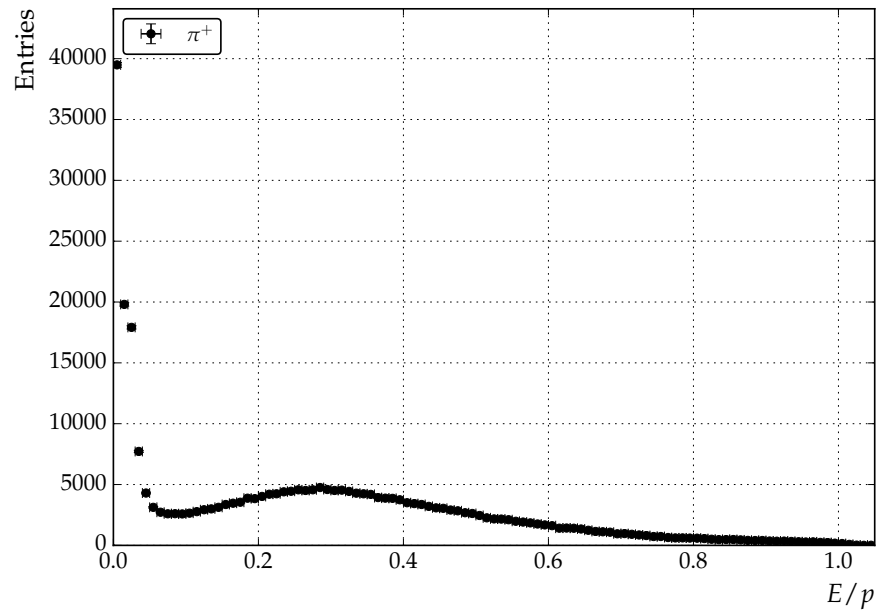


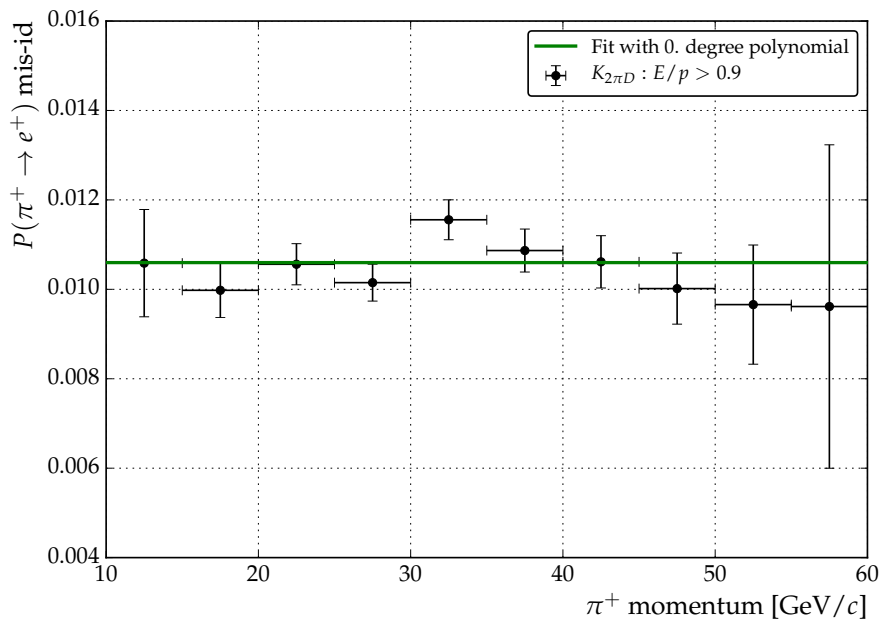
(a) The ratio E/p for an electron with an associated LKr cluster from $K_{2\pi D}$ decays.



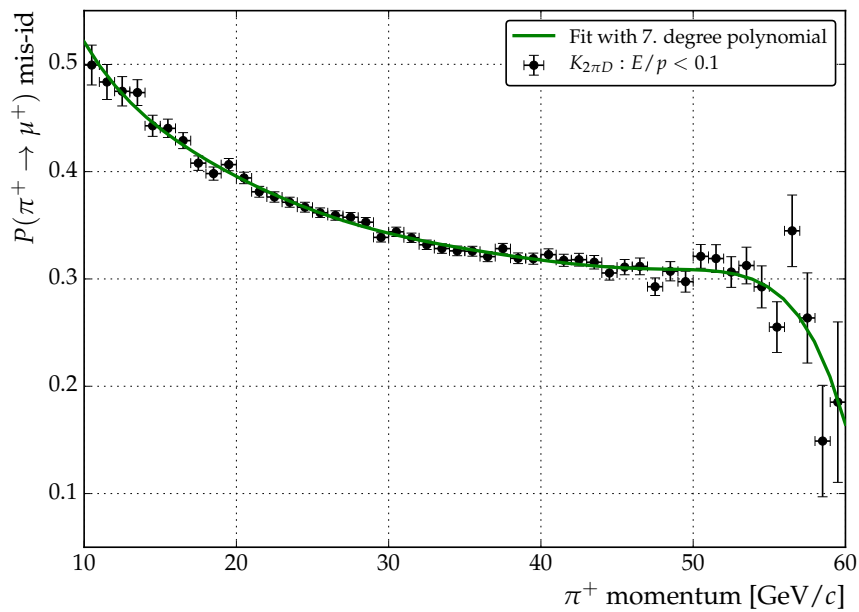
(b) Probability to identify an electron with the criterion $E/p > 0.9$ plotted against the momentum of the electron.

Figure 31: Electron E/p distribution (a) and identification efficiency (b) using the $K_{2\pi D}$ selection. In (b) is a 2nd degree polynomial fitted to the dataset.

(a) Distribution of the pion momentum from $K_{2\pi D}$ decays.(b) The ratio E/p for a pion with an associated LKr cluster from $K_{2\pi D}$ decays.Figure 32: Pion momentum and E/p distribution from $K_{2\pi D}$ decays.



(a) Probability $P(\pi^+ \rightarrow e^+)$ to misidentify a pion as an electron as function of the pion momentum.



(b) Probability $P(\pi^+ \rightarrow \mu^+)$ to misidentify a pion as a muon as function of the pion momentum.

Figure 33: Misidentification probabilities for pions. The distribution in (a) is a fitted constant function. The distribution in (b) is fitted with a 7th degree polynomial.

5.5 SELECTION CRITERIA FOR π^0

Only decays with a π^0 decaying into photons ($\pi^0 \rightarrow \gamma\gamma$) are taken into account for the main decay channels in this analysis. These photons pass the magnetic field of the DCH without deflection and eventually hit the LKr. Photons induce electromagnetic showers in the LKr. The electromagnetic showers are reconstructed from so-called clusters (Section 3.2 on Page 36). These clusters must fulfill different requirements:

- The photon cluster candidates must lay inside the acceptance of the LKr. The radial distance from the z -axis must be $r_{\text{LKr}} > 15$ cm to make sure that the cluster is not affected by the beam pipe. The same routine as applied to the extrapolated track positions into the LKr (Section 5.3.3 on Page 60) is used for the cluster positions. The outer limits of the LKr and the defective CPD electronics are taken into account. The same square region is excluded as well. A plot of the cluster position distribution and the applied criterion on the outer edges is presented in Figure 34.
- The small fraction of not properly working LKr cells is taken into account similarly to the extrapolated track positions. The minimal distance to these dead cells is smaller here due to the direct position measurement of the clusters. Each cluster must have a distance of $|\vec{x}_\gamma - \vec{x}_{\text{Dead Cell}}| > 2$ cm. This avoids having a dead cell as a central cell of a cluster. These dead cells are visible as white spots in Figure 34.
- The clusters must not be associated with a track. This information is available in COMpACT on analysis level. A routine extrapolates the track to the LKr position. If a cluster matches this position within 1.5 cm and the time difference between track and cluster is smaller than 6 ns, the cluster is associated with the track [43, Page 46].
- The energy of a cluster E_{Cluster} must be greater 5 GeV and the status of cluster smaller 4. These conditions ensure a good quality of the recorded cluster.
- The energy measurement of the clusters can be spoiled if two clusters are too close together. Therefore the distance between both photon candidate cluster must be $|\vec{x}_{\gamma 1} - \vec{x}_{\gamma 2}| > 20$ cm and between a photon candidate cluster and any other cluster likewise $|\vec{x}_{\gamma \rightarrow \text{LKr}} - \vec{x}_{\text{Any cluster}}| > 20$ cm.
- Two different timing criteria are applied on the clusters. The first requires the time difference of the clusters to be $\Delta t_{\text{Cluster}} = |t_{\gamma 1} - t_{\gamma 2}| < 10$ ns. This criterion ensures that both clusters

have the same decay as origin. The second criterion requires the time difference between the mean time of both clusters $t_{\text{Mean Cluster}}$ and the track time at the CHOD $t_{\text{Track, CHOD}}$ to be $|t_{\text{Track, CHOD}} - t_{\text{Mean Cluster}}| < 12$ ns. This requirement rejects events in which track and π^0 do not originate from the same decay. These criteria are not applied on MC. The respective distributions are presented in Figure 35. The plots show only data distributions. Additionally, the $K_{\mu 3}$ and the $K_{e 3}$ distributions are normalized with respect to the $K_{2\pi}$ distributions. The distributions of the difference between the track time and the mean cluster time have the same rate of flat background from accidental events on the left side of the peak. The distribution of $K_{2\pi}$ differs from the $K_{\mu 3}$ and the $K_{e 3}$ distributions by a factor of 10 on the right side. The reason for that is probably the less restrictive trigger used to select $K_{2\pi}$. The distributions of the time difference between both π^0 clusters agree very well.

For each pair of clusters fulfilling the requirements above, the reconstruction procedure described in Section 3.5 on Page 39 is applied. Now, further conditions are set to the reconstructed photon ($p_{\gamma,i}$, with $i = 1, 2$) and π^0 ($p_{\pi^0} = \sum_{i=0}^2 p_{\gamma,i}$) momenta.

- If more than two clusters (not counting a cluster associated with the track) are available, the π^0 candidate with the reconstructed mass closest to the nominal π^0 mass is selected. The mass is computed by Equation 3.20 on Page 41 using the distance d_{charged} from the charged vertex to the LKr:

$$m_{\pi^0} = \frac{1}{d_{\text{charged}}} \sqrt{E_1 E_2} |\vec{r}_1 - \vec{r}_2|. \quad (5.1)$$

- The reconstructed photon trajectories must have a minimal distance from the experiment z-axis at DCH₁ of $r_{\text{DCH}_1} > 12$ cm. Photons passing closer at DCH₁ may interact with the flanges of the DCH. It is found that these interactions are not well described in the MC (Figure 36). The trajectory is calculated from the modified charged vertex \vec{V}_c^* to the cluster position in the LKr \vec{V}_{Cluster} . The modified charged vertex \vec{V}_c^* allows a more conservative estimate of r_{DCH_1} . It is computed by shifting the decay z position downstream by $3 \times \sigma_{\text{Vertex}}$:

$$z_{\text{Vertex}}^* = z_{\text{Vertex}} + 3 \times \sigma_{\text{Vertex}} \quad (5.2)$$

with $\sigma_{\text{Vertex}} = 1.5$ m the resolution of the charged vertex obtained from MC.

- The energy of the reconstructed π^0 must be $E_{\pi^0} > 15$ GeV. This requirement is needed due to the E_{10} sub-trigger and insures a high trigger efficiency. This sub-trigger is used to select $K_{\mu 3}$ and

K_{e3} . The criterion is used in all selections, however, the effect on the $K_{2\pi}$ decay is negligible. The respective distributions are presented in Figure 37.

- A loose selection criterion is applied on the reconstructed π^0 mass. The agreement between Data and MC is poor in the flanks of the π^0 mass peak (see Figure 38). The mass distribution is difficult to describe in MC. As the calculation of the mass depends on the position of the charged vertex, the resolution of the DCH plays an additional role besides the energy measurement in the LKr. The slope of the kaon beam and its resolution is included as well which also depends on the DCH (Section 3.3 on Page 37). Despite that fact, the tails in Figure 38 (b) and (c) are well described. The selection criterion is chosen loose to avoid sensitivity to this disagreement. For all three main decays the criterion on the π^0 mass is

$$0.105 \text{ GeV}/c^2 < m_{\pi^0} < 0.165 \text{ GeV}/c^2. \quad (5.3)$$

The criterion is limited by the criterion in data on the π^0 mass introduced by the level 3 filter L3- $K_{\mu 3}$ (Section 2.13.1 on Page 32). This is the cause for the large discrepancy between data and MC in the tails of the distribution shown in Figure 38 (a). Various variables have been checked which may have had an influence on the π^0 measurement. However, the cause for the disagreement in the flanks could not be identified.

- The neutral vertex is computed accordingly to Section 3.5.2 on Page 40. The criterion

$$-17 \text{ m} < z_{\text{Neutral Vertex}} < 65 \text{ m} \quad (5.4)$$

is wider compared to the criterion on the charged vertex to take the resolution between both vertices into account. The neutral vertex range starts 3 m behind the last collimator and ends 25 m before the DCH₁. The criterion removes badly reconstructed $K_{3\pi}^{00}$ events. The respective distributions are shown in Figure 39. The data/MC description deteriorates for values below the charged vertex criterion $V_{\text{Charged Vertex}} < -12 \text{ m}$. Above this threshold, the data/MC agreement is good up to the charged vertex criterion $V_{\text{Charged Vertex}} > 60 \text{ m}$.

SELECTION CRITERION	VALUE
γ cluster LKr acceptance	$15 \text{ cm} < r_{\text{LKr}}$
	Inside outer boundaries (dedicated routine)
	Distance $d_\gamma > 8 \text{ cm}$ to ...
	... defective read-out electronics
	Exclude: $10 \text{ cm} < x_{\text{LKr}} < 20 \text{ cm}$
	Exclude: $25 \text{ cm} < y_{\text{LKr}} < 35 \text{ cm}$
Distance γ cluster ...	
... position to dead cell	$ \vec{x}_\gamma - \vec{x}_{\text{Dead Cell}} > 2 \text{ cm}$
Cluster energy	$E_{\text{Cluster}} > 5 \text{ GeV}$
Cluster status	< 4
Distance between candidate clusters	$ \vec{x}_{\gamma 1} - \vec{x}_{\gamma 2} > 20 \text{ cm}$
Distance between a candidate cluster to any other cluster	$ \vec{x}_\gamma - \vec{x}_{\text{Any cluster}} > 20 \text{ cm}$
Time difference of clusters	$\Delta t_{\text{Cluster}} < 10 \text{ ns}$
Time difference between track and mean time of clusters	$ t_{\text{Track, CHOD}} - t_{\text{Mean Cluster}} < 12 \text{ ns}$
γ position in DCH1	$r_{\text{DCH1}} > 12 \text{ cm}$
π^0 energy	$E_{\pi^0} > 15 \text{ GeV}$
π^0 mass	$0.105 \text{ GeV}/c^2 < m_{\pi^0} < 0.165 \text{ GeV}/c^2$
Neutral Vertex	$-17 \text{ m} < z_{\text{Neutral Vertex}} < 65 \text{ m}$

Table 11: Summary of π^0 selection criteria.

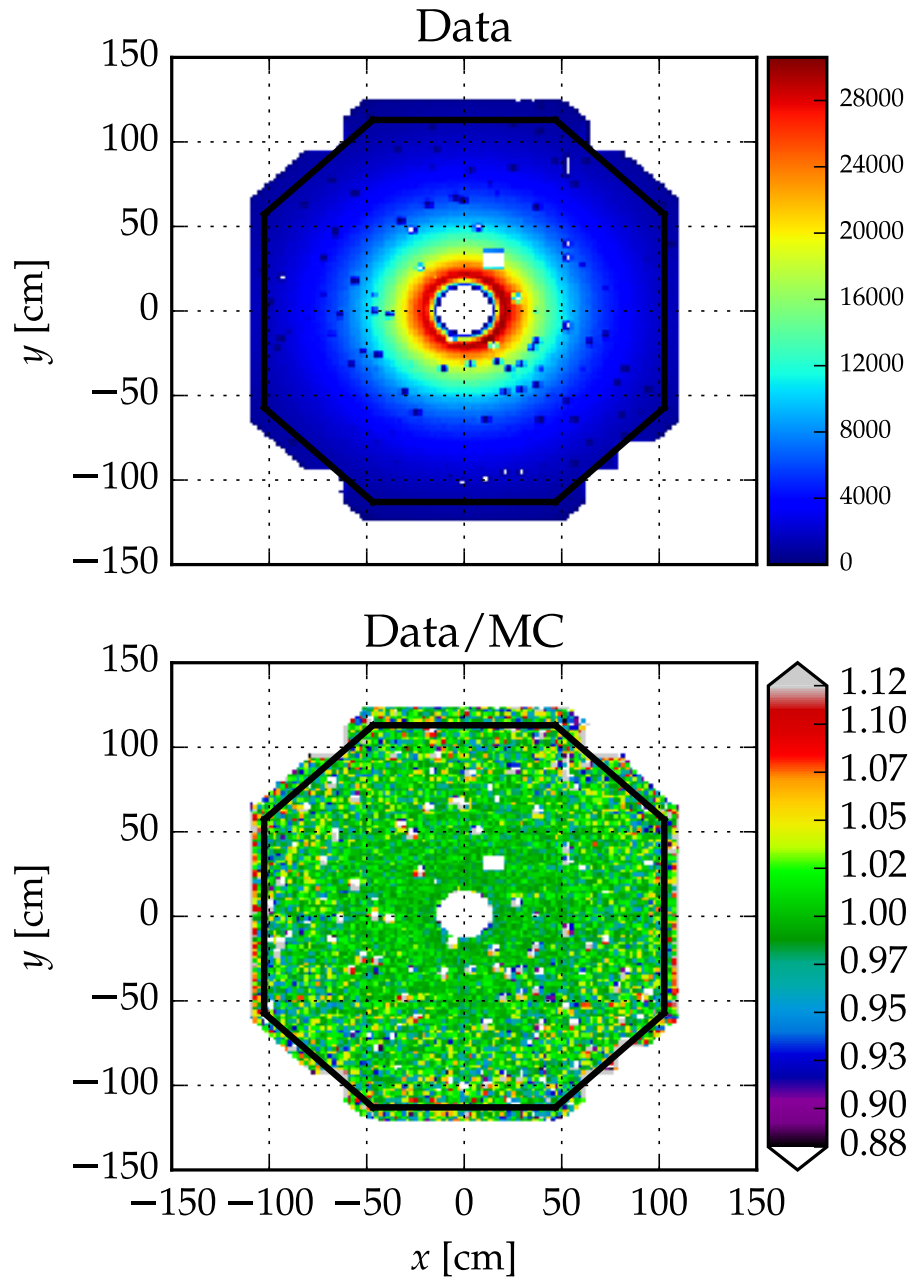


Figure 34: Two dimensional distributions of reconstructed π^0 cluster positions in the LKr ($K_{\mu 3}$ selection). Distributions of data/MC and only data are presented. The octagonal acceptance criterion on the cluster positions is shown in black. Non-functioning parts of the LKr are clearly visible in the upper plot as white spots. The region between $10 \text{ cm} < x_{\text{LKr}} < 20 \text{ cm}$ and $25 \text{ cm} < y_{\text{LKr}} < 35 \text{ cm}$ is excluded.

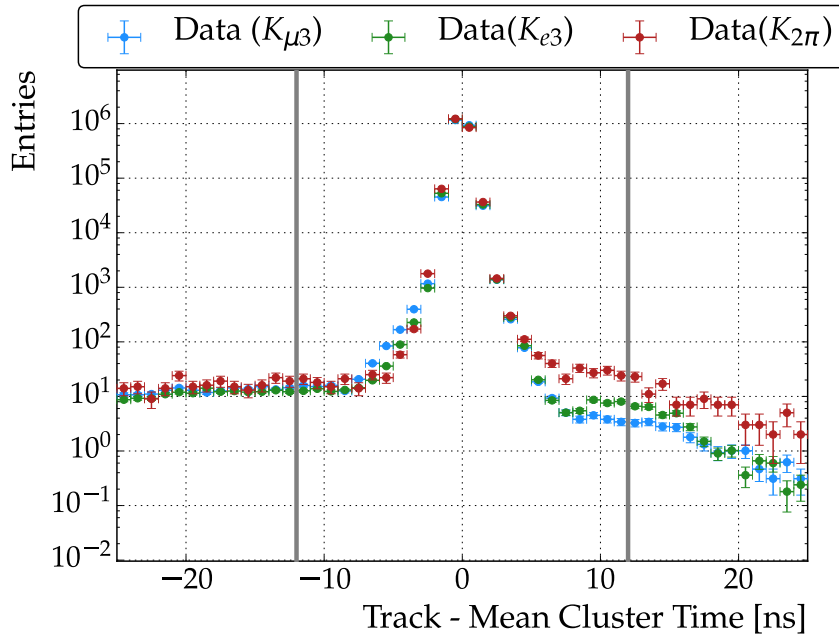
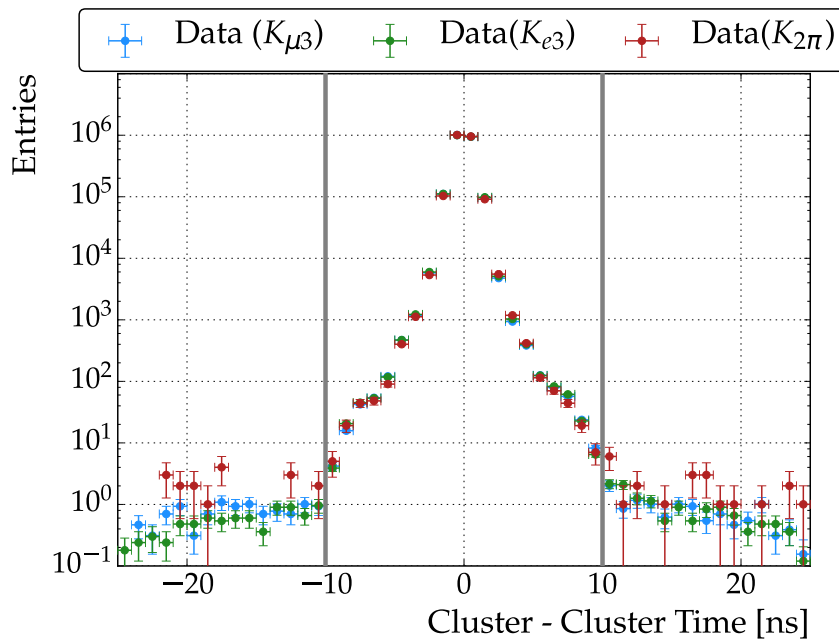
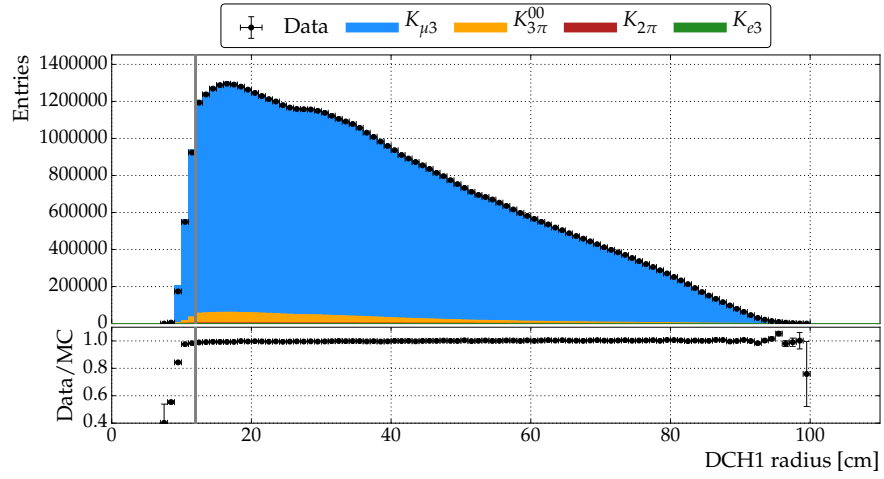
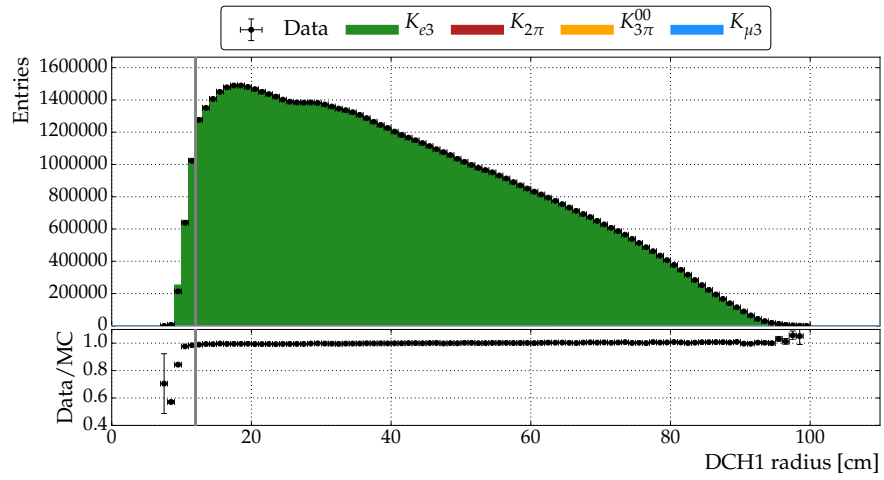
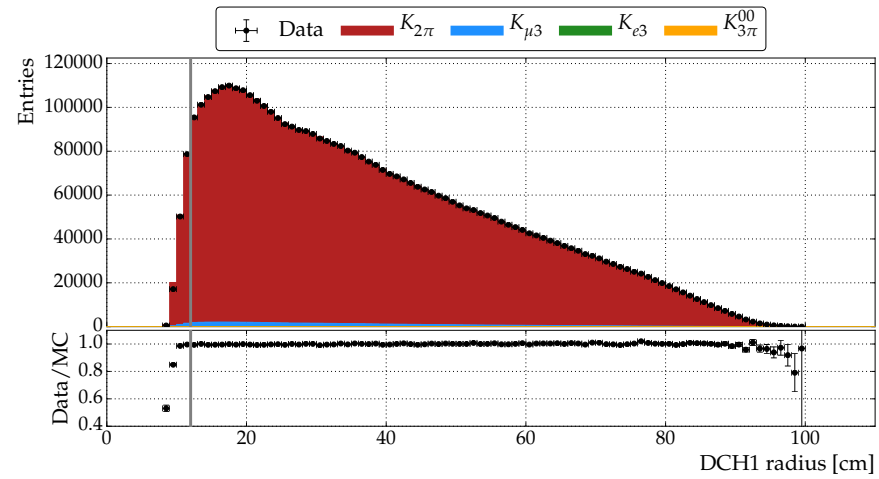
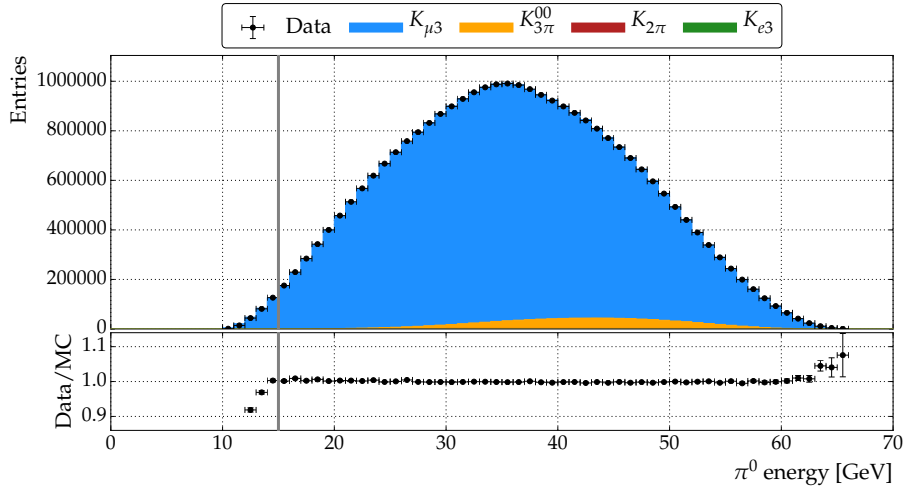
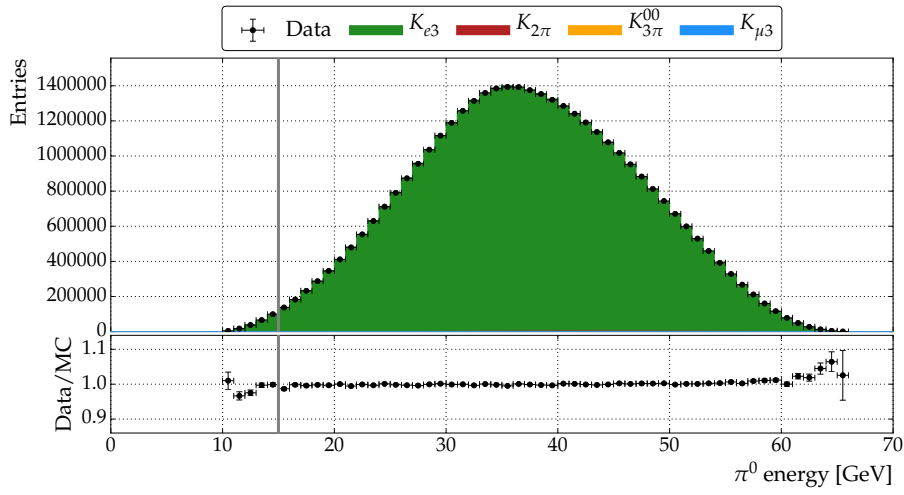
(a) The $t_{\text{Track, CHOD}} - t_{\text{Mean Cluster}}$ time.(b) The $t_{\gamma 1} - t_{\gamma 2}$ time.

Figure 35: The time requirements for the π^0 selection. The $K_{\mu 3}$ and the $K_{e 3}$ distributions are normalized with respect to the $K_{2\pi}$ distribution.

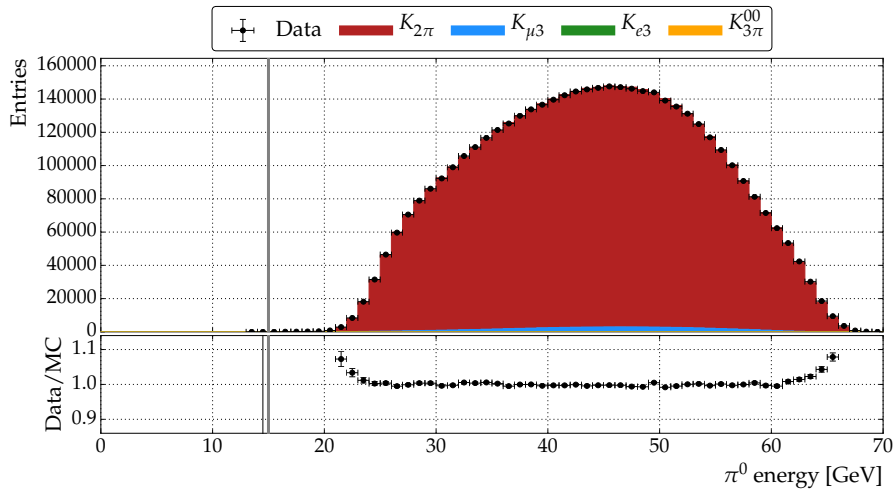
(a) $K_{\mu 3}$ selection.(b) K_{e3} selection.(c) $K_{2\pi}$ selection.Figure 36: Distribution of the distance of the photons position to the y-axis r_{DCH1} .



(a) $K_{\mu 3}$ selection.

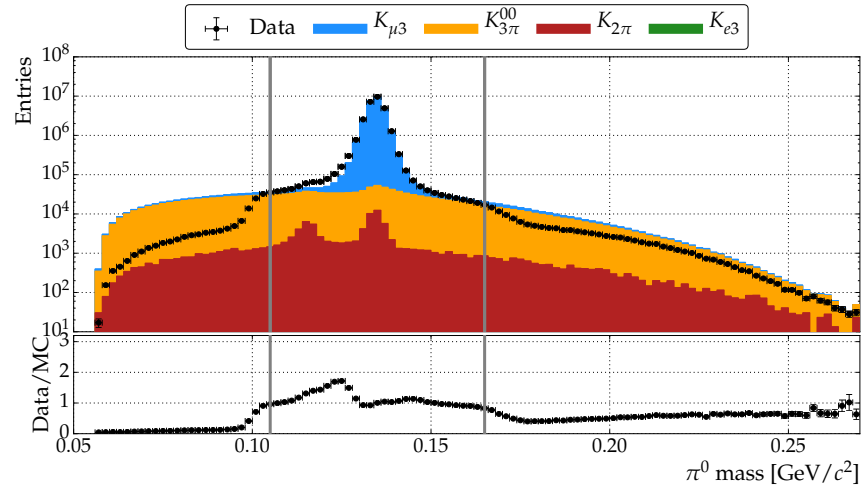
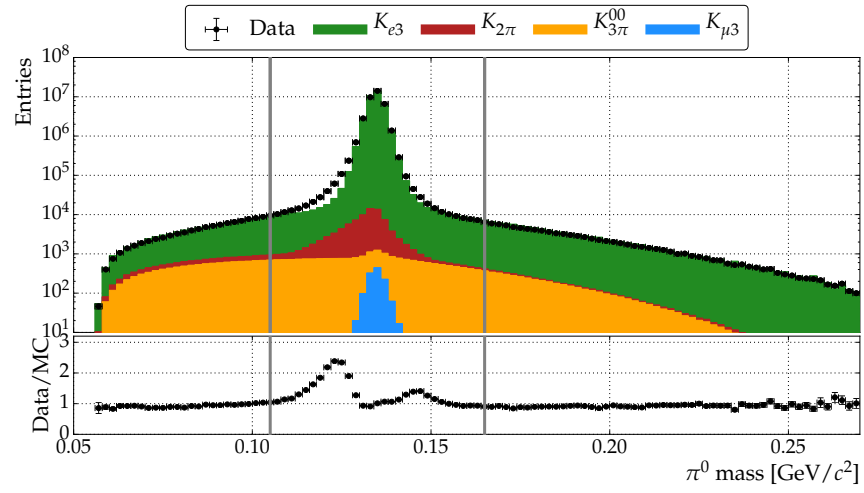
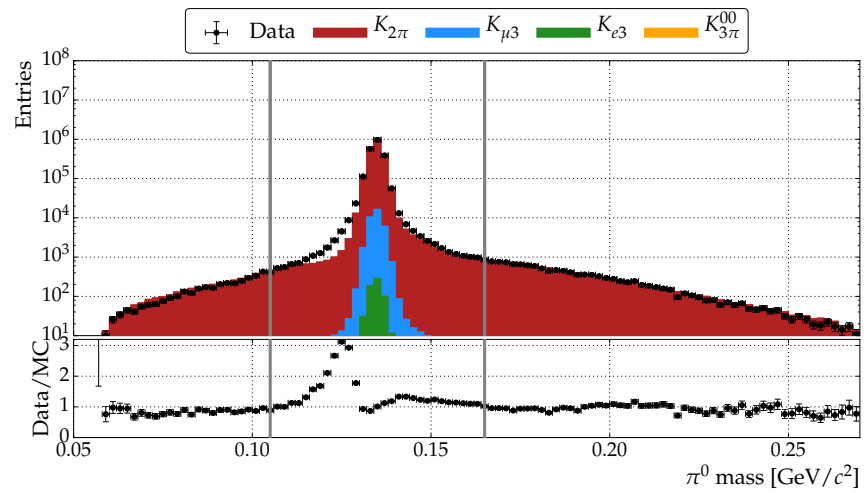


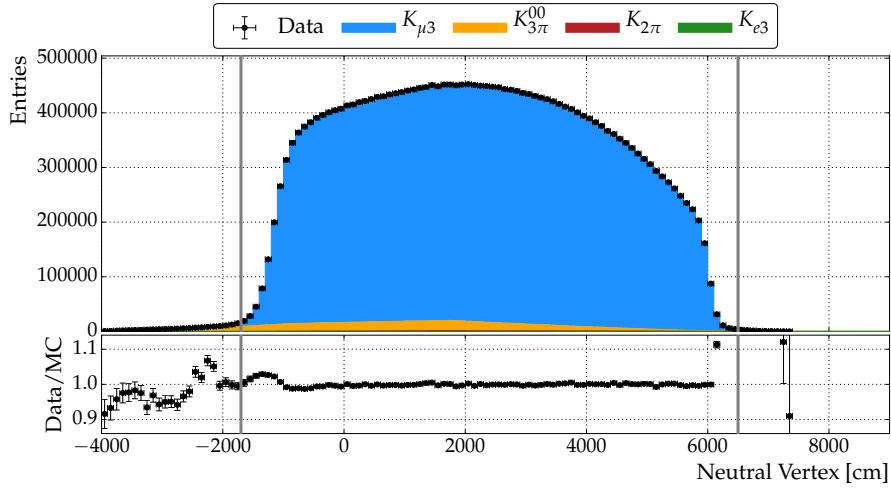
(b) K_{e3} selection.



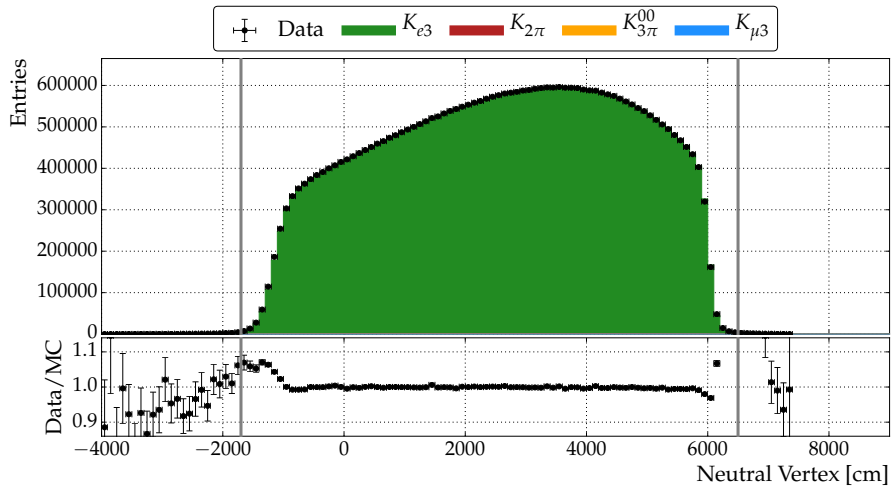
(c) $K_{2\pi}$ selection.

Figure 37: Distribution of the π^0 energy.

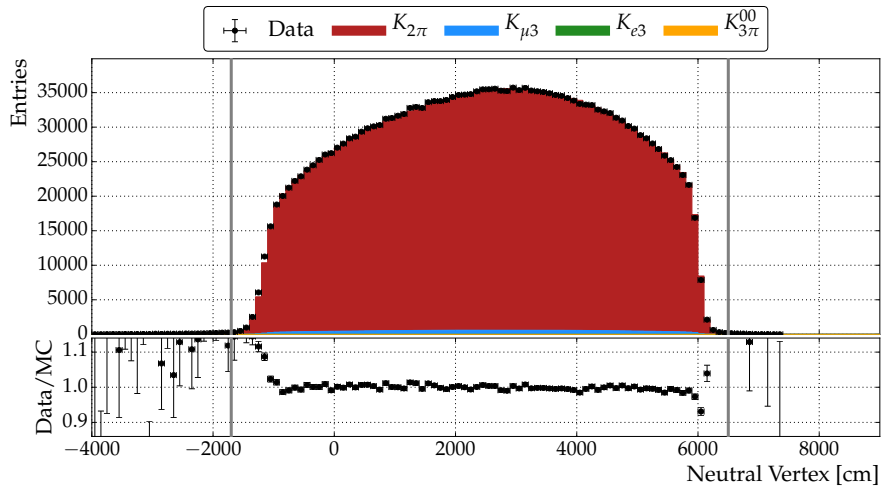
(a) $K_{\mu 3}$ selection.(b) $K_{e 3}$ selection.(c) $K_{2\pi}$ selection.Figure 38: Distribution of the π^0 mass.



(a) $K_{\mu 3}$ selection.



(b) K_{e3} selection.



(c) $K_{2\pi}$ selection.

Figure 39: Distribution of the neutral vertex.

5.6 EVENT SELECTION CRITERIA

In the following section, selection criteria are described which are signal decay specific, e.g. the track momentum and criteria which use combined information from track and π^0 , e.g. the missing mass. These latter criteria are used to further constrain the signal selections and also to reduce background. The combined information from track and π^0 are also very important to distinguish $K_{2\pi}$ from $K_{\mu 3}$. This is required due to the insufficient π/μ separation by the E/p variable which on the other hand works very well for π/e and μ/e separation (Section 5.4 on Page 64). Also the background $K_{3\pi}^{00}$ is reduced by setting conditions on combined track and π^0 variables, e.g. additional energy in the LKr. The selection criteria are summarized in Table 12. The selection criteria are not always applied to all three selections.

5.6.1 *Number of reconstructed objects*

All three studied decays have one charged particle and two photons in the final state. Thus, exactly one charged track in the spectrometer and at least two clusters in the LKr are required. One π^0 is reconstructed from the available LKr clusters. If it is possible to reconstruct more than one π^0 , the π^0 with the reconstructed mass closest to the nominal π^0 mass is chosen.

5.6.2 *Track Momentum*

The momentum of tracks is chosen to be in the range of

- $10 \text{ GeV}/c < |\vec{p}_{\text{track}}|$

as lower limit for the three main decays and as upper limit for

$$K_{\mu 3}: |\vec{p}_{\text{track}}| < 70 \text{ GeV}/c,$$

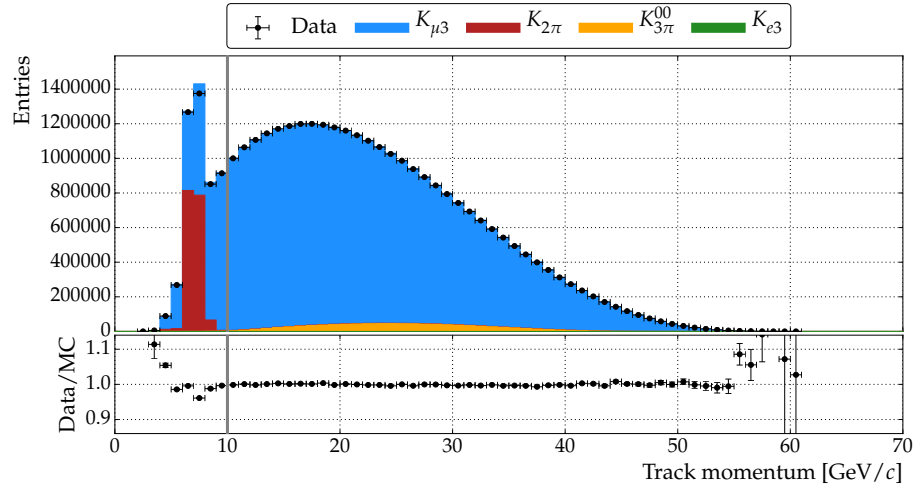
$$K_{e 3}: |\vec{p}_{\text{track}}| < 40 \text{ GeV}/c, \text{ and}$$

$$K_{2\pi}: |\vec{p}_{\text{track}}| < 50 \text{ GeV}/c.$$

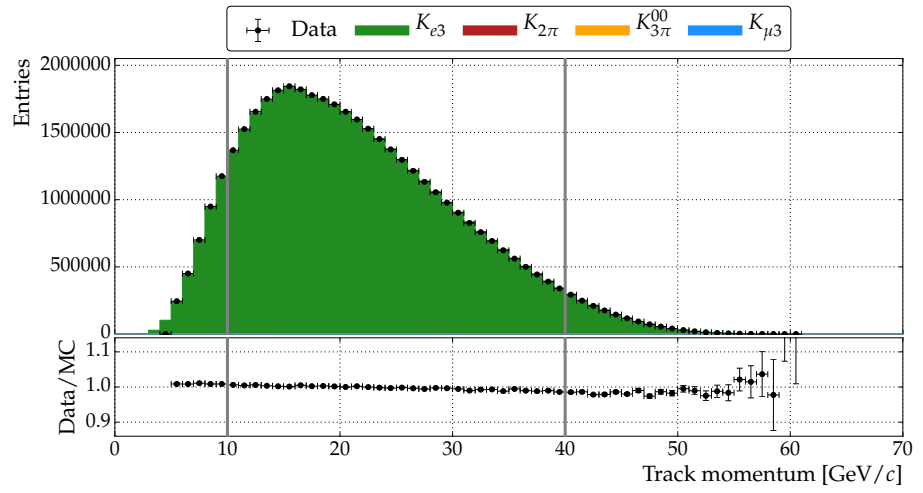
The $K_{e 2}$ trigger (used to select $K_{e 3}$ and $K_{\mu 3}$) selected events with a lower limit of $5 \text{ GeV}/c$. To be well inside the trigger window, the lower limit is set to $10 \text{ GeV}/c$ for e^+ and μ^+ . Although no lower limit is set on the $K_{\mu 2}$ trigger (used to select $K_{2\pi}$), the same limit is set for π^+ . The upper limit is given by the particle identification measured in Section 5.4. The track momentum distributions are shown in Figure 40. The strong increase of $K_{2\pi}$ background in Figure 40 (a) is related to the transversal momentum criterion described in Section 5.6.4. This criterion is not optimised to reduce the background in the momentum region $p_{\text{track}} < 10 \text{ GeV}/c$.

SELECTION CRITERION	VALUE
Number of tracks	$N_{\text{Track}} = 1$
Number of clusters	$N_{\text{Cluster}} \geq 2$
Track momentum	$K_{\mu 3}: 10 \text{ GeV}/c < \vec{p}_{\text{track}} < 70 \text{ GeV}/c$ $K_{e3}: 10 \text{ GeV}/c < \vec{p}_{\text{track}} < 40 \text{ GeV}/c$ $K_{2\pi}: 10 \text{ GeV}/c < \vec{p}_{\text{track}} < 50 \text{ GeV}/c$
Missing Mass (squared)	$K_{\mu 3}: m_{\text{miss}}^2 < 0.02 \frac{\text{GeV}^2}{c^4}$ $K_{e3}: m_{\text{miss}}^2 < 0.02 \frac{\text{GeV}^2}{c^4}$ $K_{2\pi}: -$
Transversal track momentum	$K_{\mu 3}: a_{\text{offset}}^{K_{\mu 3, \text{track}}} = 0 \text{ GeV}/c, p_{t, \text{track}} < P_4^{\text{track}}(p_{\text{track}})$ $K_{e3}: -$ $K_{2\pi}: a_{\text{offset}}^{K_{2\pi, \text{track}}} = -0.015 \text{ GeV}/c, p_{t, \text{track}} > P_4^{\text{track}}(p_{\text{track}})$
Transversal π^0 momentum	$K_{\mu 3}: a_{\text{offset}}^{K_{\mu 3, \pi^0}} = -0.015 \text{ GeV}/c, p_{t, \pi^0} < P_4^{\pi^0}(p_{\pi^0})$ $K_{e3}: -$ $K_{2\pi}: a_{\text{offset}}^{K_{2\pi, \pi^0}} = -0.05 \text{ GeV}/c, p_{t, \pi^0} > P_4^{\pi^0}(p_{\pi^0})$
Track+ π^0 momentum	$K_{\mu 3}: \vec{p}_{\text{track}} + \vec{p}_{\pi^0} < 76 \text{ GeV}/c$ $K_{e3}: \vec{p}_{\text{track}} + \vec{p}_{\pi^0} < 76 \text{ GeV}/c$ $K_{2\pi}: -$
Kaon mass	$K_{\mu 3}: -$ $K_{e3}: M_{K, \text{PDG}} - M_{\pi^+ \pi^0} > 0.02 \text{ GeV}/c^2$ $K_{2\pi}: M_{K, \text{PDG}} - M_{\pi^+ \pi^0} < 0.06 \text{ GeV}/c^2$
Additional energy in the LKr	$K_{\mu 3}: E_{\text{Add}} < 3 \text{ GeV}$ $K_{e3}: E_{\text{Add}} < 3 \text{ GeV}$ $K_{2\pi}: -$

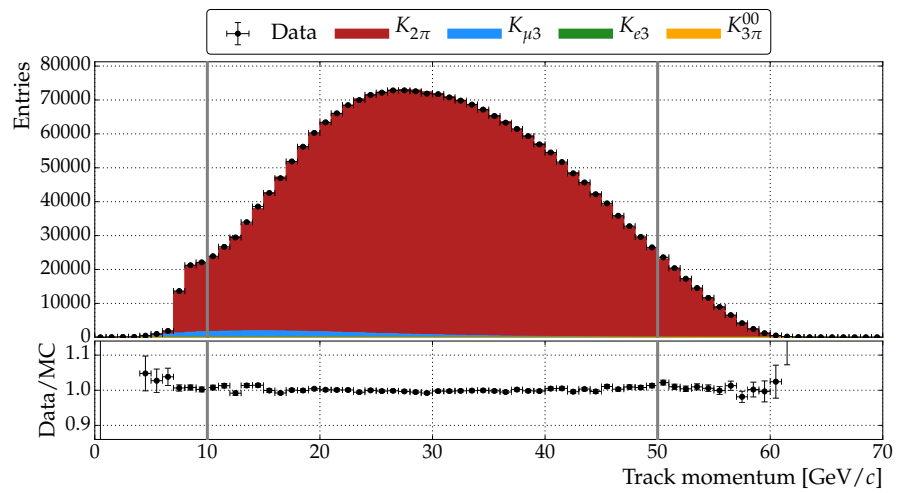
Table 12: Summary of selection criteria using combined information from the track and the π^0 .



(a) $K_{\mu 3}$ selection.



(b) K_{e3} selection.



(c) $K_{2\pi}$ selection.

Figure 40: Distribution of the track momentum.

5.6.3 Missing Mass

The squared missing mass m_{miss}^2 is calculated using the reconstructed momenta of the kaon, the track and the π^0 :

$$m_{\text{miss}}^2 := p_{\text{miss}}^2 = (p_K - p_{\text{Track}} - p_{\pi^0})^2. \quad (5.5)$$

For the decays K_{e3} and $K_{\mu3}$, p_{miss} is equivalent to the four-momentum of the neutrino p_ν . The mass of neutrinos is practically zero, therefore $m_{\text{miss}}^2 = 0$ for K_{e3} and $K_{\mu3}$. In case of the two-body decay $K_{2\pi}$, the missing mass is $m_{\text{miss}}^2 = 0$. The values for m_{miss}^2 for the background $K_{3\pi}^{00}$ are larger than zero due to the second π^0 which is not reconstructed. The selection criteria on the decays are

$$K_{e3}: m_{\text{miss}}^2 < 0.02 \frac{\text{GeV}^2}{c^4} \text{ and}$$

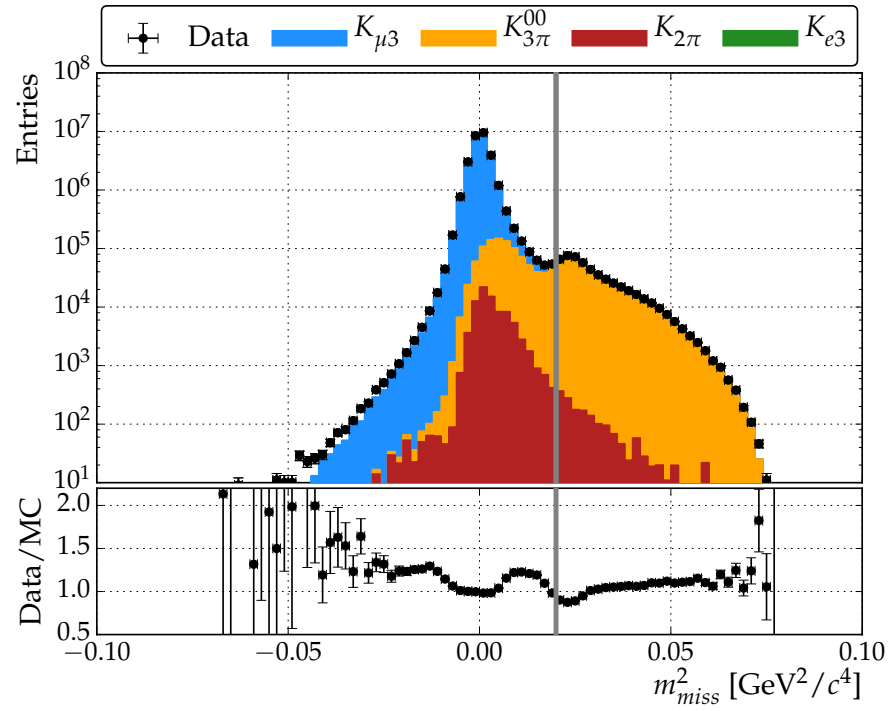
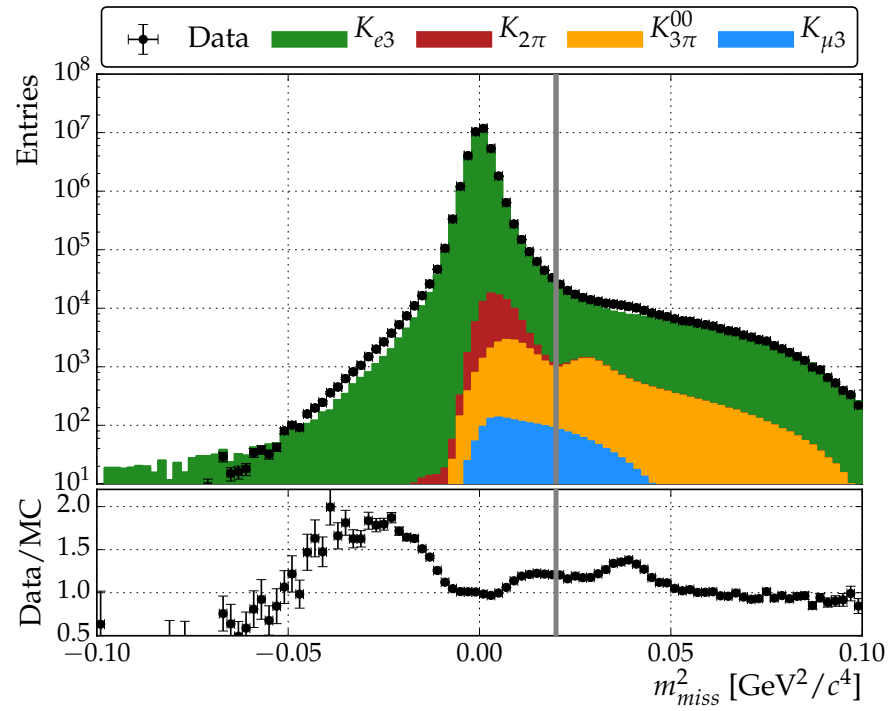
$$K_{\mu3}: m_{\text{miss}}^2 < 0.02 \frac{\text{GeV}^2}{c^4}.$$

This criterion mainly reduces the $K_{3\pi}^{00}$ background to $K_{\mu3}$ and K_{e3} . For the $K_{2\pi}$ selection, this criterion is not used since the criterion on the transversal momentum described in Section 5.6.4 reduces the three-body background $K_{3\pi}^{00}$ sufficiently. The m_{miss}^2 distributions are presented in Figure 41. The MC description of the data is not as good as for the geometric or kinematic variables. The criteria are chosen with respect to the corrections to the kaon halo in MC (Section 4.5.2 on Page 52) and the peak of the $K_{3\pi}^{00}$ background. The correction to the kaon halo needs to be taken into account because the m_{miss}^2 depends on the reconstructed kaon momentum. The distributions of $K_{\mu3}$ MC with and without the kaon halo correction and their ratio are presented in Figure 42. The correction slightly increases the width of the m_{miss}^2 distribution. The impact of this difference is visible around $|m_{\text{miss}}^2| \approx 0.01 \text{ GeV}^2 / c^4$ in Figure 42 (b). The selection criterion is therefore set at $m_{\text{miss}}^2 < 0.02 \text{ GeV}^2 / c^4$ where the influence of the changed width is smaller. The poor data/MC agreement is taken into account in the studies of systematic effects of the background in Section 7.3 on Page 114.

5.6.4 Transversal Momentum

An excellent $K_{\mu3}$ and $K_{2\pi}$ discrimination can be achieved by taking advantage of the kinematics of the three-body decay of $K_{\mu3}$ and the two-body decay of $K_{2\pi}$. The two-dimensional plots of total momentum p versus the transversal⁴ momentum p_t of the track and π^0 are very distinctive for $K_{\mu3}$ (Figure 43 and Figure 44) and $K_{2\pi}$ (Figure 45 and Figure 46). The decays of $K_{\mu3}$ fill the whole $p - p_t$ plane because the neutrino carries momentum, while for the two-body decay $K_{2\pi}$

⁴ Transversal with respect to the direction-of-flight of the kaon.

(a) $K_{\mu 3}$ selection.(b) K_{e3} selection.Figure 41: Distribution of the missing mass m_{miss}^2 .

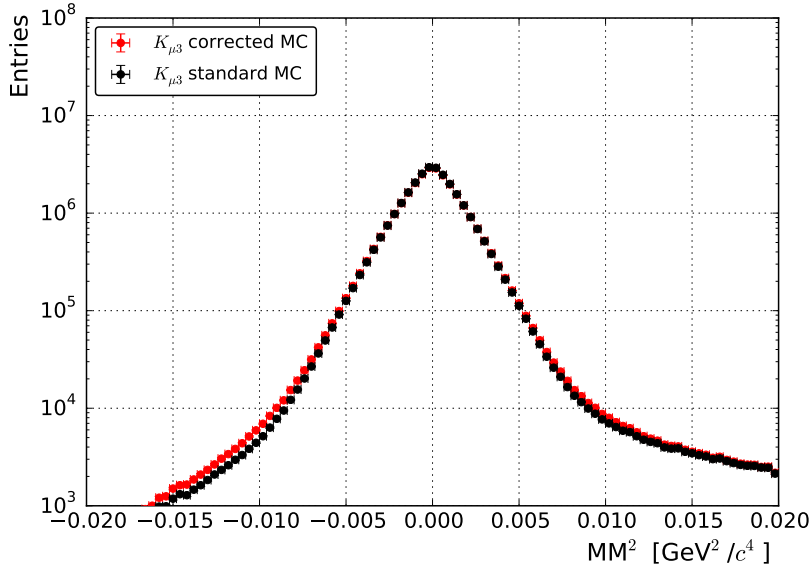
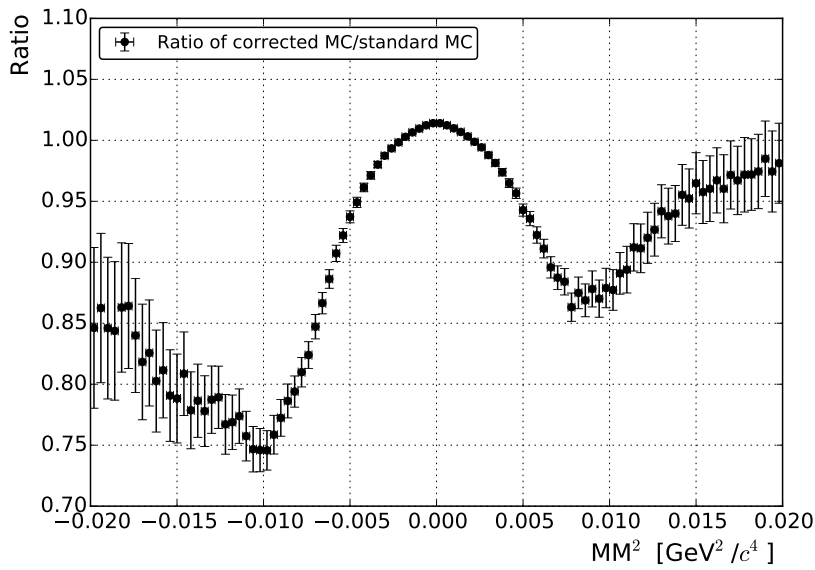
(a) $K_{\mu 3}$ MC with and without kaon halo correction.(b) Ratio of $K_{\mu 3}$ distributions with and without kaon halo correction.

Figure 42: Impact of kaon halo correction on m_{miss}^2 . (a) shows only $K_{\mu 3}$ signal MC without the kaon halo correction (black data points) and with kaon halo correction (red data points). Both distributions are normalized. (b) shows the ratio of both MC sets. The selection criterion of $m_{\text{miss}}^2 < 0.02 \text{ GeV}^2/c^4$ on m_{miss}^2 is chosen to be safely away from the large deviation at $m_{\text{miss}}^2 = 0.01 \text{ GeV}^2/c^4$. The distributions are similar for $K_{e 3}$ MC.

PARAMETER	$ p_{\text{track}} < 37 \text{ GeV}/c$	$ p_{\text{track}} \geq 37 \text{ GeV}/c$
a_0	-0.035	1.361
a_1	0.016	-0.102
a_2	-0.0004	0.003
a_3	$4.401 \cdot 10^{-6}$	$-4.712 \cdot 10^{-5}$
a_4	$-2.216 \cdot 10^{-8}$	$2.406 \cdot 10^{-7}$

Table 13: Parameters for the bi-dimensional the selection criterion on p and p_t of the track. These are rounded values, the full values used in the selection are shown in Table 21 on Page 140.

the momenta p and p_t are completely related. The $K_{\mu 3}/K_{2\pi}$ separation is achieved by applying separately a bi-dimensional selection criterion in the $p - p_t$ plane on track and π^0 respectively. The criterion is defined by a fourth-degree polynomial

$$P_4^{\text{par}}(p_{\text{par}}) = \sum_{i=0}^4 a_i p_{\text{par}}^i - a_{\text{offset}}^{\text{decay,par}} \quad (5.6)$$

with p_{par} the total momentum of the particle (track or π^0) and a decay ($K_{\mu 3}$ or $K_{2\pi}$) specific offset $a_{\text{offset}}^{\text{decay,par}}$. The selection criteria are fulfilled for

$$K_{\mu 3}: p_{t,\text{par}} < P_4^{\text{par}}(p_{\text{par}}) \text{ and}$$

$$K_{2\pi}: p_{t,\text{par}} > P_4^{\text{par}}(p_{\text{par}}).$$

The respective parameters for track and π^0 have been obtained by fitting a fourth-degree polynomial to the corresponding $K_{2\pi}$ distributions. The described selection criteria are shifted differently along the p_t -axis for $K_{\mu 3}$ and $K_{2\pi}$. This shift is controlled by the offset parameter $a_{\text{offset}}^{\text{decay,par}}$. The shifts are applied to be inside well-described regions by data/MC for each signal channel. The obtained values for the particle specific parameters are summarized in Table 13 and Table 14. The decay and particle specific offset parameters are summarized in Table 15.

The kaon halo correction in MC is taken into account for these selection criteria. The effect on the two-dimensional distributions of p_t versus p are presented in Figure 47. The distributions are the ratios of the respective MC with and without correction. For $K_{2\pi}$, two main regions exist with discrepancies larger than 10%. These are the light grey regions just above the selection criterion (grey line). Here, the smearing of the additional MC has the strongest effect. The selection criterion on $K_{2\pi}$ is chosen to completely include both regions in the selection. In case of the $K_{\mu 3}$ MC (Figure 47 (b)), no regions with discrepancies are visible. The selection criterion does not depend on the

PARAMETER	$ p_{\pi^0} < 37 \text{ GeV}/c$	$ p_{\pi^0} \geq 37 \text{ GeV}/c$
a_0	-0.315	1.269
a_1	0.064	-0.094
a_2	-0.003	0.003
a_3	$7.629 \cdot 10^{-5}$	$-4.261 \cdot 10^{-5}$
a_4	$-6.829 \cdot 10^{-7}$	$2.100 \cdot 10^{-7}$

Table 14: Parameters for the bi-dimensional the selection criterion on p and p_t of the π^0 . These are rounded values, the full values used in the selection are shown in Table 22 on Page 140.

PARTICLE	$K_{\mu 3}$ decay	$K_{2\pi}$ decay
Track	$a_{\text{offset}}^{K_{\mu 3}, \text{Track}} = 0 \text{ GeV}/c$	$a_{\text{offset}}^{K_{2\pi}, \text{Track}} = -0.015 \text{ GeV}/c$
π^0	$a_{\text{offset}}^{K_{\mu 3}, \pi^0} = -0.015 \text{ GeV}/c$	$a_{\text{offset}}^{K_{2\pi}, \pi^0} = -0.05 \text{ GeV}/c$

Table 15: Summary of the decay specific offset parameters

correction. The distributions for the total π^0 momentum and transversal π^0 momentum are similar to the track momentum distributions and are presented in Figure 48.

5.6.5 Combined Track and π^0 Momentum

Events with a reconstructed combined momentum $|\vec{p}_{\text{Track}} + \vec{p}_{\pi^0}|$ above the sum of the central beam momentum (74 GeV/c) and its spread (1.5 GeV/c) are classified as badly reconstructed. Taking a small safety margin into account, only events with

$$|\vec{p}_{\text{Track}} + \vec{p}_{\pi^0}| < 76 \text{ GeV}/c \quad (5.7)$$

are accepted. This criterion is applied to the semileptonic K_{e3} and $K_{\mu 3}$ decays while it is not used in $K_{2\pi}$ selection due to the correction of the width of the kaon momentum distribution (Section 4.5.1 on Page 50). The respective distributions are presented in Figure 49.

5.6.6 Kaon Mass

A further criterion to discriminate $K_{2\pi}$ from three-body decays is the difference between the nominal kaon mass $M_{K, \text{PDG}}$ and the invariant mass of the track+ π^0 system. For this criterion the track is always considered as π^+ which means that the $K_{2\pi}$ decay is centered at $0 \text{ GeV}/c^2$ in all selections.

The criterion is applied on the K_{e3} and the $K_{2\pi}$ selections with

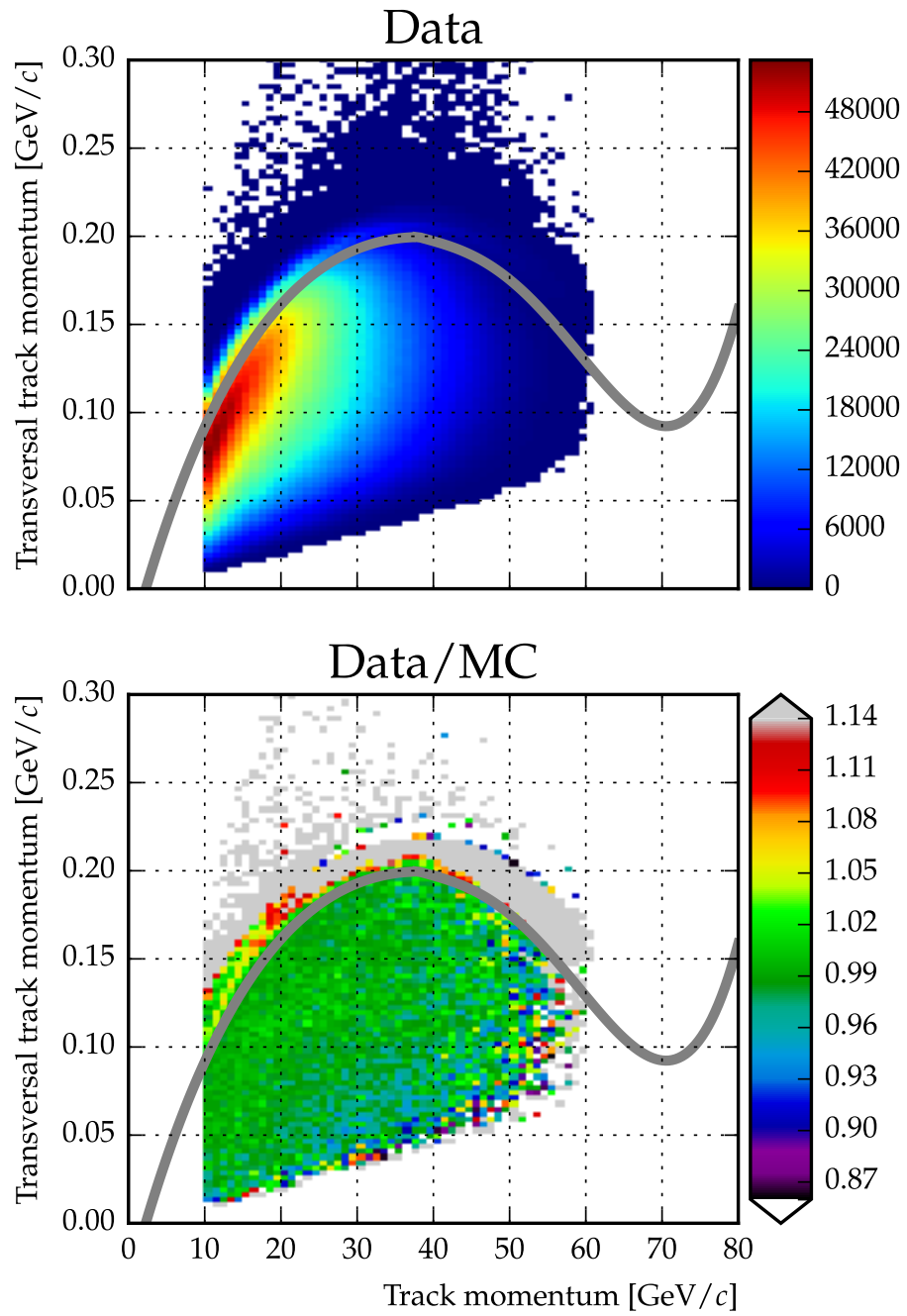


Figure 43: Distributions of $p_{t,track}$ versus p_{track} for the $K_{\mu 3}$ selection.

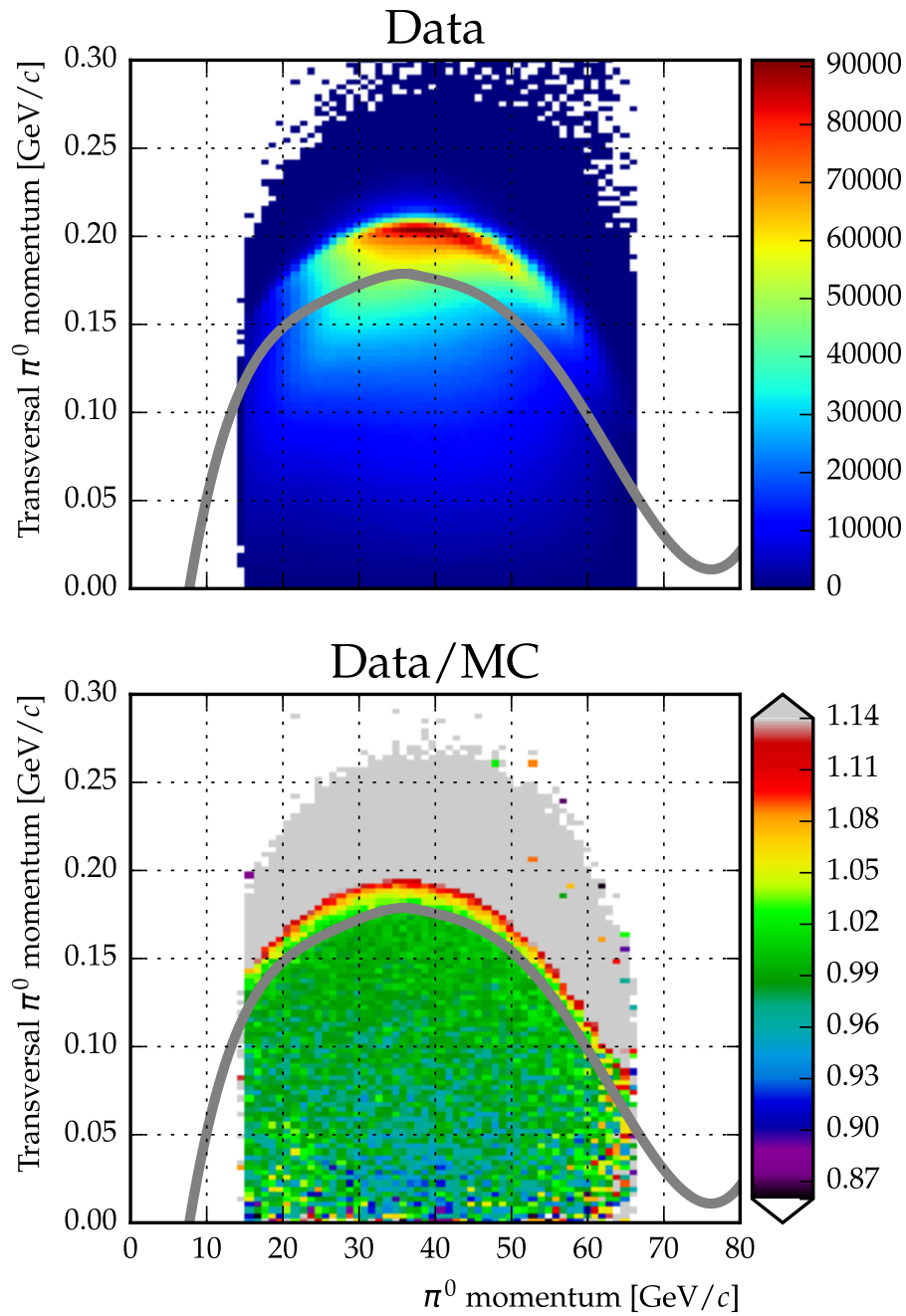


Figure 44: Distributions of p_{t,π^0} versus p_{π^0} for the $K_{\mu 3}$ selection.

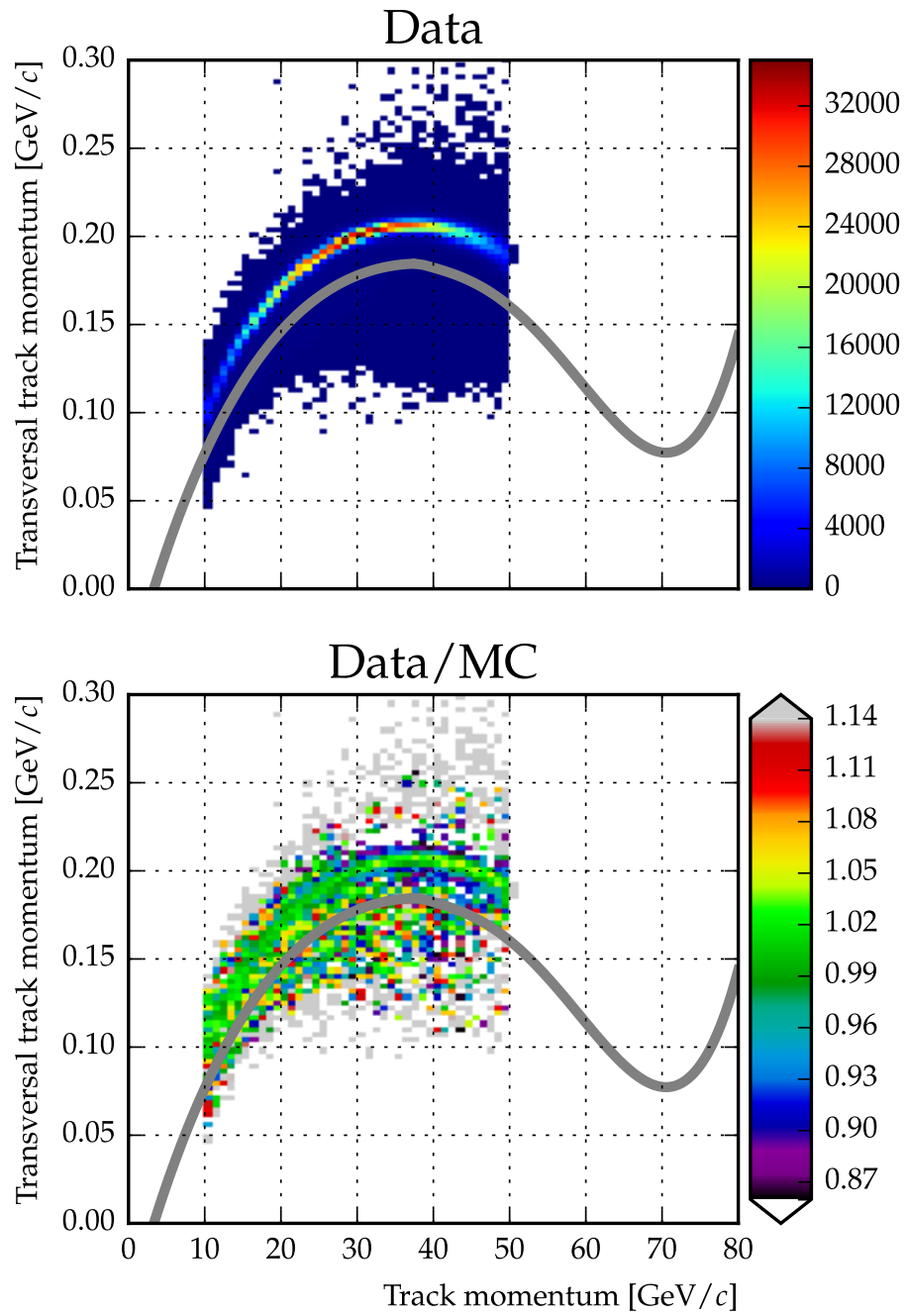


Figure 45: Distributions of $p_{t,track}$ versus p_{track} for the $K_{2\pi}$ selection.

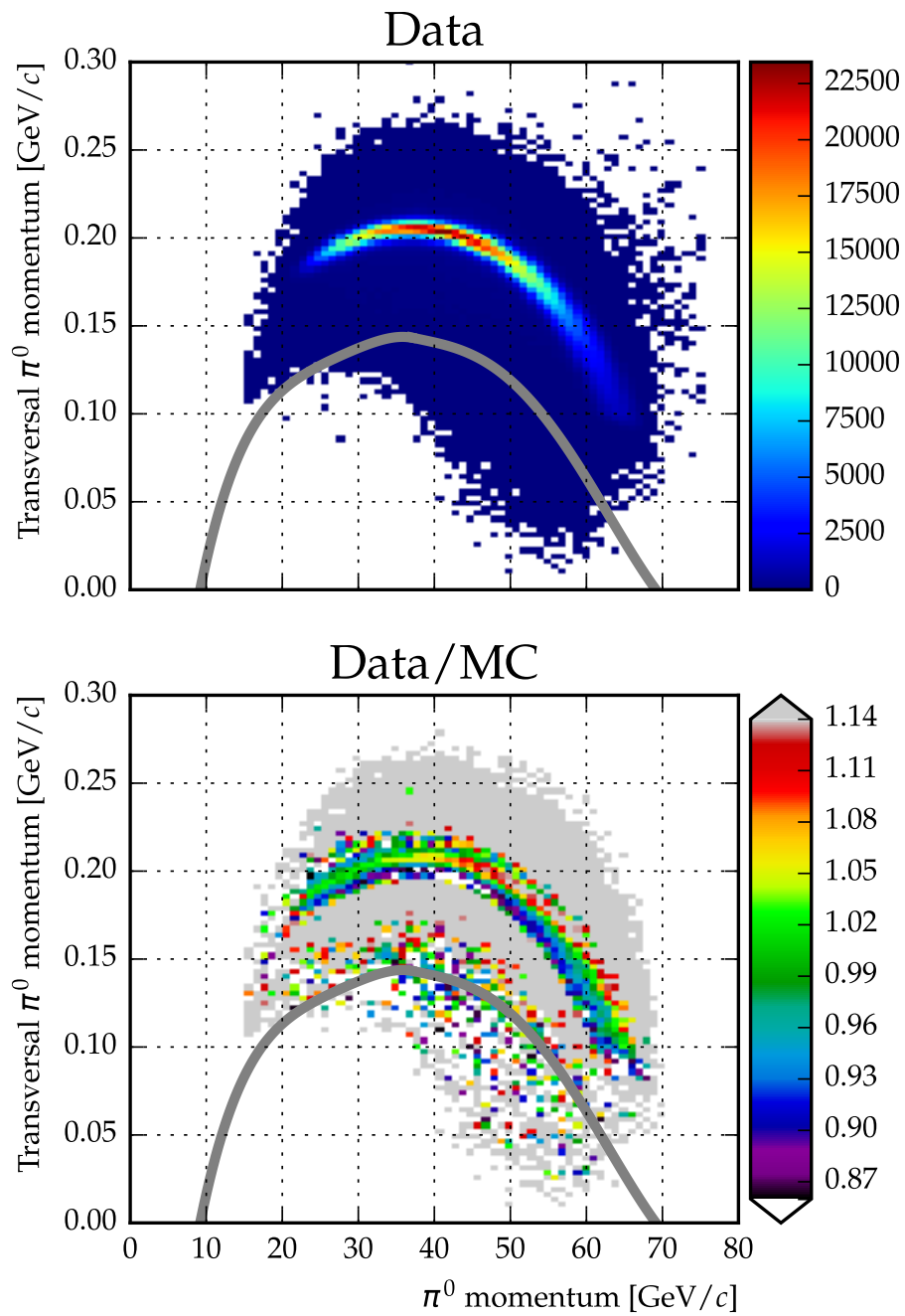


Figure 46: Distributions of p_{t,π^0} versus p_{π^0} for the $K_{2\pi}$ selection.

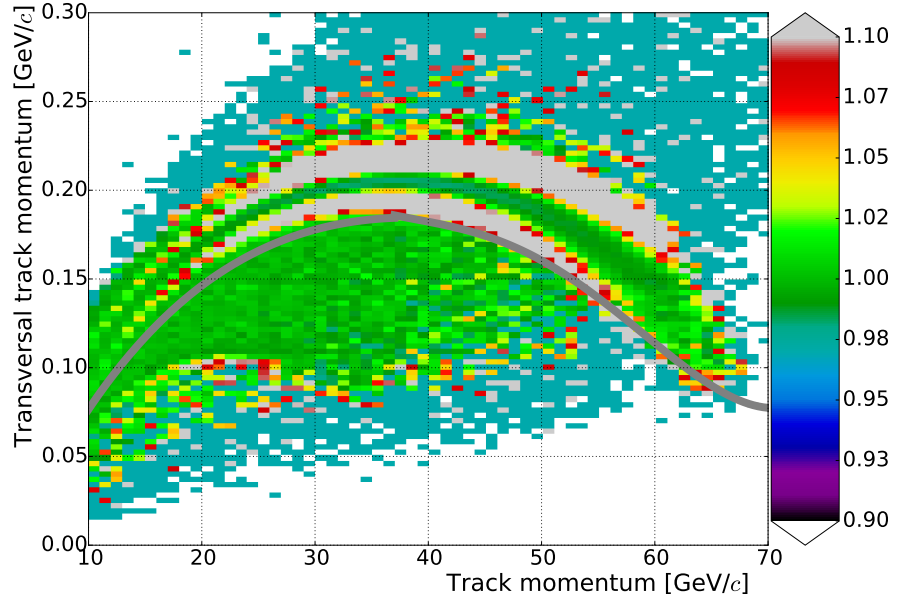
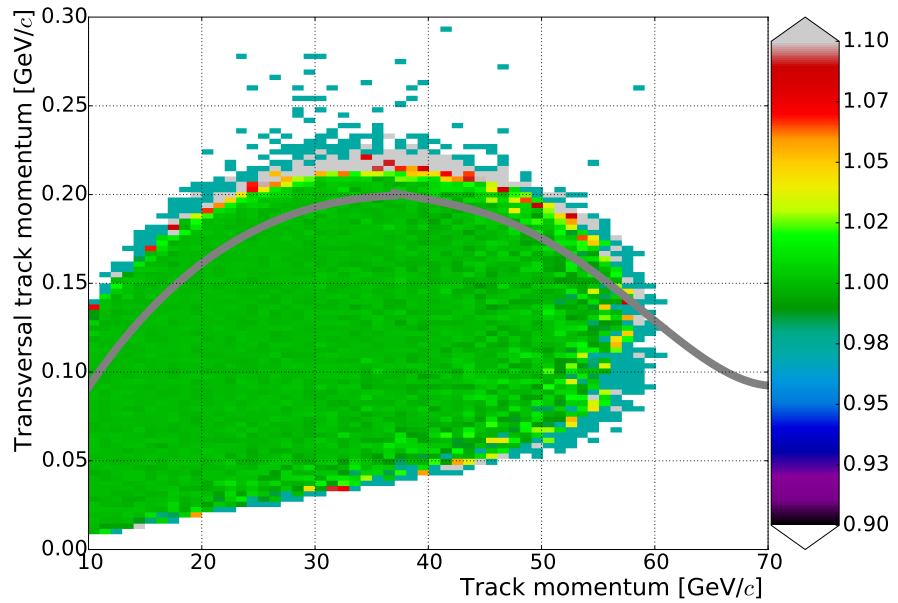
(a) $K_{2\pi}$ MC.(b) $K_{\mu 3}$ MC.

Figure 47: Kaon halo correction impact on the track momenta. Both plots show the ratio of the signal MC including the correction divided by the signal MC without the correction. The distributions are normalized to each other before division. The $K_{2\pi}$ distribution (a) show large ($> 10\%$) deviations due to the correction. No such region is visible for the $K_{\mu 3}$ distribution. The effects of the correction are smeared due to neutrino in the final state. In (a), $K_{2\pi}$ events are accepted above the grey selection criterion line. In (b), $K_{\mu 3}$ events are accepted below the grey line.

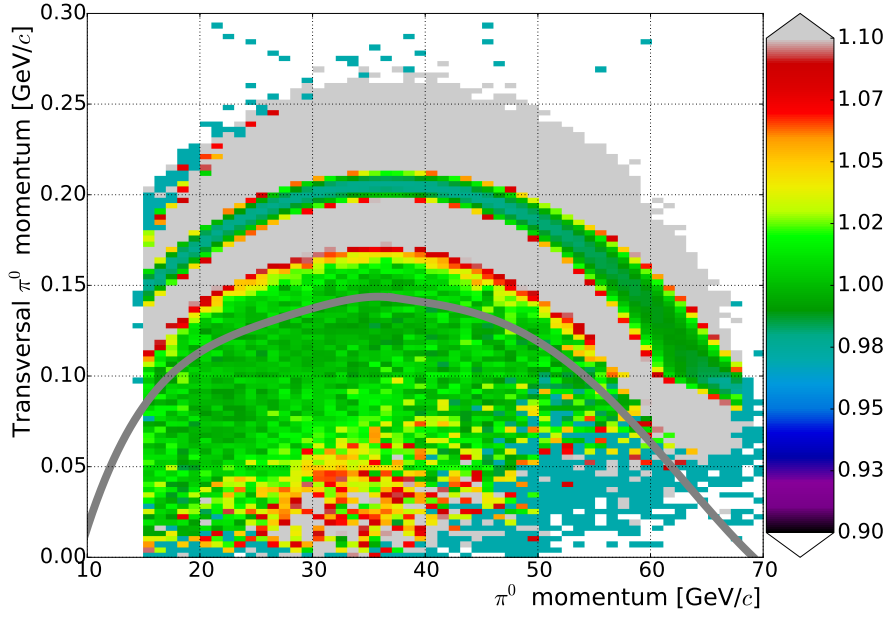
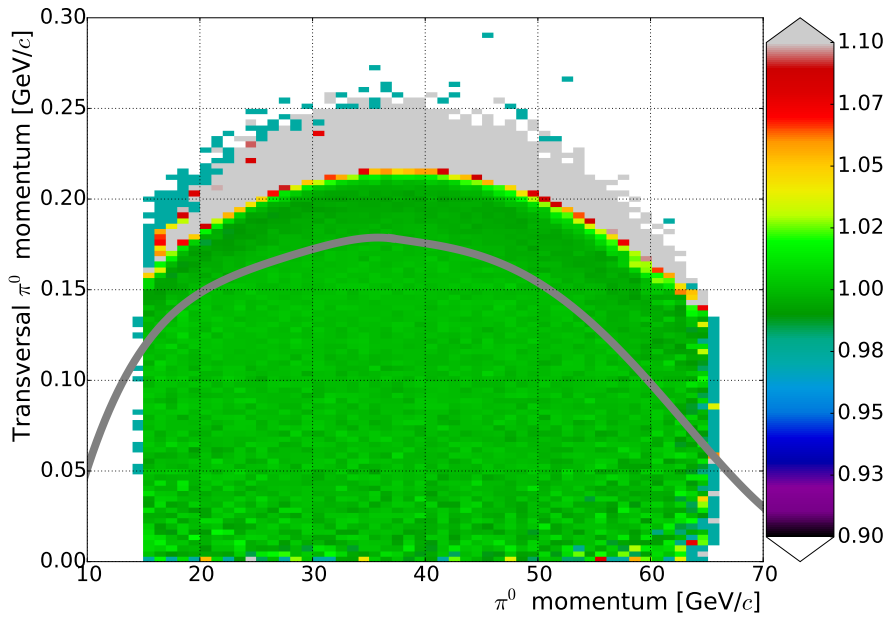
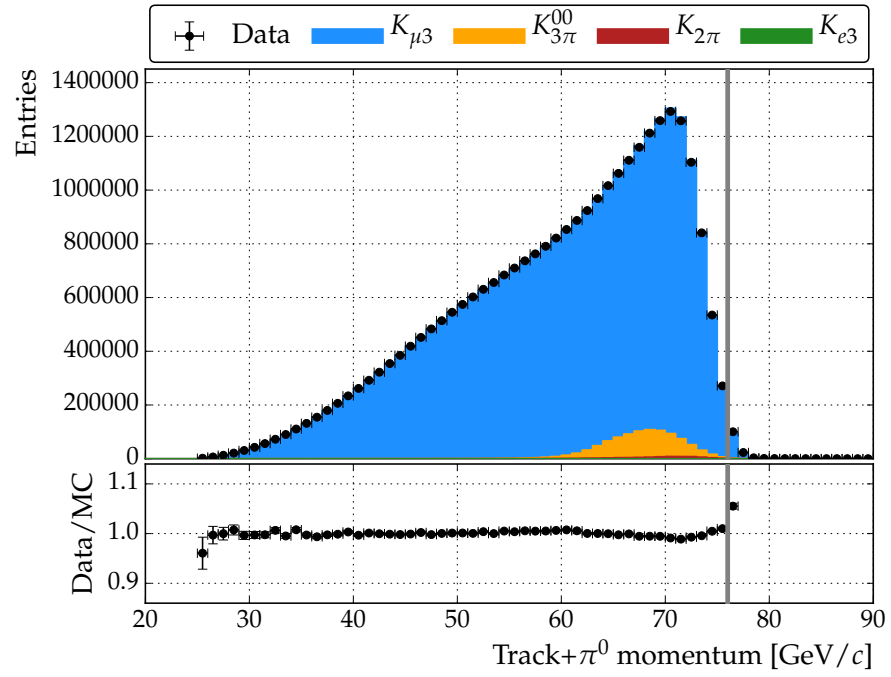
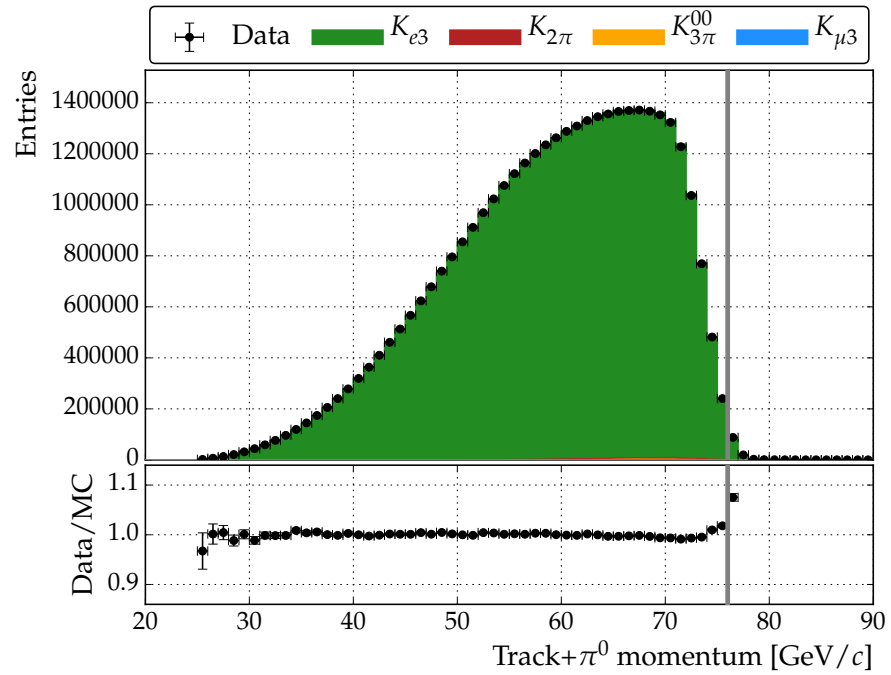
(a) $K_{2\pi}$ MC.(b) $K_{\mu 3}$ MC.

Figure 48: Kaon halo correction impact on the π^0 momenta. Both plots show the ratio of the signal MC the including correction divided by the signal MC without the correction. The distributions are normalized to each other before division. The $K_{2\pi}$ distribution (a) show large ($> 10\%$) deviations due to the correction. No such region is visible for the $K_{\mu 3}$ distribution. The effects of the correction are smeared due to neutrino in the final state. In (a), $K_{2\pi}$ events are accepted above the grey selection criterion line. In (b), $K_{\mu 3}$ events are accepted below the grey line.

(a) $K_{\mu 3}$ selection.(b) K_{e3} selection.Figure 49: Distributions of the combined track and π^0 momenta.

- K_{e3} : $|\Delta M| := |M_{K,\text{PDG}} - M_{\pi^+\pi^0}| > 0.02 \text{ GeV}/c^2$ and
- $K_{2\pi}$: $\Delta M := M_{K,\text{PDG}} - M_{\pi^+\pi^0} < 0.06 \text{ GeV}/c^2$

with $M_{K,\text{PDG}}$ the kaon mass taken from [11]. The criterion is not applied on the $K_{\mu 3}$ selection because the separation between $K_{\mu 3}$ and $K_{2\pi}$ is done by the more sophisticated criterion on the transversal momentum described in Section 5.6.4. The respective distributions are shown in Figure 50. For the K_{e3} distribution, the peak is underestimated by the Monte Carlo simulation. Farther away from the peak, the description of data is good up to $0.1 \text{ GeV}/c^2$. A slope is present after this value. For the $K_{2\pi}$ distribution, the description of the peak by MC is poor. The selection criterion chosen to $\Delta M < 0.06 \text{ GeV}/c^2$ because the data/MC stabilizes above this value.

5.6.7 Additional Energy in the LKr

The $K_{3\pi}^{00}$ background can be reduced by applying a criterion on the additional energy in the LKr. The additional energy is defined as

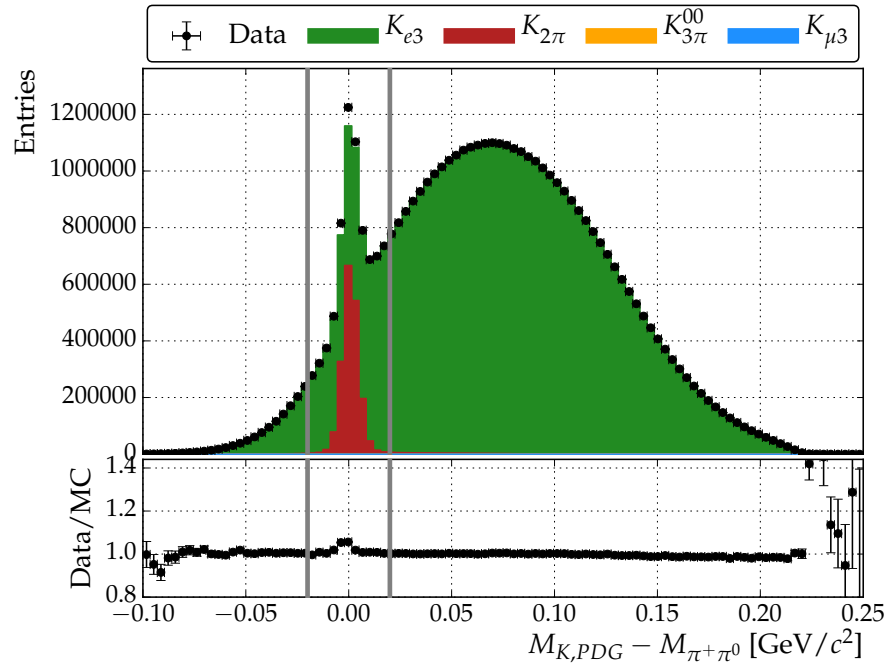
$$E_{\text{Add}} = E_{\text{LKr total}} - E_{\pi^0} - E_{\text{Track Cluster}} \quad (5.8)$$

with $E_{\text{LKr total}}$ the total measured energy in the LKr, E_{π^0} the energy of the π^0 , and $E_{\text{Track Cluster}}$ the energy of the associated cluster to the track (if such a cluster exists). In general, additional energy is deposited by $K_{3\pi}^{00}$ decays due to the second π^0 . The energy spectra of the additional energy are shown in Figure 51. The edge at 5 GeV is a reflection of the energy cluster requirement $E_{\text{Cluster}} > 5 \text{ GeV}$ of the π^0 selection. The data/MC agreement is good below 15 GeV except for the second bin which shows a larger data excess. The energy region below 10 GeV is shown in Figure 52. An energy distribution of minimum ionizing particles (brown color) obtained from the $K_{\mu 3}$ data sample has been added to these plots. They were scaled to the data excess and fit well. The width of the distributions is not perfectly described which is partly caused by a noisy LKr cell. The additional contribution of minimum ionizing particles is most probably caused by additional muons passing simultaneously the LKr together with the signal decay particles. The origin of these muons are decays from pions inside the beam pipe. The data/MC description gets worse above 15 GeV. This discrepancy can as well be caused by beam particles (most cases pions) which may hit the LKr. The requirement for $K_{\mu 3}$ and K_{e3} is set to

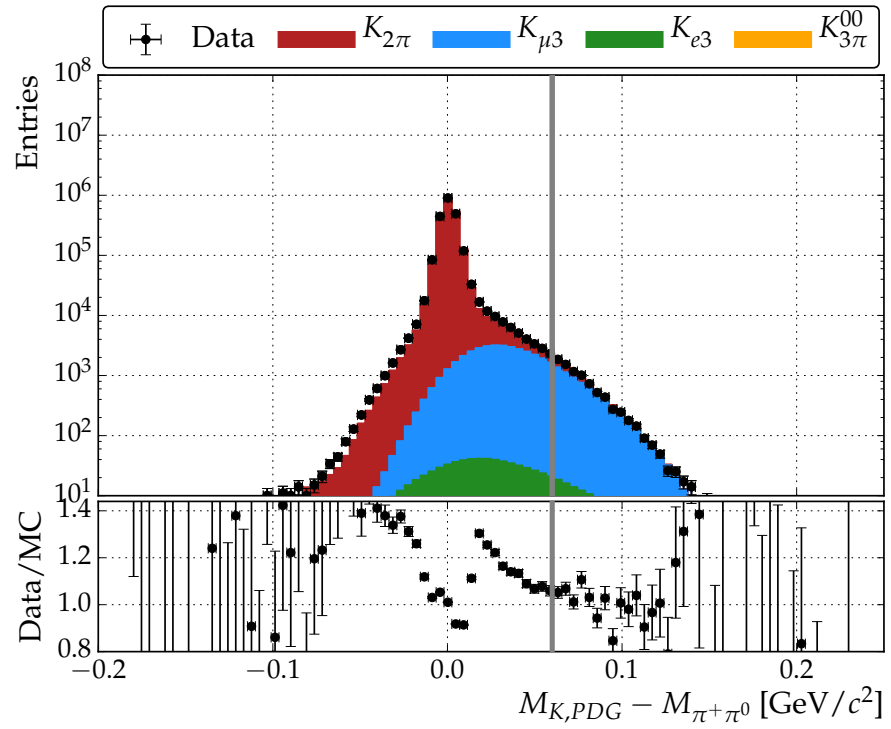
- $E_{\text{Add}} < 3 \text{ GeV}$.

5.7 RECONSTRUCTED CANDIDATES

The selections described in this chapter are applied to the reconstructed events both in data and MC. Those reconstructed events are

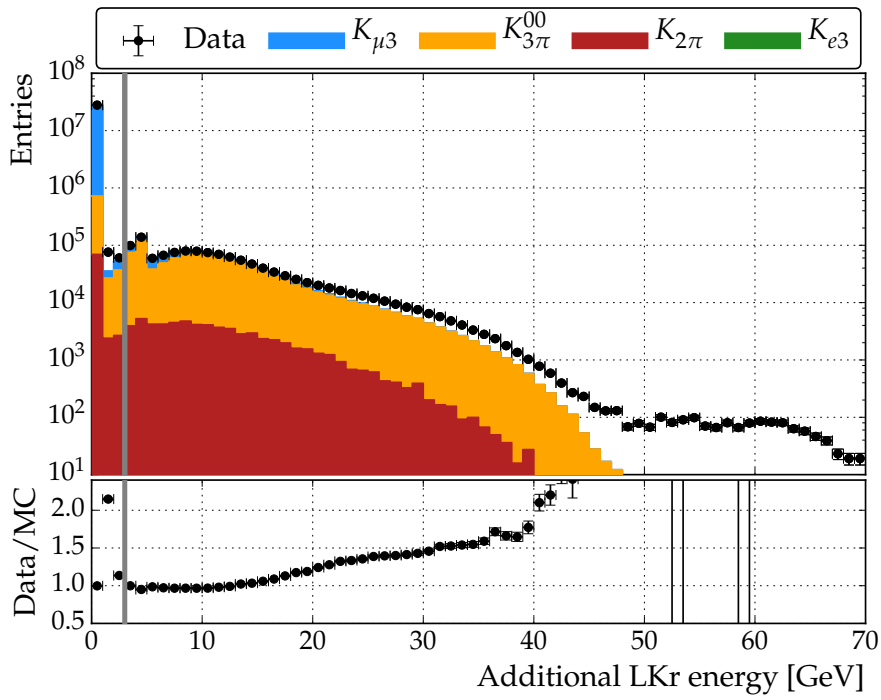


(a) K_{e3} selection.

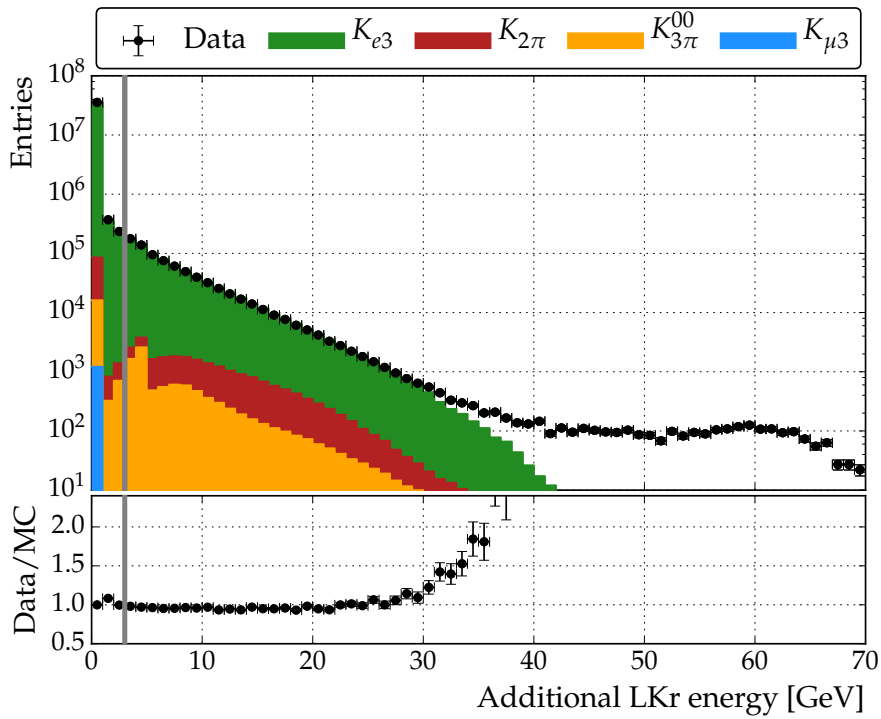


(b) $K_{2\pi}$ selection.

Figure 50: Distributions of the difference between the nominal kaon mass and $M_{\pi^+\pi^0}$.



(a) $K_{\mu 3}$ selection.



(b) K_{e3} selection.

Figure 51: Distribution of the additional energy in the LKr.

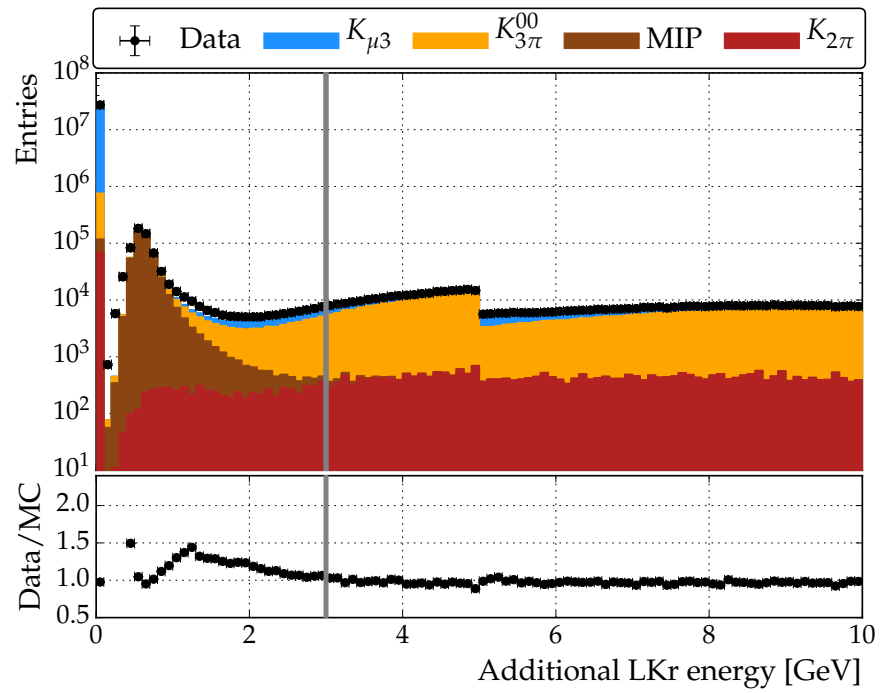
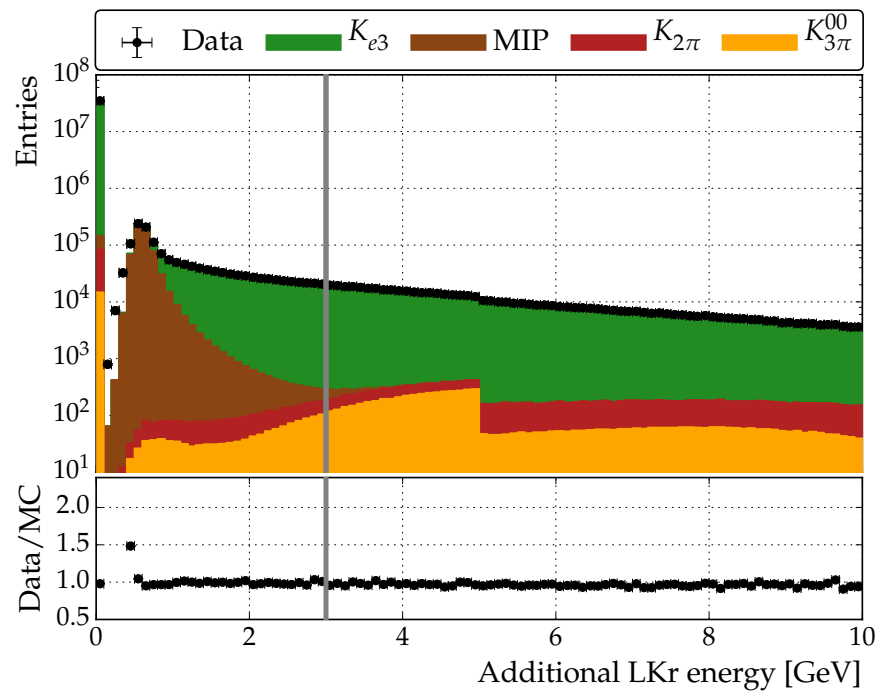
(a) $K_{\mu 3}$ selection.(b) $K_{e 3}$ selection.

Figure 52: Distribution of the additional energy in the LKr below 10 GeV. Energy distribution of minimal ionizing particles (MIP) added (brown).

corrected for trigger efficiencies (data only) and detector miscalibrations (data and MC), as described in previous sections.

Approximately 28 million $K_{\mu 3}$, 37 million $K_{e 3}$, and 2 million $K_{2\pi}$ trigger and calibration corrected signal candidates are selected. The exact numbers for the trigger corrected and uncorrected signal candidates are summarized in Table 16.

The number of accidentals, i.e. events where track and π^0 do not originate from the same source but are close together in time by chance, is estimated from Figure 35 (a) on Page 79. A Gaussian and 1st degree polynomial function are combined and fitted to the data set. The integral of the polynomial in the range of the selection gives an estimation for the number of accidentals. The estimated number of accidental events is subtracted from the data set and are summarized in Table 16.

The signal acceptance is obtained from MC (Section 4.6 on Page 54).

The background contamination of the data set is estimated from MC. The number of background MC events passing the respective selection are normalized to the kaonflux which is discussed in the next section. For the estimation of the background contribution of $K_{\mu 3}$ and $K_{e 3}$ to the respective other signal channels (cross-feed background), their branching fractions are needed. Most relevant is the background contribution of $K_{\mu 3}$ to the $K_{2\pi}$ decay because $K_{\mu 3}$ is the dominating background. However, the measurement of the branching fractions of $K_{\mu 3}$ and $K_{e 3}$ is one of the objectives of this work. These results are taken into account by an iterative ansatz. In a first step, the known branching fractions from [11] are taken to compute the background estimates. The branching fractions are computed with these estimates as discussed later in Section 8.1 on Page 127. Next, the newly obtained branching fractions are used to re-estimate the background contributions. This procedure should be repeated until the obtained branching fractions do not change anymore, however, it converges already on the second step. The changes of the background contribution to the decays $K_{\mu 3}$, $K_{e 3}$, and $K_{2\pi}$ due to this procedure are 0.01 %, 0.01 %, and 0.9 %, respectively. To obtain the background estimation, the normalized number of background events is divided by the total number of data candidates. The contamination obtained are 2.9 % for $K_{\mu 3}$ (dominated by $K_{3\pi}^{00}$), 0.26 % for $K_{e 3}$, and 1.7 % for $K_{2\pi}$ (dominated by $K_{\mu 3}$). The values are summarized in Table 16.

5.8 KAON FLUX

The different kaon decay channels simulated in MC must be normalized to data. Therefore, the selected $K_{2\pi}$ candidates are used as ref-

	$K_{\mu 3}$	$K_{e 3}$	$K_{2\pi}$
Raw Candidates	27 730 193	37 178 482	2 165 886
Corr. Candidates	27 864 293	37 293 816	2 173 226
Accidentals	3 471 (60)	4 363 (67)	452 (22)
Acceptance[%]	8.68	7.87	16.50
Background[%]	2.91	0.26	1.70
Bkgr- $K_{\mu 3}$ [%]	–	< 0.01	1.67
Bkgr- $K_{e 3}$ [%]	< 0.01	–	0.03
Bkgr- $K_{2\pi}$ [%]	0.27	0.22	–
Bkgr- $K_{3\pi}^{00}$ [%]	2.63	0.04	< 0.01

Table 16: Overview of selected candidates. Number of selected candidates after reconstruction (raw) and with applied trigger corrections. The $K_{2\pi}$ selection has been recorded with a downscale trigger factor of 150. Acceptance and background are derived from MC, accidentals are derived from data.

erence to compute the kaon flux Φ , i.e. the total amount of decayed kaons during data taking.

$$\Phi = \frac{N_{\text{Cand}}^{K_{2\pi}} \cdot D}{A_{K_{2\pi}} \cdot \text{Br}(K_{2\pi}) + B} \quad (5.9)$$

with $N_{\text{Cand}}^{K_{2\pi}}$ the measured amount of $K_{2\pi}$ candidates and $A_{K_{2\pi}}$ the acceptance as stated in Table 16, $D = 150$ to correct the trigger downscaling and

$$B = \sum_i A_i \cdot \text{Br}(i) \text{ with } i = K_{\mu 3}, K_{e 3}, \text{ and } K_{3\pi}^{00}. \quad (5.10)$$

The branching fractions :

- $\text{Br}(K_{2\pi}) = 20.67(8)\%$,
- $\text{Br}(K_{3\pi}^{00}) = 1.760(23)\%$.

are taken from [11]. The branching fractions of $K_{\mu 3}$ and $K_{e 3}$ are treated in the iterative way as discussed in the previous section. The kaon flux computes to

$$\Phi = 9.51(4) \cdot 10^9. \quad (5.11)$$

5.9 RATIOS

The values listed in Table 16 are used to calculate the ratios $\frac{\text{Br}(K_{\mu 3})}{\text{Br}(K_{2\pi})}$, $\frac{\text{Br}(K_{e3})}{\text{Br}(K_{2\pi})}$, and $\frac{\text{Br}(K_{\mu 3})}{\text{Br}(K_{e3})}$. The ratios are computed through

$$\frac{\text{Br}(K_i)}{\text{Br}(K_j)} = \frac{N_{\text{Cand},i} - N_{\text{Bkgr},i} - N_{\text{Accid},i}}{N_{\text{Cand},j} - N_{\text{Bkgr},j} - N_{\text{Accid},j}} \cdot \frac{A_j}{A_i} \quad (5.12)$$

with the measured amount of candidates N_{Cand} which have been corrected for trigger efficiencies during reconstruction, the amount of normalized background events obtained from MC N_{Bkgr} , the accidental events N_{Accid} , and the acceptance A .

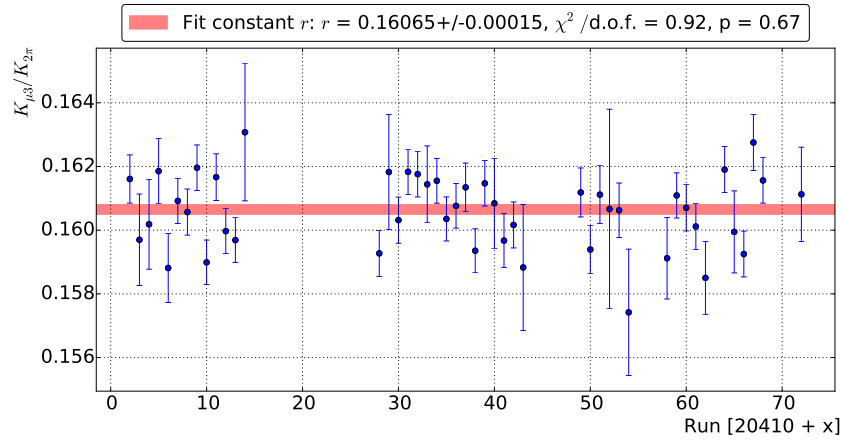
The obtained ratios are:

$$\frac{\text{Br}(K_{\mu 3})}{\text{Br}(K_{2\pi})} = 0.16066(12)_{\text{Data}}(5)_{\text{MC}} \quad (5.13)$$

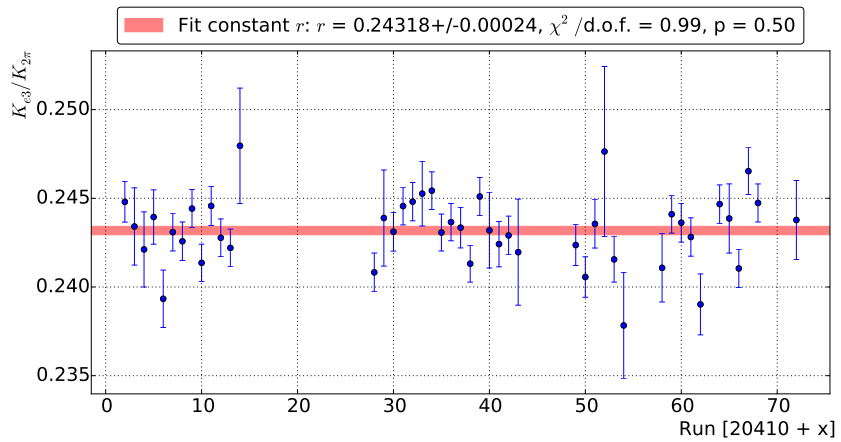
$$\frac{\text{Br}(K_{e3})}{\text{Br}(K_{2\pi})} = 0.24320(17)_{\text{Data}}(7)_{\text{MC}} \quad (5.14)$$

$$\frac{\text{Br}(K_{\mu 3})}{\text{Br}(K_{e3})} = 0.66061(17)_{\text{Data}}(20)_{\text{MC}} \quad (5.15)$$

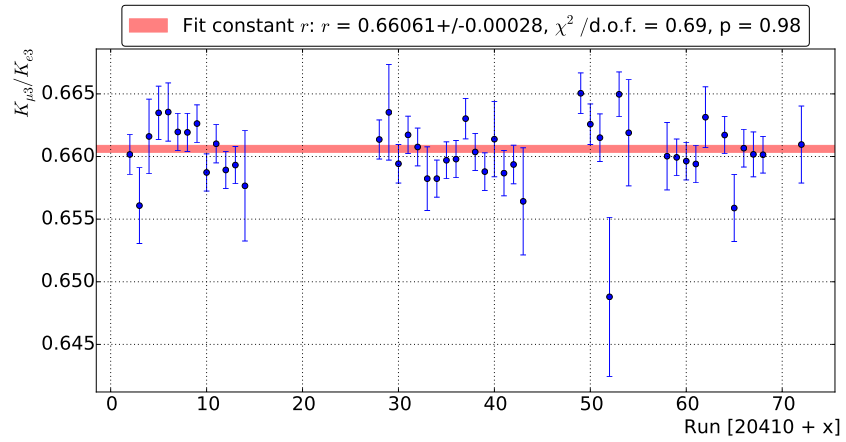
The stated uncertainties are statistical only and separated into data and MC source. These ratios are also computed for each run. Each of the runs is an independent data set. The results are shown in Figure 53. For each distribution the mean is computed. None of the runs is more than 3 standard deviations away from the mean.



(a) $\frac{\text{Br}(K_{l3})}{\text{Br}(K_{2\pi})}$ ratio in dependence of run.



(b) $\frac{\text{Br}(K_{e3})}{\text{Br}(K_{2\pi})}$ ratio in dependence of run.



(c) $\frac{\text{Br}(K_{l3})}{\text{Br}(K_{e3})}$ ratio in dependence of run.

Figure 53: Ratios of the branching fractions computed independently for each run. The uncertainties are statistical only. The red band is the computed mean of the distribution. The width of the band is the uncertainty on the mean.

TRIGGER EFFICIENCY

The trigger efficiencies for the L2-trigger are measured from data with the independent trigger for neutral particles $T0N$. $T0N$ is a suitable choice as control trigger for efficiency measurements because all selected signal decays and relevant backgrounds have at least one π^0 in their final state. The information about the status of each sub-trigger for each event is kept in the so-called Pattern Unit (PU) (Section 2.12.3 on Page 31). This makes it possible to compare the sub-triggers separately with the $T0N$ trigger. The efficiencies are calculated for each selection by keeping the selection criteria and only changing the used triggers. The efficiency is the ratio of two different sets of candidates. The first set $N(X \wedge T0N)$ is the combination of decay selection, the sub-trigger X ($X = Q_1, E_{10}$ or $TRKLM$) of which the efficiency is measured, and $T0N$. The second set $N(T0N)$ is the combination of decay selection and only $T0N$:

$$\epsilon_X = \frac{N(X \wedge T0N)}{N(T0N)}. \quad (6.1)$$

In case of fully efficient triggers both selections should yield the same number of candidates.

The uncertainty of the efficiency is the binomial uncertainty

$$\Delta\epsilon_X = \sqrt{\frac{\epsilon_X(1 - \epsilon_X)}{N(T0N)}} \quad (6.2)$$

with the assumption that the measured efficiency is the true efficiency
The total efficiency of the K_{e2} trigger is calculated as

$$\epsilon_{K_{e2}} = \frac{N(Q_1 \wedge E_{10} \wedge TRKLM \wedge T0N)}{N(T0N)}. \quad (6.3)$$

Instead of the K_{e2} trigger information from the Trigger Supervisor, the combination $Q_1 \wedge E_{10} \wedge TRKLM$ (extracted from the PU) is used. It is not possible to use the trigger signals from the Trigger Supervisor for the efficiency measurement. One physical event, e.g. a $K_{\mu3}$ decay, could have been recorded twice. This was caused by time misalignments between the independent trigger chains for charged and neutral particles. This event duplication would lead to an incorrect efficiency.

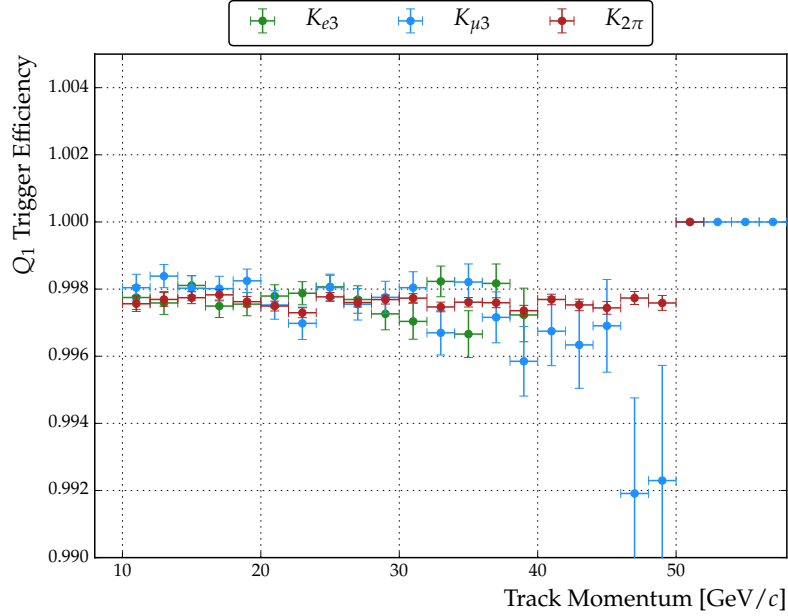
The calculation of the efficiency for the $K_{\mu2}$ trigger is

$$\epsilon_{K_{\mu2}} = \frac{N(Q_1 \wedge TRKLM \wedge T0N)}{N(T0N)}. \quad (6.4)$$

All efficiencies are summarized in Table 17.

TRIGGER	$K_{\mu 3}$	$K_{e 3}$	$K_{2\pi}$
Q_1 [%]	99.77(1)	99.77(1)	99.760(1)
E_{10} [%]	99.999(1)	> 99.999	–
$TRKLM$ [%]	99.75(1)	99.92(1)	99.900(1)
$K_{e 2}$ [%]	99.51(1)	99.69(1)	–
$K_{\mu 2}$ [%]	–	–	99.660(1)
$T0N$ trigger	168 867	217 577	1 929 439

Table 17: Trigger efficiencies for all selections.

6.1 Q_1 SUB-TRIGGER EFFICIENCYFigure 54: Q_1 sub-trigger efficiencies as function of the track momentum.

The Q_1 sub-trigger was released if both layers of one quadrant of the CHOD registered a signal in coincidence. The measured efficiencies are

$$\begin{aligned}
 \epsilon_{Q_1, K_{\mu 3}} &= 99.77(1)\%, \\
 \epsilon_{Q_1, K_{e 3}} &= 99.77(1)\%, \text{ and} \\
 \epsilon_{Q_1, K_{2\pi}} &= 99.760(1)\%.
 \end{aligned}
 \tag{6.5}$$

The efficiencies for all three selections agree well. The track momentum dependent efficiencies are shown in Figure 54. The distributions are flat over the full momentum spectrum. Also all three selections follow each other until 40 GeV/c. At higher momentum the efficiency

for $K_{\mu 3}$ decreases, however, the uncertainties do also increase. The uncertainties of $K_{2\pi}$ data points are smaller as the uncertainties of $K_{\mu 3}$ and K_{e3} data points due to higher statistics caused by higher acceptance and branching fraction.

6.2 E_{10} SUB-TRIGGER EFFICIENCY

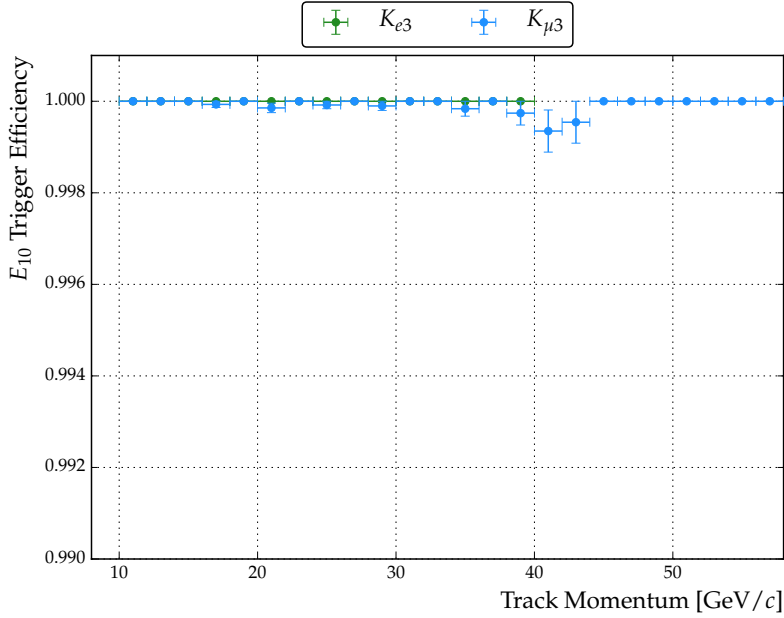


Figure 55: E_{10} sub-trigger efficiencies as function of the track momentum.

The E_{10} sub-trigger was released if more than 10 GeV were deposited in the LKr. The measured efficiencies are

$$\begin{aligned} \epsilon_{E_{10}, K_{\mu 3}} &= 99.999(1)\% \text{ and} \\ \epsilon_{E_{10}, K_{e3}} &> 99.999\% @ 90\% \text{ CL} \end{aligned} \quad (6.6)$$

The E_{10} trigger is fully efficient for K_{e3} . The track momentum dependent efficiencies are shown in Figure 55. The distribution is flat over the full momentum spectrum. The high trigger efficiency is a result of the requirement of $E_{\pi^0} > 15$ GeV in both semileptonic decay selections (Section 5.5 on Page 74.) The $K_{\mu 2}$ trigger used to select the $K_{2\pi}$ selection did not require E_{10} , so it is not taken into account.

6.3 TRKLM SUB-TRIGGER EFFICIENCY

The *TRKLM* trigger was released in case of at least one hit in more than one view and less than 15 hits in any view of DCH₁, DCH₂, and

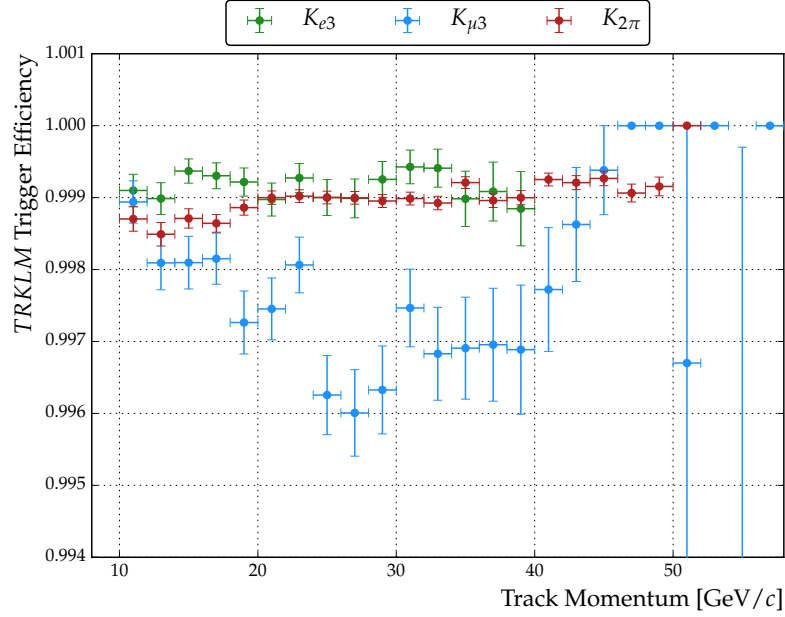


Figure 56: *TRKLM* sub-trigger efficiencies as function of the track momentum.

DCH₄. This trigger rejected events with high activity, e.g. photon conversions in the DCH. The measured efficiencies are

$$\begin{aligned}
 \epsilon_{TRKLM, K_{\mu3}} &= 99.75(1)\%, \\
 \epsilon_{TRKLM, K_{e3}} &= 99.92(1)\%, \text{ and} \\
 \epsilon_{TRKLM, K_{2\pi}} &= 99.9900(1)\%.
 \end{aligned}
 \tag{6.7}$$

Figure 56 shows the momentum dependent sub-trigger efficiency. The trigger is highly efficient for K_{e3} and $K_{2\pi}$. However, for the $K_{\mu3}$ selection the trigger is less efficient. An analysis of the inefficient events shows that they are dominated by $K_{3\pi}^{00}$ events. Figure 40 (a) on Page 86 compared to Figure 56 shows that the momentum distribution of the $K_{3\pi}^{00}$ background follows the trigger inefficiency distribution. The region where the $K_{3\pi}^{00}$ momentum distributions peaks coincides with the most inefficient part of the *TRKLM* efficiency distribution of the $K_{\mu3}$ selection. A possible cause for this behaviour are photon conversions in the DCH. $K_{3\pi}^{00}$ has four photons in the final state which may interact with the DCH. If one of the photons interacts with the DCH, it is possible to reconstruct a π^0 with the remaining three photons. In case of only one π^0 decaying, no π^0 can be reconstructed if one of the two photons interacts with the DCH. This may explain why the trigger inefficiency only affects $K_{3\pi}^{00}$ events.

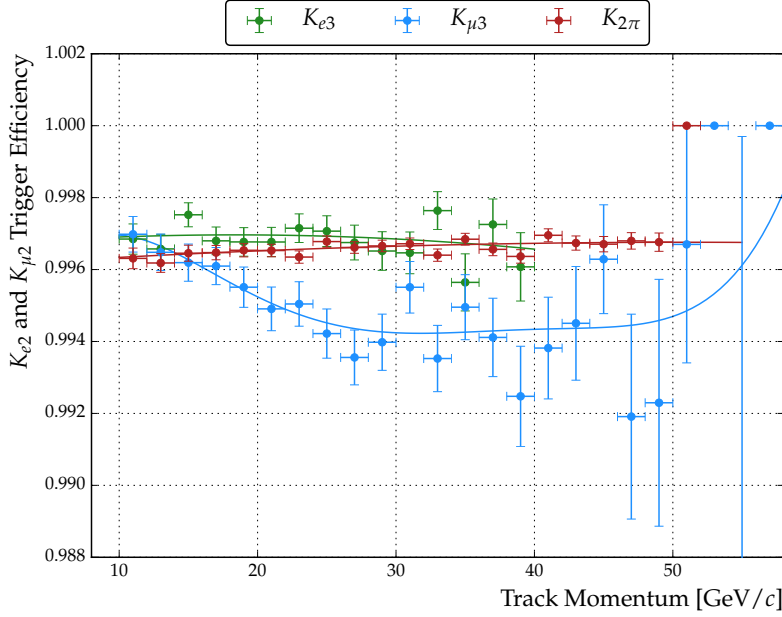


Figure 57: The K_{e2} trigger efficiency is given for the K_{e3} selection (green) and the $K_{\mu3}$ selection (blue). The $K_{\mu2}$ trigger efficiency is given for the $K_{2\pi}$ selection (red). All efficiencies are given as function of the track momentum. The solid lines are polynomial functions with parameters fitted to the efficiency distribution. The functions are used to compute weights for each event. The weights are used to correct data.

6.4 THE K_{e2} AND $K_{\mu2}$ TRIGGER EFFICIENCY

The K_{e2} and $K_{\mu2}$ trigger efficiencies are measured as coincidence between their respective sub-triggers¹. The measured efficiencies are

$$\begin{aligned}
 \epsilon_{K_{e2}, K_{\mu3}} &= 99.51(1)\%, \\
 \epsilon_{K_{e2}, K_{e3}} &= 99.69(1)\%, \text{ and} \\
 \epsilon_{K_{\mu2}, K_{2\pi}} &= 99.660(1)\%.
 \end{aligned} \tag{6.8}$$

The trigger efficiencies for K_{e3} and $K_{2\pi}$ are dominated by the Q_1 sub-trigger whereas for $K_{\mu3}$ it is dominated by the $TRKLM$ sub-trigger. The distributions shown in Figure 57 are fitted with polynomial functions. The functions are used to evaluate a momentum dependent correction weight for each event. This weight is applied to the data during reconstruction.

¹ The efficiencies are not simply the product of the sub-trigger efficiencies due to small time misalignments between the sub-triggers.

TRIGGER	$K_{\mu 3}$	$K_{e 3}$	$K_{2\pi}$
L3- $K_{\mu 3}$ [%]	99.9(1)	-	-
L3- $K_{e 2}$ [%]	-	> 99.999	-
L3- $K_{\mu 2}$ [%]	-	-	> 99.999
<i>autopass</i> trigger	554,460	744,304	42,857

Table 18: L3-filter efficiencies for all selections. The limits are given at 90% CL.

6.5 THE L3-FILTER EFFICIENCY

The efficiency of the L3-filter (Section 2.13.1 on Page 32) is measured with so-called *autopass* events. Such autopass events were written to tape regardless if they passed the L3-filter or not. This applies to 1% of the input to the $K_{e 2}$ and $K_{\mu 3}$ L3-filter and to 2% of the input to the $K_{\mu 2}$ L3-filter. The efficiencies are summarized in Table 18. The L3-filter are highly efficient, thus no further corrections are applied.

SYSTEMATIC UNCERTAINTIES

Systematic effects are all effects that affect the uncertainties of the branching fraction ratios (Section 5.9 on Page 105) which are no direct consequence of the statistical uncertainties of the number of measured candidates in data. Possible sources of systematic uncertainties are investigated by variation of parameters which are affected by these sources inside their 1σ uncertainty. The branching fraction ratios are recomputed and the difference to the central value of the ratios is taken as systematic uncertainty. The systematic effects investigated here are categorized in particle identification, trigger efficiency, the background description, applied corrections, and inputs to MC.

7.1 PARTICLE IDENTIFICATION

Particle identification is achieved through the E/p selection criterion described in Section 5.4 on Page 64. As explained there, it is not possible to directly apply the criterion on MC. The identification efficiencies are measured from data and applied as weights on MC as a function of the track momentum. These weights are computed for each event using a polynomial function. The parameters of the function are fitted to the measured efficiencies. The systematic effects are investigated by varying the weights w between $w \pm \sigma_w$. The uncertainty of each weight is computed taking into account the correlation between the fitted parameters. Let V be the covariance matrix of the fit parameters and J the Jacobian matrix of the fit function, then

$$Z = J \cdot V \cdot J^T. \quad (7.1)$$

The uncertainty on the respective weight σ_w is

$$\sigma_w = \sqrt{(\text{diag}(Z))}. \quad (7.2)$$

Each variation of the weights is performed independently for μ and e identification and for $\pi \rightarrow \mu$ and $\pi \rightarrow e$ misidentification. The mean difference $\Delta r = 0.5 \cdot |(r_{w+\sigma_w} - r_{w-\sigma_w})|$ between the central value r_w and the results for $\pm 1\sigma_w$ variation are summarized in Table 19.

7.2 TRIGGER

The trigger efficiency distributions (Figure 57 on Page 111) have been fitted with polynomials. These are used to compute weights for each event as a function of the track momentum. These weights are applied to the data only. The systematic effect of the trigger correction

is estimated by the same procedure as described in Section 7.1 for the particle identification. The obtained systematic uncertainties are presented in Table 19.

7.3 BACKGROUND ESTIMATION

The background estimation is important to correct the selected data candidates. The estimation relies on MC by simulating possible background decays. The background is normalized to data using the computed kaon flux and eventually subtracted from the data candidates. A possible source of a systematic effect is under- or overestimated background contamination. The data/MC distributions are not flat for all variables used as selection criteria, thus the background estimation may depend on the chosen selection criterion. The impact of these choices is studied by loosening or removing the respective selection criteria and thus increasing the background fraction. This is done separately for the $K_{\mu 3}$, $K_{e 3}$, and $K_{2\pi}$ selections. The systematic uncertainties are summarized in Table 19.

7.3.1 Background in $K_{\mu 3}$

The dominant background of $K_{\mu 3}$ events are $K_{3\pi}^{00}$ decays, thus the focus on the systematic uncertainties for $K_{\mu 3}$ is on them. It is difficult to remove pions because the E/p selection criterion (Section 5.4.1 on Page 64) is inefficient in discriminating muons and pions. Furthermore, no dedicated muon veto detector is available. In contrast to the $K_{2\pi}$ background, it is not possible to take advantage of different kinematics of two-body and three-body decays. However, additional $K_{3\pi}^{00}$ suppression is achieved through selection criteria on the missing mass m_{miss}^2 and the additional energy in the LKr. To estimate the possible systematics due to $K_{3\pi}^{00}$ background, the following selection criteria to suppress pions are removed or loosened simultaneously. The following changes are applied:

- The E/p criterion is changed from $E/p < 0.1$ to $E/p < 0.9$. This allows more pions into the selection but still rejects electrons. The new E/p criterion requires the change of the $L2/L3$ trigger chain from $K_{e2}/K_{\mu 3}$ to $K_{\mu 2}/K_{\mu 2}$. It is required because the $L3$ -filter $K_{\mu 3}$ uses an $E/p < 0.3$ criterion (Table 8 on Page 33). The newly used trigger chain is downscaled by a factor 150.
- The selection criterion on additional energy in the LKr is removed (Section 5.6.7 on Page 99).
- The selection criterion on the missing mass m_{miss}^2 (Section 5.6.3 on Page 87) is loosened to $MM^2 < 0.06 \text{ GeV}^2/c^4$.

The changes to the selection criteria on the additional energy in the LKr and the missing mass allow more events from regions with bad data/MC agreement to be included into the selection. This takes the badly described regions into account and reflects them in the systematic uncertainty on the background.

The trigger efficiency is recomputed for the modified selection. The inefficiency of the sub-trigger $TRKLM$ for $K_{3\pi}^{00}$ events is discussed in Section 6.3 on Page 109. The modified selection accepts more $K_{3\pi}^{00}$ events. Hence, the trigger efficiency of the sub-trigger is reduced. The computation of the new efficiency yields $\epsilon_{TRKLM} \approx 98\%$. The newly computed efficiency is applied as correction to the data.

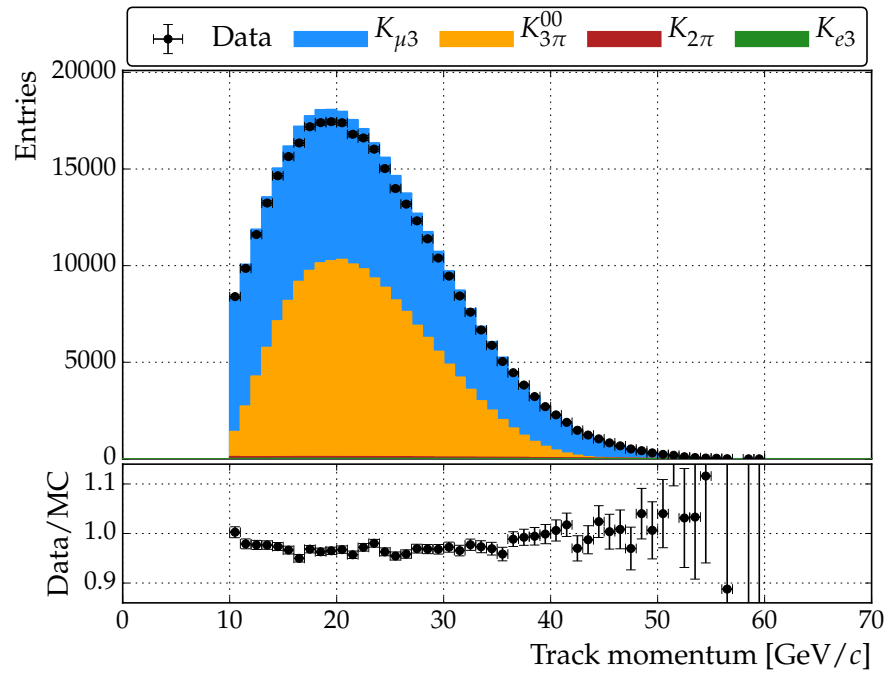
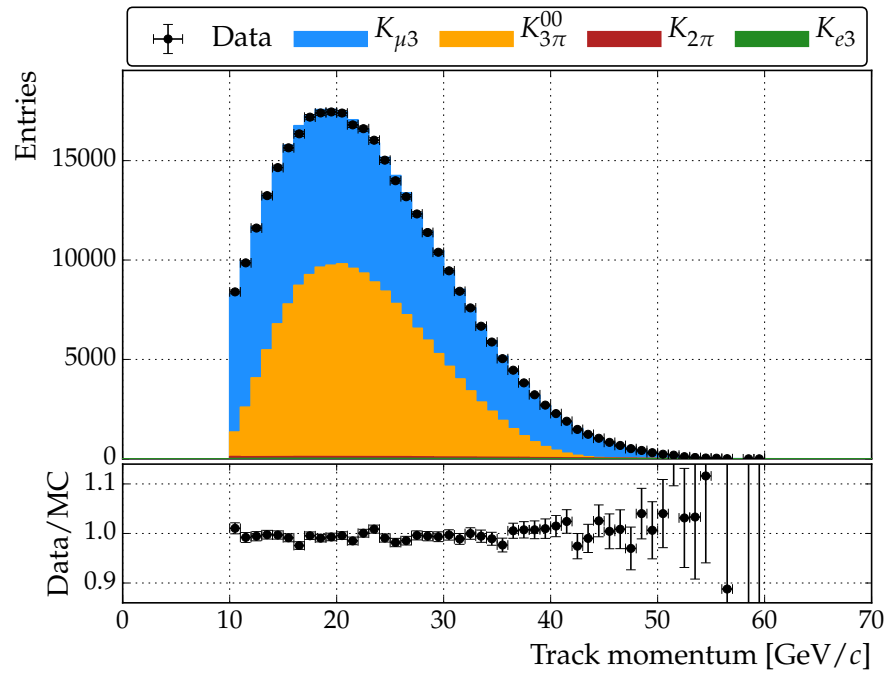
Figure 58 (a) shows the track momentum distribution with the modified $K_{\mu 3}$ selection and new trigger efficiency correction. The disagreement between data and MC is about 5% and follows the shape of the $K_{3\pi}^{00}$ MC distribution. By scaling the $K_{3\pi}^{00}$ MC by a factor $s = 0.95$ the data/MC distributions becomes flat. The corresponding plot is presented in Figure 58 (b). The branching fraction ratios are recomputed with new background estimated obtained with $K_{3\pi}^{00}$ MC scaled by $s = 0.95$. The difference to the unscaled branching fraction ratios is taken as systematic uncertainty. The values are presented in Table 19.

7.3.2 Background in K_{e3}

The uncertainties on the two background channels $K_{2\pi}$ and $K_{3\pi}^{00}$ are evaluated in two steps. For the first step, more $K_{2\pi}$ background is allowed by removing the selection criterion on the kaon mass (Section 5.6.6 on Page 91) from the selection. Figure 50 (a) on Page 100 shows the distribution $M(K) - M(\text{Track} + \pi^0)$ without the applied selection criterion. The $K_{2\pi}$ background peak is underestimated by MC by about 10%. Figure 59 shows the same distribution with the $K_{2\pi}$ background scaled by a factor $s = 1.1$.

For the second step, more $K_{3\pi}^{00}$ background is allowed by making similar changes to selection as to the $K_{\mu 3}$ selection in Section 7.3.1:

- The E/p selection criterion is changed to $E/p > 0.1$. This allows more pions into the selection but still rejects muons. This change requires to use instead of the L2/L3 trigger chain K_{e2}/K_{e2} the chain $K_{\mu 2}/K_{\mu 2}$ because the L3-filter K_{e2} uses the criterion $E/p > 0.6$ (Table 8 on Page 33). The newly used trigger chain is down-scaled by a factor 150.
- The selection criterion on additional energy in the LKr is removed (Section 5.6.7 on Page 99).
- The selection criterion on the missing mass (Section 5.6.3 on Page 87) is loosened to $MM^2 < 0.06 \text{ GeV}^2/c^4$.

(a) Modified $K_{\mu 3}$ selection which allows more $K_{3\pi}^{00}$ background.(b) Modified $K_{\mu 3}$ selection which allows more $K_{3\pi}^{00}$ background. The $K_{3\pi}^{00}$ background MC is scaled with factor $s = 0.95$.Figure 58: Track momentum distribution of the modified $K_{\mu 3}$ selection.

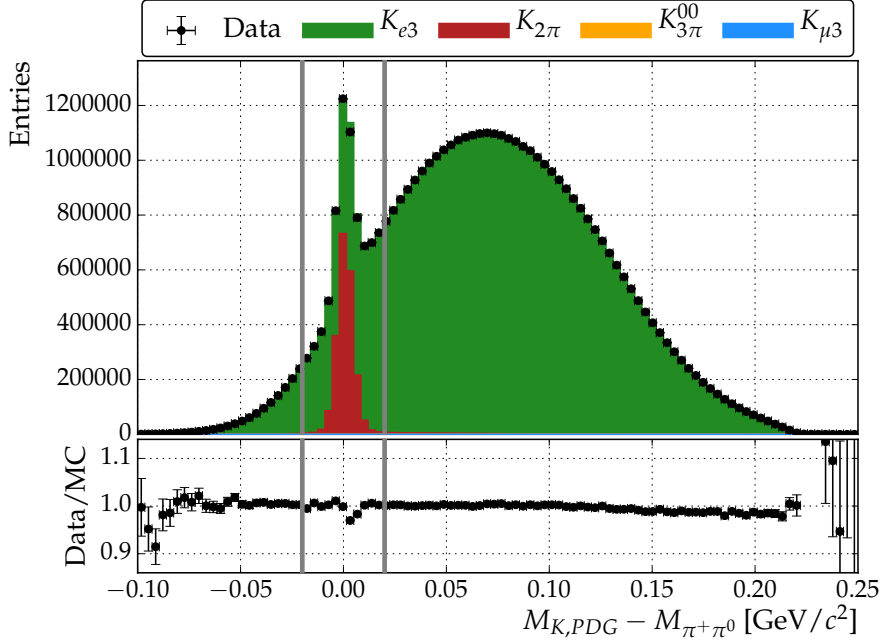


Figure 59: Modified K_{e3} selection. The $K_{2\pi}$ background MC is scaled by factor $s_{K_{2\pi}} = 1.1$.

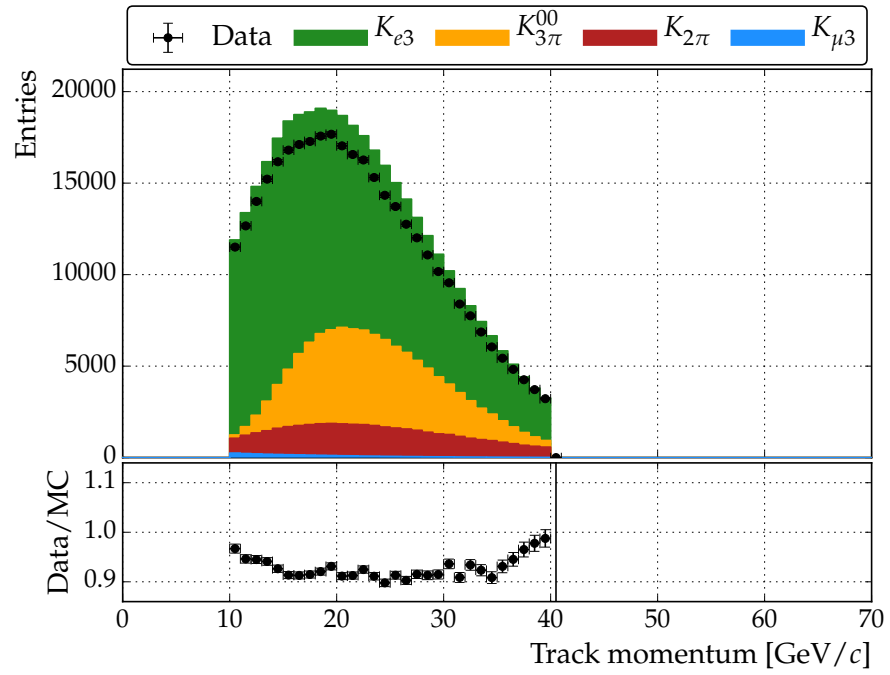
The trigger correction is recomputed due to the larger $K_{3\pi}^{00}$ background contamination and applied to the data. Figure 60 (a) shows the track momentum distribution with the modified K_{e3} selection. Figure 60 (b) shows the same variable with the $K_{2\pi}$ and $K_{3\pi}^{00}$ backgrounds scaled by factors $s_{K_{2\pi}} = 1.1$ and $s_{K_{3\pi}^{00}} = 0.8$, respectively. The $K_{2\pi}$ background scaling is kept to the value determined at the first step.

The scaled backgrounds are used to recompute the branching fraction ratios, the difference to the nominal ratio is taken as systematic uncertainty. The impact on the central values are summarized in Table 19. The systematic effects are small due to the very small background contamination of the K_{e3} candidates.

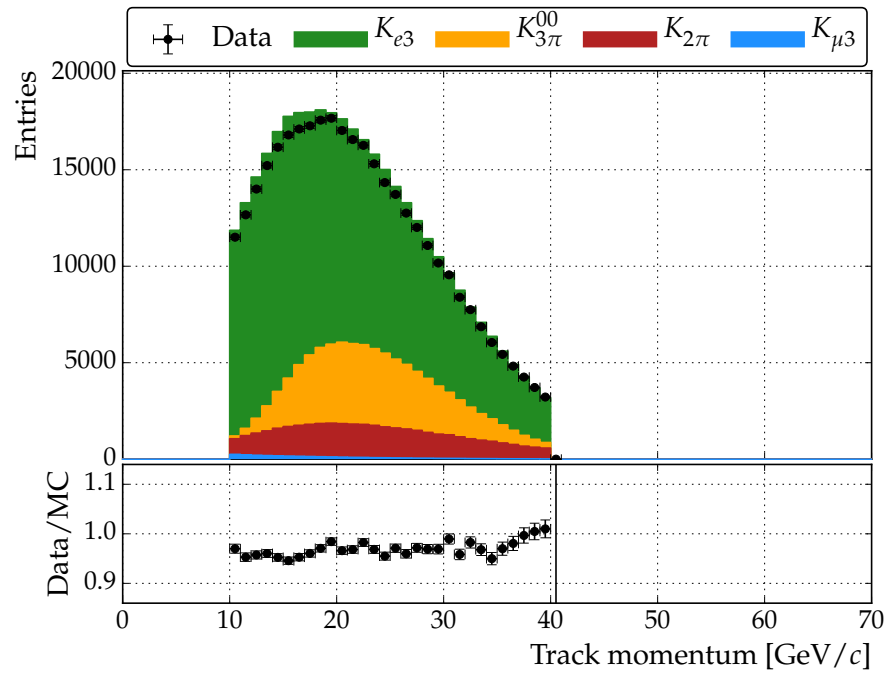
7.3.3 Background in $K_{2\pi}$

The dominant background in the $K_{2\pi}$ selection are $K_{\mu 3}$ decays. This background could be reduced by tightening the selection criterion on the transversal momenta¹ of track and π^0 . However, a tighter selection criterion would also remove a subset of events affected by the kaon halo correction (Section 7.4.2 on Page 121). To keep the impact

¹ Section 5.6.4 on Page 87. Figure 45 on Page 94 and Figure 46 on Page 95 show the relevant distributions. A tighter selection criterion means here to shift the selection criterion along the transversal momentum axis towards positive values. This is equivalent to decrease the offset parameter described in Section 5.6.4.



(a) Modified K_{e3} selection which allows more $K_{2\pi}$ and $K_{3\pi}^{00}$ background.



(b) Modified K_{e3} selection which allows more $K_{2\pi}$ and $K_{3\pi}^{00}$ background. The $K_{\mu 3}$ and $K_{3\pi}^{00}$ background MC are scaled with factors $s_{K_{2\pi}} = 1.1$ and $s_{K_{3\pi}^{00}} = 0.8$.

Figure 60: Track momentum distribution of the modified K_{e3} selection.

of the kaon halo correction small, more background is allowed in the $K_{2\pi}$ selection.

The systematic effect of the background to $K_{2\pi}$ is estimated by a modified $K_{2\pi}$ selection. The selection criteria on

- the kaon mass and
- the transversal momenta of track and π^0

are removed. The tails of both distributions are included in the modified $K_{2\pi}$ selection. This modified selection allows more $K_{\mu 3}$ and $K_{3\pi}^{00}$ background. Both backgrounds are three-body decays which is the key property to reduce background for $K_{2\pi}$.

Figure 61 (a) shows the π^0 momentum distribution selected with the modified $K_{2\pi}$ selection. The π^0 momentum distribution shows a signal free region below 20 GeV/c. This makes it a perfect region to study the background description. The data in the signal free region is poorly described by MC. The background MC is scaled until the data/MC distribution is flat. The obtained scale factor for both background MC distributions is $s = 0.92$. Figure 61 (b) shows the π^0 momentum distribution with scaled background. The systematic uncertainty is computed analogously to Section 7.3.1. The impact on the central value is summarized in Table 19.

7.4 CORRECTIONS

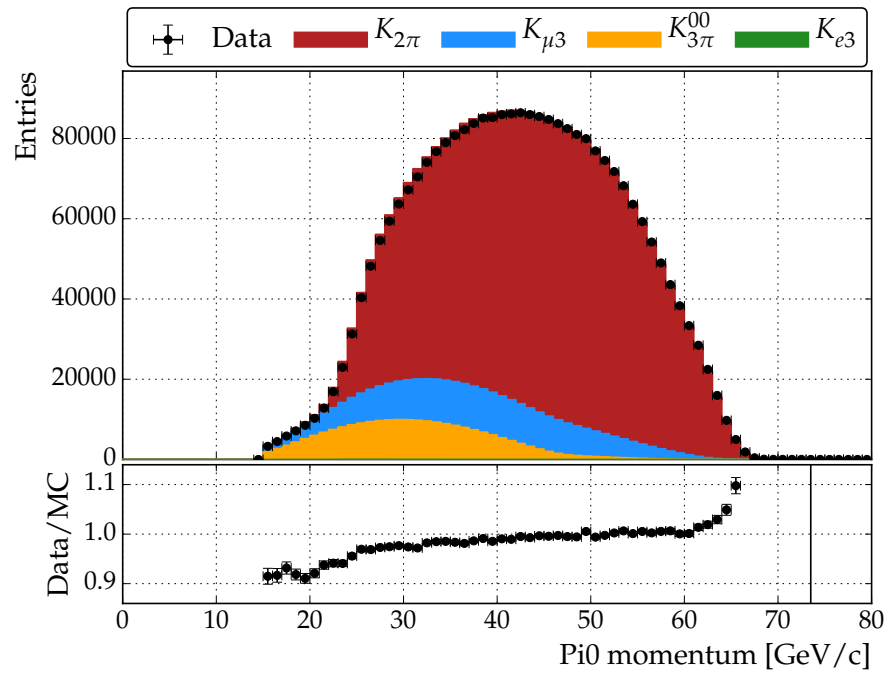
7.4.1 Width of the kaon momentum distribution

The width of the kaon momentum distribution needs a correction in MC (Section 4.5.1 on Page 50). The uncorrected and corrected momentum spectra are shown in Figure 17 on Page 51. The correction depends on the parameters b_1 and b_2 (Equation 4.12 on Page 50) which values were determined for the $R_K = \Gamma(K_{e2})/\Gamma(K_{\mu 2})$ analysis with $K^+ \rightarrow \pi^+ \pi^+ \pi^-$ decays [61]. For the systematic effects study, the impact of each parameter is treated separately.

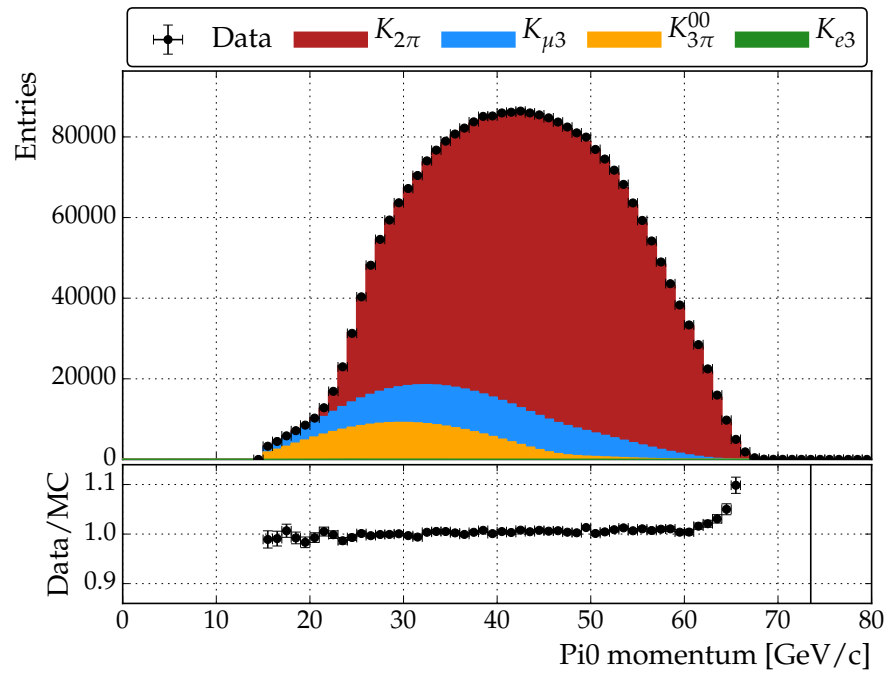
The parameter b_1 is time and true momentum independent. It represents a 1st order correction. The same parameter has been evaluated with fits to the $p_{\text{track}} + p_{\pi^0}$ distribution of the $K_{2\pi}$ selection and yielded $b_{1,K_{2\pi}} = 0.0740 \pm 0.0004$. Taking this value and $b_{1,K^+ \rightarrow \pi^+ \pi^+ \pi^-} = 0.07$ into account, the systematic effect is conservatively estimated by varying $b_1 = 0.07 \pm 0.01$.

The systematic effect of the time and true momentum dependent parameter b_2 is estimated to be the difference between the results with and without using the parameter.

The obtained systematic uncertainties are presented in Table 19.



(a) Modified $K_{2\pi}$ selection which allows more $K_{\mu 3}$ and $K_{3\pi}^{00}$ background.



(b) Modified $K_{2\pi}$ selection which allows more $K_{\mu 3}$ and $K_{3\pi}^{00}$ background. The $K_{\mu 3}$ and $K_{3\pi}^{00}$ background MC are both scaled with a factor $s = 0.92$.

Figure 61: π^0 momentum distribution of modified the $K_{2\pi}$ selection.

7.4.2 Kaon halo

The correction to the kaon halo (Section 4.5.2 on Page 52) added MC events with stronger scattered kaons. The selection criteria for $K_{2\pi}$ (Section 5.6.4 on Page 87) are chosen to include those events to minimise the effect of the correction on the final result. The effect of the correction on p and p_t of track and π^0 is presented in Figure 47 on Page 96 and in Figure 48 on Page 97, respectively. The systematic uncertainty is estimated as the difference between the central values of the branching fraction ratios and the recomputed values without the correction. The uncertainties are presented in Table 19.

7.4.3 Detector corrections

The corrections applied due to detector effects described in Section 3.6 on Page 41 and in Section 4.5.3 on Page 52 have an impact on the computed branching fraction ratios. A very conservative approach is taken to evaluate the systematic uncertainties on these effects. The difference between the branching fraction ratios computed with and without detector corrections is taken as systematic uncertainty. If the correction is applied to the data and MC, the correction is removed in both. The effects on the branching fraction ratios are summarized in Table 19. Most of the corrections have no effect at all on the final ratios: Either the corrections are too small to make a change or they modify nominator and denominator in the same way. The biggest impact is represented by the LKr non-linearity correction on $\frac{\text{Br}(K_{\mu 3})}{\text{Br}(K_{e 3})}$. However, this systematic uncertainty is still at the level of the statistical uncertainty.

7.5 MC PROPERTIES

7.5.1 Form Factors in MC

Following the description in Section 4.2 on Page 46, the decays of $K_{\mu 3}$ and $K_{e 3}$ are simulated in MC. The form factors describe the kinematics of the three-body decays. So the acceptance of the decays depends on the form factors used in MC. New Monte Carlo samples are produced to estimate the impact of form factors on the computed ratios. Two new samples are produced for $K_{e 3}$ with varying $\Lambda_+ \pm \sigma_{\Lambda_+}$. Four new samples are produced for $K_{\mu 3}$. Two for each parameter $\Lambda_+ \pm \sigma_{\Lambda_+}$ and $\ln C \pm \sigma_{\ln C}$. The correlation between Λ_+ and $\ln C$ is $\rho = -0.33$. The correlation is taken into account to compute the combined uncertainty for $K_{\mu 3}$ as described in Equation 7.1. For each of these samples, $190 \cdot 10^6$ decays have been simulated. The obtained mean differences to the central value of the ratios are summarized in Table 19.

The impact of the variation of the form factors on $\frac{\text{Br}(K_{\mu 3})}{\text{Br}(K_{2\pi})}$ is about five times larger than the statistical uncertainty. On $\frac{\text{Br}(K_{\mu 3})}{\text{Br}(K_{e3})}$ it is about nine times larger. It is the dominating uncertainty on these measurements. This implies that future improvements of the branching fraction measurement are heavily dependent on external, more precise measurements of the semileptonic form factors. The large effects are a result of the large impact on the $K_{\mu 3}$ decay.

On the other hand, for $\frac{\text{Br}(K_{e3})}{\text{Br}(K_{2\pi})}$ the impact is smaller than the statistical uncertainty. The reason for the different impact of the form factor variation on $K_{\mu 3}$ and K_{e3} is assumed to be the dependence of the form factors on the mass of the lepton as described in Equation 1.45 on Page 14.

7.5.2 Radiative processes in K_{e3}

Radiative processes are very important for K_{e3} due to the small mass of the electron. A very good description of internal and external bremsstrahlung effects in MC is needed to correctly estimate the acceptance of the decay. The generator developed by the KLOE collaboration [55] is used to simulate the K_{e3} decay. It simulates internal bremsstrahlung and creates one additional photon which is handed over to the Geant3 simulation framework. The Geant3 framework takes care of external bremsstrahlung effects in detector material. The bremsstrahlung effects have been tested and the results are presented in Figure 62 which shows the cluster energy spectrum in the LKr. The clusters are required to be within 5 cm from the extrapolated impact point of the electron. The bending caused by the dipole magnet is intentionally not included in the extrapolation. It is assumed that the clusters originate from photons created during the decay in a small angle by external bremsstrahlung in the detector material before the spectrometer magnet. The bin below 0 GeV contains events with no such cluster. The description of the data by MC is very good over a range of seven orders of magnitude and shows a good handling of the radiative processes.

The impact of the description of the inner bremsstrahlung in the decay generator on the measured branching fractions is estimated. From [55, Table 1], a $\sigma_{\text{Gen}} = 3\%$ systematic uncertainty on the generator itself is derived. A weight w_{rad} [62] is computed to evaluate the impact of the systematic uncertainty of the generator on the final ratios. Therefore, the ratio

$$R = \frac{D_R}{D_0} \quad (7.3)$$

is computed. Here D_R is the value of the radiative corrected Dalitz density distribution for a respective event and D_0 is the value for the uncorrected Dalitz value. The distribution of R is presented in Fig-

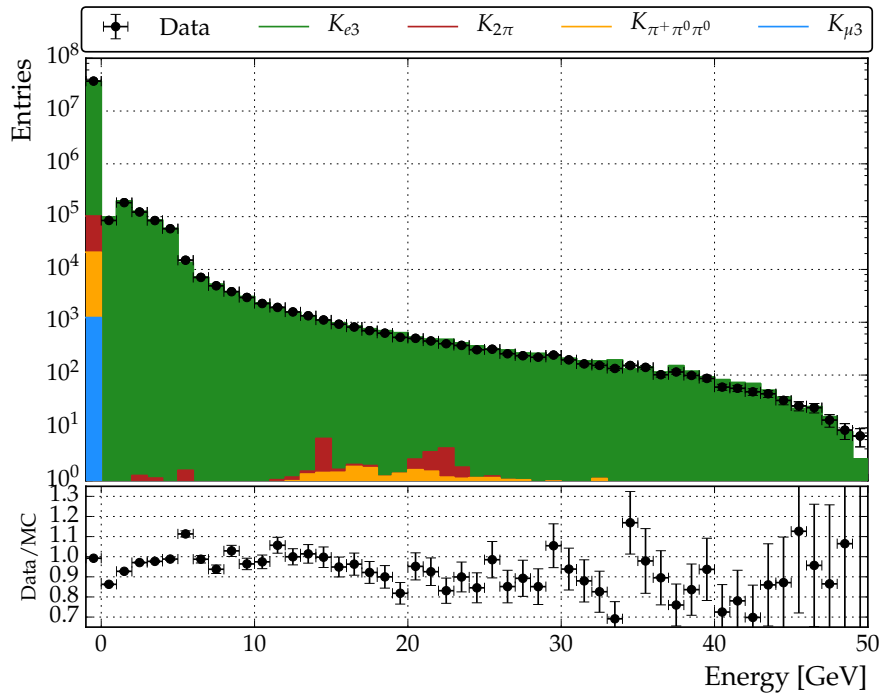


Figure 62: Distribution of cluster energy. Only the clusters with energies above 0 GeV and in a distance of 5 cm of the extrapolated impact point of the track are shown. The bin below 0 GeV represents events in which no cluster with the given requirements on energy and position were found.

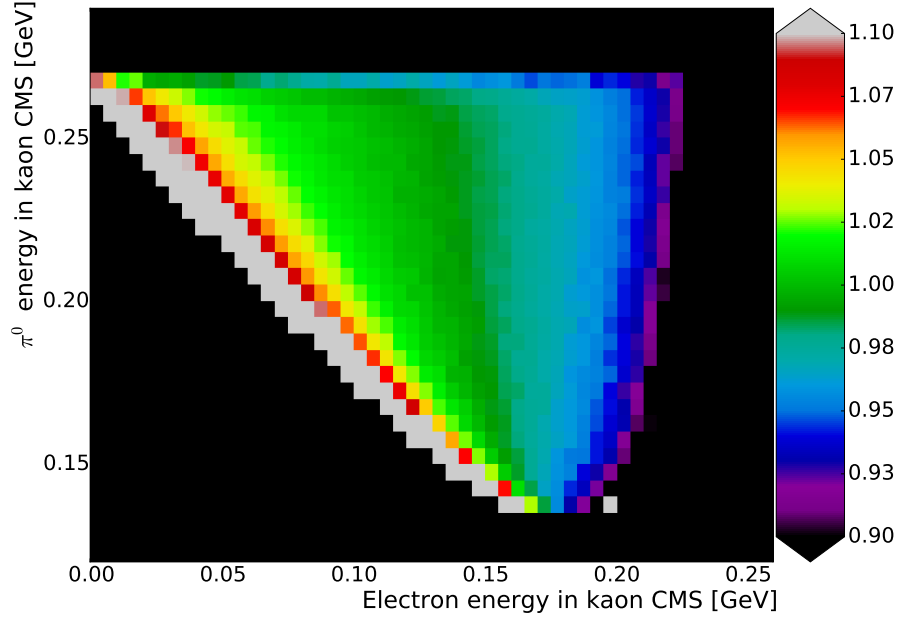


Figure 63: Distribution of the ratio R between the K_{e3} Dalitz plots with and without radiative corrections. Each of both samples consists of one billion events.

Figure 63. It is obtained by division of the Dalitz density distribution generated with the KLOE generator (D_R) by the Dalitz density distribution with a generator without any radiative corrections (D_0). So one can write

$$D_R = D_0 \cdot R = D_0 \cdot (1 + R - 1) = D_0 \cdot (1 + \Delta). \quad (7.4)$$

$\Delta = R - 1$ is a relative radiative correction to the uncorrected Dalitz density distribution. This relative correction is scaled with σ_{Gen} so that

$$w_{\text{rad}} = \frac{1 + \Delta \cdot \sigma_{\text{Gen}}}{1 + \Delta}. \quad (7.5)$$

For each event, R is read from the distribution in Figure 63 and w_{rad} is applied as weight on the K_{e3} MC. The ratios $\frac{\text{Br}(K_{e3})}{\text{Br}(K_{2\pi})}$ and $\frac{\text{Br}(K_{\mu 3})}{\text{Br}(K_{e3})}$ are recomputed and the difference to the central value taken as systematic uncertainty on the ratios. The uncertainties are presented in Table 19. Both values are smaller than the statistical uncertainty. The systematic uncertainty in the generator $\sigma_{\text{Gen}} = 3\%$ is too small to have a significant impact on the measured branching fractions.

7.6 SUMMARY

Table 19 shows the central values, the statistical uncertainties for data and MC, the contributions to the systematic uncertainties discussed

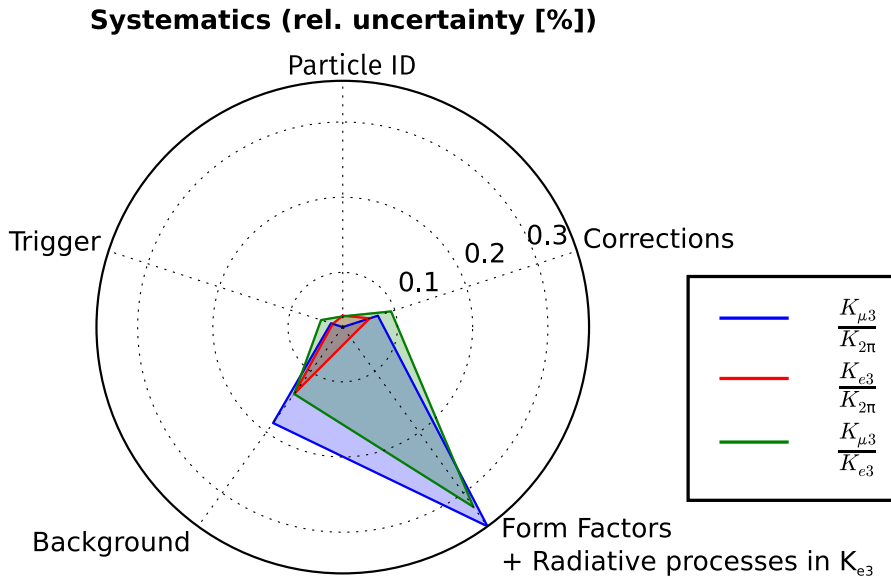


Figure 64: Systematic uncertainties shown in a radar chart. Each circle indicates 0.1 %. Each line represents the relative uncertainty of the systematic uncertainty taken from Table 19. The domination of form factors and background estimation are clearly demonstrated.

in this chapter, and the total uncertainties.. The statistical uncertainty of the MC is categorized as systematic uncertainty because its value is limited by the available computing time for the simulation.

The branching fraction ratio measurements are completely dominated by systematic effects which was expected due to the very large amount of signal candidates which lead to a very small statistical uncertainty. These systematic effects are dominated by the uncertainties in the background estimation and the form factor input to the MC. To improve the uncertainties on the background systematics, a deeper analysis of the MC is needed as a first step. Depending on the results either further corrections to the MC or no further improvements are possible to the CMC framework. However, this deeper analysis only makes sense if better values for the semileptonic form factors become available. New measurements of the semileptonic form factors would directly improve the systematic uncertainties and could reduce them to the same magnitude as the background estimation.

In addition to Table 19, the systematic uncertainties are presented in a radar chart in Figure 64.

$[10^{-5}]$	$\frac{\text{BR}(K_{\mu 3})}{\text{BR}(K_{2\pi})}$	$\frac{\text{BR}(K_{e3})}{\text{BR}(K_{2\pi})}$	$\frac{\text{BR}(K_{\mu 3})}{\text{BR}(K_{e3})}$
Central value	16066	24320	66061
Data statistical	12	17	17
MC statistical	5	7	20
Particle identification			
μ -ID	1	–	5
e -ID	–	9	23
$\pi \rightarrow \mu$ -mis-ID	3	–	14
$\pi \rightarrow e$ -mis-ID	3	5	0
Trigger	7	10	38
Background estimation			
$K_{\mu 3}$ background	21	0	90
K_{e3} background	0	3	10
$K_{2\pi}$ background	21	33	0
Corrections			
MC: Momentum width parameter b_1	1	1	1
MC: Momentum width parameter b_2	7	10	4
MC: Kaon halo	9	7	57
DCH misalignment and ...			
... magnetic field miscalibration	0	0	0
DCH-LKr mis-alignment	4	8	5
LKr projectivity	0	0	1
LKr non-linearity	2	6	25
LKr cell-by-cell	0	0	1
MC: Form factors inputs			
$\Lambda_+ \pm \sigma_{\Lambda_+}$	57	10	210
$\ln C \pm \sigma_{\ln C}$	7	–	27
Combined	55	10	204
MC: Inner bremsstrahlung ...			
... process in K_{e3}	–	4	10
Total systematics	66	41	245
Total uncertainty	70	44	246
Relative total uncertainty [%]	4	2	4

Table 19: Central values and overview of uncertainties.

RESULTS AND DISCUSSION

8.1 BRANCHING FRACTIONS

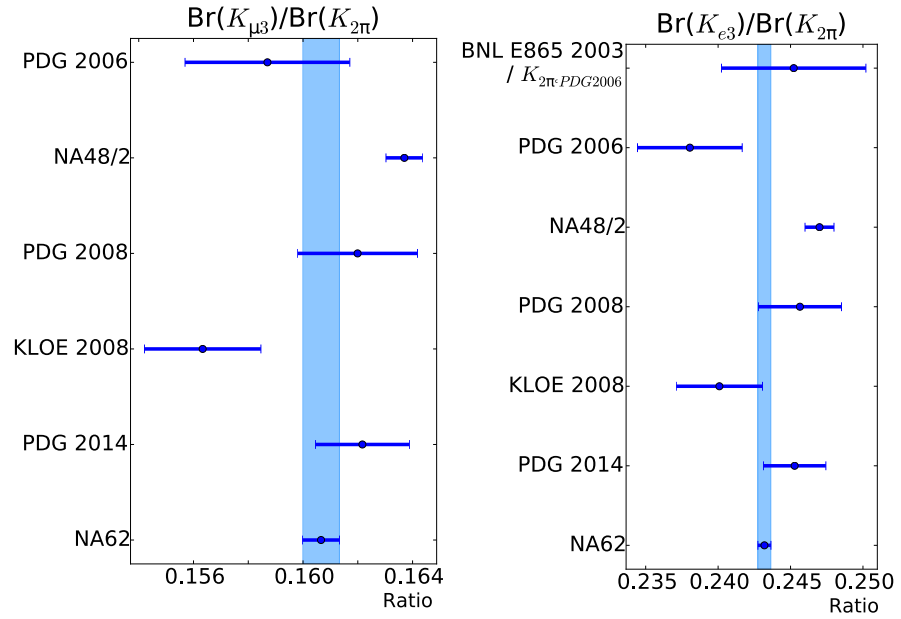
The final results for the branching fraction ratios are

$$\begin{aligned} \frac{\text{Br}(K_{\mu 3})}{\text{Br}(K_{2\pi})} &= 0.16066(12)_{\text{stat.}}(66)_{\text{syst.}} \\ &= 0.1607(7), \end{aligned} \quad (8.1)$$

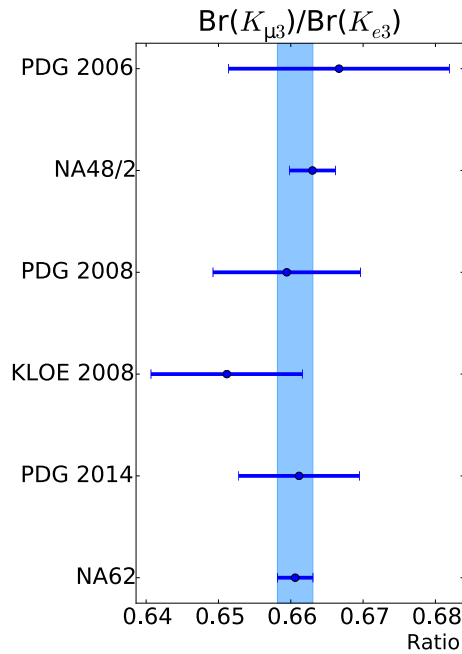
$$\begin{aligned} \frac{\text{Br}(K_{e3})}{\text{Br}(K_{2\pi})} &= 0.24320(17)_{\text{stat.}}(41)_{\text{syst.}} \\ &= 0.2432(4), \text{ and} \end{aligned} \quad (8.2)$$

$$\begin{aligned} \frac{\text{Br}(K_{\mu 3})}{\text{Br}(K_{e3})} &= 0.66061(17)_{\text{stat.}}(245)_{\text{syst.}} \\ &= 0.6606(25). \end{aligned} \quad (8.3)$$

These results are the combination of Equation 5.13, 5.14, and 5.15 on Page 105, and the systematic uncertainties summarized in Table 19 on Page 126. They represent the most precise measurement of these quantities at the current time. An unprecedented statistical precision is reached and the measurement is dominated by systematic effects. The reached precision is 0.2 % for $\frac{\text{Br}(K_{e3})}{\text{Br}(K_{2\pi})}$ and 0.4 % for $\frac{\text{Br}(K_{\mu 3})}{\text{Br}(K_{2\pi})}$ and $\frac{\text{Br}(K_{\mu 3})}{\text{Br}(K_{e3})}$. Figure 65 compares these results with world averages of the Particle Data Group from 2006 [64], 2008 [65], and 2014 [11]. Furthermore, the results are compared with the most recent single measurements from BNL E865 in 2003 [66], KLOE in 2008 [67], and NA48/2 in 2007 [68][69]. The single measurements are included in the world averages. The NA48/2 result had a large impact on the world averages. The new NA62 results agree with the world averages. The value of $\frac{\text{Br}(K_{\mu 3})}{\text{Br}(K_{2\pi})}$ lies between the results obtained by KLOE and NA48/2. The $\frac{\text{Br}(K_{e3})}{\text{Br}(K_{2\pi})}$ value agrees with the results of BNL E865 and KLOE but not with the NA48/2 result. The semileptonic ratio $\frac{\text{Br}(K_{\mu 3})}{\text{Br}(K_{e3})}$ agrees with all cited measurements. The most precise recent result is the measurement from NA48/2. The NA48/2 data set was recorded three years before the data set used in this analysis. The same detector was used,



(a) The ratio $\frac{\text{Br}(K_{\mu 3})}{\text{Br}(K_{2\pi})}$ is shown on the left side, the ratio $\frac{\text{Br}(K_{e 3})}{\text{Br}(K_{2\pi})}$ on the right



(b) The ratio $\frac{\text{Br}(K_{\mu 3})}{\text{Br}(K_{e 3})}$.

Figure 65: The final results of the ratios of this analysis are labeled NA62 and are compared with world averages and previous measurements. The light blue band indicates the full uncertainty on the results of this analysis. The world averages are the results of the Particle Data Group from 2006 [64], 2008 [65], and 2014 [11]. The previous results are from BNL E865 in 2003 [66] (divided by $\text{Br}(K_{2\pi})$ from PDG2006), KLOE in 2008 [67], and NA48/2 in 2007 [68][69].

however, the run and detector conditions were different. The results published in [68][69] are

$$\begin{aligned} \frac{\text{Br}(K_{\mu 3})}{\text{Br}(K_{2\pi})}(\text{NA48}/2) &= 0.1637(9)_{\text{stat.}}(4)_{\text{syst.}} \\ &= 0.1637(10), \end{aligned} \quad (8.4)$$

$$\begin{aligned} \frac{\text{Br}(K_{e3})}{\text{Br}(K_{2\pi})}(\text{NA48}/2) &= 0.2470(9)_{\text{stat.}}(4)_{\text{syst.}} \\ &= 0.2470(10) \text{ and} \end{aligned} \quad (8.5)$$

$$\begin{aligned} \frac{\text{Br}(K_{\mu 3})}{\text{Br}(K_{e3})}(\text{NA48}/2) &= 0.663(3)_{\text{stat.}}(1)_{\text{syst.}} \\ &= 0.663(3). \end{aligned} \quad (8.6)$$

The candidate sample consisted of $87 \cdot 10^3 K_{e3}^{\pm}$, $77 \cdot 10^3 K_{\mu 3}^{\pm}$, and $718 \cdot 10^3 K_{2\pi}^{\pm}$ candidates. In contrast to the results of the NA62 analysis, the NA48/2 results are dominated by statistical uncertainties. However, the systematic uncertainties of both analyses are in same order of magnitude. The total uncertainties of the NA62 results are smaller compared to the NA48/2 results due to the significant lower statistical uncertainties of the NA62 result. The values of $\frac{\text{Br}(K_{\mu 3})}{\text{Br}(K_{2\pi})}$ and $\frac{\text{Br}(K_{e3})}{\text{Br}(K_{2\pi})}$ do not agree but the values of $\frac{\text{Br}(K_{\mu 3})}{\text{Br}(K_{e3})}$ do. This indicates that the $K_{2\pi}$ measurement is the reason for the disagreement. The cause for the disagreement in the $K_{2\pi}$ measurements is not known.

8.2 $|V_{us}|$ AND CKM MATRIX UNITARITY

The obtained results for $\frac{\text{Br}(K_{\mu 3})}{\text{Br}(K_{2\pi})}$ and $\frac{\text{Br}(K_{e3})}{\text{Br}(K_{2\pi})}$ are multiplied with $\text{Br}(K_{2\pi}) = 20.67 \pm 0.08\%$ [11]. The obtained semileptonic branching fractions read

$$\begin{aligned} \text{Br}(K_{\mu 3}) &= 3.321(14)_{\text{NA62}}(13)_{\text{external}} \% \\ &= 3.321(19) \% \text{ and} \end{aligned} \quad (8.7)$$

$$\begin{aligned} \text{Br}(K_{e3}) &= 5.027(09)_{\text{NA62}}(19)_{\text{external}} \% \\ &= 5.027(22) \%. \end{aligned} \quad (8.8)$$

The *external* uncertainty is the propagated uncertainty of $\text{Br}(K_{2\pi})$. The current world averages $\text{Br}(K_{\mu 3})_{\text{PDG}} = 3.352(33)\%$ and $\text{Br}(K_{e3})_{\text{PDG}} = 5.07(4)\%$ [11] agree with the results of this work. The uncertainties are approximately a factor of two smaller than the of the world average.

With the newly computed semileptonic branching fractions it is possible to extract the CKM matrix element $|V_{us}|$ by using Equation 1.30

(Page 12), the parameters given in Tables 4 (Page 12) and 5 (Page 12), and the measured branching fraction given in Equation 8.7 and 8.8. The obtained values are

$$\begin{aligned} |V_{us}|_{K_{\mu 3}} \cdot f_+^{K^0 \pi^-}(0) &= 0.2146(4)_{\text{NA62}(10)_{\text{external}}} \\ &= 0.2146(11) \text{ and} \end{aligned} \quad (8.9)$$

$$\begin{aligned} |V_{us}|_{K_{e 3}} \cdot f_+^{K^0 \pi^-}(0) &= 0.2149(2)_{\text{NA62}(10)_{\text{external}}} \\ &= 0.2149(10). \end{aligned} \quad (8.10)$$

The NA62 and the *external* uncertainties are the propagated uncertainties of the branching fraction ratio measurements and of the remaining input parameters, respectively. The Particle Data Group provides averages for both decay $K_{\ell 3}^{\pm}$ channels [70] [11],

$$|V_{us}|_{K_{\mu 3}, \text{PDG}} \cdot f_+^{K^0 \pi^-} = 0.2158(13) \text{ and} \quad (8.11)$$

$$|V_{us}|_{K_{e 3}, \text{PDG}} \cdot f_+^{K^0 \pi^-} = 0.2160(11). \quad (8.12)$$

The results presented here and the world averages are compatible. By dividing with $f_+^{K^0 \pi^-}(0) = 0.9677(27)$ [23], we obtain

$$\begin{aligned} |V_{us}|_{K_{\mu 3}} &= 0.2218(5)_{\text{NA62}(12)_{\text{external}}} \\ &= 0.2218(13) \text{ and} \end{aligned} \quad (8.13)$$

$$\begin{aligned} |V_{us}|_{K_{e 3}} &= 0.2221(2)_{\text{NA62}(12)_{\text{external}}} \\ &= 0.2221(12). \end{aligned} \quad (8.14)$$

Both values from $K_{\mu 3}$ and $K_{e 3}$ can be combined assuming $e - \mu$ lepton universality and yield

$$\begin{aligned} |V_{us}| &= 0.2219(3)_{\text{NA62}(10)_{\text{external}}} \\ &= 0.2219(10). \end{aligned} \quad (8.15)$$

The uncertainties are dominated by external sources. Table 20 gives a break down of the single contributions to the uncertainty.

The unitarity test of the CKM matrix with the combined value for $|V_{us}|$ from Equation 8.15, $|V_{ud}| = 0.97417(21)$ from Fermi transitions [18], and $|V_{ub}| = 4.13(49) \cdot 10^{-3}$ from B meson decays [11, Review on Semileptonic B Meson Decays and the Determination of V_{cb} and V_{ub}] yields

$$|V_{ud}|^2 + |V_{us}|^2 + |V_{ub}|^2 = 0.9983(6). \quad (8.16)$$

This result is compatible within 2.8 standard deviations with the requirement of the Standard Model that the CKM matrix is unitary. The difference to unitarity $\Delta_{\text{CKM}} = 0.17$ is compared with the values presented in Table 3 on Page 11. The difference between the unitarity results obtained by $K_{\ell 2}$ and $K_{\ell 3}$ decays increased. The new $K_{\ell 3}$ result is

	Σ	NA62	$\text{Br}(K_{2\pi})$	τ	Δ	I	f_+^0	O
$ V_{us}^{K_{\mu 3}} \cdot f_+^0$	0.51	0.21	0.19	0.08	0.41	0.08	—	0.02
$ V_{us}^{K_{e 3}} \cdot f_+^0$	0.47	0.09	0.19	0.08	0.41	0.06	—	0.02
$ V_{us} $	0.45	0.11	0.14	0.06	0.28	0.05	0.28	0.01

Table 20: Relative uncertainties [%] on $|V_{us}|_{K_{\mu 3}} \cdot f_+^{K^0 \pi^-}(0)$, $|V_{us}|_{K_{e 3}} \cdot f_+^{K^0 \pi^-}(0)$, and the combination $|V_{us}|$ of both results divided by $f_+^{K^0 \pi^-}(0)$. The short notation $f_+^{K^0 \pi^-}(0) = f_+^0$ is used. The relative uncertainty of the total uncertainty is given as Σ . It is broken down to its single contributions. These contributions are the branching fraction ratios presented in this work (NA62), the kaon life time measurement (τ), the long distance radiative and isospin breaking corrections (Δ), the phase space integrals (I), the branching fraction of $K_{2\pi}$, the form factor at zero momentum transfer (f_+^0), and other parameters (O) with less impact on the total uncertainty.

now compatible with the τ decay result and still compatible with the old $K_{\ell 3}$ result. Further studies of $K_{\ell 3}$ branching fractions seem appropriate. However, in light of the smaller contribution of the branching fraction ratio measurement presented in this work to the uncertainty of $|V_{us}|$, improvements of the other input parameters to Table 1.30 on Page 12 are required. The two largest contributions to the uncertainty are the form factor at zero momentum transfer and the long distance radiative and isospin corrections which each have a relative uncertainty of about 0.3 % (Table 20). Therefore, future improvements in the theoretical calculations are needed to help understand the situation of the CKM unitarity.

8.3 LEPTON UNIVERSALITY

The ratio of the decay widths $\Gamma_{K_{e 3}}$ and $\Gamma_{K_{\mu 3}}$ is (Equation 1.30 on Page 12)

$$\frac{\Gamma_{K_{e 3}}}{\Gamma_{K_{\mu 3}}} = \frac{\text{Br}(K_{e 3})}{\text{Br}(K_{\mu 3})} = \frac{I_{e 3}(1 + \delta_{\text{SU}2} + \delta_{\text{EM}}^e)^2}{I_{\mu 3}(1 + \delta_{\text{SU}2} + \delta_{\text{EM}}^\mu)^2} \text{ or} \quad (8.17)$$

$$1 = \frac{\text{Br}(K_{\mu 3})}{\text{Br}(K_{e 3})} \frac{I_{e 3}(1 + \delta_{\text{SU}2} + \delta_{\text{EM}}^e)^2}{I_{\mu 3}(1 + \delta_{\text{SU}2} + \delta_{\text{EM}}^\mu)^2} =: r_{e\mu} \quad (8.18)$$

The measured $\frac{\text{Br}(K_{\mu 3})}{\text{Br}(K_{e 3})}$ ratio and the parameters given in Table 4 and in Table 5 on Page 12 are used. The result is

$$\begin{aligned} r_{e\mu} &= 0.9985(19)_{\text{NA62}}(20)_{\text{external}} \\ &= 0.9985(27) \end{aligned} \quad (8.19)$$

which is in excellent agreement with the Standard Model prediction. The uncertainty is driven almost equally by the full uncertainties on the $\frac{\text{Br}(K_{\mu 3})}{\text{Br}(K_{e 3})}$ measurement and the uncertainties on external input parameters. The reached relative uncertainty is 0.24%. NA48/2 measured the same quantity to $r_{e\mu} = 0.99(1)$ [68].

Lepton universality is tested as well in other decays. Also a kaon decay is used in the NA62 measurement $R_K = \Gamma(K_{e2})/\Gamma(K_{\mu 2}) = 2.487(13) \cdot 10^{-5}$ [36] which is in agreement with Standard Model prediction with a precision of 0.5%. The most precise test of $e - \mu$ lepton universality is currently provided by the PIENU collaboration which uses the ratio of pion decays into $\pi^+ \rightarrow \ell^+ \nu(\gamma)$ with $\ell = e, \mu$ to obtain $g_e/g_\mu = 0.9996(12)$ [71]. The reached relative uncertainty is at the level of 0.1%.

A recent $e - \mu$ lepton flavour universality test was performed by LHCb which agrees within 2.6 standard deviations with the Standard Model prediction. The ratio of the branching fractions of $B^+ \rightarrow K^+ \mu^+ \mu^-$ and $B^+ \rightarrow K^+ e^+ e^-$ yielded $R_K = 0.745^{(+90)}_{(-74)}(36)$ with asymmetric statistical and symmetric systematic uncertainties [72].

CONCLUSIONS

The up to now most precise measurements of positive charged semileptonic kaon branching fractions normalized to the $K_{2\pi}$ decay have been presented in this work. The ratio of the branching fractions read

$$\begin{aligned}\frac{\text{Br}(K_{\mu 3})}{\text{Br}(K_{2\pi})} &= 0.16066(12)_{\text{stat.}}(66)_{\text{syst.}} \\ &= 0.1607(7),\end{aligned}$$

$$\begin{aligned}\frac{\text{Br}(K_{e3})}{\text{Br}(K_{2\pi})} &= 0.24320(17)_{\text{stat.}}(41)_{\text{syst.}} \\ &= 0.2432(4), \text{ and}\end{aligned}$$

Additionally, the ratio of the branching fractions of $K_{\mu 3}$ and K_{e3} was measured to

$$\begin{aligned}\frac{\text{Br}(K_{\mu 3})}{\text{Br}(K_{e3})} &= 0.66061(17)_{\text{stat.}}(245)_{\text{syst.}} \\ &= 0.6606(25).\end{aligned}$$

The results base on 27 730 193 $K_{\mu 3}$, 37 178 482 K_{e3} , and 2 165 886 $K_{2\pi}$ candidates selected from data taken by the NA62 Collaboration in 2007. Due to the very small statistical uncertainties, the results are as expected dominated by systematic effects. On these, the knowledge about the semileptonic form factors and the background estimation has the largest impact. A future measurement with the now operational NA62 detector for the $K^+ \rightarrow \pi^+ \nu \bar{\nu}$ phase could improve the background control due to additional detectors, e.g. a RICH for μ/π separation and a silicon pixel detector used as beam spectrometer.

The $K_{\mu 3}$ and K_{e3} branching fractions are

$$\begin{aligned}\text{Br}(K_{\mu 3}) &= 3.321(14)_{\text{NA62}}(13)_{\text{external}} \% \\ &= 3.321(19) \% \text{ and}\end{aligned}$$

$$\begin{aligned}\text{Br}(K_{e3}) &= 5.027(09)_{\text{NA62}}(19)_{\text{external}} \% \\ &= 5.027(22) \%\end{aligned}$$

with NA62 being the contribution of the branching fraction ratio uncertainties as presented in this work. The as *external* summarized

contributions are all external input parameters. The here presented branching fractions are the most precise values available for the branching fractions up to this time. They are smaller than the current world averages but are compatible with them.

These branching fractions are used to compute the product of the CKM parameter $|V_{us}|$ and $f_+^{K^0\pi^-}(0)$:

$$\begin{aligned} |V_{us}|_{K_{\mu 3}} \cdot f_+^{K^0\pi^-}(0) &= 0.2146(5)_{\text{NA62}(10)_{\text{external}}} \\ &= 0.2146(11) \text{ and} \\ |V_{us}|_{K_{e 3}} \cdot f_+^{K^0\pi^-}(0) &= 0.2149(2)_{\text{NA62}(10)_{\text{external}}} \\ &= 0.2149(10). \end{aligned}$$

Both are compatible with the current world averages. Combing both results under the assumption of $e - \mu$ lepton universality and dividing by $f_+^{K^0\pi^-}(0)$ yields

$$\begin{aligned} |V_{us}| &= 0.2219(3)_{\text{NA62}(10)_{\text{external}}} \\ &= 0.2219(10). \end{aligned}$$

The NA62 contribution to the uncertainty has a relative fraction at the level of 0.1 %. The largest contributions to the uncertainty are the form factor at zero momentum transfer and the long distance radiative and isospin corrections which sum up to a relative uncertainty of 0.4 %. Further semileptonic kaon branching fraction measurements are not required for a $|V_{us}|$ determination until the theory calculations improve.

The CKM unitarity was tested with

$$|V_{ud}|^2 + |V_{us}|^2 + |V_{ub}|^2 = 0.9983(6).$$

The result is with unitarity compatible within 2.8 standard deviations. It is in agreement with unitarity tests using current world average of $|V_{us}|$ basing on τ decays.

The $e - \mu$ lepton universality is probed by

$$\begin{aligned} r_{e\mu} &:= \frac{\Gamma_{K_{\mu 3}}}{\Gamma_{K_{e 3}}} \frac{I_{e3}(1 + \delta_{\text{SU}2} + \delta_{\text{EM}}^e)^2}{I_{\mu 3}(1 + \delta_{\text{SU}2} + \delta_{\mu\text{EM}})^2} = 0.9985(19)_{\text{NA62}(20)_{\text{external}}} \\ &= 0.9985(27). \end{aligned}$$

This is the most precise measurement of $e - \mu$ lepton universality currently available using kaon decays. This measurement would benefit from better knowledge on semileptonic form factors in order to decrease the dominating systematic uncertainty on the $\frac{\text{Br}(K_{\mu 3})}{\text{Br}(K_{e 3})}$ result.

APPENDIX

A.1 CORRECTION FOR THE WIDTH OF THE KAON MOMENTUM

The full second order correction [61].

Listing 1: The code used to apply the correction as weight. The variable “MCWeight” is the same variable called “ b_1 ” in Section 4.5.1.

```
double MCWeight = 0.07;
if (RunNumber>=20410 && RunNumber<=20424) {
    MCWeight *= (1.0 - 0.01*(Kaon_Momentum_True-74.0));
    if (Kaon_Momentum_True>77.5) MCWeight *= (1.0+12.0*(Kaon_
        Momentum_True-77.5));
    if (Kaon_Momentum_True<71.2) MCWeight *= (1.0+ 2.5*(71.2-
        Kaon_Momentum_True));
}
if (RunNumber>=20438 && RunNumber<=20453) {
    MCWeight *= (1.0 - 0.015*(Kaon_Momentum_True-74.0));
    if (Kaon_Momentum_True>77.5) MCWeight *= (1.0+16.0*(Kaon_
        Momentum_True-77.5));
    if (Kaon_Momentum_True<71.1) MCWeight *= (1.0+ 5.0*(71.1-
        Kaon_Momentum_True));
}
if (RunNumber>=20459 && RunNumber<=20478) {
    MCWeight *= (1.0 - 0.01*(Kaon_Momentum_True-74.0));
    if (Kaon_Momentum_True>77.4) MCWeight *= (1.0+10.0*(Kaon_
        Momentum_True-77.4));
    if (Kaon_Momentum_True<71.0) MCWeight *= (1.0+ 3.0*(71.0-
        Kaon_Momentum_True));
}
if (RunNumber>=20482 && RunNumber<=20485) {
    MCWeight *= (1.0 + 0.00*(Kaon_Momentum_True-74.0));
    if (Kaon_Momentum_True>77.3) MCWeight *= (1.0+6.0*(Kaon_
        Momentum_True-77.3));
    if (Kaon_Momentum_True<71.0) MCWeight *= (1.0+5.0*(71.0-
        Kaon_Momentum_True));
}
}
```

A.2 $K^+ \rightarrow \mu^+ \nu_\mu$ SELECTION

The described selection follows the selection from [36] with some minor modifications:

- The trigger $K_{\mu 2}$ and the L3 filter $K_{\mu 2}$ are used.
- The number of reconstructed tracks is $N_{\text{Track}} = 1$ and the charge is $q_{\text{Track}} = +1$.
- The requirements on the momenta differ from the selection in [36]. The $R_K = \Gamma(K_{e2}) / \Gamma(K_{\mu 2})$ analysis was performed in the momentum range $13 \text{ GeV}/c < p_{\text{track}} < 65 \text{ GeV}/c$. However, as in Section 5.6 described, lower momenta are in this work accepted. The requirements set the track momentum are

$$\star 7 \text{ GeV}/c < p_{\text{track}} < 65 \text{ GeV}/c.$$

The track momentum dependent selection criteria described below are also modified for the lower momenta limits with respect to [36].

- The track trajectory must be inside the acceptance of the DCH and LKr. The same requirements as in Section 5.3.3 are set.
- Timing cuts as in Section 5.3.2 described.
- The event is rejected if a LKr cluster exists with $E_{\text{Cluster}} > 2 \text{ GeV}$ and it is not associated with the track. This requirement reduces $K_{2\pi}$ background.
- The distance of the cluster associated with the track to a dead cell has to be $d_{\text{Cluster-Dead Cell}} > 2 \text{ cm}$.
- The selection criterion on the lower boundary of the allowed z-position of the charged vertex V aims to reduce background from beam muons. The criterion is track momentum dependent:
 - $(p_{\text{Track}} < 13) \text{ GeV}/c: V_{\text{min}} = -16 \text{ m}$.
 - $(13 \leq p_{\text{Track}} < 20) \text{ GeV}/c: V_{\text{min}} = -10 \text{ m}$.
 - $(20 \leq p_{\text{Track}} < 25) \text{ GeV}/c: V_{\text{min}} = 0 \text{ m}$.
 - $(25 \leq p_{\text{Track}} < 45) \text{ GeV}/c: V_{\text{min}} = 5 \text{ m}$.
 - $(45 \leq p_{\text{Track}} < 55) \text{ GeV}/c: V_{\text{min}} = 10 \text{ m}$.
 - $(55 \leq p_{\text{Track}} < 60) \text{ GeV}/c: V_{\text{min}} = 15 \text{ m}$.
 - $(60 \leq p_{\text{Track}}) \text{ GeV}/c: V_{\text{min}} = 25 \text{ m}$.
 - The upper boundary of the z-position of the charged vertex is $V_{\text{max}} = 90 \text{ m}$.
- The selection criterion on the squared missing mass m_{miss}^2 is also momentum dependent. For the lower boundary the limits are:

- * ($p_{\text{Track}} < 20$) GeV/c: $m_{\text{miss, min}}^2 = -16 \cdot 10^{-3} (\text{GeV}/c^2)^2$.
- * ($20 \leq p_{\text{Track}} < 25$) GeV/c: $m_{\text{miss, min}}^2 = -14 \cdot 10^{-3} (\text{GeV}/c^2)^2$.
- * ($25 \leq p_{\text{Track}} < 50$) GeV/c: $m_{\text{miss, min}}^2 = -13 \cdot 10^{-3} (\text{GeV}/c^2)^2$.
- * ($50 \leq p_{\text{Track}} < 55$) GeV/c: $m_{\text{miss, min}}^2 = -14 \cdot 10^{-3} (\text{GeV}/c^2)^2$.
- * ($55 \leq p_{\text{Track}} < 60$) GeV/c: $m_{\text{miss, min}}^2 = -15 \cdot 10^{-3} (\text{GeV}/c^2)^2$.
- * ($60 \leq p_{\text{Track}}$) GeV/c: $m_{\text{miss, min}}^2 = -16 \cdot 10^{-3} (\text{GeV}/c^2)^2$.

The limits on the upper boundary are:

- * ($p_{\text{Track}} < 50$) GeV/c: $m_{\text{miss, max}}^2 = 10 \cdot 10^{-3} (\text{GeV}/c^2)^2$.
- * ($50 \geq p_{\text{Track}}$) GeV/c: $m_{\text{miss, max}}^2 = 11 \cdot 10^{-3} (\text{GeV}/c^2)^2$.

A.3 $K^+ \rightarrow \pi^+ \pi^0 \rightarrow \pi^+ e^+ e^- \gamma$ SELECTION

The selection is taken from [73] with tighter criteria:

- The trigger K_{e2} and the L3 filter K_{e2} are used.
- Vertex:
 - ★ A dedicated routine from NA48/2 which fits a three-track-vertex is used.
 - ★ Only events with the number of vertices $N_{\text{vtx}} = 1$ are allowed and the sum over all three tracks must be $Q_{\text{vtx}} = +1$.
 - ★ For the fit is $\chi_{\text{max}}^2 = 25$ required.
 - ★ The z-position of the vertex must be $-12 \text{ m} < z_{\text{vtx}} < 65 \text{ m}$.
- Tracks:
 - ★ The track quality and geometrical selection criteria are the same as described in Section 5.3
 - ★ An additional constrain is applied. The distance between e^+ and e^- must not be below 2 cm. This constrain reduces background from the $K_{2\pi}$ decay with $\pi^0 \rightarrow \gamma\gamma$ where one of the γ undergoes photon-conversion at the kevlar window of the DCH.
- Exactly one cluster in the LKr not associated with any track.
 - ★ Cluster in time with average time of tracks
 $|\bar{t}_{\text{Tracks}} - t_\gamma| < 10 \text{ ns}$.
 - ★ Distance from extrapolated positions of tracks in LKr
 $d_{\text{track}} > 20 \text{ cm}$.
 - ★ Distance from extrapolated positions of tracks in LKr not taking into account the bending caused by magnet
 $d_{\text{track, straight}} > 20 \text{ cm}$.
 - ★ $E_{\text{cluster}} > 3 \text{ GeV}$.
 - ★ The cluster must be inside the LKr acceptance.
- This cluster is used to reconstruct a photon. The extrapolated position of the photon inside the DCH₁ is required to have a radius $r_{\text{DCH}_1} > 13 \text{ cm}$.
- Following kinematic requirements must be fulfilled:
 - ★ Sum of track momenta $\sum_i p_{\text{track},i} - 74 \text{ GeV}/c < 4 \text{ GeV}/c$
 - ★ Transversal component of $p = \sum_i p_{\text{track},i} + p_\gamma$ must be
 $p_T^2 < 0.0005 \text{ GeV}^2/c^2$.

- The particle identification of the tracks is achieved through the test of a set of requirements which must be true only for one mass combination. The two combinations swap the assignment of π^+ and e^+ between both unidentified tracks with $Q = +1$:
 - ★ The Dalitz variable: $x = \frac{(p_{e^+} + p_{e^-})^2}{m_{\pi^0}^2} < 1$.
 - ★ The Dalitz variable: $y = \frac{2p_{\pi^0} \cdot (p_{e^+} + p_{e^-})}{m_{\pi^0}^2(1-x)} < 1$.
 - ★ The reconstructed π^0 mass: $115 \text{ MeV} < M_{ee\gamma} < 145 \text{ MeV}$
 - ★ The reconstructed K^+ mass: $465 \text{ MeV} < M_{ee\gamma\pi} < 510 \text{ MeV}$
- To satisfy the L2 trigger and L3 filter conditions, it is required that
 - ★ $E_\gamma + E_{\text{Cluster},e^+} + E_{\text{Cluster},e^-} > 14 \text{ GeV}$ and
 - ★ $((E/p)_{e^+} > 0.8) \wedge (p_{e^+} > 5.5 \text{ GeV}/c)$.
- In order to reject a badly described region of the DCH, only following square is accepted for electrons:
 - ★ $|x_{\text{DCH1},e^\pm}| > 20 \text{ cm} \vee |y_{\text{DCH1},e^\pm}| > 20 \text{ cm}$.

A.4 TRANSVERSAL MOMENTUM SELECTION CRITERION

PARAMETER	$ p_{\text{track}} < 37 \text{ GeV}/c$	$ p_{\text{track}} \geq 37 \text{ GeV}/c$
a_0	-0.0346157562881	1.36132774311
a_1	0.0161933566811	-0.101567242239
a_2	-0.000399185616017	0.00331139627879
a_3	$4.40054575924 \cdot 10^{-6}$	$-4.71165599269 \cdot 10^{-5}$
a_4	$-2.21606107099 \cdot 10^{-8}$	$2.40563005648 \cdot 10^{-7}$

Table 21: Parameters for the bi-dimensional the selection criterion on p and p_t of the track.

PARAMETER	$ p_{\pi^0} < 37 \text{ GeV}/c$	$ p_{\pi^0} \geq 37 \text{ GeV}/c$
a_0	-0.315320007833	1.26903868166
a_1	0.063546197258	-0.0942264376253
a_2	-0.00323372178158	0.00305004764381
a_3	$7.62898988615 \cdot 10^{-5}$	$-4.26095443607 \cdot 10^{-5}$
a_4	$-6.82940197834 \cdot 10^{-7}$	$2.09985199967 \cdot 10^{-7}$

Table 22: Parameters for the bi-dimensional the selection criterion on p and p_t of the π^0 .

LIST OF FIGURES

Figure 1	Elementary particles in the Standard Model [7].	3
Figure 2	The $K^0 \rightarrow \mu^+ \mu^-$ decay.	5
Figure 3	Comparison of $ V_{us} f_+^{K^0\pi^-}(0)$.	8
Figure 4	The CERN accelerator complex [39].	18
Figure 5	Schematic view of the NA48/2 beam line.	19
Figure 6	Overview to the helium tank and the DCHs.	21
Figure 7	Front and side view of the CHOD [37].	23
Figure 8	The LKr cell design [37].	24
Figure 9	The NHOD fibers placed inside the LKr [37].	26
Figure 10	The HAC with its two modules [37].	27
Figure 11	The MUV planes [37].	28
Figure 12	An AKL pocket [37].	29
Figure 13	The trigger and data acquisition system.	30
Figure 14	Reconstruction of charged vertex \vec{V}_c .	38
Figure 15	Reconstruction of the neutral vertex.	40
Figure 16	Projectivity correction for cluster in LKr.	43
Figure 17	The kaon momentum distribution reconstructed using $K_{2\pi}$ events.	51
Figure 18	Distribution of the track + π^0 momentum.	53
Figure 19	Sketch of the kaon halo correction.	54
Figure 20	The x - and z -components of the true vertex positions in $K_{2\pi}$ MC.	55
Figure 21	Visualization of the semileptonic kaon decays K_{e3} and $K_{\mu3}$ and the hadronic kaon decay $K_{2\pi}$.	57
Figure 22	Distributions of the track timing $t_{\text{CHOD}} - t_{\text{trigger}}$.	60
Figure 23	Distributions of the DCH ₁ radius.	62
Figure 24	Distributions of the DCH ₄ radius.	63
Figure 25	Distributions of the charged vertex.	65
Figure 26	Distribution of the distance of closest approach $ \vec{R} $.	66
Figure 27	An E/p demonstration distribution.	67
Figure 28	Distribution of the μ^+ momentum with the $K_{\mu2}$ selection.	68
Figure 29	Muon E/p distribution and identification efficiency.	69
Figure 30	Distribution of the electron momentum.	70
Figure 31	Electron E/p distribution and identification efficiency.	71
Figure 32	Pion momentum and E/p distribution from $K_{2\pi D}$ decays.	72
Figure 33	Misidentification probabilities for pions.	73

Figure 34	Two dimensional distributions of reconstructed π^0 cluster positions in the LKr. 78	
Figure 35	The time requirements for the π^0 selection. 79	
Figure 36	Distribution of the distance of the photons position to the y-axis r_{DCH1} . 80	
Figure 37	Distribution of the π^0 energy. 81	
Figure 38	Distribution of the π^0 mass. 82	
Figure 39	Distribution of the neutral vertex. 83	
Figure 40	Distribution of the track momentum. 86	
Figure 41	Distribution of the missing mass m_{miss}^2 . 88	
Figure 42	Impact of kaon halo correction on m_{miss}^2 . 89	
Figure 43	Distributions of $p_{t,\text{track}}$ versus p_{track} for the $K_{\mu 3}$ selection. 92	
Figure 44	Distributions of p_{t,π^0} versus p_{π^0} for the $K_{\mu 3}$ selection. 93	
Figure 45	Distributions of $p_{t,\text{track}}$ versus p_{track} for the $K_{2\pi}$ selection. 94	
Figure 46	Distributions of p_{t,π^0} versus p_{π^0} for the $K_{2\pi}$ selection. 95	
Figure 47	Kaon halo correction impact on the track momenta. 96	
Figure 48	Kaon halo correction impact on the π^0 momenta. 97	
Figure 49	Distributions of the combined track and π^0 momenta. 98	
Figure 50	Distributions of the difference between the nominal kaon mass and $M_{\pi^+\pi^0}$. 100	
Figure 51	Distribution of the additional energy in the LKr. 101	101
Figure 52	Distribution of the additional energy in the LKr below 10 GeV. 102	
Figure 53	Ratios of the branching fractions computed independently for each run. 106	
Figure 54	Q_1 sub-trigger efficiencies as function of the track momentum. 108	
Figure 55	E_{10} sub-trigger efficiencies as function of the track momentum. 109	
Figure 56	$TRKLM$ sub-trigger efficiencies as function of the track momentum. 110	
Figure 57	The K_{e2} and $K_{\mu 2}$ trigger efficiency. 111	
Figure 58	Track momentum distribution of the modified $K_{\mu 3}$ selection. 116	
Figure 59	Modified K_{e3} selection. 117	
Figure 60	Track momentum distribution of the modified K_{e3} selection. 118	
Figure 61	π^0 momentum distribution of modified the $K_{2\pi}$ selection. 120	

Figure 62	Distribution on bremsstrahlung photon energies in the LKr.	123
Figure 63	Distribution of the ratio R .	124
Figure 64	Systematic uncertainties shown in a radar chart.	125
Figure 65	The final results for the ratios of this analysis compared with previous measurements and world averages.	128

LIST OF TABLES

Table 1	Summary of discussed $ V_{ud} $ measurements.	8
Table 2	Summary of discussed $ V_{us} $ measurements.	10
Table 3	CKM unitarity test with different values for $ V_{us} $.	11
Table 4	Common input parameters for K_{e3} and $K_{\mu3}$ decays in Equation 1.30.	12
Table 5	Input parameters for K_{e3} and $K_{\mu3}$ decays in Equation 1.30.	12
Table 6	Triggers used for this analysis.	29
Table 7	Trigger logics used for this analysis.	31
Table 8	Available L3 filters.	33
Table 9	Overview of the signal MC samples and acceptances.	56
Table 10	Summary of common selection criteria for e^+ , μ^+ , and π^+ .	59
Table 11	Summary of π^0 selection criteria.	77
Table 12	Summary of selection criteria using combined information from the track and the π^0 .	85
Table 13	Parameters for the bi-dimensional the selection criterion on p and p_t of the track.	90
Table 14	Parameters for the bi-dimensional the selection criterion on p and p_t of the π^0 .	91
Table 15	Summary of the decay specific offset parameters	91
Table 16	Overview of selected candidates.	104
Table 17	Trigger efficiencies for all selections.	108
Table 18	L3-filter efficiencies for all selections.	112
Table 19	Central values and overview of uncertainties.	126
Table 20	Relative uncertainties on $ V_{us} $ results.	131
Table 21	Parameters for the bi-dimensional the selection criterion on p and p_t of the track.	140

Table 22	Parameters for the bi-dimensional the selection criterion on p and p_t of the π^0 .	140
----------	---	-----

LISTINGS

Listing 1	The code used to apply the correction as weight. The variable "MCWeight" is the same variable called " b_1 " in Section 4.5.1.	135
-----------	--	-----

ACRONYMS

AKL	Photon Anti-Counter	28
CERN	Conseil Européen pour la Recherche Nucléaire	17
CPD	Calorimeter Pipeline Digitizer	61
CHOD	Hodoscope for charged particles	23
CKM	Cabibbo-Kobayashi-Maskawa	3
CMC	Charged Kaons Monte Carlo	45
COMpACT	C OptiMized Program for Accessing Countless Terabytes	
DCH	Drift Chamber	20
HAC	Hadron Calorimeter	26
KABES	Kaon Beam Spectrometer	37
LHC	Large Hadron Collider	17
L1	Level 1 Trigger	30
L1C	Trigger for Charged Particles	30
L1N	Trigger for Neutral Particles	30
LKr	Liquid Krypton Calorimeter	24
LINAC	Linear Accelerator	17
MC	Monte Carlo	45
MUV	Muon Veto	27
NHOD	Hodoscope for neutral particles	25
PU	Pattern Unit	31
PMT	Photomultiplier Tube	23
PS	Proton Synchrotron	17

ROC	Read Out Controller.....	31
SPS	Super Proton Synchrotron.....	2
TURTLE	Trace Unlimited Rays Through Lumped Elements.....	45
TS	Trigger Supervisor.....	31

BIBLIOGRAPHY

- [1] F. Englert and R. Brout. Broken Symmetry and the Mass of Gauge Vector Mesons. *Phys. Rev. Lett.*, 13:321–323, Aug 1964. URL <https://doi.org/10.1103/PhysRevLett.13.321>.
- [2] P.W. Higgs. Broken symmetries, massless particles and gauge fields. *Physics Letters*, 12(2):132 – 133, 1964. URL [https://doi.org/10.1016/0031-9163\(64\)91136-9](https://doi.org/10.1016/0031-9163(64)91136-9).
- [3] P. W. Higgs. Broken Symmetries and the Masses of Gauge Bosons. *Phys. Rev. Lett.*, 13:508–509, 1964. URL <https://doi.org/10.1103/PhysRevLett.13.508>.
- [4] G. Aad et al. Observation of a new particle in the search for the Standard Model Higgs boson with the ATLAS detector at the LHC. *Physics Letters B*, 716(1):1 – 29, 2012. URL <https://doi.org/10.1016/j.physletb.2012.08.020>.
- [5] S. Chatrchyan et al. Observation of a new boson at a mass of 125 GeV with the CMS experiment at the LHC. *Physics Letters B*, 716(1):30 – 61, 2012. URL <https://doi.org/10.1016/j.physletb.2012.08.021>.
- [6] J.Ellis and T. You. Updated global analysis of Higgs couplings. *Journal of High Energy Physics*, 2013(6):103, 2013. URL [https://doi.org/10.1007/JHEP06\(2013\)103](https://doi.org/10.1007/JHEP06(2013)103).
- [7] MissMJ. Standard model of elementary particles. Wikimedia Commons (CC BY-SA 3.0), 2014-05-18 09:45. URL https://commons.wikimedia.org/wiki/File:Standard_Model_of_Elementary_Particles.svg. Modified.
- [8] G. W. Bennett et al. Final report of the E821 muon anomalous magnetic moment measurement at BNL. *Phys. Rev. D*, 73:072003, Apr 2006. URL <https://doi.org/10.1103/PhysRevD.73.072003>.
- [9] G. Anelli et al. Proposal to Measure the Rare Decay $K^+ \rightarrow \pi^+ \nu \bar{\nu}$ at the CERN SPS. Technical Report CERN-SPSC-2005-013. SPSC-P-326, CERN, Geneva, Apr 2005. URL <http://cds.cern.ch/record/832885>.
- [10] N. Cabibbo. Unitary Symmetry and Leptonic Decays. *Phys. Rev. Lett.*, 10:531–533, Jun 1963. URL <https://doi.org/10.1103/PhysRevLett.10.531>.

- [11] K.A. Olive et al. Review of Particle Physics. *Chin.Phys.*, C38:090001, 2014. URL <https://doi.org/10.1088/1674-1137/38/9/090001>.
- [12] S. L. Glashow, J. Iliopoulos, and L. Maiani. Weak Interactions with Lepton-Hadron Symmetry. *Phys. Rev. D*, 2:1285–1292, Oct 1970. URL <https://doi.org/10.1103/PhysRevD.2.1285>.
- [13] D. Ambrose et al. Improved Branching Ratio Measurement for the Decay $K_L^0 \rightarrow \mu^+ \mu^-$. *Phys. Rev. Lett.*, 84:1389–1392, Feb 2000. URL <https://doi.org/10.1103/PhysRevLett.84.1389>.
- [14] M. Kobayashi and T. Maskawa. CP-Violation in the Renormalizable Theory of Weak Interaction. *Progress of Theoretical Physics*, 49(2):652–657, 1973. URL <https://doi.org/10.1143/PTP.49.652>.
- [15] J. H. Christenson, J. W. Cronin, V. L. Fitch, and R. Turlay. Evidence for the 2π Decay of the K_2^0 Meson. *Phys. Rev. Lett.*, 13:138–140, Jul 1964. URL <https://doi.org/10.1103/PhysRevLett.13.138>.
- [16] L. Chau and W. Keung. Comments on the Parametrization of the Kobayashi-Maskawa Matrix. *Phys. Rev. Lett.*, 53:1802–1805, Nov 1984. URL <https://doi.org/10.1103/PhysRevLett.53.1802>.
- [17] E. Blucher et al. Status of the Cabibbo Angle, 2005. URL <https://arxiv.org/abs/hep-ph/0512039>. Proceedings of CKM 2005 - WG 1, arXiv:hep-ph/0512039v1.
- [18] J. C. Hardy and I. S. Towner. Superallowed $0^+ \rightarrow 0^+$ nuclear β decays: 2014 critical survey, with precise results for V_{ud} and CKM unitarity. *Phys. Rev. C*, 91:025501, Feb 2015. URL <https://doi.org/10.1103/PhysRevC.91.025501>.
- [19] W. J. Marciano and A. Sirlin. Improved Calculation of Electroweak Radiative Corrections and the Value of V_{ud} . *Phys. Rev. Lett.*, 96:032002, Jan 2006. URL <https://doi.org/10.1103/PhysRevLett.96.032002>.
- [20] F. E. Wietfeldt and G. L. Greene. *Colloquium* : The neutron lifetime. *Rev. Mod. Phys.*, 83:1173–1192, Nov 2011. URL <https://doi.org/10.1103/RevModPhys.83.1173>.
- [21] D. Počanić et al. Precise Measurement of the $\pi^+ \rightarrow \pi^0 e^+ \nu$ Branching Ratio. *Phys. Rev. Lett.*, 93:181803, Oct 2004. URL <https://doi.org/10.1103/PhysRevLett.93.181803>.
- [22] M. Antonelli et al. An evaluation of $|V_{us}|$ and precise tests of the Standard Model from world data on leptonic and semileptonic kaon decays. *The European Physical Journal C*, 69(3-4):399–424, 2010. URL <https://doi.org/10.1140/epjc/s10052-010-1406-3>.

- [23] S. Aoki and other. Review of lattice results concerning low energy particle physics. *arXiv:1607.00299 [hep-lat]*, 2016. URL <https://arxiv.org/abs/1607.00299>.
- [24] N. Cabibbo, E. Swallow, and R. Winston. Semileptonic Hyperon Decays and Cabibbo-Kobayashi-Maskawa Unitarity. *Phys. Rev. Lett.*, 92:251803, Jun 2004. URL <https://doi.org/10.1103/PhysRevLett.92.251803>.
- [25] R. Flores-Mendieta. V_{us} from hyperon semileptonic decays. *Phys. Rev. D*, 70:114036, Dec 2004. URL <https://doi.org/10.1103/PhysRevD.70.114036>.
- [26] V. Mateu and A. Pich. V_{us} determination from hyperon semileptonic decays. *J. High Energy Phys.*, 10(041), 2005. URL <https://doi.org/10.1088/1126-6708/2005/10/041>.
- [27] Heavy Flavor Averaging Group, Y. Amhis, et al. Averages of b-hadron, c-hadron, and τ -lepton properties as of summer 2014. *arXiv:1412.7515 [hep-ex]*, 2014. URL <http://arxiv.org/abs/1412.7515>.
- [28] A. Kastner and H. Neufeld. The $K_{\ell 3}$ scalar form factors in the standard model. *The European Physical Journal C*, 57(3):541–556, 2008. URL <https://doi.org/10.1140/epjc/s10052-008-0703-6>.
- [29] V. Cirigliano, M. Giannotti, and H. Neufeld. Electromagnetic effects in $K_{\ell 3}$ decays. *Journal of High Energy Physics*, 2008(11):006, 2008. URL <https://doi.org/10.1088/1126-6708/2008/11/006>.
- [30] A. Sirlin. Current algebra formulation of radiative corrections in gauge theories and the universality of the weak interactions. *Rev. Mod. Phys.*, 50:573–605, Jul 1978. URL <https://doi.org/10.1103/RevModPhys.50.573>.
- [31] W. J. Marciano and A. Sirlin. Radiative corrections to $\pi_{\ell 2}$ decays. *Phys. Rev. Lett.*, 71:3629–3632, Nov 1993. URL <https://doi.org/10.1103/PhysRevLett.71.3629>.
- [32] H. Leutwyler and M. Roos. Determination of the elements V_{us} and V_{ud} of the Kobayashi-Maskawa matrix. *Zeitschrift für Physik C Particles and Fields*, 25(1):91–101, 1984. URL <https://doi.org/10.1007/BF01571961>.
- [33] A. Bazavov et al. Kaon semileptonic vector form factor and determination of $|V_{us}|$ using staggered fermions. *Phys. Rev. D*, 87:073012, Apr 2013. URL <https://doi.org/10.1103/PhysRevD.87.073012>.

- [34] P. A. Boyle et al. The kaon semileptonic form factor in $N_f = 2 + 1$ domain wall lattice QCD with physical light quark masses. *Journal of High Energy Physics*, 2015(6):1–22, 2015. URL [https://doi.org/10.1007/JHEP06\(2015\)164](https://doi.org/10.1007/JHEP06(2015)164).
- [35] V. Bernard, M. Oertel, E. Passemar, and J. Stern. $K_{\mu 3}^L$ decay: A stringent test of right-handed quark currents. *Physics Letters B*, 638(5-6):480, 2006. URL <https://doi.org/10.1016/j.physletb.2006.05.079>.
- [36] C. Lazzeroni et al. Test of lepton flavour universality in $K^+ \rightarrow l^+ \nu$ decays. *Physics Letters B*, 698(2):105 – 114, 2011. URL <https://doi.org/10.1016/j.physletb.2011.02.064>.
- [37] V. Fanti et al. The beam and detector for the NA48 neutral kaon CP violation experiment at CERN. *Nucl. Instrum. Methods A*, 574(3):433, 2007. URL <https://doi.org/10.1016/j.nima.2007.01.178>.
- [38] J.R. Batley et al. Search for direct CP violating charge asymmetries in $K^\pm \rightarrow \pi^\pm \pi^+ \pi^-$ and $K^\pm \rightarrow \pi^\pm \pi^0 \pi^0$ decays. *Eur. Phys. J. C*, 52(4):875–891, 2007. URL <https://doi.org/10.1140/epjc/s10052-007-0456-7>.
- [39] Forthommel. Map of the cern accelerator complex. Wikimedia Commons (CC BY-SA 3.0), 15.08.2016 10:00. URL <https://commons.wikimedia.org/wiki/File:Cern-accelerator-complex.svg>.
- [40] G. Brianti. 50 years of synchrotrons: The CERN synchrotrons, 1997. URL <http://weblib.cern.ch/abstract?97-04B>.
- [41] L. Evans. The Large Hadron Collider. *New Journal of Physics*, 9(9):335, 2007. URL <https://doi.org/10.1088/1367-2630/9/9/335>.
- [42] D. Bédérède et al. High resolution drift chambers for the NA48 experiment at CERN. *Nucl. Instrum. Methods A*, 367(1-3):88–91, 1995. URL [https://doi.org/10.1016/0168-9002\(95\)00637-0](https://doi.org/10.1016/0168-9002(95)00637-0). Proceedings of the 7th International Wire Chamber Conference.
- [43] A. Romano. *Leptonic decays and kaon identification at the NA62 experiment at CERN*. PhD thesis, Birmingham U., 2012. URL <http://cds.cern.ch/record/1613783>. presented Dec 2012.
- [44] E. Griesmayer et al. Comparison of field calculations and measurements of a spectrometer magnet. *Nucl. Instrum. Methods A*, 361(3):466 – 471, 1995. URL [https://doi.org/10.1016/0168-9002\(95\)00142-5](https://doi.org/10.1016/0168-9002(95)00142-5).

- [45] G.D. Barr et al. Performance of an electromagnetic liquid krypton calorimeter based on a ribbon electrode tower structure. *Nucl. Instrum. Methods A*, 370(2-3):413 – 424, 1996. URL [https://doi.org/10.1016/0168-9002\(95\)00800-4](https://doi.org/10.1016/0168-9002(95)00800-4).
- [46] Konrad Kleinknecht. *Detektoren für Teilchenstrahlung*. Teubner, Wiesbaden, 4. edition, 2005. ISBN 3-8351-0058-0 ; 978-3-8351-0058-9.
- [47] V. Fanti et al. Performance of an electromagnetic liquid krypton calorimeter. *Nucl. Instrum. Methods A*, 344(3):507 – 520, 1994. URL [https://doi.org/10.1016/0168-9002\(94\)90871-0](https://doi.org/10.1016/0168-9002(94)90871-0).
- [48] J.B. Chèze. NA48 Drift Chamber Reconstruction Program, 1999. NA48 Documentation.
- [49] G. Unal. Neutral reconstruction, 1995. NA48 Note 95-10.
- [50] G. Unal. Reconstruction program for the LKr, 1997. NA48 Note 98-1.
- [51] B. Bloch-Devaux. Alpha and Beta corrections for NA48/2 Simulated Events, 2005. NA48 Note 05-05.
- [52] G. Lamanna. *Search for direct CP violation in charged kaons with NA48/2 experiment*. PhD thesis, Pisa U., 2006. URL <http://cds.cern.ch/record/1443013>. presented 20 Dec 2006.
- [53] E. Goudzovski. K_{e2} analysis status. NA62 Analysis Meeting, January 28 2009.
- [54] D. C. Carey. TURTLE (trace unlimited rays through lumped elements) : A Computer program for simulating charged particle beam transport systems, 1971. URL <http://inspirehep.net/record/69639>. FERMILAB-NAL-064, NAL-064.
- [55] C. Gatti. Monte carlo simulation for radiative kaon decays. *The European Physical Journal C - Particles and Fields*, 45(2):417–420, 2006. doi: 10.1140/epjc/s2005-02435-2. URL 10.1140/epjc/s2005-02435-2.
- [56] C. Gatti. MC generators for radiative kaon decas. *KLOE Note 194*, 2004.
- [57] F. James. Genbod / w515. In *CERNLIB: short writeups*, CERN Program Library. CERN, Geneva, 1996. URL <https://cds.cern.ch/record/450356>.
- [58] P. Golonka and Z. Was. PHOTOS Monte Carlo: a precision tool for QED corrections in Z and W decays. *The European Physical Journal C - Particles and Fields*, 45(1):97–107, 2006. URL <https://doi.org/10.1140/epjc/s2005-02396-4>.

- [59] S. Weinberg. New Test for $\Delta I = \frac{1}{2}$ in K^+ Decay. *Phys. Rev. Lett.*, 4:87–89, Jan 1960. URL <https://doi.org/10.1103/PhysRevLett.4.87>.
- [60] Application Software Group. GEANT - Detector Description and Simulation Tool. CERN Program Library Long Writeup W5013, 1993.
- [61] Evgueni Goudzovski. Private communication, 06 2014.
- [62] Dmitry Madigozhin. Private communication., 02 2016.
- [63] Andreas Winhart, Alan Norton, and Mauro Piccini. Private communication, 09 2016.
- [64] W.-M. Yao et al. Review of Particle Physics. *Journal of Physics G*, 33:1, 2006. URL <https://doi.org/10.1088/0954-3899/33/1/001>.
- [65] C. Amsler et al. Review of Particle Physics. *Physics Letters B*, 667(1), 2008. URL <https://doi.org/10.1016/j.physletb.2008.07.018>.
- [66] A. Sher et al. High Statistics Measurement of the $K^+ \rightarrow \pi^0 e^+ \nu$ (K_{e3}^+) Branching Ratio. *Phys. Rev. Lett.*, 91:261802, Dec 2003. URL <https://doi.org/10.1103/PhysRevLett.91.261802>.
- [67] The KLOE collaboration, F. Ambrosino, et al. Measurement of the absolute branching ratios for semileptonic K^\pm decays with the KLOE detector. *Journal of High Energy Physics*, 2008(02):098, 2008. URL <https://doi.org/10.1088/1126-6708/2008/02/098>.
- [68] J.R. Batley et al. Measurements of charged kaon semileptonic decay branching fractions $K^\pm \rightarrow \pi^0 \mu^\pm \nu$ and $K^\pm \rightarrow \pi^0 e^\pm \nu$ and their ratio. *The European Physical Journal C*, 50(2):329–340, 2007. URL <https://doi.org/10.1140/epjc/s10052-007-0253-3>.
- [69] J.R. Batley et al. Measurements of charged kaon semileptonic decay branching fractions $K^\pm \rightarrow \pi^0 \mu^\pm \nu$ and $K^\pm \rightarrow \pi^0 e^\pm \nu$ and their ratio. *The European Physical Journal C*, 52(4):1021–1023, 2007. URL <https://doi.org/10.1140/epjc/s10052-007-0454-9>. Erratum.
- [70] M. Moulson. $|V_{us}|$ from kaon decays. *arXiv:1301.3046v1 [hep-ex]*, 2013. URL <https://arxiv.org/abs/1301.3046>.
- [71] A. Aguilar-Arevalo et al. Improved Measurement of the $\pi \rightarrow e \nu$ Branching Ratio. *Phys. Rev. Lett.*, 115:071801, Aug 2015. URL <https://doi.org/10.1103/PhysRevLett.115.071801>.
- [72] R. Aaij et al. Test of Lepton Universality Using $B^+ \rightarrow K^+ \ell^+ \ell^-$ Decays. *Phys. Rev. Lett.*, 113:151601, Oct 2014. URL <https://doi.org/10.1103/PhysRevLett.113.151601>.

- [73] M. Koval. *Measurement of Neutral Pion Transition Form Factor and Contributions to TDAQ system at NA62 Experiment at CERN*. PhD thesis, Comenius University, Bratislava, 2016.